

Using the Structural Versatility of Lanthanide Metallocrowns to Tune Anion
Recognition, Self-Assembly, and Luminescence Properties

by

Joseph M. Jankolovits

A dissertation submitted in partial fulfillment
of the requirements for the degree of
Doctor of Philosophy
(Chemistry)
in The University of Michigan
2012

Doctoral Committee:

Professor Vincent L. Pecoraro, Chair
Professor Theodore G. Goodson, III
Associate Professor Naír Rodríguez-Hornedo
Assistant Professor Stephen Maldonado

© Joseph M. Janklovits
2012

Acknowledgements

There is an old Yiddish saying that “to a worm in a jar of horseradish, the world is horseradish.” For over four years, I’ve been immersed in a world of metallacrown horseradish. It’s been a true privilege to have the opportunity, resources, and freedom to explore this world so thoroughly and develop such a deep understanding of its behavior, limits, and possibilities. The research was, and still is, really really hard. However, the effort and results are incredibly fulfilling.

Vince has earned my deepest gratitude for the opportunity to learn from him and the respect and kindness he shown me. He has allowed me to make a lot of mistakes and break a lot of glassware in bringing this work to fruition. More so, he has given me tremendous freedom to develop the project on my own. His skill, passion, and success in science has been an inspiration. His guidance has shaped me into a better scientist than I thought possible.

I would also like to thank my committee members, Professors Goodson, Rodríguez-Hornedo, and Maldonado for their respect, advice, and encouragement. I am particularly appreciative of the assistance Stephen has provided in developing the cyclic voltammetry experiments and the help that Ted and his group have offered for luminescence characterization.

Endless appreciation goes out to our crystallographer, Jeff Kampf. Metallacrowns are a crystallographic nightmare, and teaching students to solve and refine metallacrown structures can’t be much better. Jeff has provided extensive time and expertise in handling the barrage of samples, twinning issues, datasets, and questions that I’ve subjected him to. He’s also been a great friend.

Thanks go out to Christopher Andolina and Kenneth Raymond for their tremendous help with the characterization of the luminescence of the $\text{LnZn}_{16}\text{L}_{16}$

complexes. Thanks also to James Windak for maintaining the electrospray ionization mass spectrometer.

I'd also like to thank the Pecoraro group for the support and good times through the years. The early mentoring from Sun, Saumen, and Curtis was highly beneficial for getting me started. Ted, thanks for inviting me to your wedding... and for being with me on the metallocrown project every step of the way. I'm glad I got to bounce ideas off you, talk sports, and work together on the magnetism of these zinc complexes. I've been happy to have worked with a number of undergraduates, and I am very appreciative of the work and dedication they put into their projects. The work of Joe Grant and Peng Zhao has been particularly fruitful in shaping parts of this thesis.

Lots of love goes out to my friends and family, my world outside of the metallocrown horseradish. I've gotten to move far away from home, live comfortably, and bury myself in books and beakers, which is a testament to how much my parents have given me. Thanks for everything. To Rachel: Our time together in Ann Arbor has been my happiest time in graduate school, while our time spent miles apart has been my most productive. Thanks for being there, and Vince thanks you for not being there. Thanks also go to the Ann Arbor contingent of the Grinnell Tennis team and the other friends I made on the court. Hitting that fuzzy yellow ball with all of you has been incredibly important to me. Lastly, Spencer and Inger, Eric and Libby, the Spinei's, and other Ann Arbor friends have my gratitude.

Table of Contents

| | |
|--|-----|
| Acknowledgements..... | ii |
| List of Figures..... | vii |
| List of Tables..... | xiv |
| Abstract..... | xvi |
| Chapter | |
| I. Molecular Recognition in Supramolecular Hosts, Self-Assembly, and Metallacrowns..... | 1 |
| Molecular Recognition..... | 1 |
| Organic Macrocycles in Host-Guest Chemistry..... | 2 |
| Metallocavitands..... | 6 |
| Self Assembled Macrocycles..... | 7 |
| Self-Assembled Hosts and Metallacrowns..... | 9 |
| Metallacrowns as Supramolecular Hosts..... | 13 |
| Applications of Supramolecular Hosts and Self-Assembled Systems..... | 15 |
| Thesis Aims..... | 21 |
| Figures..... | 25 |
| References..... | 34 |
| II. Influencing the Size and Anion Selectivity of Dimeric Ln(III)[15- Metallacrown-5] Compartments through Systematic Variation of the Host Side Chains and Central Metal..... | 42 |
| Introduction..... | 42 |
| Experimental..... | 46 |
| Results and Discussion..... | 55 |
| Compartments..... | 55 |
| Side Chain Length Constrains the Compartment Height..... | 56 |
| Factors Influencing the Number of Encapsulated Guests..... | 60 |
| ESI-MS of Ln(III)[15-MC-5](guest) complexes..... | 64 |

| | |
|---|------------|
| Mesostructured Assemblies of Ln(III)[15-MC-5] Compartments with Unsaturated Dicarboxylate Guests..... | 65 |
| Conclusions..... | 69 |
| Figures..... | 72 |
| References..... | 88 |
| III. Characterizing the Side Chain Dependent Guest Binding Affinity and Enantioselectivity of Ln(III)[15-Metallacrown-5] Metallocavitands with a Novel Voltammetric Competitive Binding Assay..... | 90 |
| Introduction..... | 90 |
| Experimental..... | 94 |
| Results..... | 101 |
| Establishing the Voltammetric Assay..... | 101 |
| Selective Binding of α -Amino Acid Analogs..... | 108 |
| Side Chain Dependent Guest Affinity and Selectivity | 109 |
| Discussion..... | 113 |
| Establishing the Voltammetric Assay..... | 113 |
| Selective Binding of α -Amino Acid Analogs..... | 118 |
| Side Chain Dependent Guest Affinity and Selectivity | 121 |
| Conclusion | 124 |
| Figures..... | 126 |
| References..... | 141 |
| IV. Solvent Directed Assembly of Luminescent Lanthanide Metallacrowns from Building Blocks with Incompatible Symmetry Preferences and Open Coordination Sites..... | 144 |
| Introduction..... | 144 |
| Experimental..... | 148 |
| Results..... | 163 |
| Assembly and Structures with Zn(II) and picHA | 163 |
| Assembly and Structures of Ln(III)[15-MC-5] complexes | 164 |
| Solvent Dependent Assembly and Structures of other LnMCs .. | 165 |
| Solution Integrity of MCs with Zn(II) Ring Ions..... | 170 |
| LnZn ₁₆ L ₁₆ Solution Integrity..... | 173 |
| Zn ₅ L ₄ Conversion to LnMCs | 175 |

| | |
|--|-----|
| Luminescence of the LnZn ₁₆ L ₁₆ | 177 |
| Discussion..... | 178 |
| Synthesis..... | 178 |
| Structural Aspects of Ln(III)[15-MC _{Zn(II)} -5] Complexes..... | 179 |
| Structural Aspects of Complexes with [12-MC _{Zn(II)} -4] Motifs... | 180 |
| Structural Aspects of the Ln ₂ Cluster..... | 186 |
| Theoretical Framework for Solvent Directed Assemblies with Symmetry Incompatible Building Blocks..... | 188 |
| Solvent Directed Assembly of PicHA, Zn(II), and Ln(III)..... | 190 |
| Solution Integrity of MCs with Zn(II) Ring Ions..... | 193 |
| Zn ₅ L ₄ Stability..... | 193 |
| LnMC Stability..... | 196 |
| Luminescence of the LnZn ₁₆ L ₁₆ | 198 |
| Prospects for MCs with Zn(II) Ring Ions in Second Harmonic Generation Applications..... | 201 |
| Conclusion..... | 203 |
| Figures..... | 205 |
| References..... | 240 |
| V. Conclusions and Future Directions..... | 244 |
| Conclusions and Future Directions..... | 244 |
| Figures..... | 255 |
| References..... | 258 |

List of Figures

| | |
|--|----|
| Figure 1.1 Depictions of the crystal structure of the pentameric cholera toxin (left) and the cholera toxin (right) with the catalytically active enzyme bound in the center of the cholera toxin pentamer. ³ | 25 |
| Figure 1.2 Representations of various crown ethers. | 25 |
| Figure 1.3. An N-substituted lariat ether (top-left), [2, 2, 1] cryptand (top-right), a spherand (bottom-left), and a podand (bottom-right). | 26 |
| Figure 1.4 Depictions of a cyclodextrin (top left), cucurbituril (top right), calix[4]arene (bottom left), and [4]resorcinarene (bottom right). | 26 |
| Figure 1.5 A representative supramolecular host that binds guests through multiple hydrogen bond donor groups. | 27 |
| Figure 1.6 Representations of Kersting's binuclear macrocyclic thiophenolate metallocavitand (depicted with a bridging carboxylate guest, left) and Rebek's Zn(II)-resorcinarene (shown as an calculated structure with a phosphocholine ester, one wall of the host was removed for clarity). | 27 |
| Figure 1.7 Diagram of Fujita's molecular square (right) and self-assembled M ₆ L ₄ octahedron (left). | 28 |
| Figure 1.8 Diagram and crystal structure of Raymond's M ₄ L ₆ tetrahedron. Images taken from reference. | 28 |
| Figure 1.9 Diagram of a weak-link macrocycle that undergoes a structural change in the presence of CO. | 28 |
| Figure 1.10 Diagrams of the 9-MC-3 (top), 12-MC-4 (middle), and 15-MC-5 (bottom) motifs that highlight the MC ring (left) and the ligand connectivity that generates the MC (right). | 29 |
| Figure 1.11 Crystal structures of [9-MC _{V(V), shi-3}] and Mn(II)[12-MC _{Mn(III), shi-4}](acetate). | 29 |
| Figure 1.12 Chemdraw diagram and crystal structure of Gd(III)[15-MC _{Cu(II), L-pheHA-5}](NO ₃) _{1.5} (OH) _{1.5} | 30 |
| Figure 1.13 Crystal structure of an [18-MC _{Mn(III), salicylhydrazidate-6}] (left), NH ₄ [15-MC _{Cu(II), di-<i>t</i>-butyl-ketipinate-6}] sandwich complex (center), and a Na(III) ₃ [12-MC _{Ga(III), shi-4}] ₂ (OH) ₄ metallacryptate (right). | 30 |
| Figure 1.14 Diagram of the relationship between fused chelate ring size and the MC size. | 31 |

| | |
|---|----|
| Figure 1.15 Diagram of Severin's 12-MC-3 complex and crystal structure of the MC with a LiF guest bound in the interior. | 31 |
| Figure 1.16 Crystal structures of the dimeric Gd(III)[15-MC _{Cu(II), L-tyrHA-5}] compartment with encapsulated nitrate guests. | 31 |
| Figure 1.17 Crystal structures of Gd(III)[15-MC _{Cu, pheHA-5}] compartments with nitrate, terephthalate, and naphthalene dicarboxylate guests. | 32 |
| Figure 1.18 Crystal structures of La(III)[15-MC _{Cu(II), pheHA-5}](hydrocinnamate) ₂ (NO ₃) and Eu(III)[15-MC _{Cu(II), pheHA-5}](benzoate) ₃ complexes. | 32 |
| Figure 1.19 <i>cis</i> -bromination reaction in the interior of Kersting's metallocavitand (top) and the tandem Nazarov cyclization and Diels-Alder reaction catalyzed by the M ₄ L ₆ tetrahedron. | 33 |
| Figure 1.20 Crystal structure of the Gd(III)[15-MC _{Cu(II), L-pheHA-5}](isonicotinate) ₂ (NO ₃) ₂ complex displaying the alignment of dipolar isonicotinate guests such that there is a net dipole moment in the chiral compartment. | 33 |
| Figure 2.1 Chemdraw diagrams of (a) Ln(III)[15-MC _{Cu(II), S-α-aminoHA-5}], (b) S-pgHA, (c) S-pheHA, (d) S-hpheHA, (e) isonicotinate, (f) terephthalate, (g) btDC. | 75 |
| Figure 2.2 Crystal structure and compartment diagrams of La(III)[15-MC _{Cu(II), pheHA-5}](btDC) showing the binding of the <i>trans</i> - (top) and <i>cis</i> -rotomers (bottom). | 76 |
| Figure 2.3 Crystal structure of Gd(III)[15-MC _{Cu(II), pgHA-5}](terephthalate). | 76 |
| Figure 2.4 Crystal structure and compartment diagrams for La(III)[15-MC _{Cu(II), pgHA-5}](btDC) showing the MC dimers bridged by <i>cis</i> -btDC (top) and <i>trans</i> -btDC (bottom). | 77 |
| Figure 2.5 Highlight of intermolecular interactions between the pgHA side chains and btDC in the La(III)[15-MC _{Cu(II), pgHA-5}](btDC) crystal structure. | 77 |
| Figure 2.6 Top) Crystal structure and compartment diagram of Gd(III)[15-MC _{Cu(II), hpheHA-5}](btDC), and bottom) highlight of the CH-O interaction between the hpheHA side chain and a carboxylate oxygen on btDC ²⁻ | 78 |
| Figure 2.7 Thermal ellipsoid plot and compartment diagram of La(III)[15-MC _{Cu(II), hpheHA-5}](isonicotinate). | 79 |
| Figure 2.8 Crystal structure and compartment diagram of La(III)[15-MC _{Cu(II), pheHA-5}](isonicotinate). | 79 |
| Figure 2.9 Crystal structure and compartment diagram of La(III)[15-MC _{Cu(II), pgHA-5}](isonicotinate). | 80 |
| Figure 2.10 Crystal structure and compartment diagram of La(III)[15-MC _{Cu(II), pheHA-5}](terephthalate). | 82 |
| Figure 2.11 Crystal structures and compartment diagrams of top) Gd(III)[15-MC _{Cu(II), hpheHA-5}](terephthalate), and bottom) La(III)[15-MC _{Cu(II), hpheHA-5}](terephthalate). ... | 82 |
| Figure 2.12 Mass spectrum of La(III)[15-MC _{Cu(II), pheHA-5}](terephthalate) taken in 4:1 methanol/water (v/v) injected via syringe pump. | 83 |

| | |
|---|-----|
| Figure 2.13 Chemdraw diagrams of adipate, pimelate, suberate, azelate, and sebacate. . | 83 |
| Figure 2.14 Crystal structure images of the $\text{La(III)[15-MC}_{\text{Cu(II), pheHA-5}}\text{](pimelate)}$ complex highlighting different aspect of the mesostructured assembly..... | 84 |
| Figure 2.15 UV-VIS absorption spectra from a guest absorption experiment of a 5.8×10^{-5} M methyl orange sodium salt solution in acetone in the absence of the mesostructure (blue) and after soaking with the mesostructure for 18 hours (red). | 85 |
| Figure 2.16 Crystal structure of top) $\text{Dy(III)[15-MC}_{\text{Cu(II), pheHA-5}}\text{](pimelate)}$ | 86 |
| Figure 2.17 Crystal structures of $\text{Gd(III)[15-MC}_{\text{Cu(II), hpheHA-5}}\text{](adipate)}$ (left) and $\text{La(III)[15-MC}_{\text{Cu(II), pgHA-5}}\text{](adipate)}$ (right). | 87 |
| Figure 3.1 Chemdraw diagrams of the $\text{Ln(III)[15-MC}_{\text{Cu(II), L-pheHA-5}}\text{]$ host and guests discussed in this chapter. | 126 |
| Figure 3.2 Chemdraw diagrams representing the binding modes of carboxylate guests with $\text{Ln(III)[15-MC}_{\text{Cu(II), pheHA-5}}\text{]$ hosts. | 127 |
| Figure 3.3 Cyclic voltammograms of FcC^- in the absence (a) and presence (b) of 10.7 equivalents of $\text{Dy(III)[15-MC}_{\text{Cu(II), pheHA-5}}\text{]Cl}_3$ taken in 1:1 methanol and 0.1 M aq MOPS buffer, pH 7.5, 0.1 M KCl, 25 °C. | 127 |
| Figure 3.4 Plot of $E_{1/2}$ versus the concentration of $\text{Ln(III)[15-MC}_{\text{Cu(II), pheHA-5}}\text{]Cl}_3$ from MC binding CV titrations to FcC^- in 1:1 methanol and 0.1 M aq MOPS buffer, pH 7.5, 0.1 M KCl, 25 °C..... | 128 |
| Figure 3.5 CV's from a competition titration of a) FcC^- with 10.8 equivalents of $\text{Dy(III)[15-MC}_{\text{Cu(II), pheHA-5}}\text{]Cl}_3$ and b) after the addition of 170 equivalents of sodium benzoate in 1:1 methanol and 0.1 M aq MOPS buffer, pH 7.5, 0.1 M KCl, 25 °C. | 129 |
| Figure 3.6 Plot of $E_{1/2}$ vs. [benzoate] from a competition titration of the guest to a solution of FcC^- and 10.8 equivalents of $\text{Dy(III)[15-MC}_{\text{Cu(II), pheHA-5}}\text{]Cl}_3$ in 1:1 methanol and 0.1 M aq MOPS buffer, pH 7.5, 0.1 M KCl, 25 °C. | 130 |
| Figure 3.7 Representation of the crystal structure of $\text{La(III)(FcC}^-)_2\text{[15-MC}_{\text{Cu(II), pheHA-5}}\text{](NO}_3\text{)}$ | 131 |
| Figure 3.8 Representation of the crystal structure of $\text{La(III)(FcDC}^{2-})\text{[15-MC}_{\text{Cu(II), pheHA-5}}\text{](NO}_3\text{)}$ | 131 |
| Figure 3.9 Representation of the crystal structure of $\text{Dy(III)(benzoate)}_2\text{[15-MC}_{\text{Cu(II), pheHA-5}}\text{](benzoate)}_{0.75}\text{Cl}_{0.25}$ | 132 |
| Figure 3.10 Representation of the crystal structure of $\text{La(III)(FcDC}^{2-})\text{[15-MC}_{\text{Cu(II), pheHA-5}}\text{](NO}_3\text{)}$ highlighting the orientation of the ferrocene group in the hydrophobic cavity. | 132 |
| Figure 3.11 Representation of the X-ray crystal structures of $\text{Gd(III)[15-MC}_{\text{Cu(II), pheHA-5}}\text{]}$ with S-phenylalanine (top) and R- phenylalanine (bottom) that highlight hydrogen bonding interactions (purple lines). | 133 |
| Figure 3.12 Chemdraw diagrams of ligands investigated in the side-chain substitution studies. | 135 |

| | |
|---|-----|
| Figure 3.13 Structural representations of A) 1-picHA, B) 1-pgHA, C) 1-pheHA, and D) 1-hpheHA taken from previously crystal structures..... | 136 |
| Figure 3.14 Images of the crystal structure of La(III)[15-MC _{Cu(II), hpheHA-5}](FcC ⁻) showing the two crystallographically independent monomeric metallocavitands with two FcC ⁻ guests (top) and one FcC ⁻ (bottom) encapsulated in the hydrophobic cavity. | 136 |
| Figure 3.15 CVs from a MC binding titration showing FcC ⁻ in the presence of 0 equivalents (A) and 10 equivalents (B) of Gd(III)[15-MC _{Cu(II), hpheHA-5}]Cl ₃ in pH 8.5 0.1 M sodium triflate solution containing 60% ACN, 40 % 0.1 M aqueous EPPS buffer. | 137 |
| Figure 3.16 Plot of E _{1/2} vs. [Gd(III)[15-MC _{Cu(II), hpheHA-5}]Cl ₃] from a MC binding CV titration in pH 8.5 0.1 M sodium triflate solution containing 60% ACN, 40 % 0.1 M aqueous EPPS buffer. | 138 |
| Figure 3.17 CVs of FcC ⁻ from a competitive binding titration in the presence of 4.7 eq Gd(III)[15-MC _{Cu(II), hpheHA-5}]Cl ₃ and 0 eq (A) and 200 eq (B) of S-mandelate in pH 8.5 0.1 M sodium triflate solution containing 60% ACN, 40 % 0.1 M aqueous EPPS buffer. | 139 |
| Figure 3.18 Plot of E _{1/2} vs. [S-mandelate] from a competitive binding CV titration performed in pH 8.5 0.1 M sodium triflate solution containing 60% ACN, 40 % 0.1 M aqueous EPPS buffer..... | 139 |
| Figure 4.1 Diagrams displaying the design strategy for MCs based on the chelate ring geometry. | 205 |
| Figure 4.2 Chemdraw representations of picHA (left) and quinHA (right). | 205 |
| Figure 4.3 Mass spectra of the assembly of 1:2:1 H ₂ picHA, triethylamine, and Zn(NO ₃) ₂ in the indicated solvents at room temperature after 24 hours. | 208 |
| Figure 4.4 Chemdraw diagram (left) and crystal structure images of the Zn ₅ (picHA) ₄ (OTf) ₂ complex viewed down the convex face (center) and from the side (right)..... | 210 |
| Figure 4.5 Chemdraw diagram (top left) and crystal structure images of the Zn ₅ (quinHA) ₄ (BF ₄) ₂ complex viewed down the convex face (top right) and from the side (bottom)..... | 210 |
| Figure 4.6 Mass spectra of assembly reactions at room temperature of 5:10:5:1 H ₂ picHA, triethylamine, Zn(NO ₃) ₂ , and La(NO ₃) ₃ in the indicated solvents after 24 hours. | 213 |
| Figure 4.7 Mass spectra of assembly reactions performed at 65 °C of 5:10:5:1 H ₂ picHA, triethylamine, Zn(NO ₃) ₂ , and La(NO ₃) ₃ in the indicated solvents after 24 hours. | 213 |
| Figure 4.8 Chemdraw diagram (top left) and crystal structure images of the EuZn ₅ (picHA) ₅ (NO ₃) ₃ complex highlighting the 15-MC-5 motif (top right) and ruffled topology (center)..... | 214 |

| | |
|---|-----|
| Figure 4.9 Mass spectra of assembly reactions at room temperature of 5:10:5:1 H ₂ picHA, triethylamine, Zn(NO ₃) ₂ , and Y(NO ₃) ₃ in the indicated solvents after 24 hours. | 214 |
| Figure 4.10 Mass spectra of assembly reactions performed at 65 °C of 5:10:5:1 H ₂ picHA, triethylamine, Zn(NO ₃) ₂ , and Y(NO ₃) ₃ in the indicated solvents after 24 hours. | 215 |
| Figure 4.11 Chemdraw diagram (left) and crystal structure images of the DyZn ₅ (quinHA) ₅ (NO ₃) ₃ complex highlighting the 15-MC-5 motif (left) and ruffled topology (right). | 215 |
| Figure 4.12 Chemdraw diagram (left) and crystal structure images of the DyZn ₄ (quinHA) ₄ (DMF) ₄ (NO ₃) ₃ complex. | 216 |
| Figure 4.13 Chemdraw diagram (left) and crystal structure images of the LaZn ₈ (picHA) ₈ Cl ₂ complex viewed perpendicular to the concave 12-MC-4 units (right). | 216 |
| Figure 4.14 Crystal structure images of the DyZn ₈ (quinHA) ₈ (OH) ₃ complex shown with elemental colors and in orange to highlight the 12-MC-4 units. | 217 |
| Figure 4.15 Crystal structure images of the DyZn ₄ (quinHA) ₄ (12-crown-4)(py) ₄ | 217 |
| Figure 4.16 Crystal structure images of the Dy ₂ Zn ₉ (quinHA) ₁₀ complex. | 218 |
| Figure 4.17 Comparisons of the different structural motifs in the Dy ₂ Zn ₉ (quinHA) ₁₀ (OH) cluster (top left, bottom left) with the Ln(III)[14-MC _{Mn(III),shi} -5](OH) (top right) and Dy(III)[15-MC _{Zn(II),quinHA} -5] (bottom right) complexes. | 219 |
| Figure 4.18 Crystal structure images of the TbZn ₁₆ (picHA) ₁₆ (OTf) ₃ complex viewed from the side (left) and down the C4 axis (right) in colors meant to highlight the 12-MC-4 units (orange), 24-MC-8 (right), and central Tb(III) ion (green). | 220 |
| Figure 4.19 Highlight of the separate Tb(III)[12-MC-4] ₂ sandwich complex (top-left), the [24-MC-8] (top-right) from the crystal structure of the TbZn ₁₆ (picHA) ₁₆ and a diagram of the alternating Λ and Δ chirality in the 24-MC-8 (bottom). | 220 |
| Figure 4.20 Crystal structure images of the Zn ₄ (picHA) ₂ (acetate) ₄ (DMF) ₂ complex highlighting the along the picHA ligand plane and perpendicular to the plane | 221 |
| Figure 4.21 ESI-MS of isolated MCs in the indicated solvents. | 221 |
| Figure 4.22 ¹ H NMR and ESI-MS spectra of the titration of 0.8 equivalents of La(NO ₃) ₃ to Zn ₅ (picHA) ₄ (OTf) ₂ in pyridine-D ₅ | 222 |
| Figure 4.23 Mass spectra from ligand exchange experiments of the Zn ₅ (picHA) ₄ (OTf) ₂ and four equivalents of H ₂ quinHA in methanol | 223 |
| Figure 4.24 ¹ H NMR and ESI-MS spectra of the titration of 0.8 equivalents of La(NO ₃) ₃ to Zn ₅ (picHA) ₄ (OTf) ₂ in 4:1 D ₂ O/pyridine-D ₅ | 224 |
| Figure 4.25 ¹ H NMR and ESI-MS spectra of the titration of 0.8 equivalents of Y(NO ₃) ₃ to Zn ₅ (picHA) ₄ (OTf) ₂ in methanol-D ₄ | 225 |

| | |
|---|-----|
| Figure 4.26 ^1H NMR and ESI-MS spectra of the titration of 0.8 equivalents of $\text{La}(\text{NO}_3)_3$ to $\text{Zn}_5(\text{picHA})_4(\text{OTf})_2$ in methanol- D_4 . | 226 |
| Figure 4.27 Mass spectra showing evidence for ligand exchange in the $\text{LaZn}_{16}(\text{picHA})_{16}(\text{OTf})_3$ (top) and $\text{YZn}_{16}(\text{picHA})_{16}(\text{OTf})_3$ (bottom) complexes. | 227 |
| Figure 4.28 ESI-MS of the $\text{YbZn}_{16}(\text{picHA})_{16}(\text{OTf})_3$ in aqueous HEPES buffer (top) and ^1H NMR spectrum of the $\text{YZn}_{16}(\text{picHA})_{16}$ in D_2O (bottom). | 227 |
| Figure 4.29: ^1H NMR and ESI-MS spectra of the titration of 0.8 equivalents of $\text{Y}(\text{NO}_3)_3$ to $\text{Zn}_5(\text{picHA})_4(\text{OTf})_2$ in pyridine- D_5 . | 228 |
| Figure 4.30 ^1H NMR and ESI-MS spectra of the titration of 0.8 equivalents of $\text{La}(\text{NO}_3)_3$ to $\text{Zn}_5(\text{picHA})_4(\text{OTf})_2$ in 9:1 DMF/pyridine. | 229 |
| Figure 4.31 ^1H NMR and ESI-MS spectra of the titration of 0.8 equivalents of $\text{Y}(\text{NO}_3)_3$ to $\text{Zn}_5(\text{picHA})_4(\text{OTf})_2$ in 9:1 DMF/pyridine. | 230 |
| Figure 4.32 ^1H NMR and ESI-MS spectra of the titration of 0.8 equivalents of $\text{Y}(\text{NO}_3)_3$ to $\text{Zn}_5(\text{picHA})_4(\text{OTf})_2$ in 4:1 D_2O /pyridine- D_5 . | 231 |
| Figure 4.33 ^1H NMR and ESI-MS spectra of the titration of 0.8 equivalents of $\text{La}(\text{NO}_3)_3$ to $\text{Zn}_5(\text{picHA})_4(\text{OTf})_2$ in DMF. | 232 |
| Figure 4.34 ^1H NMR and ESI-MS spectra of the titration of 0.8 equivalents of $\text{Y}(\text{NO}_3)_3$ to $\text{Zn}_5(\text{picHA})_4(\text{OTf})_2$ in DMF. | 233 |
| Figure 4.35 Absorption (top left) and emission spectra (top right) for $\text{YbZn}_{16}(\text{picHA})_{16}(\text{OTf})_3$ in methanol at 25.0 °C. | 234 |
| Figure 4.36 Emission spectra (4 nm bandpass) of $\text{YbZn}_{16}(\text{picHA})_{16}(\text{OTf})_3$ at 25.0 °C in MeOH (-) and CD_3OD (-). | 234 |
| Figure 4.37 Crystal structure images of $\text{Eu}(\text{III})[15\text{-MC}_{\text{M}(\text{II}),\text{picHA}-5}](\text{NO}_3)_3$ complexes (M = Ni (top), Cu (middle), and Zn (bottom)) viewed perpendicular and parallel to the C_5 axis. | 235 |
| Figure 4.38 Crystal structure images of the <i>P</i> (left) and <i>M</i> (right) enantiomers of the inherently chiral $\text{Zn}(\text{II})[12\text{-MC}_{\text{Zn}(\text{II}),\text{picHA}-4}](\text{OTf})_2$ viewed down the concave face. | 236 |
| Figure 4.39 Overlay of $\text{Ln}(\text{III})[12\text{-MC}-4]$ units of the $\text{DyZn}_8(\text{picHA})_8(\text{OH})_3$ (purple) and $\text{LaZn}_8(\text{picHA})_8\text{Cl}_3$ (green) complexes. | 236 |
| Figure 4.40 A minimal scheme of a possible assembly pathway for the conversion of the Zn_5L_4 to the monolanthanide MCs. | 237 |
| Figure 4.41 Chart that relates the LnMC that selectively assembles in solution to the presence of DMF and/or pyridine (or aqueous pyridine). | 237 |
| Figure 4.42 A model of the proposed $\text{Ln}(\text{III})[12\text{-MC}_{\text{Zn}(\text{II}),\text{picHA}-4}][24\text{-MC}_{\text{Zn}(\text{II}),\text{picHA}-8}](\text{DMF})_4$ structure for the $\text{LnZn}_{12}\text{L}_{12}$. | 238 |
| Figure 4.43 Fluorescence spectra of the $\text{GdZn}_{16}(\text{picHA})_{16}$ in 1:4 methanol/ethanol at 77 K with a no time delay (top left) and with 100 μs time delay (top right) and cyclic voltammograms of $\text{LnZn}_{16}(\text{picHA})_{16}(\text{OTf})_3$ complexes in 0.1 M aqueous KCl. | 238 |

| | |
|--|-----|
| Figure 4.44 Thermogravimetric analysis plot showing mass loss of the $\text{YZn}_4(\text{quinHA})_4(\text{DMF})_4(\text{NO}_3)_3$ as a function of temperature. | 239 |
| Figure 5.1 Crystal structures of $\text{Gd(III)[15-MC}_{\text{Cu(II),hpheHA-5}}\text{](ferrocenedicarboxylate)}$ (left), $\text{La(III)[15-MC}_{\text{Cu(II),pheHA-5}}\text{](ferrocenedicarboxylate)}^{15}$ (center) and $\text{Gd(III)[15-MC}_{\text{Cu(II),pheHA-5}}\text{](cobaltoceniumdicarboxylate)}$ (right) that demonstrate how the side chain length and guest charge can influence how the MC host recognizes metallocene dicarboxylate guests. | 255 |
| Figure 5.2 General Ln(III)[15-MC-5] ligand designs that could lead to enhanced chiral selectivity. | 255 |
| Figure 5.3 Diagrams of reactions that could probe catalysis with Ln(III)[15-MC-5] complexes. | 256 |
| Figure 5.4 H_2picHA derivatives that incorporate electron donating groups for sensitization of Ln(III) ions via charge transfer states. | 256 |
| Figure 5.5 ESI-MS showing the MCs that assemble in reaction mixtures of pheHA, $\text{Zn(NO}_3)_2$, and $\text{La(NO}_3)_3$ in the indicated ratios and solvents. | 257 |
| Figure 5.6 Crystal structure of a $\text{LaZn}_4(\text{L-pheHA})_2(\text{L-HpheHA})_2(\text{NO}_3)_5(\text{py})_7$ complex viewed perpendicular and parallel to the saddled 16-MC-6 ring. | 257 |

List of Tables

| | |
|--|-----|
| Table 2.1 Crystal structure data for [a] Gd(III)[15-MC _{Cu(II)} , pgHA-5](terephthalate), [b] La(III)[15-MC _{Cu(II)} , pgHA-5](btDC), [c] Gd(III)[15-MC _{Cu(II)} , hpheHA-5](btDC), [d] La(III)[15-MC _{Cu(II)} , hpheHA-5](isonicotinate)..... | 72 |
| Table 2.2 Crystal structure data for [a] La(III)[15-MC _{Cu(II)} , pheHA-5](isonicotinate), [b] La(III)[15-MC _{Cu(II)} , pgHA-5](isonicotinate), [c] La(III)[15-MC _{Cu(II)} , pheHA-5](terephthalate), [d]..... | 73 |
| Table 2.3 Crystal structure data for [a] Gd(III)[15-MC _{Cu(II)} , hpheHA-5](terephthalate), [b] La(III)[15-MC _{Cu(II)} , pheHA-5](btDC), [c] Dy(III)[15-MC _{Cu(II)} , pheHA-5](pimelate). | 74 |
| Table 2.4 Size and guest inclusion parameters for Ln(III)[15-MC-5] compartments. | 81 |
| Table 2.5 Unit cell parameters for Ln(III)[15-MC _{Cu(II)} -5] complexes with adipate and pimelate guests. | 85 |
| Table 2.6 Unit cell parameters for Ln(III)[15-MC _{Cu(II)} -5] clathratocomplexes with suberate, azelate, and sebacate guests. | 86 |
| Table 3.1 Binding constants between Ln(III)[15-MC _{Cu(II)} ,pheHA-5] and FcC ⁻ or FcC and the diffusion coefficient for the LnMC-FcC ⁻ complex determined in 1:1 methanol and 0.1 M aq MOPS buffer, pH 7.5, 0.1 M KCl, 25 °C..... | 129 |
| Table 3.2 Binding constants between Ln(III)[15-MC _{Cu(II)} ,pheHA-5] and benzoate determined by the competitive CV assay, ITC, and Fluorimetry..... | 130 |
| Table 3.3 Thermodynamic data from competition titrations of Gd(III)[15-MC _{Cu(II)} ,pheHA-5] and α -amino acid analogues..... | 134 |
| Table 3.4 Enantiomeric discrimination of the α -amino acid analog guests by Gd(III)[15-MC _{Cu(II)} ,pheHA-5]. | 135 |
| Table 3.5 Thermodynamic data for guest binding to Gd(III)[15-MC _{Cu(II)} -5] determined with the CV competitive binding assay in pH 8.5 0.1 M sodium triflate solution containing 60% ACN, 40 % 0.1 M aqueous EPPS buffer..... | 138 |
| Table 3.6 Thermodynamic data on the binding of S- and R-mandelate to Gd(III)[15-MC _{Cu(II)} -5] determined with the competitive binding CV assay in pH 8.5 0.1 M sodium triflate solution containing 60% ACN, 40 % 0.1 M aqueous EPPS buffer. | 140 |
| Table 3.7 K _S /K _R values for mandelate binding to Gd(III)[15-MC _{Cu(II)} -5] determined with the competitive binding CV assay in pH 8.5 0.1 M sodium triflate solution containing 60% ACN, 40 % 0.1 M aqueous EPPS buffer. | 140 |
| Table 4.1 Crystallographic data for DyZn ₄ (quinHA) ₄ (DMF) ₄ (NO ₃) ₃ , TbZn ₁₆ (picHA) ₁₆ (OTf) ₃ , ErZn ₁₆ (picHA) ₁₆ (OTf) ₃ , Zn ₄ (picHA) ₂ (acetate) ₂ (DMF) ₂ | 206 |

| | |
|--|-----|
| Table 4.2 Crystallographic data for DyZn ₄ (quinHA) ₄ (12-crown-4)(OTf) ₃ , DyZn ₅ (quinHA) ₅ (NO ₃) ₃ , EuZn ₅ (picHA) ₅ (NO ₃) ₃ , DyZn ₁₆ (picHA) ₁₆ (OTf) ₃ | 207 |
| Table 4.3 MC species observed by ESI-MS for the reaction of H ₂ picHA, triethylamine, Zn(NO ₃) ₂ , and Ln(NO ₃) ₃ (5:10:5:1 ratio) in the indicated solvent..... | 209 |
| Table 4.4 Selected geometric parameters for selected MCs with Zn(II) ring metals. | 211 |
| Table 4.5 Selected bond lengths and angles in Eu(III)[15-MC _{M(II),picHA-5}](NO ₃) ₃ complexes where M = Ni, Cu, Zn. | 212 |

Abstract

Using the Structural Versatility of Lanthanide Metallocrowns to Tune Anion Recognition, Self-Assembly, and Luminescence Properties

by

Joseph M. Jankolovits

Chair: Vincent L. Pecoraro

Natural and artificial supramolecular systems utilize weak, reversible interactions to control the organization of matter and facilitate separations, catalysis, and materials design. Metallocrowns are metal dense macrocycles assembled through dative bonds. This thesis explores how structural changes to the building blocks can enhance the solid state organization, anion recognition, structure, and physical properties of the metallocrown.

A systematic crystallographic study was performed to assess how the side chain and central metal influences the size and selectivity of dimeric Ln(III)[15-MC-5] compartments. Phenyl side chains with 0-2 methylene spacers generate dimeric compartments ranging from 9.7 to 15.2 Å in height that selectively encapsulate 4.3 to 9.2 Å long dicarboxylate guests. Up to five carboxylate guests can be encapsulated based on

considerations of side chain sterics and the coordination number of the central metal. Solution studies were performed with a novel voltammetric binding assay. Chiral Gd(III)[15-MC_{Cu(II),L-pheHA-5}]Cl₃ metallocavitands bind α -amino acid analogs with affinity constants ranging from 70 ± 7 to $3260 \pm 70 \text{ M}^{-1}$ in 50% aqueous methanol for N-acetyl-R-phenylalanine and S-mandelate, respectively. Increasing the methylene spacers in the phenyl side chain from 0 to 2 increases the binding constant for benzoate from 800 ± 100 to $3000 \pm 300 \text{ M}^{-1}$ in 40% aqueous acetonitrile. Mandelate enantioselectivity is enhanced (K_S/K_R up to 2.2 ± 0.6) by changing the phenyl side chain.

Optically transparent lanthanide metallocrowns with Zn(II) ring metals were assembled for their luminescence properties. Six distinct metallocrown motifs were assembled from picoline hydroxamic acid, Zn(II), Ln(III) through a strict solvent dependence and structurally characterized: Zn(II)[12-MC-4], Ln(III)[12-MC-4], Ln(III)[15-MC-5], Ln(III)[12-MC-4]₂, Ln(III)[12-MC-4]₂[24-MC-8], and Ln(III)₂Zn₉. The Yb(III)[12-MC-4]₂[24-MC-8] is luminescent in methanol, emitting at 980 nm upon excitation at 325 nm with a quantum yield of 0.89 % and lifetime of 14 μs . This complex is the brightest near-infrared emitting lanthanide coordination complex in protic solvents due to reduced vibrational quenching through the removal of C-H oscillators from the proximity of the lanthanide ion by the metallocrown. These results reveal that the unique topology and structural versatility of metallocrowns create great promise for chiral separations, catalysis, and molecular materials.

Chapter I

Molecular Recognition in Supramolecular Hosts, Self-Assembly, and Metallacrowns

Molecular Recognition

Chemists aspire to control the organization of matter at the molecular level to facilitate challenging chemical transformations, highly selective substrate sensing, and the preparation of functional materials and molecular devices. Molecular recognition provides a route to controlling molecular organization through the specific association of different substrates through complementary, weak, reversible interactions. Such interactions include hydrogen bonds, hydrophobic interactions, and dative bonds.¹ Biological systems provide the proof-of-principle that molecular recognition is a viable route to constructing highly complex and selective edifices. Proteins, DNA, and RNA rely on weak, reversible interactions for their structure and function. For example, the Cholera toxin contains a macrocyclic pentameric protein, called the cholera toxin B subunit, that assembles through hydrophobic interactions and hydrogen bonds.² The cholera toxin B subunit uses non-covalent interactions to encapsulate the catalytically active enzyme, cholera toxin A subunit, in its central cavity. Furthermore, the cholera toxin B subunit targets intestinal cells through the recognition of gangliosides on epithelial cells in the intestine (figure 1.1).³ Also, the Zn(II) metalloenzyme, Carbonic Anhydrase, catalyzes carbon dioxide hydration at nearly diffusion limited rates through recognition of the reaction transition state by a hydrogen bonding network. Mutagenesis studies reveal that removal of key hydrogen bonding residues near the Zn(II) active site drastically reduces the rate of the reaction.⁴

The field of supramolecular chemistry seeks to realize the broad potential of molecular recognition in artificial systems. Supramolecular chemistry is concerned with “chemistry beyond the molecule,” or the study of molecular recognition from fundamental principles to application.^{1,5} The field aims to address areas of need in

catalysis, sensing, materials, electronics, and molecular devices by controlling how substrates interact or assemble into elaborate edifices at the molecular level.⁶⁻⁸

This thesis addresses the topic of achieving enhanced functionality in coordination complexes using molecular recognition. The research covers aspects of the supramolecular chemistry of metallocrowns (MCs), which are a class of discrete inorganic macrocycles assembled from metal ions and ligands.⁹⁻¹¹ The original research in this thesis addresses how changes to the metal ions and ligands can tune the MCs solid-state organization, anion recognition behavior, structural motif, and physical properties. In this introductory chapter, fundamental principles of supramolecular chemistry relevant to this thesis are discussed, including organic macrocyclic receptors, metal-based self-assembled systems, and metallocrowns. Later the promising applications of supramolecular systems are presented. The introductory chapter concludes with a discussion of the specific aims of this thesis and how these aims contribute toward the broad goals for MCs and supramolecular chemistry in general.

Organic Macrocycles in Host-Guest Chemistry

Much of the fundamental principles of supramolecular chemistry were established through research on organic macrocyclic receptors.¹² A macrocycle is a cyclic molecule containing 9 or more atoms in the ring, or containing three or more donor atoms that can bind a substrate. Pedersen, Lehn, and Cram won the Nobel prize in chemistry in 1987 for their work on these organic macrocycles.^{5,13,14} The important breakthrough in using weak, reversible interactions to control molecular organization occurred in the late 1960's with the realization that macrocyclic polyethers bind alkali cations. To that point, stable complexes with alkali cations were rare due to the strong solvation energy and lack of covalency of the cations. The initial discovery was made by Charles Pedersen, who had synthesized an 18-membered polyether macrocycle accidentally. This macrocycle has a [C-C-O] motif that repeats 6 times through the ring and a central electron-rich cavity with a radius of 1.3-1.6 Å ([18]crown-6, figure 1.2). Following the initial discovery,¹⁵ similar macrocycles of varying sizes were prepared that were also capable of binding cations (figure 1.2). Pedersen named this class of compounds crown ethers due to their physical resemblance to a crown. Cations are observed crystallographically binding in the central cavity of crown ethers. In complexes where the cation is significantly larger in radius

than the crown ether, sandwich complexes tend to form.^{16,17} Stronger binding is often observed for crown ethers with more donor atoms, and potassium tends to bind the strongest of all alkali metals due to its relatively low solvation energy. Crown ethers show limited selectivity based on the match between cavity and cation size, though this size selectivity is less significant than the effect of solvation. Crown ethers can also be derivitized by appending functionalities off of the carbon atoms, substituting atoms in the ring, and altering the repeat unit of the ring. This class of molecular recognition agent with a single organic macrocycle that binds guests using donor atoms in a central cavity are known as corands.

It was discovered that enhanced cation binding affinity could be achieved in crown ethers by appending a coordinating side chain off of the macrocycle. These complexes, known as lariat ethers, typically exhibit greater binding affinity than the related corand.¹⁸ A typical lariat ether is shown in figure 1.3. This complex binds Na^+ with a $\log K_{11}$ of 4.58 in methanol. The analogous corand without the side chain binds Na^+ with a modest $\log K_{11}$ of 2.69.¹⁹ Other organic macrocycles with varying structural rigidity have been explored. Cryptands are macrobicyclic complexes with multiple donor-atoms that saturate the coordination sites on cations.^{20,21} Metal ions bind in the center of the host with greater affinities than related crown ethers (figure 1.3). Cryptands also have greater cation selectivity than crown ethers due to the constrained volume of the metal binding site.²² Spherands are another related macrocycle with even greater structural rigidity (figure 1.3).²³ The polyphenol motif locks the donor atoms into the optimal orientation for cation binding, leading to particularly strong cation affinity. The spherand in figure 1.3 binds Na(I) with a binding strength of -19.2 kcal/mol in water saturated dichloromethane.²⁴ More flexible systems called podands are also known to bind cations. Podands are polyether chains, not macrocycles, and they typically show weaker binding than crown ethers (figure 1.4). These hosts wrap around cations, so the receptor structure is templated by the cation or other substrate.²⁵

As a whole, the cation binding chemistry of these systems helped to establish the fundamental principles of supramolecular chemistry.^{1,26} The strong cation binding in these systems is a result of complementary interactions between the polyethers and the cations. Polyether complementarity with the cations is evident in the formation of

multiple, stable 5-membered chelate rings and the absence of unfavorable interactions. The summation of multiple associative interactions leads to strong association. The strong effects of solvation are also apparent. The cation coordination sphere is saturated with multiple solvent molecules in solution. Displacement of multiple solvent molecules during complexation by the polydentate polyethers is favored entropically, promoting association. This phenomenon is termed the chelate effect, and the enhancement with macrocyclic ligands is known as the macrocyclic effect. Furthermore, guest binding strength is dependent on the solvation energy, demonstrating the importance of substrate solvation in the complexation process.

The cation binding affinity of the polyethers generally follows the trend podand < crown ether < lariat ether < cryptand < spherand. This trend follows the conformational flexibility of the ligands. Podands are very flexible, meaning they incur a significant reorganization energy penalty in adopting the appropriate conformation for guest binding. This reorganization energy arises from the entropy penalty of adopting a more organized structure and the enthalpic penalty for desolvating the polyether. Spherands are rigidly preorganized for binding, meaning the macrocycle is in the same conformation in its complexed and uncomplexed form. Thus, it incurs a smaller reorganization penalty and the guest affinity is greater.

An expense of increased preorganization is slower complexation and decomplexation kinetics. Even the highly preorganized spherands show relatively fast complexation rates, with the spherand in figure 1.3 binding Na^+ in water saturated dichloromethane with a k_1 of $4 \times 10^5 \text{ M}^{-1}\text{s}^{-1}$ at $25.0 \text{ }^\circ\text{C}$. However, exceptionally slow decomplexation rates of $3 \times 10^{-9} \text{ s}^{-1}$ were observed with the highly preorganized host.²⁶ 15-crown-5 and 18-crown-6 hosts bind alkali cations with complexation rates on the order of $10^8 \text{ M}^{-1}\text{s}^{-1}$ in water at $25 \text{ }^\circ\text{C}$, and decomplexation rates of 10^6 - 10^7 s^{-1} . Various cryptands show rates of complexation and decomplexation in water at $25 \text{ }^\circ\text{C}$ of 10^6 - $10^8 \text{ M}^{-1}\text{s}^{-1}$ and 10^1 - 10^3 s^{-1} , respectively.²⁷ So more preorganized macrocycles display modestly slower complexation rates, though the decomplexation rates are significantly lower.

The name host-guest chemistry was given to the study of artificial receptors that recognize substrates through convergent, weak, reversible interactions.²⁸ The term

convergent implies that multiple functionalities on the host associate with the guest through complementary, associative interactions. Host-guest chemistry is an expansive field, covering cation, anion, and neutral molecule binding.

Beyond the aforementioned polyethers and related complexes, there are a variety of macrocyclic hosts with large internal cavities that bind guests. Cyclodextrins are toroid-shaped macrocyclic oligosaccharides (figure 1.4). They most commonly contain 6, 7, or 8 D-glucopyranoside units linked by a 1,4-glycosidic bond (α -CD, β -CD, γ -CD, respectively).^{29,30} CDs have a hydrophobic interior and hydroxyl groups at the edges. CDs bind a wide variety of neutral and anionic guests with moderate affinity in their central cavity (typically 10^2 - 10^3 M⁻¹ in water).³⁰ Guest binding is primarily driven by the hydrophobic effect, which is the entropically favored release of highly ordered solvent molecules surrounding a solvated hydrophobic guest upon inclusion. Van der Waals interactions in the central cavity and electrostatic interactions with the hydroxyl groups on the edges also contribute to guest binding. Cucurbiturils are another macrocyclic host that is topologically similar to cyclodextrins (figure 1.4). Cucurbiturils bind metal ions with their carbonyl oxygen atoms,³¹ and also bind neutral or cationic molecules in the central cavity in water.^{32,33} Notably, avidin-biotin levels of affinity have been achieved with a cucurbituril and a cationic ferrocene derivative.³⁴

Macrocycles that are sealed at one end and have an opening at the other, known as cavitands, are prolific host topologies.^{1,14} Similar to cyclodextrins, the curved, hydrophobic topology in cavitands leads to a strong hydrophobic contribution to guest binding. Calixarenes and resorcinarenes are prototypical cavitands (figure 1.4). Cavitands are also described as molecular containers, as the cavity can encapsulate a substrate, just like a macroscopic container.^{35,36} Calixarenes and resorcinarenes are poly-benzyl macrocycles with varying functionalities at their rims. Both calixarenes and resorcinarenes are adept hosts for hydrophobic substrates^{35,37}. Particular interest in calixarenes and resorcinarenes stems from the facile tuning of their chemistry through substitutions at their rims. Hydrogen bonding residues on the upper rim can lead to the formation of dimeric capsules in solution. Such hosts have been used widely to explore fundamental behavior of encapsulated substrates in confined environments.^{36,38,39}

Chirality can also be introduced to these cavitands by modifying the rim functionalities.^{40,41} Calixarenes can also act as ligands for metal ions.^{42,43}

Numerous hosts exploit hydrogen bond acceptors or donors to bind guests. Frequently multiple hydrogen bonding interactions or the assistance of hydrophobic interactions are needed to form stable complexes, particularly in polar solvents.⁵ A representative example is the protonated macrocycle shown in figure 1.5. This complex binds carboxylate anions through hydrogen bonding interactions with the protonated amine groups. Notable, the limited size of the macrocycle leads to selectivity based on guest length. Log K values of 4.4 ± 0.2 and 3.2 ± 0.2 were obtained in aqueous solution for saturated dicarboxylates with carbon chains of 4 and 6 atoms, respectively. Stronger binding is observed as the size of the macrocycle is more complementary with the shorter guest.⁴⁴ Hosts with hydrogen bond donors can be effective anion receptors, which is impressive given the many challenges in anion recognition. These challenges include the strong solvation of anions, particularly in protic solvents, leading to weak binding with hosts. Also anions are highly polarizable, so their interactions with hosts tend to be less directional and less dependent on size factors. Furthermore, anions are larger than cationic guests, thus they have a lower charge to size ratio and electrostatic interactions are relatively weaker. For these reasons, anion hosts tend to have less affinity and selectivity than hosts for neutral or cationic guests.⁴⁵⁻⁴⁷

Metallocavitands

Numerous organic hosts have been developed that associate with anions, cations, and neutral substrates. A number of supramolecular hosts have been described that incorporate metal ions for both structural and guest recognition faculties, though these systems are less developed than their organic counterparts. These metalated container molecules are named metallocavitands.⁴⁸ Potential advantages of metallocavitands over their organic counterparts include stronger and more directional anion binding by the acidic metal ions, particularly in water. Also, the metal ions can impart catalytic functionality or addressable physical properties, such as magnetism, spectroscopic features, or redox behavior.

A variety of metallocavitands have been realized that bind anions or neutral Lewis bases.⁴⁹⁻⁵⁶ Two particularly noteworthy examples are Kersting's macrocyclic

thiophenolate and Rebek's Zn(II) resorcinarene. Kersting's macrocyclic thiophenolate (figure 1.6) is a binuclear metallocavitand with a hydrophobic cavity generated from a macrocyclic tert-butyl-thiophenol ligand.⁵⁷ The metal ions coordinate a variety of anions, such as carboxylates, pyrazole, nitrate, and unconventional guests like nitrite and hydrazine.^{58,59} Bridging guests, like dicarboxylates, template the formation of dimeric complexes.⁶⁰ Rebek's metallocavitand contains a resorcinarene functionalized with a Zn(II) salen at the rim. This system strongly binds a phosphocholine ester in chloroform at 300 K ($K = 6.0 \pm 0.9 \times 10^5 \text{ M}^{-1}$). The resorcinarene recognizes hydrophobic guest functionalities while the Zn(II) binds the anionic phosphate diester. Synergistic effects between the cavitaand and Zn(II) ion are observed, as the binding affinity is significantly less without the Zn(II) salen unit ($K = 180 \pm 30 \text{ M}^{-1}$).⁶¹

Self Assembled Macrocycles

The molecular recognition displayed by artificial host-guest systems parallels the receptors and enzymatic binding pockets found in biological systems. Nature also uses weak, reversible interactions to assemble large, functional structures, which is exemplified by the macrocyclic pentamer topology of the cholera toxin B subunit (figure 1.1),² or the double-helix of DNA. Self-assembly is the formation of supramolecular edifices from multiple molecular building blocks. The building blocks are programmed with molecular recognition faculties to direct the assembly of the structure. The self-assembly approach allows for the synthesis of nanoscale supermolecules by simply combining appropriately designed molecular building blocks. The appeal of the self-assembly approach is its ease relative to multistep covalent synthesis. Furthermore, the self-assembled complex can exhibit distinct functionality from that of the individual building blocks. Self-assembly approaches are largely based on molecular recognition chemistry developed with host-guest systems. Effective self-assembly strategies for preparing helicates,⁶² infinite networks,⁶³ nanoscale aggregates,⁶⁴ mechanically interlocked molecules,^{65,66} and discrete macrocycles⁶⁷ have been developed, giving rise to a tremendously large and diverse array of self-assembled systems. As self-assembled macrocycles are most relevant to this thesis, only these systems and the specific design strategies for their preparation will be discussed. Furthermore, while there are a number of macrocyclic systems assembled through hydrogen-bonding interactions,⁶⁸

coordination-driven assemblies are the focus of this thesis and only these metal-based systems will be discussed.⁶⁹

Metal-ligand interactions provide robust and directional linkages that are useful in self-assembly. Bridging ligands that connect metal ions can be utilized to prepare discrete macrocycles. The design of coordination-driven self-assembled macrocycles is best understood from the standpoint of symmetry. Metal and ligand building blocks are programmed to generate the symmetry elements of the overall complex. To take a straightforward, benchmark example, the synthesis of a supramolecular square can be achieved with four building blocks that form 90° angles bridged by four linear linkers. A molecular square was prepared by Fujita et. al. using square planar Pd(II)(ethylenediamine) complexes bridged by bipyridyl linkers (figure 1.7). The assembly of this molecular square is driven by the formation of strong metal-ligand bonds and the entropic effect of forming a discrete macrocycle as opposed to a coordination polymer.⁷⁰ It should be noted that this complex is known to be in a temperature and concentration dependent equilibrium with a Pd₃(bipyridyl)₃ molecular triangle. The formation of the molecular triangle is facilitated by slight bending in the ligand and changes to the Pd-ligand bond angles.⁷¹ This approach to using rigid linkers that bind to coordinatively unsaturated metal ions based on the symmetry of the metal ion is often referred to as the molecular library approach.⁷²

Three-dimensional macrocycles can also be realized through a similar approach. Raymond's M₄L₆ tetrahedron exemplifies the design strategy. Considering a tetrahedron, there are six C₂ symmetric edges that are linked by four C₃ symmetric vertices. These symmetry elements can be generated by an octahedral metal ion and a dicatechol ligand. Furthermore, a tetrahedron has 70.6° angles between the vertices. Thus, the bridging ligand must generate this angle based on the approach angle between the ligands and metals. With a properly designed ligand, the reaction of four metal ions, such as Ga(III), and six ligands generates the tetrahedral assembly shown in figure 1.8.⁷³ This design strategy of using the approach angles of the bridging ligands to generate symmetry elements in the assembly can be referred to as the symmetry interaction model.⁷² Three dimensional macrocycles can also be generated with building blocks that template the face of an assembly. This strategy is exemplified by Fujita's M₆L₄ octahedron. A C₃

symmetric tripyridyl ligand is employed to form the C_3 symmetric face of the octahedron, and square planar Pd(ethylenediamine) ligands are used to arrange these faces at 90° angles. The reaction of these species in the appropriate stoichiometry in water generates the octahedral cluster shown in figure 1.7.⁷⁴ These strategies have been applied to the preparation of a large variety of self-assembled compounds using dative bonds. Ligand and metal geometry in these systems tends to be very important, as deviations from the ideal geometry can lead to the assembly of entirely different complexes. This phenomenon is best exemplified in the case of a $Pd_{24}L_{48}$ polyhedron that forms a different $Pd_{12}L_{24}$ complex when the bridging ligand bending angle is changed from 149° to 127° .⁷⁵ The design of self-assembled macrocycles based on symmetry considerations has been extensively reviewed.^{67,76-79}

A number of self-assembled macrocycles have also been prepared that adopt different structures in different conditions.⁸⁰ The weak-link approach best exemplifies this type of complex. The weak-link approach relies on bridging ligands that form chelate rings with one strong donor, such as a phosphine, and a weak donor, such as an ether. The weakly bound ligand can be displaced by a strongly bound substrate with a greater affinity for the metal ion, such as a carbonyl or halide.^{81,82} This difference in affinity leads to the complex adopting two different structures based on the presence of a particular substrate (figure 1.9). Another example of a responsive system was reported by the Dunbar group, who prepared a molecular square that assembles into a pentagon when SbF_6^- is present.⁸³ Raymond's M_4L_6 tetrahedron with an anthracene spacer is stable with a cationic guest such as tetramethylammonium, but it converts to a triple helicate in the absence of the guest.⁸⁴ Conformationally flexible ligands can also promote the formation of a variety of self-assembled macrocycles, evidenced by Raymond's ferrocene-based catecholamide ligand that forms Ge_2L_3 and Ge_2L_2 complexes.⁸⁵ A number of solvent dependent assemblies have also been realized.⁸⁶⁻⁸⁹ These systems typically assemble into different structures based on differences in the polarity or coordination ability of the solvent.

Self-Assembled Hosts and Metallacrowns

Similar to benchmark organic macrocycles, many self-assembled macrocycles are adept supramolecular hosts. Coordination-driven assemblies can be highly charged,

which can lead to different electrostatic interactions with guests. Advantageously, the facile synthesis of coordination-driven assemblies allows for the generation of large hosts that can encapsulate large guests or multiple guests, which is of particular interest for practical applications (*vide infra*). A Noteworthy example of a metal-based self-assembled host is Raymond's M_4L_6 tetrahedron. This assembly carries a -12 charge, so it readily encapsulates cationic guests, such as tetraethylammonium ($\text{Log } K = 4.55 \pm 0.06$ in water at 25°C , 0.1 M KCl) and a metalated crown ether through charge assisted Van der Waals and hydrophobic interactions.^{90,91} Fujita's M_6L_4 octahedron encapsulates multiple neutral guests in its hydrophobic chamber. The large cavity can accommodate up to four ferrocene molecules in its interior.⁹²

Certain macrocycles assembled with dative bonds have been recognized as analogues of classic organic macrocycles, such as corands, cryptands, and crown ethers. Similar to their organic counterparts, many of these self-assembled macrocycles bind cations, anions, or neutral molecules in their central cavities. This class of metallamacrocycle is generally called metallacrowns (MCs),^{10,11} though they can be described as metallacoronates or metallacryptates depending on the structure of the macrocycle.⁹³ MCs are defined as macrocycles with a ring composed of a metal ion and mostly heteroatoms. Many examples propagate a metal-nitrogen-oxygen motif. The nomenclature for MCs used in this work is as follows: $M[\text{ring size-MC}_{M', L-\# \text{ring donor atoms}}](X)$ where M is the central metal, M' is the ring metal, L is the ligand, and X is the counterion. Thus $\text{Mn(II)}[12\text{-MC}_{\text{Mn(III), shi-4}}](\text{acetate})$ describes a 12 membered macrocycle with four Mn(III) ring metals, 4 shi^{3-} (salicylhydroxamate) ligands, and 4 oxygen-donor atoms that bind a Mn(II) ion in the central cavity and has acetate counterions (figure 1.10, 1.11).

Historically, MCs have been some of the first self-assembled polygons, with a number of examples being reported in the 1970's.⁹⁴⁻⁹⁶ MCs were first recognized for the analogy to crown ethers by the Pecoraro group in the late 1980's. One of the first MCs from the Pecoraro group was a $[9\text{-MC}_{\text{V(V), shi-3}}]$ complex (figure 1.10, 1.11).⁹⁷ The 3-fold symmetric MC ring is generated by the hydroxamate group on shi^{3-} . The fused-chelate ring formed by shi^{3-} coordinates one V(V) ion bidentate through the $\text{O}_{\text{carbonyl}}$ and $\text{O}_{\text{hydroxamate}}$ and another bidentate through the $\text{O}_{\text{phenolate}}$ and $\text{N}_{\text{hydroxamate}}$. Mass spectrometry,

NMR spectroscopy, and UV-Vis absorption spectroscopy show that the complex is stable in methanol, DMF, and acetonitrile.⁹⁸ A related 9-MC-3 was also obtained with Fe(III) ring metals that had an Fe(III) ion bound in the center.⁹⁹ As the central cavity is too small for the Fe(III), it rests above the oxygen mean plane and is stabilized by three acetate ligands that bridge with the Fe(III) ring metals.

A Mn(II)[12-MC_{Mn(III), shi-4}](acetate)⁹ was prepared that had a planar topology and showed similar connectivity to the 9-MC-3, with fused bidentate chelate rings on shi³⁻ generating the MC ring (figure 1.10). The planarity of the 12-MC-4 results from the Jahn-Teller axis on Mn(III), which promotes an equatorial arrangement of the bidentate shi³⁻ ligands to avoid ring strain. Fe(III) is isotropic, thus it can form the 9-MC-3. The [12-MC_{Mn(III), shi-4}] motif is notably a functional analog of crown-ethers, as it can bind alkali cations such as Na⁺ and Li⁺.^{100,101} The 12-MC-4 was also amenable to ring metal substitutions, accommodating Cu(II) and Fe(III) ring metals.^{102,103} A Cu(II)[12-MC_{Cu(II), β-alaHA-4}](ClO₄), where H₂β-alaHA is β-alaninehydroxamic acid has also been prepared, demonstrating that MCs form with different ligands as well.¹⁰⁴ The H₂β-alaHA loses two protons upon MC formation, thus it is bound as the dianion β-alaHA.

15-MC-5 complexes have been prepared as planar and non-planar complexes. The non-planar complex is a Mn(II)[15-MC_{Mn(III), shi-5}](acetate) that forms in the presence of pyridine.¹⁰⁵ The planar complex is a more general construct. It is assembled with picoline hydroxamic acid (H₂picHA, figure 1.10) or H₂α-amino hydroxamic acid (H₂α-aminoHA) ligands (figure 1.12).¹⁰⁶⁻¹⁰⁸ These planar 15-MC-5 complexes assemble with Cu(II) and Ni(II) ring metals. As the central cavity is larger than the 9-MC-3 or 12-MC-4 species, large central metals such as lanthanides, the uranyl cation, Ca(II) or Pb(II) are encapsulated.¹⁰⁹ In the absence of an appropriate cation, an M(II)[12-MC-4] assembles in solution.^{110,111} It has been proposed that a vacant 15-MC-5 assembles with Ni(II) ring metals.¹¹² Ln(III)[15-MC_{Cu(II), α-aminoHA-5}] complexes are exceptionally stable in water (log β = 53.82 ± 0.03 with a Gd(III) central metal).¹¹³⁻¹¹⁵

Planar 15-MC-5 complexes are particularly noteworthy constructs due to the facile introduction of chirality through synthesis with resolved α-aminoHA ligands. The chiral centers on the ligands differentiate the two faces of the MC. The side-chains drape over the hydrophobic face, while the other face is unencumbered and hydrophilic (figure

1.12).¹⁰⁷ The chiral ligands also introduce inherent chirality in the directionality of the ring.⁴¹ Considering even larger MCs, a non planar 18-MC-6 has also been synthesized with a vacant cavity. This motif is achieved with salicylhydrazide ligands and octahedral Mn(III) ring metals that have alternating Δ and Λ absolute chirality (figure 1.13). Even larger MCs have been synthesized, with the largest being a 60-MC-20. Many of these larger MCs are non planar and rely on octahedral metal ions with alternating Δ and Λ absolute configurations.¹¹⁶

MCs are known to adopt more complex structures than the relatively simple macrocycles described heretofore. Sandwich complexes are known in instances where the guest does not fit within the central cavity, which parallels observations with crown ethers.¹¹⁷ Saalfrank et al. have prepared MC sandwich complexes with ammonium and potassium cations (figure 1.13). Smaller cations such as Na(I) and Ca(II) lead to 1:1 complexes in these systems.¹¹⁸ Metallacryptates have also been isolated with encapsulated guests (figure 1.13) or with vacant cavities.¹¹⁹⁻¹²¹ The open coordination sites on MCs can also lead to the formation of stacked MCs or helices.¹²²⁻¹²⁵ Mixed-ligand and mixed-ring metal MCs have also been realized.¹²⁶

As a whole, the structural diversity of MCs is remarkable from a self-assembly standpoint and because different structures give rise to distinct properties and functionality (*vide infra*). MCs are well suited to preparing diverse self-assembled complexes because their assembly can be influenced by structural changes to the ligand, ring metal, central metal, or counterions. There is continued interest in expanding the library of MCs, and more importantly, developing a better understanding of how MCs assemble to allow for the design of complexes with specific properties or functionality. Rolf Saalfrank has stated that the assembly of MCs and related supramolecular coordination complexes arises from the synergistic effects of serendipity and rational design.⁹³ There are three key tenants of MC design that have been established. First, central cations that are too large for the central cavity will sit above the MC plane and tend to promote the formation of sandwich complexes. Second, Jahn-Teller distorted ring metals promote a planar MC, while isotropic ring metals can lead to non-planar MCs. The third tenant of MC design is a symmetry argument based on the geometry of the fused-chelate rings in the ligand. Fused 5- and 6-membered chelate rings, such as with

shi³⁻, generate a 90° between the metal ions, thus promoting a 12-MC-4 as four ligands are required to complete the macrocycle. Ligands with two fused 5-membered chelate rings, such as picHA, generate a 72° external angle between the metal ions. This geometry promotes a 15-MC-5 as propagation of the chelate motif five times generates the 360° needed for a macrocycle (figure 1.14).¹⁰⁶ It should be noted that these design tenants are merely guidelines. The numerous open coordination sites in MCs can complicate the assembly process and lead to the formation of elaborate clusters that defy these design concepts.¹²⁷⁻¹²⁹

Metallacrowns as Supramolecular Hosts

A number of MCs with stable structures bind guests reversibly.¹³⁰⁻¹³³ 12-MC-3 complexes with alkali cation central metals prepared by Severin are adept at binding small cations, exhibiting significant selectivity for lithium (figure 1.15).¹³⁴ Furthermore, the substituents off of the cyclopentadienyl rings can be substituted to change the anion selectivity. For example, the tight binding pocket created by the pentamethylcyclopentadienyl rings on the metal ions discriminates between halides based on size, as F⁻ binds with over 1600 times greater affinity than other halides or nitrate.¹³⁵ An ester modified cyclopentadienyl ring can selectively extract LiCl from water over other salts. Furthermore, the redox active metal ions can sense lithium ions voltammetrically.¹³⁶ The MC selectively forms dimeric complexes with Na₂SiF₆, while BF₄⁻ and halide anions lead to 1:1 complexes.¹³⁷ This system demonstrates how the MC topology can generate unique molecular recognition chemistry, as cation and anion selectivity can arise from interactions with both the MC ring and substituents on the ligand.

The Pecoraro group has developed chiral Ln(III)[15-MC_{Cu(II)}, α-aminoHA-5] complexes into supramolecular hosts for anions. As the side chains on the α-aminoHA ligands drape over one face of the MC, hydrophobic ligands generate a hydrophobic cavity. Thus MC metallocavitands are assembled with ligands such as L-phenylalanine hydroxamic acid (H₂L-pheHA, figure 1.12). These hosts have been shown to form dimeric compartments in the solid-state with bridging guests and monomeric complexes in solution with monocarboxylates. The first dimeric compartment was obtained with Gd(III)[15-MC_{Cu(II)}, L-tyrHA-5] (L-tyrHA = L-tyrosine hydroximate). The two MCs

associate primarily through coordination of the tyrHA phenol to Cu(II) ring metals on the opposite MC. Hydrophobic interactions between the phenyl side chains are also observed. Nitrate anions are selectively encapsulated in the interior of the compartment, bridging two Cu(II) ring metals (figure 1.16). Chloride is excluded from the interior, likely because it is too small to bridge the 7.7 Å tall compartment.¹³⁸ Compartment height is measured in this work based on the distance between the centroids of the O_{hydroximate} atoms in the MC. This is the most appropriate reference point for the measurement as the central Ln(III) ion and atoms in the MC shift in different structures.¹³⁹

The height of the compartment is increased to ~11 Å with L-pheHA ligands. Ln(III)[15-MC_{Cu(II), pheHA}-5] complexes associate in the solid-state through hydrophobic interactions between the phenyl side chains (figure 1.17).¹³⁹ Gd(III)[15-MC_{Cu(II), pheHA}-5] compartments selectively encapsulate saturated dicarboxylates such as terephthalate in their interior. The guests are observed coordinating bidentate to the acidic Gd(III) central ion and engaged in π -stacking interactions with the phenyl side chains. Carboxylates are also observed binding on the hydrophilic face, though this tends to be indiscriminate as there is little consistency between structures. Saturated dicarboxylates with up to six atoms in the carbon chain are excluded from the compartment. The long guest naphthalene dicarboxylate disrupts dimerization, presumably because the excessively long guest prevents association of the pheHA side chains on opposite MCs (figure 1.17).^{140,141} Notably, this selectivity based on size parallels earlier dicarboxylate hosts that rely on hydrogen bonding interactions (figure 1.5).^{44,47}

Solution studies of Ln(III)[15-MC_{Cu(II), L-pheHA}-5] anion recognition has focused on monocarboxylate guests. Mass spectrometry reveals peaks for 1:1 and 1:2 MC-carboxylate species, suggesting that the carboxylates are bound in solution.^{140,142} As host paramagnetism precludes the most versatile NMR techniques, the first quantitative measure of guest binding was performed with isothermal titration calorimetry (ITC) in pH 7.6 aqueous buffer at 298 K. The binding affinity of benzoate increased with more acidic Ln(III) central metals from $370 \pm 20 \text{ M}^{-1}$ with La(III) to $760 \pm 20 \text{ M}^{-1}$ for Dy(III). This trend implicates the central metal as the primary coordination site in solution, which correlates with the crystallographic trend. Guest binding was found to be entropically driven, which can be rationalized by the displacement of two water molecules upon

bidentate carboxylate coordination and the hydrophobic contribution of burying benzoate in a hydrophobic cavity. The sequential binding of a second guest was found to be modest ($< 60 \text{ M}^{-1}$). Two guests are frequently observed binding crystallographically, most commonly on the hydrophilic face, but occasionally in the hydrophobic face to a nine-coordinate La(III) ion (figure 1.18).¹⁴³ A later study by Tegoni et. al. found a similar binding affinity of benzoate to Eu(III)[15-MC_{Cu(II), pheHA}-5] ($389 \pm 9 \text{ M}^{-1}$) using ¹H NMR, UV-Vis, and fluorescence spectroscopy. Notably, acetate binds with a significantly lower affinity of $98 \pm 3 \text{ M}^{-1}$. The opposite trend is expected based on electrostatic effects, suggesting that hydrophobic interactions between the guest and pheHA side chains strongly contribute to guest binding. Such a phenomenon is supported by the crystallographic observation of hydrophobic interactions between guests and the pheHA side chains (figure 1.17).¹⁴⁴ Based on these initial results, it is evident that Ln(III)[15-MC-5] complexes are discriminating anion hosts.

Applications of Supramolecular Hosts and Self-Assembled Systems

The research described heretofore is fundamental research on effective strategies for controlling the organization of matter with artificial hosts or through self-assembly. The cutting edge of supramolecular chemistry now focuses on novel applications of host-guest chemistry and self-assembled systems, with particular emphasis on using these supramolecular systems to achieve chemistry that is not possible with traditional covalent constructs. Much of this work is at the “proof-of-concept” stage, though significant promise is evident in the many examples in the literature. Of course, nature provides the ultimate demonstration of the intricate chemistry that can be achieved by harnessing molecular recognition. In this section, novel applications of supramolecular chemistry are highlighted, with particular attention to areas where MCs and metallocavitands in general provide examples or hold particular promise.

The mere act of binding a guest can be useful for many applications, which is best exemplified with cyclodextrins (CDs). Upon complexation with CDs, the volatility of a substrate is reduced. Furthermore, the complex can have greater water solubility and be protected from undesired reactions or other decomposition pathways. These effects can increase the solubility or shelf life of a drug or other chemical properties, which has led to the use of CD's in many pharmaceutical, food, and cosmetics applications.²⁹ CDs are

also the active ingredient in deodorizing treatments, such as Febreze®. Guest binding in supramolecular hosts can also be used to stabilize molecules, such as reaction intermediates or reactive molecules. The trapping of cyclobutadiene and the stabilization of white phosphorus in water are two notable examples.^{145,146} Supramolecular hosts have also been shown to bind amino acid residues and influence protein folding, which could be the basis for treating disorders such as Alzheimer's disease.^{147,148}

Supramolecular hosts attract interest as sensors. There is significant interest in highly selective hosts that exhibit a physical signal, such as a color change or redox behavior, in response to substrate binding. The strong, selective, and reversible guest recognition by many hosts make them optimal platforms for sensors.¹⁴⁹ Many supramolecular sensors involve the displacement of a tethered guest upon substrate binding, such as a chromophore or fluorophore.¹⁵⁰⁻¹⁵² Other designs signal the presence of an analyte through the displacement or chemical transformation of a bound responsive guest.^{153,154} Fabbrizzi et al. have developed a fluorescent Zn(II)-metallocavitand sensor for aromatic amino acids. The binding of an aromatic amino acid generates π -stacking interactions that quench the fluorescence of an anthracene residue on the metallocavitand.¹⁵⁵ Fujita et al. have reported a self-assembled host that induces spin crossover upon encapsulating certain coordination compounds. Such a phenomenon could be the basis for magnetic sensing.¹⁵⁶

There is interest in supramolecular systems where guest binding can be controlled by an external stimulus for stimuli responsive materials and devices.¹⁵⁷ CDs with ferrocene guests display such behavior. Ferrocene carboxylate binds to β -cyclodextrin in water at 20° C with an affinity of $2200 \pm 100 \text{ M}^{-1}$, while the binding affinity of the oxidized ferrocenium carboxylate is less than 20 M^{-1} .¹⁵⁸ Stoddart and Zink have prepared a redox-responsive drug delivery device from hollow silica particles that are capped with CD-ferrocene complexes. Application of an oxidizing potential disrupts the host-guest complex, opening the silica and releasing compounds in the interior.¹⁵⁹ A variety of stimuli responsive gelators, polymers, and devices have been prepared through similar uses of responsive supramolecular systems.¹⁶⁰⁻¹⁶³

Supramolecular hosts can aid in the separation of guest molecules from mixtures. Selective binding of one product could be used in separations by chromatography,

precipitation, crystallization, or other methods.^{29,164,165} Atwood has reported the purification of C₆₀ and C₇₀ from carbon soot using calixarene hosts.¹⁶⁶ The separation or resolution of enantiomers is of particular interest given the general challenge of purifying racemic mixtures. Enantioselective guest binding by organic macrocycles is well established,¹⁶⁷ though enantioselective guest binding by coordination driven self-assembled macrocycles has not been investigated thoroughly. This is due in part to the dearth of chiral self-assembled macrocycles. To the author's knowledge, the only previous reports of enantioselective guest binding to self-assembled macrocycles involve a chiral M₄L₆ tetrahedron that kinetically resolves racemic mixtures of chiral ruthenium and phosphonium complexes with diastereomeric excesses of up to 70%.^{168,169}

One of the most promising and well developed applications of supramolecular systems is in chemical transformations. Supramolecular hosts and self-assembled complexes can behave like enzymes, using weak, reversible interactions to modify guest reactivity and facilitate selective and efficient chemical transformations.^{170,171} This phenomenon is referred to as supramolecular catalysis.¹⁷² Stoichiometric reactions are still described under the umbrella term supramolecular catalysis. Molecular hosts that function as supramolecular catalysts are often referred to as molecular flasks.¹⁷³ Supramolecular catalysis can be achieved by using a host as a reaction template, with a catalytically active host, or by encapsulating a functional catalyst in the interior of a host. Furthermore, metallocavitands can enhance catalytic activity or selectivity through supramolecular interactions from the second-coordination sphere with the catalytically active metal ion.

Supramolecular hosts can confine guests in a localized environment and influence their orientation. This phenomenon is exploited to perform selective transformations of bound guests using hosts as templates. Importantly, reactant confinement can lead to significant rate enhancements, while control over relative guest orientation can lead to the formation of products that do not form in bulk solution. [2+2] olefin photodimerizations have been particularly useful reactions for templated supramolecular catalysis based on a strong precedent in solid-state templated reactions.¹⁷⁴ In one example, cucurbituril and CD are effective templates for the selective photodimerization of *trans*-cinnamic acid, yielding exclusively *syn*-dimerized products. The reaction does not proceed without the

hosts in solution, and the *anti* product is obtained in the reaction of crystalline *trans*-cinnamic acid.¹⁷⁵ A chiral derivative of Fujita's M_6L_4 octahedron templates the photodimerization of fluoranthene derivatives and maleimide with 100% regioselectivity and enantiomeric excesses of up to 50%. The confines of the octahedron force the two guests to adopt a specific relative orientation that leads to such selectivity.¹⁷⁶ Kersting has reported the *cis*-bromination of an alkene within the interior of his dimetallic metallocavitand (figure 1.19). Only the *trans* diastereomer forms in the absence of the host.¹⁷⁷ The selectivity demonstrated by these three examples has been observed in many other instances.^{173,178-180} Fujita et al. have also reported the use of a self-assembled host as a reaction template for monodisperse nanoparticles. Self-assembled $M_{12}L_{24}$ spheres with diameters of 20-40 Å serve as the template for the sol-gel condensation of tetramethoxysilane. The confines of the self-assembled host led to the formation of silica nanoparticles with nearly perfect monodispersity ($M_w/M_n < 1.01$). The particle size could be shifted from 170 - 500 SiO₂ units by changing the size of the template.¹⁸¹

Unfortunately, the above examples of supramolecular reactivity are stoichiometric transformations due to the effects of product inhibition. The products of these reactions bind strongly to the host, limiting catalytic turnover by preventing the binding of fresh reactant. Selective hosts are needed to overcome product inhibition, as a product that is weakly bound can easily be displaced by fresh reactant. A number of catalytic reactions have been reported in supramolecular hosts.¹⁸²⁻¹⁸⁴ Catalytic turnover in a Diels-Alder reaction has been achieved by using a host with a limited interior volume. The bimolecular reaction generates a product that is too large for the host, and is therefore weakly bound. The size of the product limited the effects of product inhibition and a 10-fold rate enhancement was observed.¹⁸⁵ Raymond and Bergman have demonstrated supramolecular catalysis using the M_4L_6 tetrahedron host. The -12 charged host recognizes positively charged guests, frequently binding substrates in their protonated form. The M_4L_6 achieves turnover in reactions with charged intermediates but neutral products, such as orthoformate hydrolysis and acetal deprotection.¹⁸⁶⁻¹⁸⁸ Using a tandem reaction strategy, Raymond and Bergman achieved a 2.1×10^6 fold rate enhancement in a catalytic Nazarov cyclization in the M_4L_6 host.¹⁸⁹ The Nazarov cyclization (figure 1.19) proceeds through a cationic intermediate to prepare pentamethylcyclopentadiene. The

cationic intermediate is strongly recognized by the host, which facilitates the reaction. Such incredible rate enhancements are achieved in this example through a rapid, irreversible Diels-Alder reaction of the product with maleimide. Without this tandem reaction, the Nazarov cyclization rates are lower due to product inhibition.

Another effective strategy in supramolecular catalysis is encapsulation of a catalytic substrate in the interior of a host. The host can increase rates and turnover numbers by stabilizing the catalyst.^{190,191} Furthermore the host can impart substrate selectivity based on how the reactants fit into the host, or enhance product selectivity and enantioselectivity.¹⁹²⁻¹⁹⁵ A related strategy in supramolecular catalysis utilizes metallocavitand topologies. Inclusion of a catalytically active metal site in the interior of a molecular cavity, or proximal to the cavity, can lead to enhanced reactivity through secondary-sphere interactions.^{196,197} This approach is a direct mimic of metalloenzymes and has been exploited in a noteworthy hydrogen evolution catalyst.¹⁹⁸ Reek et al. have developed efficient and selective self-assembled catalysts that have rhodium ions in the confines of cavitands.^{199,200} In one such complex, hydroformylation of *cis*-2-octene was catalyzed with up to 93% enantioselectivity, which is noteworthy considering the challenge of enantioselective reactions on internal olefins. Such enantioselectivity resulted from how the long guest was oriented within the confines of the host.²⁰¹ Rebek's Zn(II)-resorcinarene metallocavitand catalyzes the formation of acetylcholine and a hydrolysis reaction.^{202,203} In both reactions, the resorcinarene enhances catalysis by preorganizing the reactive functionality on the reactant in the proximity of the catalytically active Zn(II) site.

Discrete supramolecular hosts and metal-based self-assembled macrocycles have been used as building blocks for different materials. Polymers and nanofibers have been developed that form upon guest binding in covalently linked supramolecular hosts. Maclachlan et. al. used self-assembled Pt₄ macrocycles to prepare organized columnar phases in non-polar solvents. The neutral charge facilitates stacking of the macrocycles. Such assemblies are of interest for liquid crystalline displays.²⁰⁴ There is particular interest in preparing stimuli responsive materials with host-guest systems that can be controlled through an external stimulus.^{205,206} Porous networks can also be prepared from supramolecular systems, which could be of use in separations or gas storage.²⁰⁷⁻²¹⁰ Fujita

et al. prepared a porous network of the M_6L_4 octahedron that selectively absorb C_{70} over C_{60} .²¹¹ Porous networks have also been prepared with MCs.^{212,213}

Chiral host-guest systems are of interest for preparing second-order nonlinear optical (NLO) materials. Nonlinear optical materials emit radiation at different wavelengths than the incident radiation, which is of interest for optical and electronic devices. Second-order NLO, or second-harmonic generation (SHG), is the frequency doubling of light, meaning that two photons are absorbed by a material and emitted at half the wavelength. SHG chromophores are dipolar molecules with electron-donating groups in conjugation with electron-acceptors. The second hyperpolarizability tensor, β , is a measure of the SHG response of a compound. In order to observe SHG intensity, the chromophore must be in a non-centrosymmetric environment at both the molecular and macroscopic level. Fulfilling this requirement has been the primary challenge in preparing SHG materials.²¹⁴ One effective approach has been to isolate SHG chromophores in chiral hosts.^{215,216} The chiral host generates the noncentrosymmetric environment at the molecular level and enforces crystallization in a chiral space group. The challenge is arranging the chromophores in the lattice such that there is a net dipole at the macroscopic level. Crystalline inclusion complexes of chiral $Ln(III)[15-MC_{Cu(II), pheHA-5}]$ compartments with the SHG chromophore, isonicotinate, have been prepared. The compartments bind three isonicotinates such that there is a net dipole within the interior of the compartment (figure 1.20). Furthermore, the compartments are packed as parallel chains, leading to a net dipole moment through the non-centrosymmetric crystal. These complexes displayed modest SHG intensity ($I/I_0 = 1/100$ potassium diphosphate) due to the scattering of frequency doubled light by the visible absorbing $Cu(II)$ ions in the MC. Nevertheless, this example demonstrates the promise of preparing crystalline SHG materials through host-guest chemistry.¹⁴²

Lastly, supramolecular systems, self-assembled systems in particular, can be of interest for their physical properties. Coordination driven assemblies can localize multiple metal ions within a localized area, giving rise to some interesting properties. These properties can be used in sensing or materials. For example, Hupp and Rheingold have prepared a series of luminescent rhenium macrocycles that strongly absorb visible radiation.²¹⁷ Bünzli and Piguet have prepared a $Cr(III)$ - $Yb(III)$ triple helix that fluoresces

with millisecond lifetimes in the near-infrared. This assembly employs a Cr(III) chromophore that has long lived Cr(III) lifetimes. The Cr(III) ion sensitizes the luminescent Yb(III) ion, which then emits at 980 nm with an overall lifetime of 2.05 ± 0.03 ms at 10 K.²¹⁸ The luminescence lifetime of this assembly is significantly longer than the <50 μ s lifetimes that are common for Yb(III) complexes.²¹⁹ Metal-based self-assembled systems are also studied as potential single-molecule magnets (SMMs). SMMs are molecules that can retain their magnetization in the absence of a magnetic field below certain temperatures due to an intrinsic energy barrier to spin relaxation. Research has focused on assembling metal clusters with increased spin or anisotropy to increase the energy barrier for relaxation, or blocking temperature, so that SMMs can operate at higher temperatures.^{220,221} Recent demonstrations of SMM with high blocking temperatures constructed from single-ions, such as a Tb(III)(phthalocyanine)₂ sandwich complex,²²² has generated particular interest in the magnetic properties of high symmetry lanthanide clusters.²²³ MCs have proven to be particularly good constructs for preparing SMMs. The first Mn-Ln(III) SMM was a MC,²²⁴ and numerous other examples of MC SMMs are known,^{225-228 129,229} including Dy(III)[15-MC_{Cu(II), pheHA-5}](NO₃).²³⁰

Thesis Aims

The field of supramolecular chemistry explores fundamental aspects of molecular recognition and their application in areas of need, such as catalysis, sensing, materials, and molecular devices. Building on the results of a substantial amount of previous work, this thesis aims to further develop the molecular recognition chemistry of MCs for a variety of applications. Early work on MCs has focused largely on their synthesis and structural characterization to develop an understanding of the breadth of this class of molecules. Recently, the focus has shifted to exploiting the MC structure type to generate unique functionality. The most promising applications of MCs have been in the preparation of SMMs and in selective guest binding by chiral MC hosts. In a broader sense, MCs are envisioned as a possible route to multifunctional molecular materials. Multifunctional molecules are complexes that have multiple, synergistic addressable properties. They are sought for potential use in molecular data storage or other devices. One could envision accessing MCs magnetically, electrochemically, spectroscopically, or through other means using responsive guests, ring metals, central metals, or ligands.

Early work on MCs has shown that MCs are robust, general constructs that are amenable to substitutions of the ligands, ring metals, central metals, and bound guests. Changes to the MC building blocks can change the physical properties and guest recognition behavior of the MC while maintaining the same overall structural motif or predictably giving rise to a different, familiar motif. Traditional inorganic complexes do not offer the structural versatility, consistency, and facile synthesis that allows for convenient molecular design. Thus, MCs have great potential as multifunctional molecules.

This thesis fundamentally explores how the anion recognition, spectroscopic properties, and self-assembly of MCs can be tuned through structural changes to the building blocks. The aim of this work is to understand better how to design MC building blocks for a particular application. These results have direct implications for metallocavitand chemistry and self-assembly while also making progress toward the long term goal of multifunctional molecules. There are three specific aims and one unifying goal for this work.

The first aim is to develop a theoretical framework for how the central lanthanide ion and ligand side chain influence the size and guest selectivity of dimeric Ln(III)[15-MC-5] compartments in the solid state. Such a theoretical framework would be used to engineer crystalline MC-guest assemblies for use in materials or as templates for molecular transformations. These results would also provide information for considering the chemistry of dimeric Ln(III)[15-MC-5] compartments in solution. This work is presented in chapter 2 as a systematic crystallographic study of the inclusion complexes of bridging carboxylate guests with Ln(III)[15-MC_{Cu(II)}, α -aminoHA-5] hosts bearing phenyl side chains of varying lengths.

The second aim is to develop an understanding of how guest affinity and selectivity in solution is influenced by the Ln(III)[15-MC-5] side chain. Such information is critical for the development of Ln(III)[15-MC-5] complexes in separations, as building blocks for materials, as supramolecular catalysts, or as metal-based catalysts that can be influenced by substituents in the second-coordination sphere. This study was conducted using a novel voltammetric competitive binding assay to quantify guest affinity and is presented in chapter 3. Particular emphasis is placed on enantioselective guest binding.

Enantioselective guest binding by Ln(III)[15-MC-5] complexes has only been reported previously with Gd(III)[15-MC_{Cu(II), pheHA}-5] and phenylalanine enantiomers.²³¹

These first two aims emphasize fundamental aspects of guest recognition by Ln(III)[15-MC-5] hosts that are most relevant to applications in separations, chemical transformations, and materials design because MC metallocavitands have the greatest potential for advancing these areas. The features that differentiate Ln(III)[15-MC-5] metallocavitands from the wealth of supramolecular hosts in the literature are the significant metal-density of the MC ring, the unique chirality of the MC ring, their synthesis by self-assembly with inexpensive chiral ligands, and their size. Metallocavitands are a particularly promising host motif for supramolecular catalysis because second-coordination sphere interactions can influence the reactivity of the metal center. Though metallocavitands are established motifs, metallocavitand chemistry is not well developed in comparison to the vast literature on organic and self-assembled hosts. Ln(III)-metallocavitands in particular are poorly explored, which is unfortunate considering that Ln(III) complexes can be potent catalysts for a variety of symmetric and asymmetric transformations.²³²⁻²³⁴ The possibility of synergistic effects between the Ln(III) ion, Cu(II) ions, ligand side-chains, and chiral MC ring in catalytic transformations make Ln(III)[15-MC-5] metallocavitands an exciting construct. Furthermore, self-assembled hosts with inexpensive chiral ligands are amenable for efficient combinatorial screening, which could be used to identify effective MC complexes for catalysis and separations. Enantioselective catalysis and separations are particularly promising considering the distinctive type of chirality in Ln(III)[15-MC-5] complexes. Furthermore, Ln(III)[15-MC-5] complexes are particularly large hosts, thus they can be expected to accommodate large substrates. These considerations of Ln(III)[15-MC-5] metallocavitands in separations, catalysis, and materials design emphasize the advantages of this host.

The third aim of this thesis is to optimize MCs for lanthanide luminescence by synthesizing MCs with Zn(II) ring metals. Ln(III)-MCs are promising complexes for near-infrared luminescence because the MC topology removes C-H bonds from the proximity of the lanthanide, which should lead to bright luminescence by reducing the effects of vibronic quenching.^{235,236} Unfortunately, *d-d* transitions on the Cu(II) ring

metals of Ln(III)[15-MC_{Cu(II)}-5] complexes can quench electronically excited Ln(III) ions, decreasing luminescence intensity.^{237,238} Synthesis of Ln(III)-MCs with Zn(II) ring metals can overcome this problem, as the d^{10} metal ion will not quench luminescence. Chapter 4 presents the synthesis and characterization of Zn(II)-MCs synthesized with picHA ligands.

The unifying goal of this thesis is to develop the foundation for preparing crystalline SHG materials through MC host-guest chemistry. It was envisioned that chiral Ln(III)[15-MC-5] compartments could be used to arrange SHG chromophores in the solid state and enforce non-centrosymmetric packing. Meanwhile the use of Zn(II)-MCs would lead to optically transparent supramolecular hosts, which would avoid the unwanted scattering seen with the Cu(II)-MCs.¹⁴² The thought is that the crystal engineering, guest binding, and synthetic investigations would provide the basis for realizing crystalline MC host-guest complexes that display significant frequency doubling intensity. The prospects of using MCs in SHG materials, as well as in separations, chemical transformations, luminescence, and other applications will be discussed as concluding remarks in chapter 5.

Figures

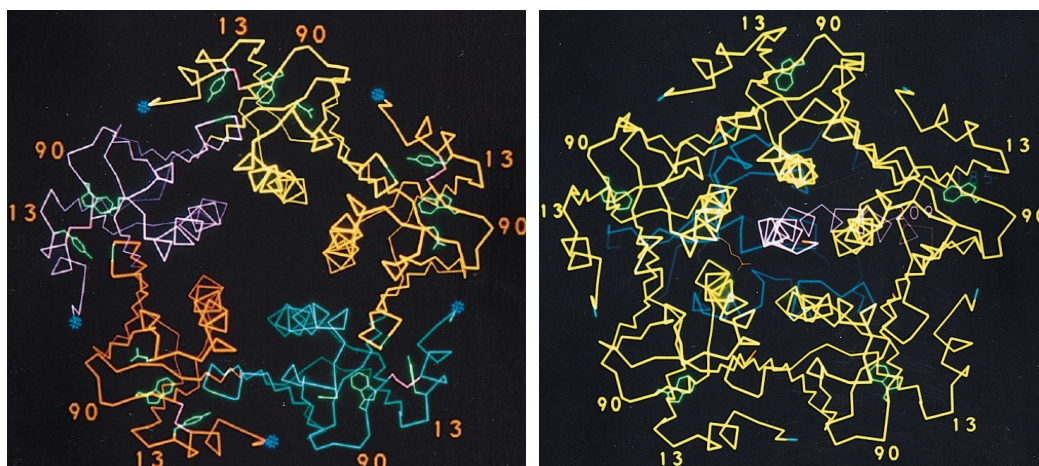


Figure 1.1: Depictions of the crystal structure of the pentameric cholera toxin² (left) and the cholera toxin (right) with the catalytically active enzyme bound in the center of the cholera toxin pentamer.³ The images were taken from the indicated references.

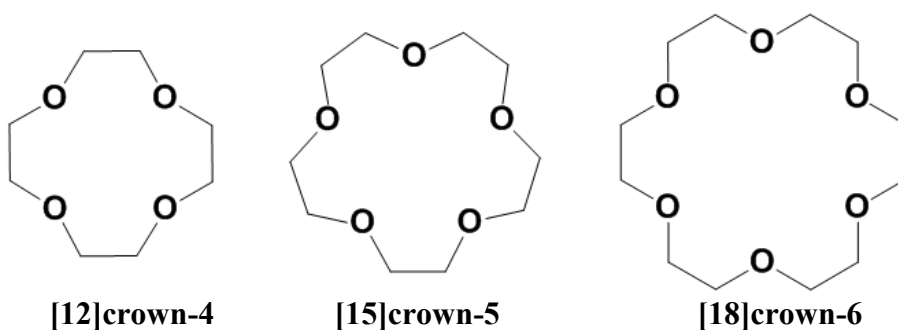


Figure 1.2: Representations of various crown ethers. The bottom images were produced in chemdraw.

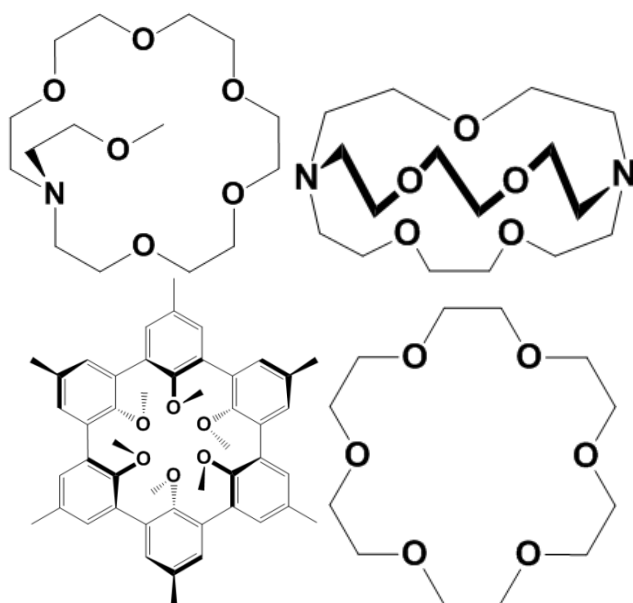


Figure 1.3: An N-substituted lariat ether (top-left), [2, 2, 1] cryptand (top-right), a spherand (bottom-left), and a podand (bottom-right). The bottom images were produced in chemdraw.

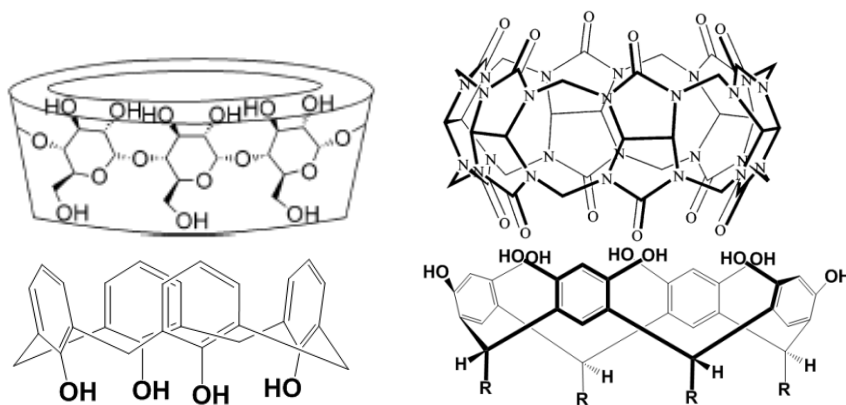


Figure 1.4: Depictions of a cyclodextrin (top left),²³⁹ cucurbituril (top right),³¹ calix[4]arene (bottom left), and [4]resorcinarene (bottom right). The top images were taken from the specified references, while the bottom images were produced in chemdraw.

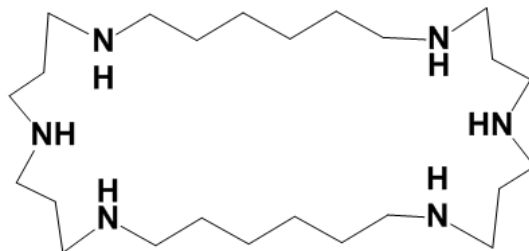


Figure 1.5: A representative supramolecular host that binds guests through multiple hydrogen bond donor groups. The image was reproduced from a diagram originally reported in reference 44.

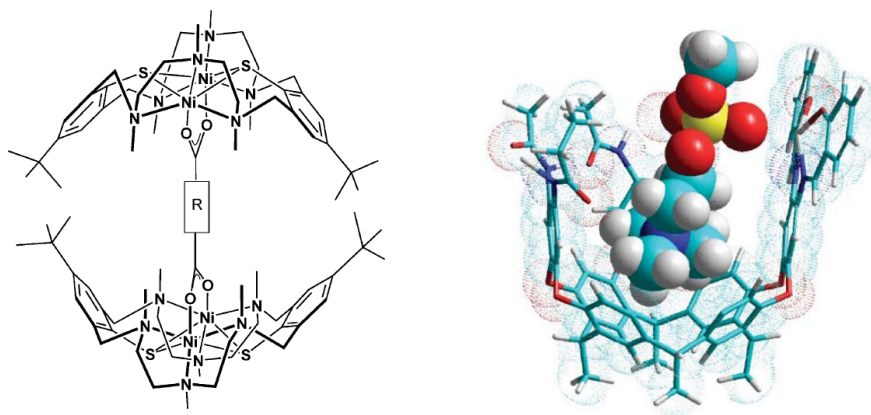


Figure 1.6: Representations of Kersting's binuclear macrocyclic thiophenolate metallocavitand (depicted with a bridging carboxylate guest, left) and Rebek's Zn(II)-resorcinarene (shown as an calculated structure with a phosphocholine ester, one wall of the host was removed for clarity). Images were taken from references 60 and 61.

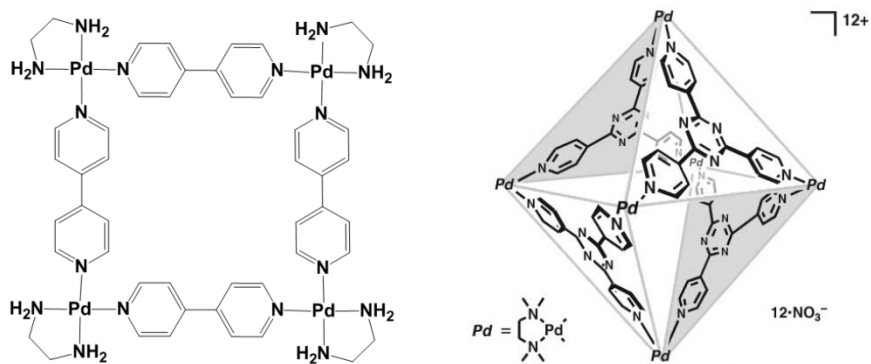


Figure 1.7: Diagram of Fujita's molecular square (right) and self-assembled M_6L_4 octahedron (left). The molecular square image was reproduced from an image published in reference 70 and the M_6L_4 image was taken from reference 184.

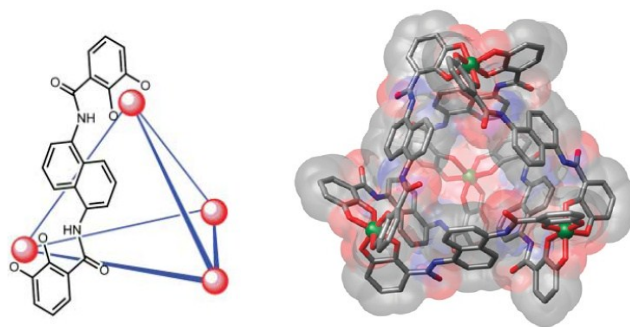


Figure 1.8: Diagram and crystal structure of Raymond's M_4L_6 tetrahedron. Images taken from reference ²⁴⁰.

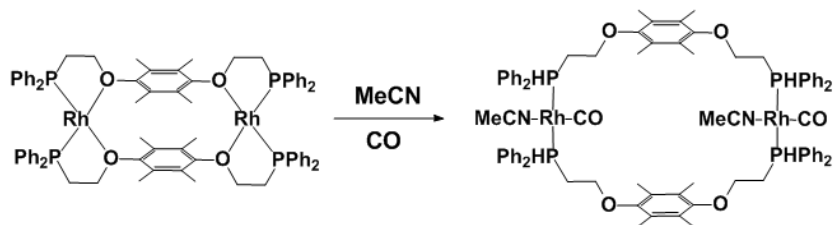


Figure 1.9: Diagram of a weak-link macrocycle that undergoes a structural change in the presence of CO. Diagram is reproduced from an image originally reported in reference 82.

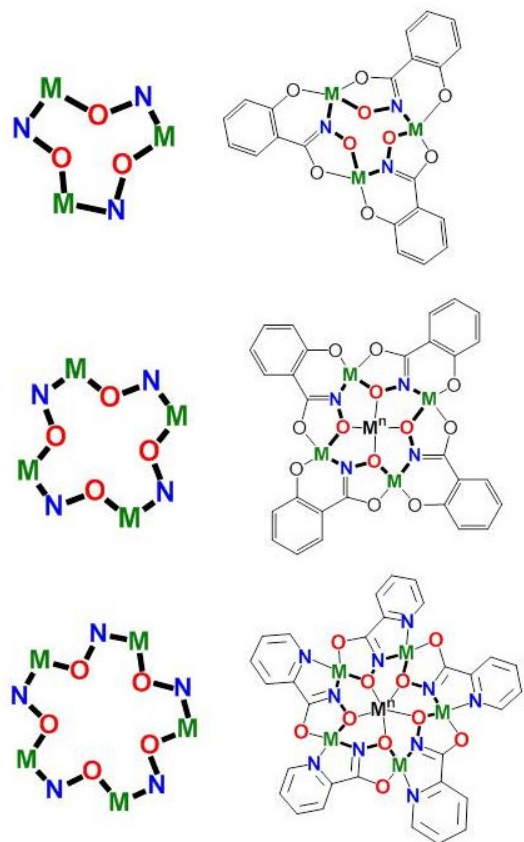


Figure 1.10: Diagrams of the 9-MC-3 (top), 12-MC-4 (middle), and 15-MC-5 (bottom) motifs that highlight the MC ring (left) and the ligand connectivity that generates the MC (right). The 9-MC-3 and 12-MC-4 complexes are shown with shi^{3-} ligands, while the 15-MC-5 has picHA ligands. Diagrams were reproduced in chemdraw based on figures in references 11 and 106.

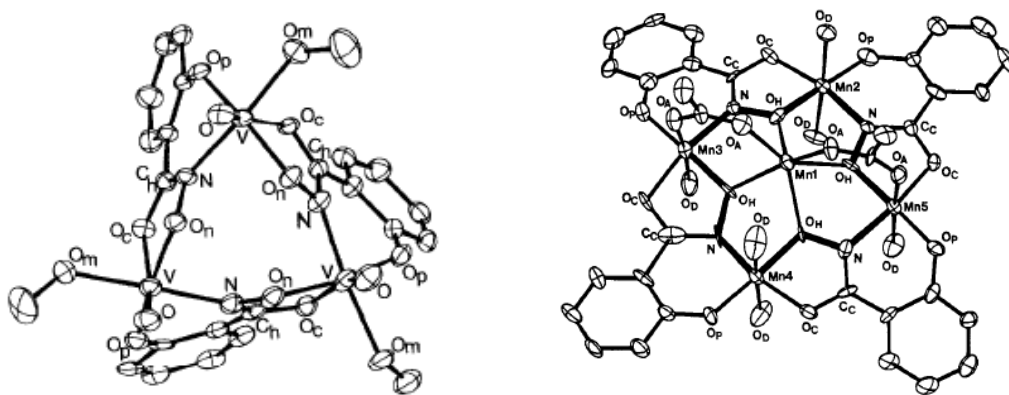


Figure 1.11: Crystal structures of $[\text{9-MC}_{\text{V}(\text{V})}, \text{shi-3}]^{97}$ and $\text{Mn}(\text{II})[\text{12-MC}_{\text{Mn}(\text{III})}, \text{shi-4}](\text{acetate})$.⁹ Images were taken from the indicated references.

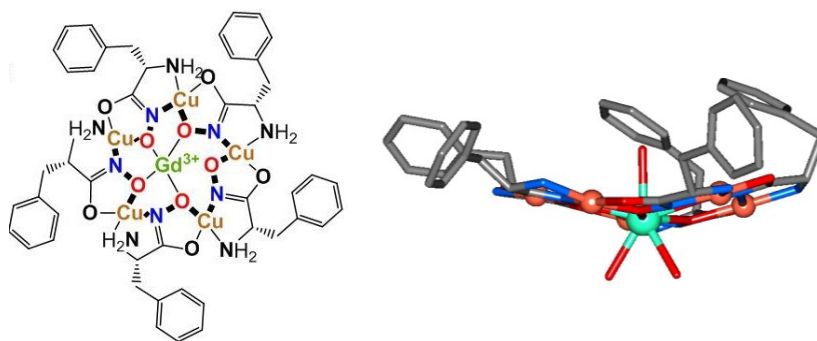


Figure 1.12: Chemdraw diagram and crystal structure of Gd(III)[15-MC_{Cu(II)}, L-pheHA-5].(NO₃)_{1.5}(OH)_{1.5}. Counterions and solvent molecules were removed for clarity. The structure image was created with the structure originally reported in reference 139.

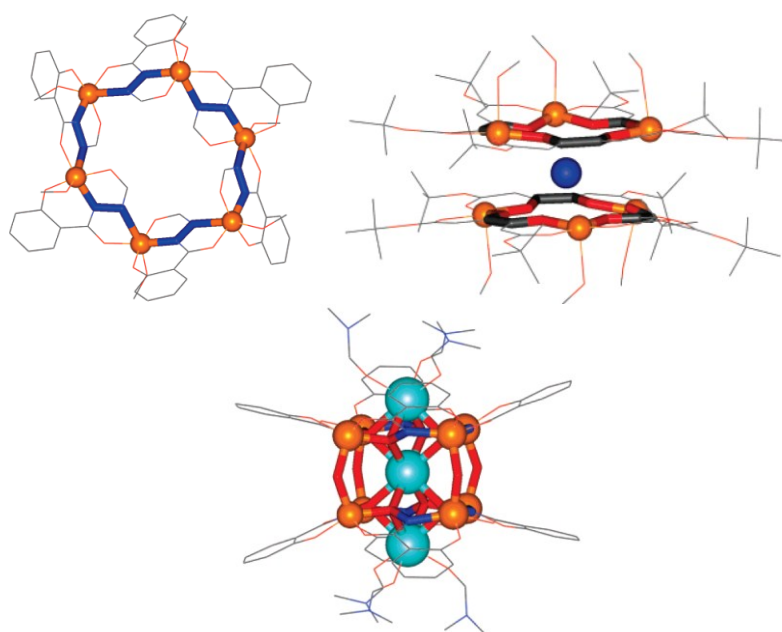


Figure 1.13: Crystal structure of an [18-MC_{Mn(III)}, salicylhydrazidate-6]²⁴¹ (left), NH₄[15-MC_{Cu(II)}, di-*t*-butyl-ketipinate-6]²⁴² (center), and a Na₃[12-MC_{Ga(III)}, shi-4]₂(OH)₄ metallacryptate¹²⁰ (right). Images were taken from reference 11.

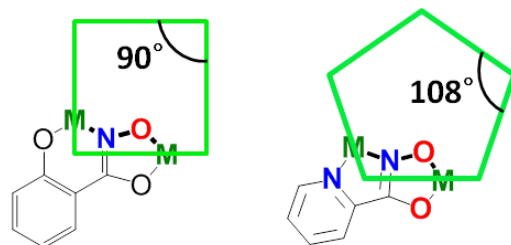


Figure 1.14: Diagram of the relationship between fused chelate ring size and the MC size. Diagram was reproduced and modified from figures originally published in reference 106.

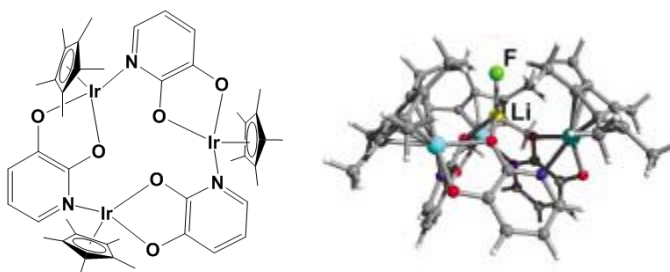


Figure 1.15: Diagram of Severin's 12-MC-3 complex and crystal structure of the MC with a LiF guest bound in the interior. Crystal structure image taken from reference 135.

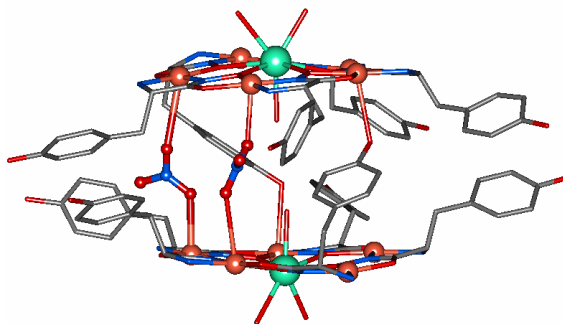


Figure 1.16: Crystal structures of the dimeric $\text{Gd(III)[15-MC}_{\text{Cu(II), L-tyrHA-5}}$ compartment with encapsulated nitrate guests. Counterions and solvent molecules bound to Cu(II) ring metals on the hydrophilic face or in the lattice were removed for clarity. The image was created with the structure originally reported in reference 138.

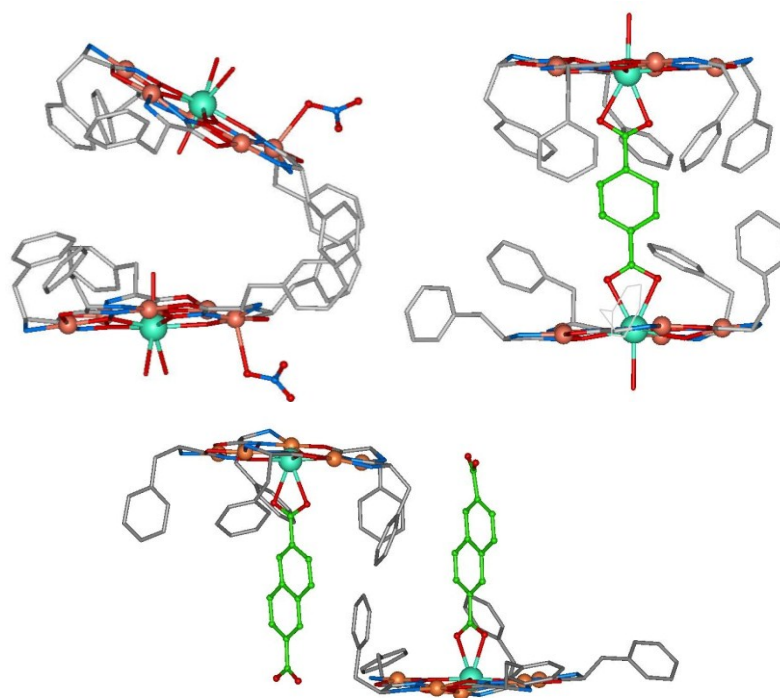


Figure 1.17: Crystal structures of $\text{Gd(III)[15-MC}_{\text{Cu, pheHA-5}}]$ compartments with nitrate,¹³⁹ terephthalate,²⁴³ and naphthalene dicarboxylate guests.¹⁴¹ Counterions and solvent molecules bound to Cu(II) ring metals on the hydrophilic faces or in the lattice were removed for clarity. The images were created with structures that were reported in the indicated references.

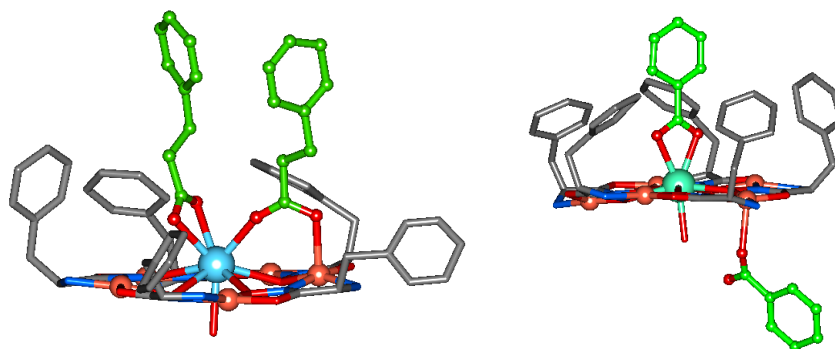


Figure 1.18: Crystal structures of $\text{La(III)[15-MC}_{\text{Cu(II), pheHA-5}}](\text{hydrocinnamate})_2(\text{NO}_3)$ ¹⁴³ and $\text{Eu(III)[15-MC}_{\text{Cu(II), pheHA-5}}](\text{benzoate})_3$ ¹⁴⁴ complexes. Counterions and solvent molecules bound to Cu(II) ring metals on the hydrophilic face or in the lattice were removed for clarity. The images were created with structures that were originally reported in the indicated references.

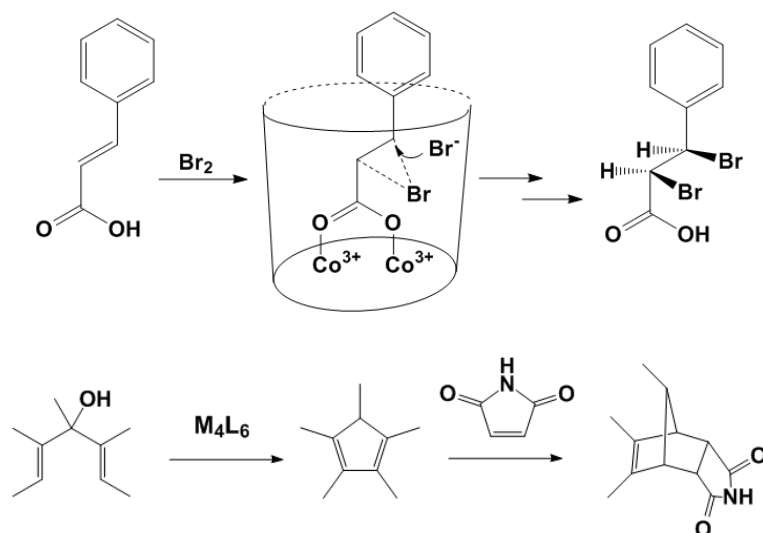


Figure 1.19: *cis*-bromination reaction in the interior of Kersting's metallocavitand¹⁷⁷ (top) and the tandem Nazarov cyclization and Diels-Alder reaction catalyzed by the M_4L_6 tetrahedron.¹⁸⁹ Diagrams were reproduced based on diagrams in the indicated references.

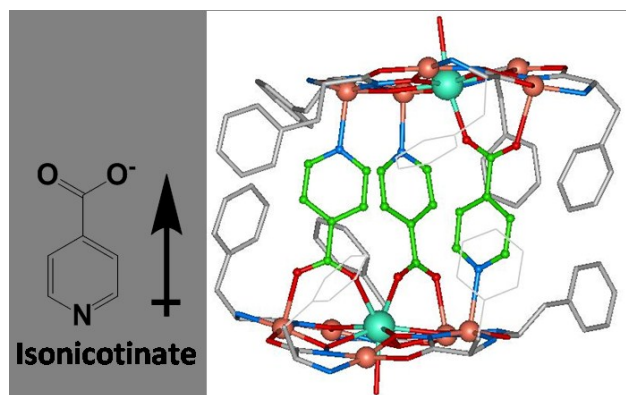


Figure 1.20: Crystal structure of the $\text{Gd(III)[15-MC}_{\text{Cu(II), L-pheHA-5}}\text{](isonicotinate)}_2(\text{NO}_3)_2$ complex displaying the alignment of dipolar isonicotinate guests such that there is a net dipole moment in the chiral compartment.¹⁴² Three side-chains are displayed as thin lines for clarity. Counterions and solvent molecules bound to Cu(II) ring metals on the hydrophilic face or in the lattice were removed for clarity. The image was created with the structure originally reported in reference 142.

References

- (1) Steed, J. W.; Atwood, J. L. *Supramolecular Chemistry*; John Wiley & Sons, Ltd: West Sussex, 2000.
- (2) Zhang, R.-G.; Westbrook, M. L.; Westbrook, E. M.; Scott, D. L.; Otwinowski, Z.; Maulik, P. R.; Reed, R. A.; Shipley, G. G. *J. Mol. Biol.* **1995**, *251*.
- (3) Zhang, R.-G.; Scott, D. L.; Westbrook, M. L.; Nance, S.; Spangler, B. D.; Shipley, G. G.; Westbrook, E. M. *J. Mol. Biol.* **1995**, *251*, 563.
- (4) Christianson, D. W.; Fierke, C. A. *Acc. Chem. Res.* **1996**, *29*, 331.
- (5) Lehn, J. M. *Angew. Chem. Int. Ed. Engl.* **1988**, *27*, 89.
- (6) Lehn, J. M. *Science* **2002**, *295*, 2400.
- (7) Whitesides, G. M.; Grzybowski, B. *Science* **2002**, *295*, 2418.
- (8) Reinhoudt, D. N.; Crego-Calama, M. *Science* **2002**, *295*, 2403.
- (9) Lah, M. S.; Pecoraro, V. L. *J. Am. Chem. Soc.* **1989**, *111*, 7258.
- (10) Pecoraro, V. L.; Stemmler, A. J.; Gibney, B. R.; Bodwin, J. J.; Wang, H.; Kampf, J. W.; Barwinski, A. In *Prog. Inorg. Chem.*; Karlin, K. D., Ed.; John Wiley and Sons, Inc.: New York, 1997; Vol. 45, p 83.
- (11) Mezei, G.; Zaleski, C. M.; Pecoraro, V. L. *Chem. Rev.* **2007**, *107*, 4933.
- (12) Christensen, J. J.; Hill, J. O.; Izatt, R. M. *Science* **1971**, *174*, 459.
- (13) Pedersen, C. J. *Angew. Chem. Int. Ed. Engl.* **1988**, *27*, 1021.
- (14) Cram, D. J. *Angew. Chem. Int. Ed. Engl.* **1988**, *27*, 1009.
- (15) Pedersen, C. J. *J. Am. Chem. Soc.* **1967**, *89*, 2495.
- (16) Pedersen, C. J. *J. Am. Chem. Soc.* **1970**, *92*, 386.
- (17) Desreux, J. F.; Duyckaerts, G. *Inorg. Chim. Acta.* **1979**, *35*, L313.
- (18) Gokel, G. W.; Arnold, K. A.; Delgado, M.; Echevarria, L.; Gatto, V. J.; Gustowski, D. A.; Hernandez, J.; Kaifer, A.; Miller, S. R.; Echegoyen, L. *Pure. & Appl. Chem.* **1988**, *60*, 461.
- (19) Schultz, R. A.; White, B. D.; Dishong, D. M.; Arnold, K. A.; Gokel, G. W. *J. Am. Chem. Soc.* **1985**, *107*, 6659.
- (20) Dietrich, B.; Lehn, J. M.; Sauvage, J. P. *Tet. Lett.* **1969**, *34*, 2885.
- (21) Dietrich, B.; Lehn, J. M.; Sauvage, J. P. *Tet. Lett.* **1969**, *34*, 2889.
- (22) Lehn, J. M.; Sauvage, J. P. *J. Am. Chem. Soc.* **1975**, *97*, 6700.
- (23) Trueblood, K. N.; Knobler, C. B.; Maverick, E.; Helgeson, R. C.; Brown, S. B.; Cram, D. J. *J. Am. Chem. Soc.* **1981**, *103*, 5594.
- (24) Cram, D. J.; Lein, G. M.; Kaneda, T.; Helgeson, R. C.; Knobler, C. B.; Maverick, E.; Trueblood, K. N. *J. Am. Chem. Soc.* **1981**, *103*, 6228.
- (25) Vogtle, F.; Weber, E. *Angew. Chem. Int. Ed. Engl.* **1979**, *18*, 753.
- (26) Cram, D. J. *Angew. Chem. Int. Ed. Engl.* **1986**, *25*, 1039.
- (27) Izatt, R. M.; Bradshaw, J. S.; Nielsen, S. A.; Lamb, J. D.; Christensen, J. J. *Chem. Rev.* **1985**, *85*, 271.
- (28) Cram, D. J.; Cram, J. M. *Science* **1974**, *183*, 803.
- (29) Szejtli, J. *Chem. Rev.* **1998**, *98*, 1743.
- (30) Saenger, W. *Angew. Chem. Int. Ed. Engl.* **1980**, *19*, 344.
- (31) Gerasko, O. A.; Mainicheva, E. A.; Naumova, M. I.; Neumaier, M.; Kappes, M. M.; Lebedkin, S.; Fedin, V. P. *Inorg. Chem.* **2008**, *47*, 8869.
- (32) Jeon, W. S.; Moon, K.; Park, S. H.; Chun, H.; Ko, Y. H.; Lee, J. Y.; Lee, E. S.; Samal, S.; Selvapalam, N.; Rekharsky, M. V.; Sindelar, V.; Sobransingh, D.; Inoue, Y.; Kaifer, A. E.; Kim, K. *J. Am. Chem. Soc.* **2005**, *127*, 12984.
- (33) Lee, J. W.; Samal, S.; Selvapalam, N.; Kim, H.-J.; Kim, K. *Acc. Chem. Res.* **2003**, *36*, 621.

- (34) Rekharsky, M. V.; Mori, T.; Yang, C.; Ko, Y. H.; Selvapalam, N.; Gilson, M. K.; Kim, K.; Inoue, Y. *Proc. Nat. Acad. Sci* **2007**, *104*, 20737.
- (35) Cram, D. J.; Cram, J. M. In *Container molecules and their guests*; Stoddart, J. F., Ed.; Royal Society of Chemistry: 1994, p 1.
- (36) Hof, F.; Craig, S. L.; Nuckolls, C.; Rebek, J. J. *Angew. Chem. Int. Ed.* **2002**, *41*, 1488.
- (37) Bohmer, V. *Angew. Chem. Int. Ed. Engl.* **1995**, *34*, 713.
- (38) Conn, M. M.; Rebek, J. *Chem. Rev.* **1997**, *97*, 1647.
- (39) Rebek, J. *Acc. Chem. Res.* **2009**, *42*, 1660.
- (40) Castellano, R. K.; Kim, B. H.; J. Rebek, J. *J. Am. Chem. Soc.* **1997**, *119*, 12671.
- (41) Szumna, A. *Chem. Soc. Rev.* **2010**, *39*, 4274.
- (42) Jeunesse, C.; Armspach, D.; Matt, D. *Chem. Commun.* **2005**, 5603.
- (43) Atwood, J. L.; Barbour, L. J.; Hardie, M. J.; Raston, C. L. *Coord. Chem. Rev.* **2001**, *222*, 3.
- (44) Hosseini, M. W.; Lehn, J. M. *J. Am. Chem. Soc.* **1982**, *104*, 3525.
- (45) Beer, P. D.; Gale, P. A. *Angew. Chem. Int. Ed.* **2001**, *40*, 486.
- (46) Schmidtchen, F. P. *Chem. Soc. Rev.* **2010**, *39*, 3916.
- (47) Ballester, P. *Chem. Soc. Rev.* **2010**, *39*, 3810.
- (48) Kersting, B.; Lehmann, U. *Adv. Inorg. Chem.* **2009**, *61*, 407.
- (49) Amendola, V.; Fabbrizzi, L.; Mangano, C.; Pallavicini, P.; Poggi, A.; Taglietti, A. *Coord. Chem. Rev.* **2001**, *219-221*, 821.
- (50) Fabbrizzi, L.; Foti, F.; Taglietti, A. *Org. Lett.* **2005**, *7*, 2603.
- (51) Damsyik, A.; Lincoln, S. F.; Wainwright, K. P. *Inorg. Chem.* **2006**, *45*, 9834.
- (52) Garon, C. N.; Gorelsky, S. I.; Sigouin, O.; Woo, T. K.; Fontaine, F.-G. *Inorg. Chem.* **2009**, *48*, 1699.
- (53) Sigouin, O.; Garon, C. N.; Delaunais, G.; Yin, X.; Woo, T. K.; Decken, A.; Fontaine, F. G. *Angew. Chem. Int. Ed.* **2007**, *46*, 4979.
- (54) Frischmann, P. D.; Facey, G. A.; Ghi, P. Y.; Gallant, A. J.; Bryce, D. L.; Lelj, F.; MacLachlan, M. J. *J. Am. Chem. Soc.* **2010**, *132*, 3895.
- (55) Frischmann, P. D.; Gallant, A. J.; Chong, J. H.; MacLachlan, M. J. *Inorg. Chem.* **2008**, *47*, 101.
- (56) O'Neil, E. J.; Smith, B. D. *Coord. Chem. Rev.* **2006**, *250*, 3068.
- (57) Lozan, V.; Loose, C.; Kortus, J.; Kersting, B. *Coord. Chem. Rev.* **2009**, *253*, 2244.
- (58) Hausmann, J.; Klingele, M. H.; Lozan, V.; Steinfeld, G.; Siebert, D.; Journaux, Y.; Girerd, J. J.; Kersting, B. *Chem. Eur. J.* **2004**, *10*, 1716.
- (59) Lozan, V.; Buchholz, A.; Plass, W.; Kersting, B. *Chem. Eur. J.* **2007**, *13*, 7305.
- (60) Klingele, J.; Klingele, M. H.; Baars, O.; Lozan, V.; Buchholz, A.; Leibel, G.; Plass, W.; Meyer, F.; Kersting, B. *Eur. J. Inorg. Chem.* **2007**, *2007*, 5277.
- (61) Zelder, F. H.; Salvio, R.; Rebek, J., Jr. *Chem. Commun.* **2006**, 1280.
- (62) Albrecht, M. *Topics. Curr. Chem.* **2004**, *248*, 105.
- (63) Moulton, B.; Zaworotko, M. J. *Chem. Rev.* **2001**, *101*, 1629.
- (64) Ikkala, O.; ten Brinke, G. *Science* **2002**, *295*, 2407.
- (65) Amabilino, D. B.; Stoddart, J. F. *Chem. Rev.* **1995**, *95*, 2725.
- (66) Forgan, R. S.; Sauvage, J. P.; Stoddart, J. F. *Chem. Rev.* **2011**, *111*, 5434.
- (67) Chakrabarty, R.; Mukherjee, P. S.; Stang, P. J. *Chem. Rev.* **2011**, *111*, 6810.
- (68) Whitesides, G. M.; Simanek, E. E.; Mathias, J. P.; Seto, C. T.; Chin, D. N.; Mammen, M.; Gordon, D. M. *Acc. Chem. Res.* **1995**, *28*, 37.
- (69) Holliday, B. J.; Mirkin, C. A. *Angew. Chem. Int. Ed.* **2001**, *40*, 2022.
- (70) Fujita, M.; Yazaki, J.; Ogura, K. *J. Am. Chem. Soc.* **1991**, *112*, 5645.

- (71) Fujita, M.; Sasaki, O.; Mitsuhashi, T.; Fujita, T.; Yazaki, J.; Yamaguchi, K.; Ogura, K. *Chem. Commun.* **1996**, 1535.
- (72) Leininger, S.; Olenyuk, B.; Stang, P. J. *Chem. Rev.* **2000**, *100*, 853.
- (73) Caulder, D. L.; Powers, R. E.; Parac, T. N.; Raymond, K. N. *Angew. Chem. Int. Ed.* **1998**, *37*, 1840.
- (74) Fujita, M.; Oguro, D.; Miyazawa, M.; Oka, H.; Yamaguchi, K.; Ogura, K. *Nature* **1995**, *378*, 469.
- (75) Sun, Q. F.; Iwasa, J.; Ogawa, D.; Ishido, Y.; Sato, S.; Ozeki, T.; Sei, Y.; Yamaguchi, K.; Fujita, M. *Science* **2010**, *328*, 1144.
- (76) Caulder, D. L.; Raymond, K. N. *J. Chem. Soc., Dalton Trans.* **1999**, 1185.
- (77) Caulder, D. L.; Raymond, K. N. *Acc. Chem. Res.* **1999**, *32*, 975.
- (78) Fujita, M.; Tominaga, M.; Hori, A.; Therrien, B. *Acc. Chem. Res.* **2005**, *38*, 317.
- (79) Dalgarno, S. J.; Power, N. P.; Atwood, J. L. *Coord. Chem. Rev.* **2008**, *252*, 825.
- (80) Johnson, D. W.; Raymond, K. N. *Supramol. Chem.* **2001**, *13*, 639.
- (81) Farrell, J. R.; Mirkin, C. A.; Guzei, I. A.; Liable-Sands, L. M.; Rheingold, A. L. *Angew. Chem. Int. Ed.* **1998**, *37*, 465.
- (82) Gianneschi, N. C.; III, M. S. M.; Mirkin, C. A. *Acc. Chem. Res.* **2005**, *38*, 825.
- (83) Campos-Fernandez, C. S.; Schottel, B. L.; Chifotides, H. T.; Bera, J. K.; Bacsa, J.; Koomen, J. M.; Russell, D. H.; Dunbar, K. R. *J. Am. Chem. Soc.* **2005**, *127*, 12909.
- (84) Scherer, M.; Caulder, D. L.; Johnson, D. W.; Raymond, K. N. *Angew. Chem. Int. Ed.* **1999**, *38*, 1588.
- (85) Mugridge, J. S.; Fiedler, D.; Raymond, K. N. *J. Coord. Chem.* **2010**, *63*, 2779.
- (86) Kilbas, B.; Mirtschin, S.; Scopelliti, R.; Severin, K. *Chem. Sci.* **2012**, *3*, 701.
- (87) Suzuki, K.; Kawano, M.; Fujita, M. *Angew. Chem. Int. Ed.* **2007**, *46*, 2819.
- (88) Mamula, O.; Lama, M.; Stoeckli-Evans, H.; Shova, S. *Angew. Chem. Int. Ed.* **2006**, *45*, 4940.
- (89) Baxter, P. N. W.; Khoury, R. G.; Lehn, J.-M.; Baum, G.; Fenske, D. *Chem. Eur. J.* **2000**, *6*, 4140.
- (90) Sgarlata, C.; Mugridge, J. S.; Pluth, M. D.; Tiedemann, B. E. F.; Zito, V.; Arena, G.; Raymond, K. N. *J. Am. Chem. Soc.* **2010**, *132*, 1005.
- (91) Parac, T. N.; Scherer, M.; Raymond, K. N. *Angew. Chem. Int. Ed.* **2000**, *39*, 1239.
- (92) Sun, W.-Y.; Kusukawa, T.; Fujita, M. *J. Am. Chem. Soc.* **2002**, *124*, 11571.
- (93) Saalfrank, R. W.; Maid, H.; Scheurer, A. *Angew. Chem. Int. Ed.* **2008**, *47*, 8794.
- (94) Beckett, R.; Hoskins, B. F. *J. Chem. Soc., Dalton Trans.* **1972**, 291.
- (95) Constable, A. G.; McDonald, W. S.; Sawkins, L. C.; Shaw, B. L. *J. Chem. Soc., Chem. Commun.* **1978**, 1061.
- (96) Bertrand, J. A.; Smith, J. H.; VanDerveer, D. G. *Inorg. Chem.* **1977**, *16*, 1477.
- (97) Pecoraro, V. L. *Inorg. Chim. Acta.* **1989**, *155*, 171.
- (98) Gibney, B. R.; Stemmler, A. J.; Pilotek, S.; Kampf, J. W.; Pecoraro, V. L. *Inorg. Chem.* **1993**, *32*, 6008.
- (99) Lah, M. S.; Kirk, M. L.; Hatfield, W.; Pecoraro, V. L. *J. Chem. Soc., Chem. Commun.* **1989**, 1606.
- (100) Lah, M. S.; Pecoraro, V. L. *Inorg. Chem.* **1991**, *30*, 878.
- (101) Gibney, B. R.; Wang, H.; Kampf, J. W.; Pecoraro, V. L. *Inorg. Chem.* **1996**, *35*, 6184.
- (102) Gibney, B. R.; Kessissoglou, D. P.; Kampf, J. W.; Pecoraro, V. L. *Inorg. Chem.* **1994**, *33*, 4840.
- (103) Lah, M. S.; Pecoraro, V. L. *Comments Inorg. Chem.* **1990**, *11*, 59.
- (104) Kurzak, B.; Farkas, E.; Glowiak, T.; Kozłowski, H. *J. Chem. Soc., Dalton Trans.* **1991**, 163.

- (105) Kessissoglou, D. P.; Kampf, J. F.; Pecoraro, V. L. *Polyhedron* **1994**, *13*, 1379.
- (106) Stemmler, A. J.; Kampf, J. W.; Pecoraro, V. L. *Angew. Chem. Int. Ed. Engl.* **1996**, *35*, 2841.
- (107) Stemmler, A. J.; Barwinski, A.; Baldwin, M. J.; Young, V.; Pecoraro, V. L. *J. Am. Chem. Soc.* **1996**, *118*, 11962.
- (108) Stemmler, A. J.; Kampf, J. W.; Kirk, M. L.; Atasi, B. H.; Pecoraro, V. L. *Inorg. Chem.* **1999**, *38*, 2807.
- (109) Seda, S. H.; Janczak, J.; Lisowski, J. *Eur. J. Inorg. Chem.* **2007**, *2007*, 3015.
- (110) Dallavalle, F.; Tegoni, M. *Polyhedron* **2001**, *20*, 2697.
- (111) Tegoni, M.; Remelli, M.; Bacco, D.; Marchio, L.; Dallavalle, F. *Dalton Trans.* **2008**, 2693.
- (112) Bacco, D.; Bertolasi, V.; Dallavalle, F.; Galliera, L.; Marchetti, N.; Marchio, L.; Remelli, M.; Tegoni, M. *Dalton Trans.* **2011**, *40*, 2491.
- (113) Dallavalle, F.; Remelli, M.; Sansone, F.; Bacco, D.; Tegoni, M. *Inorg. Chem.* **2010**, *49*, 1761.
- (114) Tegoni, M.; Furlotti, M.; Tropiano, M.; Lim, C.-S.; Pecoraro, V. L. *Inorg. Chem.* **2010**, *49*, 5190.
- (115) Tegoni, M.; Remelli, M. *Coord. Chem. Rev.* **2012**, *256*, 289.
- (116) Moon, D.; Lee, K.; John, R. P.; Kim, G. H.; Suh, B. J.; Lah, M. S. *Inorg. Chem.* **2006**, *45*, 7991.
- (117) Mezei, G.; Baran, P.; Raptis, R. G. *Angew. Chem. Int. Ed.* **2004**, *43*, 574.
- (118) Saalfrank, R. W.; Low, N.; Kareth, S.; Seitz, V.; Hampel, F.; Stalke, D.; Teichert, M. *Angew. Chem. Int. Ed.* **1998**, *37*, 172.
- (119) Saalfrank, R. W.; Stark, A.; Peters, K.; Schering, H. G. v. *Angew. Chem. Int. Ed. Engl.* **1988**, *27*, 851.
- (120) Lah, M. S.; Gibney, B. R.; Tierney, D. L.; Penner-Hahn, J. E.; Pecoraro, V. L. *J. Am. Chem. Soc.* **1993**, *115*, 5857.
- (121) Saalfrank, R. W.; Seitz, V.; Caulder, D. L.; Raymond, K. N.; Teichert, M.; Stalke, D. *Eur. J. Inorg. Chem.* **1998**, 1313.
- (122) Butcher, R. J.; O'Connor, C. J.; Sinn, E. *Inorg. Chem.* **1981**, *20*, 537.
- (123) Psomas, G.; Dendrinou-Samara, C.; Alexiou, M.; Tsohos, A.; Raptopoulou, C. P.; Terzis, A.; Kessissoglou, D. P. *Inorg. Chem.* **1998**, *37*, 6556.
- (124) Pavlishchuk, A. V.; Kolotilov, S. V.; Zeller, M.; Thompson, L. K.; Fritsky, I. O.; Addison, A. W.; Hunter, A. D. *Eur. J. Inorg. Chem.* **2010**, *2010*, 4851.
- (125) Johnson, J. A.; Kampf, J. W.; Pecoraro, V. L. *Angew. Chem. Int. Ed.* **2003**, *42*, 546.
- (126) Psomas, G.; Stemmler, A. J.; Dendrinou-Samara, C.; Bodwin, J. J.; Schneider, M.; Xlexiou, M.; Kampf, J. W.; Kessissoglou, D. P.; Pecoraro, V. L. *Inorg. Chem.* **2001**, *40*, 1562.
- (127) Zaleski, C. M.; Depperman, E. C.; Kampf, J. W.; Kirk, M. L.; Pecoraro, V. L. *Angew. Chem. Int. Ed.* **2004**, *43*, 3912.
- (128) Zaleski, C. M.; Kampf, J. W.; Mallah, T.; Kirk, M. L.; Pecoraro, V. L. *Inorg. Chem.* **2007**, *46*, 1954.
- (129) Boron, T. T., 3rd; Kampf, J. W.; Pecoraro, V. L. *Inorg. Chem.* **2010**, *49*, 9104.
- (130) Dendrinou-Samara, C.; Psomas, G.; Iordanidis, L.; Tangoulis, V.; Kessissoglou, D. P. *Chem. Eur. J.* **2001**, *7*, 5041.
- (131) Pavlishchuk, A. V.; Kolotilov, S. V.; Zeller, M.; Shvets, O. V.; Fritsky, I. O.; Lofland, S. E.; Addison, A. W.; Hunter, A. D. *Eur. J. Inorg. Chem.* **2011**, *2011*, 4826.
- (132) Jones, L. F.; Kilner, C. A.; Halcrow, M. A. *Chem. Eur. J.* **2009**, *15*, 4667.
- (133) Jones, L. F.; Barrett, S. A.; Kilner, C. A.; Halcrow, M. A. *Chem. Eur. J.* **2008**, *14*, 223.

- (134) Piotrowski, H.; Polborn, K.; Hilt, G.; Severin, K. *J. Am. Chem. Soc.* **2001**, *1263*, 2699.
- (135) Lehaire, M.-L.; Scopelliti, R.; Piotrowski, H.; Severin, K. *Angew. Chem. Int. Ed.* **2002**, *41*, 1419.
- (136) Piotrowski, H.; Severin, K. *Proc. Natl. Acad. Sci.* **2002**, *99*, 4997.
- (137) Lehaire, M.-L.; Scopelliti, R.; Severin, K. *Chem. Commun.* **2002**, 2766.
- (138) Cutland, A. D.; Malkani, R. G.; Kampf, J. W.; Pecoraro, V. L. *Angew. Chem. Int. Ed.* **2000**, *39*, 2690.
- (139) Zaleski, C. M.; Lim, C. S.; Cutland-Van Noord, A. D.; Kampf, J. W.; Pecoraro, V. L. *Inorg. Chem.* **2011**, *50*, 7707.
- (140) Cutland, A. D.; Halfen, J. A.; Kampf, J. W.; Pecoraro, V. L. *J. Am. Chem. Soc.* **2001**, *123*, 6211.
- (141) Lim, C.-S.; Cutland Van Noord, A.; Kampf, J. W.; Pecoraro, V. L. *Eur. J. Inorg. Chem.* **2007**, *2007*, 1347.
- (142) Mezei, G.; Kampf, J. W.; Pan, S.; Poepelmeier, K. R.; Watkins, B.; Pecoraro, V. L. *Chem. Commun.* **2007**, 1148.
- (143) Lim, C. S.; Kampf, J. W.; Pecoraro, V. L. *Inorg. Chem.* **2009**, *48*, 5224.
- (144) Tegoni, M.; Tropiano, M.; Marchio, L. *Dalton Trans.* **2009**, 6705.
- (145) Mal, P.; Breiner, B.; Rissanen, K.; Nitschke, J. R. *Science* **2009**, *324*, 1697.
- (146) Cram, D. J.; Tanner, M. E.; Thomas, R. *Angew. Chem. Int. Ed. Engl.* **1991**, *30*, 1024.
- (147) Dolain, C.; Hatakeyama, Y.; Sawada, T.; Tashiro, S.; Fujita, M. *J. Am. Chem. Soc.* **2010**, *132*, 5564.
- (148) Sinha, S.; Lopes, D. H.; Du, Z.; Pang, E. S.; Shanmugam, A.; Lomakin, A.; Talbiersky, P.; Tennstaedt, A.; McDaniel, K.; Bakshi, R.; Kuo, P. Y.; Ehrmann, M.; Benedek, G. B.; Loo, J. A.; Klarner, F. G.; Schrader, T.; Wang, C.; Bitan, G. *J. Am. Chem. Soc.* **2011**.
- (149) Ogoshi, T.; Harada, A. *Sensors* **2008**, *8*, 4961.
- (150) Hamasaki, K.; Ikeda, H.; Nakamura, A.; Ueno, A.; Toda, F.; Suzuki, I.; Osa, T. *J. Am. Chem. Soc.* **1993**, *115*, 5035.
- (151) Ueno, A.; Kuwabara, T.; Nakamura, A.; Toda, F. *Nature* **1992**, *356*, 136.
- (152) Mortellaro, M. A.; Nocera, D. G. *J. Am. Chem. Soc.* **1996**, *118*, 7414.
- (153) Wiskur, S. L.; Ait-Haddou, H.; Lavigne, J. J.; Anslyn, E. V. *Acc. Chem. Res.* **2001**, *34*, 963.
- (154) Wang, J.; He, C.; Wu, P.; Duan, C. *J. Am. Chem. Soc.* **2011**, *133*, 12402.
- (155) Fabbrizzi, L.; Licchelli, M.; Perotti, A.; Poggi, A.; Rabaioli, G.; Sacchi, D.; Taglietti, A. *J. Chem. Soc., Perkin Trans. 2* **2001**, 2108.
- (156) Ono, K.; Yoshizawa, M.; Akita, M.; Kato, T.; Tsunobuchi, Y.; Ohkoshi, S.-i.; Fujita, M. *J. Am. Chem. Soc.* **2009**, *131*, 2782.
- (157) Kaifer, A. E. *Acc. Chem. Res.* **1999**, *32*, 62.
- (158) Matsue, T.; Evans, D. H.; Osa, T.; Kobayashi, N. *J. Am. Chem. Soc.* **1985**, *107*, 3411.
- (159) Khashab, N. M.; Trabolsi, A.; Lau, Y. A.; Ambrogio, M. W.; Friedman, D. C.; Khatib, H. A.; Zink, J. I.; Stoddart, J. F. *Eur. J. Org. Chem.* **2009**, *2009*, 1669.
- (160) Klajn, R.; Stoddart, J. F.; Grzybowski, B. A. *Chem. Soc. Rev.* **2010**, *39*, 2203.
- (161) Green, J. E.; Choi, J. W.; Boukai, A.; Bunimovich, Y.; Johnston-Halperin, E.; DeIonno, E.; Luo, Y.; Sheriff, B. A.; Xu, K.; Shin, Y. S.; Tseng, H. R.; Stoddart, J. F.; Heath, J. R. *Nature* **2007**, *445*, 414.
- (162) Tomatsu, I.; Hashidzume, A.; Harada, A. *Macromol. Rapid Commun.* **2006**, *27*, 238.
- (163) Wojtecki, R. J.; Meador, M. A.; Rowan, S. J. *Nat. Mater.* **2011**, *10*, 14.
- (164) Liu, S.; Hermann, A. T.; Rick, S. W.; Gibb, B. C. *Nat. Chem.* **2010**, *2*, 847.

- (165) Newcomb, M.; Toner, J. L.; Helgeson, R. C.; Cram, D. J. *J. Am. Chem. Soc.* **1979**, *101*, 4941.
- (166) Atwood, J. L.; Koutsantonis, G. A.; Raston, C. L. *Nature* **1994**, *368*, 229.
- (167) Xin, X.; Bradshaw, J. S.; Izatt, R. M. *Chem. Rev.* **1997**, *97*, 3313.
- (168) Fiedler, D.; Leung, D. H.; Bergman, R. G.; Raymond, K. N. *J. Am. Chem. Soc.* **2004**, *126*, 3674.
- (169) Brumaghim, J. L.; Michels, M.; Raymond, K. N. *Eur. J. Org. Chem.* **2004**, *2004*, 4552.
- (170) Breslow, R. *Acc. Chem. Res.* **1995**, *28*, 146.
- (171) Breslow, R.; Dong, S. D. *Chem. Rev.* **1998**, *98*, 1997.
- (172) *Supramolecular Catalysis*; Leeuwen, P. W. N. M. v., Ed.; Wiley-VCH, Weinheim, 2008.
- (173) Yoshizawa, M.; Klosterman, J. K.; Fujita, M. *Angew. Chem. Int. Ed.* **2009**, *48*, 3418.
- (174) MacGillivray, L. R.; Papaefstathiou, G. S.; Friscic, T.; Hamilton, T. D.; Bucar, D.-K.; Chu, Q.; Varshney, D. B.; Georgiev, I. G. *Acc. Chem. Res.* **2008**, *41*, 280.
- (175) Pattabiraman, M.; Natarajan, A.; Kaanumalle, L. S.; Ramamurthy, V. *Org. Lett.* **2005**, *7*, 529.
- (176) Nushioka, Y.; Yamaguchi, T.; Kawano, M.; Fujita, M. *J. Am. Chem. Soc.* **2008**, *130*, 8160.
- (177) Steinfeld, G.; Lozan, V.; Kersting, B. *Angew. Chem. Int. Ed.* **2003**, *42*, 2261.
- (178) Kass, S.; Gregor, T.; Kersting, B. *Angew. Chem. Int. Ed.* **2006**, *45*, 101.
- (179) Murase, T.; Nishijima, Y.; Fujita, M. *J. Am. Chem. Soc.* **2012**, *134*, 162.
- (180) Murase, T.; Horiuchi, S.; Fujita, M. *J. Am. Chem. Soc.* **2010**, *132*, 2866.
- (181) Suzuki, K.; Sato, S.; Fujita, M. *Nat. Chem.* **2010**, *2*, 25.
- (182) Kang, J.; J. Rebek, J. *Nature* **1997**, *385*, 50.
- (183) Nakash, M.; Sanders, J. K. M. *J. Org. Chem.* **2000**, *65*, 7266.
- (184) Yoshizawa, M.; Tamura, M.; Fujita, M. *Science* **2006**, *312*, 251.
- (185) Kang, J.; Santamaria, J.; Hilmersson, G.; J. Rebek, J. *J. Am. Chem. Soc.* **1998**, *120*, 7389.
- (186) Pluth, M. D.; Bergman, R. G.; Raymond, K. N. *Acc. Chem. Res.* **2009**, *41*, 1650.
- (187) Pluth, M. D.; Bergman, R. G.; Raymond, K. N. *Science* **2007**, *316*, 85.
- (188) Pluth, M. D.; Bergman, R. G.; Raymond, K. N. *Angew. Chem. Int. Ed.* **2007**, *46*, 8587.
- (189) Hastings, C. J.; Pluth, M. D.; Bergman, R. G.; Raymond, K. N. *J. Am. Chem. Soc.* **2010**, *132*, 6938.
- (190) Brown, C. J.; Miller, G. M.; Johnson, M. W.; Bergman, R. G.; Raymond, K. N. *J. Am. Chem. Soc.* **2011**, *133*, 11964.
- (191) Wang, Z. J.; Brown, C. J.; Bergman, R. G.; Raymond, K. N.; Toste, F. D. *J. Am. Chem. Soc.* **2011**, *133*, 7358.
- (192) Leung, D. H.; Fiedler, D.; Bergman, R. G.; Raymond, K. N. *Angew. Chem. Int. Ed.* **2004**, *43*, 963.
- (193) Sarmentero, M. A.; Fernandez-Perez, H.; Zuidema, E.; Bo, C.; Vidal-Ferran, A.; Ballester, P. *Angew. Chem. Int. Ed.* **2010**, *49*, 7489.
- (194) Merlau, M. L.; Mejia, M. d. P.; Nguyen, S. T.; Hupp, J. T. *Angew. Chem. Int. Ed.* **2001**, *40*, 4239.
- (195) Cavarzan, A.; Scarso, A.; Sgarbossa, P.; Strukul, G.; Reek, J. N. H. *J. Am. Chem. Soc.* **2011**, *133*, 2848.
- (196) Kleij, A. W.; Reek, J. N. H. *Chem. Eur. J.* **2006**, *12*, 4218.
- (197) van Axel Castelli, V.; Cort, A. D.; Mandolini, L.; Reinhoudt, D. N.; Schiaffino, L. *Chem. Eur. J.* **2000**, *6*, 1193.

- (198) DuBois, M. R.; DuBois, D. L. *Acc. Chem. Res.* **2009**, *42*, 1974.
- (199) Dydio, P.; Rubay, C.; Gadzikwa, T.; Lutz, M.; Reek, J. N. H. *J. Am. Chem. Soc.* **2011**.
- (200) Dydio, P.; Dzik, W. I.; Lutz, M.; de Bruin, B.; Reek, J. N. H. *Angew. Chem. Int. Ed.* **2011**, *50*, 396.
- (201) Gadzikwa, T.; Bellini, R.; Dekker, H. L.; Reek, J. N. H. *J. Am. Chem. Soc.* **2012**, doi/10.1021/ja211455.
- (202) Zelder, F. H.; Rebek, J., Jr. *Chem. Commun.* **2006**, 753.
- (203) Richeter, S.; J. Rebek, J. *J. Am. Chem. Soc.* **2004**, *126*, 16280.
- (204) Frischmann, P. D.; Guieu, S.; Tabeshi, R.; MacLachlan, M. J. *J. Am. Chem. Soc.* **2010**, *132*, 7688.
- (205) Castellano, R. K.; Rudkevich, D. M.; Jr, J. R. *Proc. Nat. Acad. Sci. USA* **1997**, *94*, 7132.
- (206) Hui, J. K. H.; MacLachlan, M. J. *Coord. Chem. Rev.* **2010**, *254*, 2363.
- (207) Inokuma, Y.; Kawano, M.; Fujita, M. *Nat. Chem.* **2011**, *3*, 349.
- (208) Enright, G. D.; Udachin, K. A.; Moudrakovski, I. L.; Ripmeester, J. A. *J. Am. Chem. Soc.* **2003**, *125*, 9896.
- (209) Ananchenko, G. S.; Udachin, K. A.; Dubes, A.; Ripmeester, J. A.; Perrier, T.; Coleman, A. W. *Angew. Chem. Int. Ed.* **2006**, *45*, 1585.
- (210) Ananchenko, G. S.; Moudrakovski, I. L.; Coleman, A. W.; Ripmeester, J. A. *Angew. Chem. Int. Ed.* **2008**, *47*, 5616.
- (211) Inokuma, Y.; Arai, T.; Fujita, M. *Nat. Chem.* **2010**, *2*, 780.
- (212) Bodwin, J. J.; Pecoraro, V. L. *Inorg. Chem.* **2000**, *39*, 3434.
- (213) Moon, M.; Kim, I.; Lah, M. S. *Inorg. Chem.* **2000**, *39*, 2710.
- (214) Verbiest, T.; Houbrechts, S.; Kauranen, M.; Clays, K.; Persoons, A. *J. Mater. Chem.* **1997**, *7*, 2175.
- (215) Verbiest, T. *Science* **1998**, *282*, 913.
- (216) Eaton, D. F.; Anderson, A. G.; Tam, W.; Wang, Y. *J. Am. Chem. Soc.* **1987**, *109*, 1886.
- (217) Slone, R. V.; Benkstein, K. D.; Belanger, S.; Hupp, J. T.; Guzei, I. A.; Rheingold, A. L. *Coord. Chem. Rev.* **1998**, *171*, 221.
- (218) Imbert, D.; Cantuel, M.; Bunzli, J.-C. G.; Bernardinelli, G.; Piguet, C. *J. Am. Chem. Soc.* **2003**, *125*, 15698.
- (219) Eliseeva, S. V.; Bunzli, J. C. *Chem Soc Rev* **2010**, *39*, 189.
- (220) Benelli, C.; Gatteschi, D. *Chem. Rev.* **2002**, *102*, 2369.
- (221) Sessoli, R.; Powell, A. K. *Coord. Chem. Rev.* **2009**, *253*, 2328.
- (222) Ishikawa, N.; Sugita, M.; Ishikawa, T.; Koshihara, S.; Kaizu, Y. *J. Am. Chem. Soc.* **2003**, *125*, 8694.
- (223) Rinehart, J. D.; Long, J. R. *Chem. Sci.* **2011**, *2*, 2078.
- (224) Zaleski, C. M.; Depperman, E. C.; Kampf, J. W.; Kirk, M. L.; Pecoraro, V. L. *Angew. Chem. Int. Ed.* **2004**, *43*, 3912.
- (225) Dendrinou-Samara, C.; Alexiou, M.; Zaleski, C. M.; Kampf, J. W.; Kirk, M. L.; Kessissoglou, D. P.; Pecoraro, V. L. *Angew. Chem. Int. Ed.* **2003**, *42*, 3763.
- (226) Zaleski, C. M.; Depperman, E. C.; Dendrinou-Samara, C.; Alexiou, M.; Kampf, J. W.; Kessissoglou, D. P.; Kirk, M. L.; Pecoraro, V. L. *J. Am. Chem. Soc.* **2005**, *127*, 12862.
- (227) Zaleski, C. M.; Kampf, J. W.; Mallah, T.; Kirk, M. L.; Pecoraro, V. L. *Inorg. Chem.* **2007**, *46*, 1954.
- (228) Emerich, B.; Smith, M.; Zeller, M.; Zaleski, C. M. *J. Chem. Crystallogr.* **2010**, *40*, 769.
- (229) Zaleski, C. M.; Tricard, S.; Depperman, E. C.; Wernsdorfer, W.; Mallah, T.; Kirk, M. L.; Pecoraro, V. L. *Inorg. Chem.* **2011**, *50*, 11348.

- (230) Zaleski, C. M.; Depperman, E. C.; Kampf, J. W.; Kirk, M. L.; Pecoraro, V. L. *Inorg. Chem.* **2006**, *45*, 10022.
- (231) Lim, C.-S., *Graduate Thesis*, University of Michigan, 2008.
- (232) Kobayashi, S.; Sugiura, M.; Kitigawa, H.; Lam, W. W.-L. *Chem. Rev.* **2002**, *102*, 2227.
- (233) Shibasaki, M.; Yoshikawa, N. *Chem. Rev.* **2002**, *102*, 2187.
- (234) Inanaga, J.; Furuno, H.; Hayano, T. *Chem. Rev.* **2002**, *102*, 2211.
- (235) Beeby, A.; Clarkson, I. M.; Dickins, R. S.; Faulkner, S.; Parker, D.; Royle, L.; de Sousa, A. S.; Williams, J. A. G.; Woods, M. *J. Chem. Soc., Perkin Trans. 2* **1999**, 493.
- (236) Bischof, C.; Wahsner, J.; Scholten, J.; Trosien, S.; Seitz, M. *J. Am. Chem. Soc.* **2010**, *132*, 14334.
- (237) Sabbatini, N.; Perathoner, S.; Lattanzi, G.; Dellonte, S.; Balzani, V. *Inorg. Chem.* **1988**, *27*, 1628.
- (238) Bunzli, J. C.-G.; Piguet, C. *Chem. Rev.* **2002**, *102*.
- (239) Hapoit, F.; Tilloy, S.; Monflier, E. *Chem. Rev.* **2006**, *106*, 767.
- (240) Pluth, M. D.; Johnson, D. W.; Szigethy, G.; Davis, A. V.; Teat, S. J.; Oliver, A. G.; Bergman, R. G.; Raymond, K. N. *Inorg. Chem.* **2009**, *48*, 111.
- (241) Kwak, B.; Rhee, H.; Park, S.; Lah, M. S. *Inorg. Chem.* **1998**, *37*, 3599.
- (242) Saalfrank, R. W.; Low, N.; Hampel, F.; Stachel, H.-D. *Angew. Chem. Int. Ed. Engl.* **1996**, *35*, 2209.
- (243) Bodwin, J. J.; Cutland, A. D.; Malkani, R. G.; Pecoraro, V. L. *Coord. Chem. Rev.* **2001**, *216-217*, 489.

Chapter II

Influencing the Size and Anion Selectivity of Dimeric Ln(III)[15-Metallacrown-5] Compartments through Systematic Variation of the Host Side Chains and Central Metal

Introduction

The controlled organization of molecules in the solid state is important for the design of porous solids, solid-state chemical reactions, and molecular materials. Porous solids, such as metal-organic frameworks, zeolites, and networks of molecular containers, can be applied in separations or catalysis.¹⁻⁴ Crystals containing reactive species arranged in molecular templates are used in solid-state reactions that proceed with 100% selectivity. For example, many [2+2] olefin photodimerization reactions that use hydrogen bond donors or acceptors as templates have been performed in the solid state.⁵ From a materials standpoint, many molecules exhibit physical properties that would be of use in a material or device if they were properly organized into ordered crystalline networks. Excellent examples are the wide variety of dipolar chromophores with large hyperpolarizabilities. Large hyperpolarizabilities lead to effective second-harmonic generation, or the frequency-doubling of light. Thus, many dipolar chromophores are attractive for use in second-order nonlinear optical materials (NLO).⁶ Control over molecular organization in NLO materials is particularly important as the chromophores must be arranged in a non-centrosymmetric environment with a net dipole moment for second-harmonic generation to be observed.

Controlling the organization of molecules in the solid state is a significant challenge given the weak forces that influence crystal packing and the complex topology of most molecules. One effective approach to engineering specific crystalline topologies utilizes particularly strong, directional interactions, such as dative bonds or hydrogen bonds, to organize molecules into symmetrical networks. In these systems, the symmetry

of the metal nodes and organic linkers dictates the architecture of the network.^{7,8} A benchmark example of this approach is the series of non-centrosymmetric metal-organic frameworks with pyridyl-carboxylate linkers from Wenbin Lin's group. The network topology arranged the pyridyl-carboxylates with the molecular dipole moments aligned, and odd-numbers of interpenetrated networks promoted non-centrosymmetric lattices. With certain pyridyl-carboxylates, MOFs displaying SHG intensity that exceeded the commercially relevant LiNbO_3 were realized.⁹⁻¹² A major challenge in crystal engineering with metal atoms is ensuring controlled ligand organization, as opposed to the indiscriminate binding or packing that is commonly observed with flexible compounds or in mixtures of metal ions or ligands. Also, engineering non-centrosymmetric environments, a requirement for second-order NLO materials, is difficult. Lastly, few systems reliably form crystalline networks that arrange multiple guests in a solid state environment for templated solid state reactions.

Metallocavitands¹³ have the potential to be useful constructs in crystal engineering. Metallocavitands can be used to predictably arrange guest molecules in the solid state through both dative bonds with the metal ions and supramolecular interactions with the ligand topology. The metal ions can bind guest molecules while the cavitand topology can influence guest orientation, discriminate guests, and guide the organization of metallocavitands in the lattice. Kersting's thiophenolate metallocavitand exemplify the type of complexes that can be realized in the solid-state through this approach, as dimers consistently form with dicarboxylates (figure 1.6).^{14,15} Furthermore, the ligand scaffold or metal ions can be designed to impart useful properties to the crystalline complex, such as chirality or magnetism. Crystal engineering with functional molecules and functional hosts could provide a route to multifunctional materials.

This chapter details solid-state investigations of dimeric $\text{Ln(III)[15-MC}_{\text{Cu(II)}}\text{-5]}$ compartments¹⁶ meant to develop a fundamental understanding of factors that influence compartment formation and guest recognition in the solid state. Such information will aid in the application of the compartment as a solid-state reaction template, as a building block for porous solids, or in the design of molecular materials. Regarding the latter, the use of $\text{Ln(III)[15-MC}_{\text{Cu(II)}}\text{-5]}$ compartments as a construct for controlling the arrangement of NLO chromophores in the solid state is of particular interest given that the chirality of

the MC ensures all MC-guest complexes crystallize in non-centrosymmetric space groups.¹⁷ Furthermore, the crystallographic characterization will provide information on guest recognition and MC assembly relevant to applications of the compartment or monomeric metallocavitand as a catalyst or in separations. Advantages of Ln(III)[15-MC_{Cu(II)}-5] complexes include the chirality of the host, which ensures non-centrosymmetric crystalline compounds and could lead to enantioselective catalysis or separations. Also, the side chains on Ln(III)[15-MC_{Cu(II)}-5] complexes can potentially influence the size and selectivity of the compartment, leading to significant degrees of control over guest inclusion and the solid-state architecture. Lastly, Dy(III)[15-MC_{Cu(II)}-5] complexes are single molecule magnets,¹⁸ which is appealing from the standpoint of multifunctional materials.

Ln(III)[15-MC_{Cu(II)}-5] dimerization in the solid state occurs through associative interactions between phenyl side chains on the host (figure 1.17).^{19,20} Dimerization generates chiral, Lewis-Acidic compartments capable of encapsulating anionic guests. A 7.6 Å tall cylindrical compartment is generated with tyrosine hydroxamic acid (tyrHA) ligands through coordination of the phenol to a copper ring metal. This relatively compact compartment selectively encapsulates nitrate anions while excluding chloride (figure 1.16).²¹ PheHA side chains (figure 2.1c) on the Ln(III)[15-MC_{Cu(II)}-5] (figure 2.1a) associate through hydrophobic interactions between the phenyl rings, generating a larger dimeric compartment that ranges in height from range in height from 10.3¹⁷ - 12.1 Å¹⁶. Ln(III)[15-MC_{Cu(II), pheHA}-5] compartments encapsulate bridging carboxylate guests, such as isonicotinate and terephthalate (figure 2.1e, 2.1f) through guest coordination to metal ions on the MC face and hydrophobic interactions with the phenyl side chains.^{22,23}

Preliminary investigations of Ln(III)[15-MC_{Cu(II), pheHA}-5] compartments focused on guest selectivity. These studies show that unsaturated guests such as terephthalate are encapsulated in the compartment (figure 1.17), while all saturated dicarboxylates with an alkyl chain of up to six carbon atoms are excluded from the hydrophobic interior.²² Importantly, these extensive studies revealed that the compartment is quite general, as the topology is observed with a variety of guests and central Ln(III) ions on the host.^{16,19} The only instance where a compartment was not observed was with the naphthalene dicarboxylate guest (figure 1.17), which was attributed to the considerable length of the

guest. Associative π -stacking interactions between phenyl side chains on the two MCs likely can't form when the MCs are bridged by naphthalene dicarboxylate.¹⁶

Considering the aim of preparing second-order NLO materials, the Pecoraro group has prepared Ln(III)[15-MC_{Cu(II), pheHA}-5] compartments that encapsulate the SHG chromophore, isonicotinate (figure 1.20).²⁴ The compartment encapsulated three isonicotinate guests such that the chiral crystalline host-guest complex possesses a permanent dipole. Though the complexes displayed modest SHG intensity ($I/I_{\text{KDP}} = 0.01$), these examples underscore the promise of these supramolecular hosts in the preparation of functional chiral solids. Furthermore, the encapsulation of multiple anionic guests in close proximity is promising from the standpoint of performing polymolecular reactions in the supramolecular container.

The many crystal structures of dimeric Ln(III)[15-MC_{Cu(II), pheHA}-5] compartments demonstrate broad potential for using the construct in crystal engineering pursuits and also as a supramolecular host in solution. Of particular interest, the structural versatility of the MC allows for substitution of the side chains or metal ions, which could influence guest recognition and organization in the solid state. Based on the promise of MC structural versatility, the general aim of this chapter is to investigate how structural changes to the Ln(III)[15-MC-5] host influences compartment formation and guest recognition. Specifically, work presented in this chapter seeks to establish a theoretical framework for predicting how the length of the phenyl side chain and the central lanthanide influences the compartment size and number of encapsulated guests in dimeric Ln(III)[15-MC-5] containers.

We hypothesized that the constraints on compartment height seen with naphthalene dicarboxylate originate from the length of the phenyl side chain. Considering that the Ln(III)[15-MC_{Cu(II), pheHA}-5] compartment encapsulates terephthalate, we suspected that an MC with a shorter side chain would not form a compartment with the 5.8 Å long guest. Following similar reasoning, we expected that a MC with a longer side chain would effectively encapsulate long guests that disrupt the Ln(III)[15-MC_{Cu(II), pheHA}-5] compartment. Lastly, we predicted that the side chain would limit the extent that a compartment can compress to encapsulate a short guest. Concerning the inclusion of multiple guests in the compartments, we suspected that the nine-coordinate La(III) central

metal would promote the inclusion of two guests based on the precedent in monomeric Ln(III)[15-MC_{Cu(II)}, pheHA-5] complexes (figure 1.18).^{25,26} Furthermore, we hypothesized that steric effects from the phenyl side chain would influence the number of encapsulated guests.

This chapter reports a systematic investigation of how the size and selectivity of dimeric Ln(III)[15-MC-5] compartments is influenced by the central metal and the side chain on the host. A series of Ln(III)[15-MC_{Cu(II)}-5] complexes have been synthesized from ligands bearing phenyl side chains that differ in the number of methylene carbons; S-phenylglycine hydroxamic acid (pgHA), pheHA, and S-homophenylalanine hydroxamic acid (hpheHA) (figure 2.1b-d, respectively). The size and selectivity of this series of dimeric containers were assessed by examining the crystal structures of their inclusion complexes with a set of bridging guests that serve as molecular rulers: terephthalate, bithiophene dicarboxylate (btDC), and isonicotinate (scheme 1e-g, respectively). Ln(III)[15-MC_{Cu(II)}-5] hosts with the 9-coordinate La(III) and 8-coordinate Gd(III) central metals have been studied to consider how the central metal coordination number influences the selectivity of the compartments. Importantly, these investigations present a systematic study that describes how supramolecular considerations of the structural features on a metallocavitand can provide control over molecular organization in the solid state. This chapter also reports the application of Ln(III)[15-MC_{Cu(II)}-5] compartments in the construction of a chiral porous crystalline solid. This example provides a direct demonstration of utilizing the host-guest chemistry of Ln(III)[15-MC_{Cu(II)}-5] compartments in crystal engineering pursuits. The research presented in this chapter has been published previously in three manuscripts.²⁷⁻²⁹

Experimental

Hydroxamic acid ligands were synthesized from the hydrochloric acid salts of their corresponding methyl esters following a modification of a previously reported general procedure.³⁰ The procedure is outlined below for S-phenylglycine hydroxamic acid. The esters were obtained by refluxing a solution of the carboxylic acid and 1.5 equivalents of thionyl chloride in dry methanol for three hours followed by removal of the solvent under vacuum. Bithiophene dicarboxylic acid was prepared according to a

literature method.³¹ Sodium salts of isonicotinate, suberate, azelate, sebacate and bithiophene dicarboxylic acid were prepared by neutralizing the respective carboxylic acids with sodium hydroxide in a water/methanol solution and precipitating with ether. Dilithium pimelate and dilithium adipate were prepared by neutralizing the dicarboxylic acid with 2 equivalents of lithium hydroxide and precipitating with ether. ESI-MS was performed with a Micromass LCT Time-of-Flight Electrospray Mass Spectrometer at cone voltages ranging from 10-75 V on samples containing ~0.1 mg of compound dissolved in 1 mL of 4:1 methanol/water (v/v), or 4:1 DMF/water (v/v) for complexes with bithiophene dicarboxylate guests. Samples were injected via syringe pump. ESI-MS data was processed with MassLynx 4.0 software.

S-phenylglycine hydroxamic acid: Potassium hydroxide (0.045 mol, 2.88 g) was dissolved in 75 mL of degassed methanol and added to (S)-(+)-2-phenylglycine methyl ester hydrochloride (0.045 mol, 9.0 g). White potassium chloride quickly precipitated and was filtered after 10 minutes of cooling in an ice bath. Separately, hydroxylamine hydrochloride (0.134 mol, 9.30 g) was dissolved in 150 mL of degassed methanol and another sample of potassium hydroxide (0.134 mol, 8.6 g) was dissolved in 125 mL of degassed methanol. The two solutions were combined and cooled in an ice bath under a stream of nitrogen to generate hydroxylamine and precipitate potassium chloride. The precipitate was filtered off and the two filtrates were combined and stirred under a nitrogen atmosphere at room temperature. After 1 day, the hydroxamic acid precipitated as a white powder and was filtered. The filtrate was subjected to another portion of hydroxylamine, stirred overnight under nitrogen, and the hydroxamic acid precipitate was filtered. This filtrate was reduced to a volume of 40 mL under vacuum and allowed to sit for four days. Additional hydroxamic acid was isolated by filtration. The filtered solids were combined, stirred in 100 mL of water for 2 hours as a fine suspension and filtered. The solid was then stirred in 100 mL dichloromethane for 1 hour as a fine suspension and filtered. The solid was washed with ether and vacuum dried. Yield = 5.86 g (71%). ¹H NMR [(CD₃)₂SO, 400 MHz]: δ 8.8 (broad s, 1H, NH) 7.35 (d, J = 7 Hz, 2H, *o*-Ph), 7.31 (t, J = 7 Hz, 2H, *m*-Ph), 7.22 (t, J = 7 Hz, 1H, *p*-Ph), 4.22 (s, 1H, C_αH), MP = 172 °C, IR (KBr, cm⁻¹): 3032 br (NH, NH₂, OH), 2878 br (CH), 2646 s (CH), 1612 s (C=O), 1542 m, 1467 m, 1362 m, 1312 w, 1276 w, 1199 w, 1017 w, 922 m, 819w, 776 w, 716 w, 693

m, 609 w. CHN found(calc'd) for C₈H₁₀N₂O₂: C = 58.11 (57.82), H = 6.17 (6.07), N = 16.75(16.86).

S-phenylalanine hydroxamic acid: Reaction was run on a 0.08 mol S-phenylalanine methyl ester hydrochloride scale. Yield = 12.19 g (85%). ¹H NMR [(CD₃)₂SO, 400 MHz]: δ 7.23 (m, 5H, Ph), 3.25 (t, J = 7 Hz, 1H, C_αH), 2.84 (q, J₁ = 13 Hz, J₂ = 6 Hz, 1H, C_βH), 2.61 (q, J₁ = 14 Hz, J₂ = 8 Hz, 1H, C_βH). MP = 190 °C, IR (KBr, cm⁻¹): 3028 br (NH, NH₂, OH), 2857 br (CH), 1615 s (C=O), 1557 m, 1534 m, 1466 m, 1383 s, 1288 s, 1174 w, 1072 w, 913 m, 886 m, 698 m. CHN found(calc'd) for C₉H₁₂N₂O₂: C = 60.14 (59.97), H = 6.77 (6.71), N = 15.50(15.55).

S-homophenylalanine hydroxamic acid: Reaction was run on a 0.075 mol (S)-homophenylalanine methyl ester hydrochloride scale. Yield = 12.61 g (87%). ¹H NMR [(CD₃)₂SO, 400 MHz]: δ 7.27 (t, J = 7 Hz, 2H, *m*-Ph), 7.17 (m, 3H, *o*-Ph, *m*-Ph) 3.02 (t, J = 7 Hz, 1H, C_αH), 2.62 (m, 1H, C_γH), 2.54 (m, 1H, C_γH), 1.78 (m, 1H, C_βH), 1.63 (m, 1H, C_βH). MP = 177.5 °C, IR (KBr, cm⁻¹): 3029 br (NH, NH₂, OH), 2859 br (CH), 1614 s (C=O), 1543 m, 1468 m, 1454 m, 1365 s, 1315 w, 1059 w, 942 w, 876 w, 775 w, 744 w, 696 w. CHN found (calc'd) for C₁₀H₁₄N₂O₂: C = 62.07 (61.84), H = 7.41 (7.27), N = 14.32 (14.42).

Metallacrown Syntheses

La(III)[15-MC_{Cu(II)}, *pheHA-5*](NO₃), Gd(III)[15-MC_{Cu(II)}, *pheHA-5*](NO₃), and Dy(III)[15-MC_{Cu(II)}, *pheHA-5*](NO₃) were prepared as previously described.³²

La(III)[15-MC_{Cu(II)}, *pgHA-5*](NO₃): S-phenylglycine hydroxamic acid (5 mmol, 0.83 g), copper acetate monohydrate (5 mmol, 1.00 g), and lanthanum nitrate hexahydrate (1 mmol, 0.43 g) were stirred overnight in 60 mL of methanol. The solution was filtered through a 2.5 cm shortpad of basic alumina (Brockman 1, Sigma-Aldrich), and rinsed through with 10 mL of methanol. The filtrate was dried under vacuum, yielding a dark purple solid. Yield: 1.293g, 89%. ESI-MS: *m/z* 668.8²⁺ (668.9²⁺ calc'd for [La(III)[15-MC_{Cu(II)}, *pgHA-5*](NO₃⁻)₂)²⁺, 1399.8⁺ (1398.8⁺ calc'd for [La(III)[15-MC_{Cu(II)}, *pgHA-5*](NO₃⁻)₂)⁺, CHN found (calc'd) for LaCu₅C₄₀H₄₀N₁₀O₁₀(NO₃)_{1.5}(OH)_{1.5}(H₂O)_{3.5}: C = 32.93 (32.96), H = 3.35 (3.24), N = 11.04 (11.04).

Gd(III)[15-MC_{Cu(II)}, *pgHA-5*](NO₃): This compound was synthesized via the procedure for La(III)[15-MC_{Cu(II)}, *pgHA-5*](NO₃), substituting gadolinium nitrate hexahydrate for

lanthanum nitrate hexahydrate. Yield: 0.8213g, 89%. ESI-MS: m/z 676.9²⁺ (678.4²⁺ calc'd for [Gd(III)[15-MC_{Cu(II)}, pgHA-5](NO₃⁻)₂]²⁺), 1418.8⁺ (1417.8⁺ calc'd for [Gd(III)[15-MC_{Cu(II)}, pgHA-5](NO₃⁻)₂]⁺), CHN found (calc'd) for GdCu₅C₄₀H₄₀N₁₀O₁₀(NO₃)_{0.5}(OH)_{2.5}(H₂O)_{3.5}: C = 33.43 (33.54), H = 3.32 (3.48), N = 10.27 (10.30).

La(III)[15-MC_{Cu(II)}, hpheHA-5](NO₃): This compound was synthesized via the procedure for La(III)[15-MC_{Cu(II)}, pgHA-5](NO₃), substituting S-homopheHA for S-phenylglycineHA. Yield: 1.3899g, 87%. ESI-MS: m/z 738.9²⁺ (740.0²⁺ calc'd for [La(III)[15-MC_{Cu(II)}, hpheHA-5](NO₃⁻)₂]²⁺), 1540.0⁺ (1541.0⁺ calc'd for [La(III)[15-MC_{Cu(II)}, hpheHA-5](NO₃⁻)₂]⁺), CHN found (calc'd) for LaCu₅C₅₀H₆₀N₁₀O₁₀(NO₃)_{1.5}(OH)_{1.5}(H₂O)_{3.5}: C = 37.49 (37.55), H 4.11 (4.32), N = 10.11 (10.07).

Gd(III)[15-MC_{Cu(II)}, hpheHA-5](NO₃): This compound was synthesized via the procedure for La(III)[15-MC_{Cu(II)}, hpheHA-5](NO₃), substituting gadolinium nitrate hexahydrate for lanthanum nitrate hexahydrate. Yield = 1.4726 g, 92%. ESI-MS: m/z 746.9²⁺ (748.5²⁺ calc'd for [Gd(III)[15-MC_{Cu(II)}, hpheHA-5](NO₃⁻)₂]²⁺), 1558.1⁺ (1558.0⁺ calc'd for [Gd(III)[15-MC_{Cu(II)}, hpheHA-5](NO₃⁻)₂]⁺), CHN found (calc'd) for GdCu₅C₅₀H₆₀N₁₀O₁₀(NO₃)_{1.5}(OH)_{1.5}(H₂O)₄: C = 37.44 (37.44), H 4.07 (4.44), N = 9.63 (9.66).

Synthesis of Host-Guest Complexes

Gd(III)[15-MC_{Cu(II)}, pheHA-5](terephthalate),²² Gd(III)[15-MC_{Cu(II)}, pheHA-5](isonicotinate),²⁴ and La(III)[15-MC_{Cu(II)}, pheHA-5](pimelate)²⁷ were synthesized as previously described.

La(III)[15-MC_{Cu(II)}, s-pgHA-5](isonicotinate): La(III)[15-MC_{Cu(II)}, pgHA-5](NO₃) (.021 mmol, 30 mg) and sodium isonicotinate (0.069 mmol, 10 mg) were dissolved in 5 mL of a 2:1 methanol/water mixture and filtered. Slow evaporation of the solvent yielded crystals within one month. Yield: 9.1 mg, 24%. ESI-MS: m/z 698.8²⁺ (698.9²⁺ calc'd for {La(III)[15-MC_{Cu(II)}, pgHA-5](isonicotinate⁻)₂]²⁺), 973.2³⁺ (973.3³⁺ calc'd for {La(III)[15-MC_{Cu(II)}, pgHA-5]₂(isonicotinate⁻)₃]³⁺), 1521.9⁺ (1520.9⁺ calc'd for {La(III)[15-MC_{Cu(II)}, pgHA-5](isonicotinate⁻)₂]⁺), CHN found (calc'd) for LaCu₅C₄₀H₄₀N₁₀O₁₀(C₆H₄NO₂)_{2.5}(OH)_{0.5}(H₂O)_{4.5}: C = 39.32 (39.50). H = 3.38 (3.59), N = 10.33 (10.47).

La(III)[15-MC_{Cu(II)}, S-pheHA-5](isonicotinate): This complex was originally crystallized by Dr. Choong-Sun Lim. La(III)[15-MC_{Cu(II)}, pheHA-5](NO₃) (0.018 mmol, 30 mg) and sodium isonicotinate (0.069 mmol, 10 mg) were mixed in 6 mL of a 2:1 methanol/water mixture. The solution was filtered, and crystals were obtained within two months upon slow evaporation of the solvent. Yield = 14.6 mg, 46%. ESI-MS: *m/z* 733.9²⁺ (735.0²⁺ calc'd for {La(III)[15-MC_{Cu(II)}, pheHA-5](isonicotinate⁻)₂}²⁺), 1019.9³⁺ (1020.0 calc'd for {(La(III)[15-MC_{Cu(II)}, pheHA-5]₂(isonicotinate⁻)₃}³⁺), 1590.0⁺ (1591.0⁺ calc'd for {La(III)[15-MC_{Cu(II)}, pheHA-5](isonicotinate⁻)₂}⁺), CHN found (calc'd for LaCu₅C₄₅H₅₀N₁₀O₁₀(C₆H₄NO₂)₂(NO₃)(H₂O)₆): C = 38.74 (38.85), H = 3.98 (4.01), N = 10.08 (10.34).

La(III)[15-MC_{Cu(II)}, hpheHA-5](isonicotinate): This complex was originally crystallized by Dr. Gellert Mezei. La(III)[15-MC_{Cu(II)}, hpheHA-5](NO₃) (0.019 mmol, 30 mg) and sodium isonicotinate (0.069 mmol, 10mg) were combined in 8 mL of a 3:1 methanol/water mixture. The solution was filtered and set aside to evaporate slowly. Crystals formed in two weeks. Yield: 9.8 mg, 29%. ESI-MS: *m/z* 768.9²⁺ (770.0²⁺ calc'd for {La(III)[15-MC_{Cu(II)}, hpheHA-5](isonicotinate⁻)₂}²⁺), 1066.7³⁺ (1067.4³⁺ calc'd for {(La(III)[15-MC_{Cu(II)}, hpheHA-5]₂(isonicotinate⁻)₃}³⁺), 1660.1⁺ (1661.0⁺ calc'd for {La(III)[15-MC_{Cu(II)}, hpheHA-5](isonicotinate⁻)₂}⁺), CHN found (calc'd for LaCu₅C₅₀H₆₀N₁₀O₁₀(C₆H₄NO₂)₂(NO₃)(H₂O)_{3.5}): C = 41.50 (41.67), H = 4.15 (4.23), N = 9.72 (10.19).

La(III)[15-MC_{Cu(II)}, pheHA-5](terephthalate): This complex was originally crystallized by Kiefer Forsch. La(III)[15-MC_{Cu(II)}, pheHA-5](NO₃) (0.018 mmol, 30 mg) and terephthalic acid sodium salt (0.027 mmol, 5.7 mg) were dissolved in 8 mL of a 3:1 methanol/water mixture. The solution was set to slowly evaporate, yielding crystals within 1 month. Yield: 22.7 mg, 76%. ESI-MS: *m/z* 755.4²⁺ (756.5 calc'd for {La(III)[15-MC_{Cu(II)}, pheHA-5](terephthalateH⁻)₂}²⁺), 973.3³⁺ (973.3³⁺ calc'd for {(La(III)[15-MC_{Cu(II)}, pheHA-5]₂(terephthalate²⁻)(NO₃⁻)₃}³⁺), 1007.6³⁺ (1007.6³⁺ calc'd for [La(III)[15-MC_{Cu(II)}, pheHA-5](terephthalate²⁻)(terephthalateH⁻)₃}³⁺), 1511.0⁺ (1509.9⁺ calc'd for {La(III)[15-MC_{Cu(II)}, pheHA-5](terephthalate²⁻)₂}⁺), 1511.0²⁺ (1511.0²⁺ calc'd for [(La(III){15-MC_{Cu(II)}, pheHA-5]₂(terephthalate²⁻)₂}²⁺), CHN found (calc'd for

LaCu₅C₄₅H₅₀N₁₀O₁₀(C₈H₄O₄)(NO₃)(H₂O)₅: C = 38.38 (38.26), H = 3.77 (3.88), N = 9.11 (9.26).

La(III)[15-MC_{Cu(II)}, hpheHA-5](terephthalate): This complex was originally crystallized by Dr. Gellert Mezei. La(III)[15-MC_{Cu(II)}, hpheHA-5](NO₃) (0.019 mmol, 30 mg) and terephthalic acid sodium salt (0.048 mmol, 10 mg) were mixed in 8 mL of a 3:1 methanol/water fixture and filtered. The solvent slowly evaporated, yielding crystals in two weeks. Yield = 16.3 mg, 49%. ESI-MS: *m/z* 790.5²⁺ (791.5²⁺ calc'd for {La(III)[15-MC_{Cu(II)}, hpheHA-5](terephthalateH)}²⁺), 1055.0³⁺ (1055.0³⁺ calc'd for {(La(III)[15-MC_{Cu(II)}, hpheHA-5]₂(terephthalate²⁻)(terephthalateH)}³⁺), 1061.7³⁺ (1062.3 calc'd for {(La(III)[15-MC_{Cu(II)}, hpheHA-5]₂(terephthalate²⁻)(terephthalateH)(H₂O)}³⁺), 1581.0⁺ (1581.6⁺ calc'd for {La(III)[15-MC_{Cu(II)}, hpheHA-5](terephthalate²⁻)}⁺), 1581.0²⁺ (1581.6²⁺ calc'd for {(La(III)[15-MC_{Cu(II)}, hpheHA-5]₂(terephthalate²⁻)₂}²⁺), CHN found (calc'd for LaCu₅C₅₀H₆₀N₁₀O₁₀(C₈H₄O₄)_{1.5}(H₂O)₅) : C = 42.36 (42.46), H = 4.17 (4.37), N = 7.95 (7.99).

Gd(III)[15-MC_{Cu(II)}, pgHA-5](terephthalate): This complex was originally crystallized by Dr. Choong-Sun Lim.²⁶ Gd(III)[15-MC_{Cu(II)}, pgHA-5](NO₃) (.021 mmol, 30 mg) was dissolved in 5 mL of water. Terephthalic acid sodium salt (0.06 mmol, 12.6 mg) was dissolved in about 2 mL of water. The solution was filtered and crystals were obtained upon slow evaporation of the solvent. Yield: 3.4 mg, 8.7%. ESI-MS: *m/z* 729.9²⁺ (729.9²⁺ calc'd for {Gd(III)[15-MC_{Cu(II)}, pgHA-5](terephthalateH)}²⁺), 972.8³⁺ (973.6³⁺ calc'd for {Gd(III)[15-MC_{Cu(II)}, pgHA-5](terephthalate²⁻)(terephthalateH)}³⁺), 1460.0⁺ (1458.9⁺ calc'd for [Gd(III)[15-MC_{Cu(II)}, pgHA-5](terephthalate²⁻)}⁺, 1460.0²⁺ (1460.0²⁺ calc'd for [(Gd(III)[15-MC_{Cu(II)}, pgHA-5]₂(terephthalate²⁻)₂}²⁺), 1625.0⁺ (1624.9⁺ calc'd for {Gd(III)[15-MC_{Cu(II)}, pgHA-5](terephthalateH)₂}⁺), CHN found (calc'd for GdCu₅C₄₀H₄₀N₁₀O₁₀(C₈H₄O₄)(C₈H₅O₄)(H₂O)₁₃): C = 35.53 (36.18), H = 3.51 (4.07), N = 8.14 (7.53).

Gd(III)[15-MC_{Cu(II)}, hpheHA-5](terephthalate): Gd(III)[15-MC_{Cu(II)}, hpheHA-5](NO₃) (0.019 mmol, 30 mg) and terephthalic acid sodium salt (0.027 mmol, 5.7 mg) were dissolved in 10 mL ethanol and 3 mL of water. The solution was filtered, and deep purple crystals were obtained upon slow evaporation of the solvent. Yield = 8.7 mg, 27%. ESI-MS: *m/z* 800.0²⁺ (800.0²⁺ calc'd for {Gd(III)[15-MC_{Cu(II)}, hpheHA-5](terephthalateH)}²⁺), 1067.7³⁺

(1067.0³⁺ calc'd for {(Gd(III)[15-MC_{Cu(II), hpheHA-5}]₂(terephthalate²⁻)(terephthalateH⁻)}³⁺), 1074.4³⁺ (1073.0³⁺ calc'd for {(Gd(III)[15-MC_{Cu(II), hpheHA-5}]₂(terephthalate²⁻)(terephthalateH⁻)(H₂O)}³⁺, 1600.1⁺ (1600.0⁺ calc'd for {Gd(III)[15-MC_{Cu(II), hpheHA-5}](terephthalate²⁻)}⁺, 1600.1²⁺ (1600.0²⁺ calc'd for {(Gd(III)[15-MC_{Cu(II), hpheHA-5}]₂(terephthalate²⁻)₂}²⁺), CHN found (calc'd for GdCu₅C₅₀H₆₀N₁₀O₁₀(C₈H₄O₄)(OH)(C₂H₆O)_{0.5}(H₂O)₄): C = 41.47 (41.39), H = 4.12 (4.47), N = 7.83 (8.18).

Gd(III)[15-MC_{Cu(II), hpheHA-5}](btDC): Gd(III)[15-MC_{Cu(II), hpheHA-5}](NO₃) (0.019 mmol, 30 mg) and 2,2'-bithiophene dicarboxylic acid disodium salt (0.027 mmol, 8.2 mg) were mixed in 6 mL of a 2:1 DMF/water mixture. The solution was filtered. Water (4 mL) was slowly added until the blue precipitate persisted. Methanol (1 mL) was added to clarify the solution, which was slowly evaporated to yield crystals in under two weeks. Yield: 13.5 mg, 37%. ESI-MS: *m/z* 843.9²⁺ (845.0²⁺ calc'd for {Gd(III)[15-MC_{Cu(II), hpheHA-5}](btDCH⁻)²⁺), 880.5²⁺ (881.5²⁺ calc'd for {Gd(III)[15-MC_{Cu(II), hpheHA-5}](btDCH⁻)(DMF)}²⁺), 1125.6³⁺ (1125.7²⁺ calc'd for {(Gd(III)[15-MC_{Cu(II), hpheHA-5}]₂(btDC²⁻)(btDCH⁻)³⁺, 1688.0⁺ (1688.0⁺ calc'd for {Gd(III)[15-MC_{Cu(II), hpheHA-5}](btDC²⁻)⁺), 1688.0²⁺ (1688.0²⁺ calc'd for {(Gd(III)[15-MC_{Cu(II), hpheHA-5}]₂(btDC²⁻)₂}⁺), CHN found (calc'd for GdCu₅C₅₀H₆₀N₁₀O₁₀(C₁₀H₄O₄S₂)_{1.5}(H₂O)₇): C = 40.05 (40.23), H = 4.13 (4.16), N = 7.37 (7.22).

La(III)[15-MC_{Cu(II), pgHA-5}](btDC): La(III)[15-MC_{Cu(II), pgHA-5}](NO₃) (0.021 mmol, 30 mg) and 2,2'-bithiophene dicarboxylic acid disodium salt (0.034 mmol, 10 mg) were mixed in 12 mL of a 2:2:1 methanol/water/acetonitrile mixture. A blue precipitate formed and was redissolved upon the addition of 3 mL of DMF. The solution was filtered and set to slowly evaporate, yielding crystals in one month. Yield: 8.4 mg, 22%. ESI-MS: *m/z* 765.3²⁺ (765.4²⁺ calc'd for {La(III)[15-MC_{Cu(II), pgHA-5}](btDCH⁻)²⁺), 801.9²⁺ (801.9²⁺ calc'd for {La(III)[15-MC_{Cu(II), pgHA-5}](btDCH⁻)(DMF)}²⁺), 1529.8⁺ (1528.8⁺ calc'd for {La(III)[15-MC_{Cu(II), pgHA-5}](btDC²⁻)⁺), 1529.8²⁺ (1528.8²⁺ calc'd for {(La(III)[15-MC_{Cu(II), pgHA-5}]₂(btDC²⁻)₂}²⁺), CHN found (calc'd for LaCu₅C₄₀H₄₀N₁₀O₁₀(C₁₀H₄O₄S₂)_{1.5}(H₂O)₉): C = 36.23 (36.34), H = 3.62 (3.55), N = 7.88 (7.70).

La(III)[15-MC_{Cu(II), pheHA-5}](btDC): 2,2'-bithiophene dicarboxylic acid disodium salt (15 mg, 0.051 mmol) was added to La(NO₃)_{2.5}[15-MC_{Cu(II), pheHA-5}](NO₃) (0.03 g, 0.018 mmol) dissolved in 8 mL of a 1:1 ethanol/water mixture. A precipitate quickly formed, which was filtered and dissolved in DMF. The solution was slowly evaporated to yield crystals in one month. Yield: 11.2 mg, 27%. ESI-MS (4:1 DMF/H₂O): *m/z* 800.5²⁺ (800.4²⁺ calc'd for La(III)[15-MC_{Cu(II), pheHA-5}](btDCH)²⁺), 837.0²⁺ (837.0²⁺ calc'd for La(III)[15-MC_{Cu(II), pheHA-5}](btDCH)(DMF)²⁺), 1600.0⁺ (1598.9⁺ calc'd for La(III)[15-MC_{Cu(II), pheHA-5}](btDC)¹⁺, (La(III)[15-MC_{Cu(II), pheHA-5}](btDC))₂²⁺). IR (KBr disk): 3406, 1652, 1582, 1516, 1496, 1454, 1433, 1360, 1081, 1026, 776, 701, 593 cm⁻¹. CHN found (calc'd) C = 39.75 (40.56), H = 4.06 (5.26), N = 8.62 (9.65).

Dy(III)[15-MC_{Cu(II), pheHA-5}](pimelate): Dy(III)[15-MC_{Cu(II), pheHA-5}](NO₃) (0.03 g, 0.019 mmol) was dissolved in 10 mL of water. Dilithium pimelate (0.017 g, 0.09 mmol) was added and the solution was slowly evaporated to grow single crystals. Yield 41 %. Analysis for C₁₁₁H₁₇₈N₂₀O₅₆Cu₁₀Dy₂, found (calc'd): C = 35.97 (36.53), H = 4.86 (4.92), N = 7.63 (7.68). ESI-MS gave *m/z* = 1528.9⁺ (1528.0⁺ calc'd for Dy(III)[15-MC_{Cu(II), pheHA-5}](pimelate)⁺)

Gd(III)[15-MC_{Cu(II), hpheHA-5}](adipate): Gd(III)[15-MC_{Cu(II), hpheHA-5}](NO₃) (0.018 mmol, 30 mg) and adipic acid dilithium salt (0.028 mmol, 4.4 mg) were dissolved in 6 mL of a 3:1 methanol/water mixture. The solution was filtered, and purple crystals were obtained upon slow evaporation of the solvent. Yield: 18.4 mg. CHN found C = 37.89, H = 4.68, N = 8.68.

La(III)[15-MC_{Cu(II), hpheHA-5}](adipate): La(III)[15-MC_{Cu(II), hpheHA-5}](NO₃) (0.018 mmol, 30 mg) and adipic acid dilithium salt (0.028 mmol, 4.4 mg) were dissolved in 6 mL of a 3:1 methanol/water mixture. The solution was filtered, and purple crystals were obtained upon slow evaporation of the solvent. Yield: 9.7 mg. CHN found C = 39.94, H = 4.49, N = 8.91.

La(III)[15-MC_{Cu(II), hpheHA-5}](pimelate): La(III)[15-MC_{Cu(II), hpheHA-5}](NO₃) (0.018 mmol, 30 mg) and pimelic acid dilithium salt (2.8 mmol, 4.8 mg) were dissolved in 6 mL of a 3:1 methanol/water mixture. The solution was filtered, and purple crystals were obtained upon slow evaporation of the solvent. Yield: 11.3 mg. CHN found C = 39.94, H = 4.49, N = 8.91.

Gd(III)[15-MC_{Cu(II)}, _{hpheHA-5}](suberate): Gd(III)[15-MC_{Cu(II)}, _{hpheHA-5}](NO₃) (0.018 mmol, 30 mg) and suberic acid disodium salt (0.028 mmol, 10 mg) were dissolved in 6 mL of a 3:1 methanol/water mixture. The solution was filtered, and purple crystals were obtained in two weeks upon slow evaporation of the solvent. Yield: 13.3 mg. CHN found C = 41.59, H = 4.76, N = 7.87.

La(III)[15-MC_{Cu(II)}, _{pgHA-5}](adipate): La(III)[15-MC_{Cu(II)}, _{pgHA-5}](NO₃) (0.018 mmol, 30 mg) and adipic acid dilithium salt (0.063 mmol, 10 mg) were mixed in 5 mL of a 4:1 water/methanol mixture. The solution was filtered and set to slowly evaporate. Deep blue crystals were obtained in just over two months. Yield: 4.7 mg.

Crystallography

Complexes described in this chapter were prepared by myself unless specified otherwise. Diffraction data was collected and processed by either Jeff W. Kampf or at the Advanced Light Source at Lawrence Berkeley National Laboratory. Initial structures were solved and refined primarily by myself or, in a few instances, with the assistance of Jeff W. Kampf.

Intensity data for La(III)[15-MC_{Cu(II)}, _{pgHA-5}](btDC) was collected at 150 K on a D8 goniostat equipped with a Bruker APEXII CCD detector at Beamline 11.3.1 at the Advanced Light Source (Lawrence Berkeley National Laboratory) using synchrotron radiation tuned to $\lambda=0.7749\text{\AA}$. A series of 3-s frames measured at 0.2° increments of ω were collected to calculate a unit cell. For data collection frames were measured for a duration of 3-s for low angle data and 5-s for high angle data at 0.3° intervals of ω with a maximum 2θ value of $\sim 60^\circ$. The data frames were collected using APEX2 and processed using the program SAINT³³ routine within APEX2. The data were corrected for absorption and beam corrections based on the multi-scan technique as implemented in SADABS³⁴. The structure was solved and refined with the Bruker SHELXTL (version 2008/4) software package.³⁵

Intensity data for La(III)[15-MC_{Cu(II)}, _{pheHA-5}](isonicotinate) was collected at 85(2) K on a standard Bruker SMART-APEX CCD-based X-ray diffractometer equipped with a low temperature device and fine focus Mo-target X-ray tube ($\lambda = 0.71073\text{ \AA}$) operated at 1500 W power (50 kV, 30 mA). Indexing was performed by use of the CELL_NOW³⁶ program which indicated that the crystal was a two-component, non-merohedral twin.

Analysis of the data showed negligible decay during data collection; the data were processed with TWINABS³⁷ and corrected for absorption. The domains are related by a rotation of 2.3 degrees about the reciprocal [0.660 1.000 0.274] axis or direct [0.505 1.000 -0.169] axis. For this refinement, single and composite reflections from the primary domain were used. Merging of the data was performed in TWINABS and an HKLF 4 format file used for refinement. The structures were solved and refined with the Bruker SHELXTL (version 2008/4) software package.³⁵

Intensity data for all other samples were collected at 85(2) K on a standard Bruker SMART-APEX CCD-based X-ray diffractometer equipped with a low temperature device and fine focus Mo-target X-ray tube ($\lambda = 0.71073$ Å) operated at 1500 W power (50 kV, 30 mA). The frames were integrated with the Bruker SAINT³⁸ software package with a narrow frame algorithm. The data were processed with SADABS³⁴ and corrected for absorption. The structures were solved and refined with the Bruker SHELXTL (version 2008/4) software package.³⁵ All other experimental details are presented in tables 2.1-2.3.

Visible absorption spectroscopy guest absorption experiments

Visible absorption spectroscopy was performed on a Varian Cary-100 Bio UV-Visible spectrophotometer. Crystalline La(III)[15-MC_{Cu(II), pheHA-5}](pimelate) was ground until microcrystalline, and 2-10 mg of the solid was added to ~60 μ M solutions of a guest in acetone or methylene chloride. The suspensions sat at room temperature for the desired length of time in sealed vials and were analyzed by visible absorption spectroscopy.

Results and Discussion

Compartments

In terms of their covalent structure, Ln(III)[15-MC_{Cu(II), pheHA-5}] complexes are monomeric metallocavitands. Crystal structures of the hosts with certain bridging carboxylate guests reveal dimeric compartments that associate through hydrophobic interactions between phenyl rings on the ligand side chains. Certain structural criteria for Ln(III)[15-MC_{Cu(II), pheHA-5}] compartments have been recognized.^{23,39,40} First, compartments contain hydrophobic interactions between phenyl side chains on adjacent LnMCs, effectively creating the walls of the container. Second, compartments typically

possess an approximately cylindrical shape in order to maximize associative contacts between phenyl side chains and completely encapsulate the guests. Third, the Ln(III)[15-MC_{Cu(II)}-5] phenyl side chains recognize guests through directional, convergent intermolecular interactions. As a whole, these features define the compartment as a dimeric container that recognizes guests through both dative bonds and intermolecular interactions. Importantly, the associative hydrophobic interactions between ligand side chains would contribute to compartment formation in the absence of solid-state packing forces, suggesting the possibility of solution applications for these hosts.

Compartment height is an important characteristic of Ln(III)[15-MC_{Cu(II)}-5] dimers, as the height dictates the length of the guests that can be encapsulated. Compartment heights (or MC-MC distance) are reported herein as the distance between the centroid of the oxygen-mean planes of each MC.⁴¹ Given that the location of the central metal varies from approximately 0.2-0.7 Å above or below the center of the oxygen-mean plane,³² referencing compartment dimensions to the center of the oxygen-mean plane allows for more direct comparisons of different structures. As the compartment dimensions vary with guest size, guests with different lengths have been investigated in order to assess how side chain variation effects compartment size and selectivity. Guest length is defined as the distance between carboxylate-carbons for dicarboxylates, or the carboxylate-carbon to pyridyl nitrogen distance for isonicotinate. Referencing guest length to the carboxylate carbon eliminates the disparity between *endo* and *exo* carboxylate binding modes. In the specific case of the btDC guest, the length can vary by over 0.3 Å angstroms depending on the torsion angle between the two thiophene rings. The *trans* rotamer distance is reported in figure 2.1.

Side Chain Length Constrains the Compartment Height

It has previously been demonstrated that the 5.8 Å long terephthalate guest is effectively encapsulated by the dimeric Gd(III)[15-MC_{Cu(II), pheHA}-5] compartment.³⁹ It has also been shown that the maximum compartment height is constrained, as the compartment does not form with naphthalene dicarboxylate.^{23,28} The constraint on maximum compartment height is also evident in the La(III)[15-MC_{Cu(II), pheHA}-5](btDC) complex (figure 2.2).²⁹ The crystal structure reveals complete disruption of the hydrophobic cavity by the long guest. The phenyl side chains splay out, giving the entire

La(III)[15-MC_{Cu(II), pheHA-5}] a planar topology. The central La(III) ions are 9-coordinate, with three water molecules bound on the hydrophobic face. The hydrophobic faces associate via bridging btDC guests, though the compartment motif is not observed. In one dimer, the btDC binds monodentate with a roughly perpendicular orientation with the MC face in the *trans*-rotamer, engaging in hydrogen bonding interactions with La(III) bound water molecules on an adjacent MC hydrophobic face. The other dimer is bridged by a *cis*-btDC guest bound to Cu (II) ring metals. The MCs are significantly displaced relative to each other. Though the MCs dimerize across the hydrophobic faces through bridging btDC guests, no compartment motif is observed. There is no association between MC phenyl side chains across the hydrophobic faces or between the side chains and btDC guests. Thus the La(III)[15-MC_{Cu(II), pheHA-5}](btDC) complex demonstrates the importance of matching guest and side chain length in forming solid state compartments.

The complexes of Ln(III)[15-MC_{Cu(II), pgHA-5}] with terephthalate and btDC guests establish further that long guests prevent compartment formation by disrupting associative intermetallacrown interactions between the phenyl side chains that are necessary for compartment integrity. In the Gd(III)[15-MC_{Cu(II), pgHA-5}](terephthalate) complex (figure 2.3), a monomeric host is observed with terephthalate bound bidentate on the hydrophilic face. The other carboxylate on this terephthalate forms hydrogen bonds with lattice water molecules. On the hydrophobic face, a water is bound to Gd(III). An unbound terephthalate forms a hydrogen-bond with this coordinated water and π -stacking interactions with pgHA phenyl rings. Unlike other MC structures, the saturated guest is not bound to the lanthanide central metal on the hydrophobic face. This is attributed to the orientation of the inflexible phenyl side chain toward the periphery of the MC, which limits how effectively the phenyl side chains can recognize a guest bound to the central metal. Importantly, this structure shows that the short pgHA side chain prevents compartment formation with the 5.8 Å long terephthalate. In contrast, a compartment is observed in the Ln(III)[15-MC_{Cu(II), pheHA-5}](terephthalate) complexes with La(III) (*vide infra*) and Gd(III), which further demonstrates that the maximum allowed compartment height is constrained by side chain length.

Unsurprisingly, the prototypical cylindrical compartment is not observed in the La(III)[15-MC_{Cu(II), pgHA-5}](btDC) complex. The two La(III)[15-MC_{Cu(II), pgHA-5}] dimers

in the asymmetric unit are bridged by either a *cis*- or *trans*-btDC (figure 2.4, top and bottom, respectively). A second btDC is bound to the hydrophobic face of each MC. This guest extends bridges a Cu(II) ring metal on the hydrophilic face of another MC in the lattice, resulting in a coordination polymer. Extensive π -stacking and CH-O interactions are observed between the pgHA side chains and btDC guests at the periphery of the MC. One hydrophobic face distorts significantly, leading to supramolecular interactions with a btDC guest bound in the center of the cavity (figure 2.5). In the La(III)[15-MC_{Cu(II)}, pgHA-5](btDC) structure, the length of btDC prevents the formation of the cylindrically shaped compartment, as the MCs in the dimer are horizontally displaced by over 8 Å. Importantly, the pgHA phenyl rings on opposite MCs do not associate through π -stacking interactions. While some Van der Waals interactions between pgHA side chains are observed, the association of the side chains primarily occurs through the packing of interstitial DMF solvent molecules. Overall, this structure does not fit the criteria of a compartment (*vide supra*), further demonstrating how long guests can disrupt intermetallacrown interactions.

As expected, the longer hpheHA side chain renders the Ln(III)[15-MC_{Cu(II)}, hpheHA-5] host capable of encapsulating longer guests than hosts with pheHA or pgHA side chains. The crystal structure of the Gd(III)[15-MC_{Cu(II)}, hpheHA-5](btDC) complex reveals a 15.2 Å cylindrical compartment that encapsulates the 9.2 Å btDC guest (figure 2.6). The btDC guest is bound bidentate to 8-coordinate Gd(III) central metals. Many π -stacking interactions are observed between ligands across the hydrophobic faces and the aromatic rings on the guest. A CH-O interaction is observed between the hpheHA side chain and a bound carboxylate oxygen atom (figure 2.6 bottom). Interestingly, the pheHA side chain does not allow for CH-O interactions with bound guests. As a whole, these structures reveal that the maximum height of the compartment is dictated by the side chain length. The encapsulation of the 5.8 Å long terephthalate is observed with the pheHA side chain and not with the shorter pgHA. Similarly, the encapsulation of the 9.2 Å long btDC is observed with the hpheHA side chain, and not with pheHA or pgHA.

Expanding on these findings, the La(III)[15-MC_{Cu(II)}, hpheHA-5](isonicotinate) complex reveals that compartments can also be disrupted by excessively short guests. Isonicotinate is effectively encapsulated in compartments with Gd(III)[15-MC_{Cu(II)}, pheHA-

5], $\text{La(III)[15-MC}_{\text{Cu(II), pheHA-5}]}$, and $\text{La(III)[15-MC}_{\text{Cu(II), pgHA-5}]}$ hosts (*vide infra*). However, the $\text{La(III)[15-MC}_{\text{Cu(II), hpheHA-5}]}$ does not form a compartment with the 4.3 Å long isonicotinate. In the structure, two isonicotinate guests are bound in a monomeric $\text{La(III)[15-MC}_{\text{Cu(II), hpheHA-5}]}$ hydrophobic cavity (figure 2.7). The inclusion of two guests is afforded by an additional coordination site on the nine-coordinate La(III) central metal. The isonicotinate guests are bound through their carboxylates, with one bidentate to La^{III} , and the other bridging the central metal and a Cu^{II} ring metal. The pyridyl nitrogens are unbound, extending out of the hydrophobic cavity and hydrogen bonding to lattice water molecules. The two monomeric MCs associate via π -stacking interactions with a 16.1 Å MC-MC distance. However, the monomers are significantly offset, with a 7.3 Å horizontal displacement relative to each other. This demonstrates that though compartments can compress to accommodate short guests, the extent that they will compress is limited by the side chain length.

As a whole, the $\text{Ln(III)[15-MC}_{\text{Cu(II)-5}]}$ compartments structures described heretofore and in previous work^{23,24,28,32,39,40} reveal that the side chain length constrains the maximum and minimum compartment height. The assembly of the compartment through non-directional hydrophobic interactions between the flexible side chains gives the dimeric compartment a margin of a few angstroms where it can adapt to the size of a guest. However, the compartment can be readily disrupted by extremely long or short guests. These results suggest that as a guideline for designing $\text{Ln(III)[15-MC}_{\text{Cu(II)-5}]}$ compartment inclusion complexes, the guest length should be complementary with the predicted compartment height within a few angstroms. Such predictions can be made by simply considering the length of the MC-MC distance bridged by the guest and the length of the side chain. For example, the crystal structures show that $\text{Ln(III)[15-MC}_{\text{Cu(II), hpheHA-5}]}$ compartments can compress down 11.9 Å. Also the hpheHA side chain can extend up to ~ 8.25 Å from the MC face based the Van der Waals radii. Therefore hpheHA compartments can probably range from ~12-16.5 Å, and guests that generate compartments within this range should be encapsulated by the host. Guests lengths are measured from the carboxylate-carboxylate carbon distance. An estimate of the compartment height generated by a guest can be obtained by adding the guest length and twice the typical MC-carboxylate carbon distance (~3-3.2 Å). So compartments with

hpheHA side chains should be capable of encapsulating guests ranging from 5.6 to 10.5 Å in length.

Factors Influencing the Number of Encapsulated Guests

The inclusion of multiple guests is appealing from the viewpoint of multimolecular reactions in the interior of a host or the design of materials. We sought to establish the factors that promote the inclusion of multiple guests in dimeric Ln(III)[15-MC_{Cu(II)}-5] compartments. Analysis of the crystal structures of the series of Ln(III)[15-MC_{Cu(II)}-5] host-guest complexes reveals that steric interactions with the side chain, compartment compression or elongation, and the central lanthanide coordination number all influence the number of encapsulated guests.

The effect of side chain sterics is most evident by comparing the La(III)[15-MC_{Cu(II), pheHA}-5](isonicotinate) and La(III)[15-MC_{Cu(II), pgHA}-5](isonicotinate) structures. Three isonicotinate guests are encapsulated in the La(III)[15-MC_{Cu(II), pheHA}-5] compartment (figure 2.8), while five are encapsulated in the La(III)[15-MC_{Cu(II), pgHA}-5] complex (figure 2.9). The La(III)[15-MC_{Cu(II), pheHA}-5](isonicotinate) complex closely resembles the previously reported structure that had a Gd(III) central metal.²⁴ The La(III)[15-MC_{Cu(II), pheHA}-5] compartment has a height of 10.5 Å. Two isonicotinates are aligned antiparallel, with the pyridine coordinated to a Cu(II) ring metal and at least one carboxylate oxygen atom bound to a La(III) central metal. The third isonicotinate binds bidentate to a La(III) and does not span the dimer, instead extending toward the periphery of the MC.

The La(III)[15-MC_{Cu(II), pgHA}-5](isonicotinate) compartment is 9.7 Å in height and encapsulates 5 guests. The structure is disordered between two components with 75% and 25% occupancy (figure 2.9, top and bottom, respectively). In the dominant component, the five isonicotinate guests are aligned parallel as they bridge the compartment. One carboxylate bridges a nine-coordinate La(III) and a ring metal, while the remaining four are bound monodentate to a ring metal. In the less dominant component, only four of the isonicotinates are parallel. The fifth is roughly perpendicular, with the pyridine group oriented to the periphery of the host.

The distinction between the inclusion of three or five guests in the La(III)[15-MC_{Cu(II), pheHA}-5](isonicotinate) and La(III)[15-MC_{Cu(II), pgHA}-5](isonicotinate)

compartments suggests that the length and orientation of the phenyl side chain can influence the number of encapsulated guests. With pgHA, the phenyl side chain is rigidly extended to the periphery of the MC where there are minimal steric effects obstructing the inclusion of multiple guests. In contrast, the pheHA side chains are longer and more flexible. They are observed converging on guests bound in the hydrophobic cavity. This recognition mode by the more flexible side chain likely introduces steric interactions which hinder the binding of additional guests. This effect of side chain convergence limiting guest accessibility is most evident in compartment volume measurements. Compartment volumes were estimated with Platon⁴² by comparing the void space of the crystal structure with and without encapsulated guests. The solvent-accessible void space of the structure was measured with and without the encapsulated substrates in the interior of the compartment, which entails the carboxylate guests and other counterions or solvent molecules. The difference in the void spaces of the complete structure from that of the empty compartment gave the estimate for the volume of the host. These values are tabulated in table 2.4 for complexes with well defined compartments. The guest volume was measured in Discovery Studio Visualizer by rolling a 1.4 Å probe over the surface of the guest. The volume of a water molecule was set as 11.5 Å³.⁴³ The compartment and guest volumes were used to determine the packing coefficient, defined as the percentage of the host volume filled by the guests. A previous study has reported that the optimal packing coefficient for guest inclusion is 55 ± 9 %, though this is expected to be higher in assemblies with highly polar host-guest interactions.⁴⁴ Packing coefficients for select Ln(III)[15-MC-5] compartments are listed in table 2.4. The volume of the La(III)[15-MC_{Cu(II), pgHA-5}](isonicotinate) compartment is 710.3 Å³. The volume of the La(III)[15-MC_{Cu(II), pheHA-5}](isonicotinate) compartment is over 30% less at 480.3 Å³. These compartment volumes reflect how longer, more flexible side chains converge on substrates in the hydrophobic cavity, which introduces a steric constraint on the number of encapsulated guests. The orientation of the flexible side chains toward the center of the MC face limits the space available to guest molecules.

The inclusion of multiple guests also seems to be promoted by compartment compression. When compartments compress with a short bridging guest, the side chains tend to splay out toward the periphery of the MC. This removes the bulky phenyl side

chains from the vicinity of the MC face, effectively widening the compartment and increasing the guest-accessible volume of the host. The effects of compartment compression are evident when comparing the inclusion complexes of the Ln(III)[15-MC_{Cu(II), pheHA-5}] hosts with isonicotinate and terephthalate. As previously described, the La(III)[15-MC_{Cu(II), pheHA-5}](isonicotinate) compartment compresses to a mere 10.5 Å in height. This compression promotes the inclusion of three guests.

In contrast, the taller Ln(III)[15-MC_{Cu(II), pheHA-5}](terephthalate) compartments are consequentially narrower, which likely explains why only one guest is encapsulated. The structure of the La(III)[15-MC_{Cu(II), pheHA-5}](terephthalate) complex (figure 2.10) resembles the previously reported Gd(III) complex. The La(III)[15-MC_{Cu(II), pheHA-5}](terephthalate) compartment has a height of 12.4 Å, with one encapsulated terephthalate bridging the La(III) central metals. With terephthalate, the compartment is elongated, which forces the side chains toward the center in order to maintain associative interactions with the opposite MC in the dimer. The narrow compartment can only accommodate one guest. Thus, these structures demonstrate that compressed compartments can have wider interiors, which promote the inclusion of multiple guests.

Differences in guest charge likely do not influence the number of encapsulated guests because MCs typically achieve charge balance with unbound anions in the lattice and by binding anions on the hydrophilic face. Though the overall +6 charged MC dimer would be expected to bind more -1 charged isonicotinates than -2 charged terephthalates, guest binding on the hydrophilic face prevents guest charge from factoring significantly in inclusion in the interior of the compartment. All MCs in La(III)[15-MC_{Cu(II), pheHA-5}](isonicotinate) and La(III)[15-MC_{Cu(II), pheHA-5}](terephthalate) have two bound carboxylates. This suggests the number of encapsulated guests in the hydrophobic compartment arises largely from the supramolecular behavior of the container and not merely electrostatic effects. It should also be noted that the soft pyridyl group prefers to bind to the Cu(II) ring metal, while the hard carboxylate has a higher affinity for the hard Ln(III) central metal. This drives isonicotinate to bind further toward the periphery of the compartment, while terephthalate has the highest affinity for the center of the compartment. The peripheral binding of isonicotinate can also factor into the inclusion of multiple guests.

The effect of compartment compression is further demonstrated in the La(III)[15-MC_{Cu(II), hpheHA-5}](terephthalate) complex (figure 2.11), which contains two terephthalate guests encapsulated in a 12.2 Å compartment. The terephthalates are bound with one carboxylate bidentate to a nine-coordinate La(III) ion and the other bridging the central metal and a Cu(II) ring metal. The terephthalate guests engage in π -stacking interactions and a CH-O interaction with the phenyl side chains. The compartment is roughly cylindrical, with the MC faces offset by 2.7 Å. The effect of compartment compression is reflected in the 526.7 Å³ host volume. This volume is almost 150 Å³ larger than the La(III)[15-MC_{Cu(II), pheHA-5}](terephthalate) compartment, which encapsulates only one terephthalate guest.

Comparison with the Ln(III)[15-MC_{Cu(II), hpheHA-5}](terephthalate) complexes with La(III) and Gd(III) central metals demonstrates that the central metal coordination number is also a factor in the number of encapsulated guests. In the Gd(III)[15-MC_{Cu(II), hpheHA-5}](terephthalate) structure (figure 2.11), one terephthalate guest is encapsulated in an 11.9 Å tall compartment. The terephthalate is bound bidentate at each carboxylate group to an 8-coordinate Gd(III) central metal. The volume of the compartment is merely 277.5 Å³, about half of the La(III)[15-MC_{Cu(II), hpheHA-5}](terephthalate) compartment. The disparity between the number of encapsulated guests with Gd(III) and La(III) complexes is from the different coordination number on the metal ions. Similar to the structures of monomeric MC-guest complexes, the eight-coordinate Gd(III) preferentially accommodates one bidentate carboxylate, thus Gd(III)[15-MC-5] compartments are likely to bind one dicarboxylate guest. In contrast, the nine-coordinate La(III) can bind one bidentate carboxylate and one carboxylate that bridges with a Cu(II) ring metal, leading to the inclusion of two carboxylate guests.

It is worth considering why La(III) central metals are occasionally 8-coordinate in certain compartment complexes. Lanthanide ions are known to adopt lower coordination numbers due to steric clashes with bound substrates. It is likely that steric effects from substituents near the MC face, such as side chains converging with bound guests, lead to lower coordination numbers. The La(III)[15-MC_{Cu(II), pheHA-5}](terephthalate) compartment is slightly stretched in order to accommodate terephthalate, which forces the side chains inward. Steric effects from this side chain conformation cause a La(III) ion to be 8-

coordinate. Due to the somewhat constrained volume of the compartment, guest inclusion can also reduce the central metal coordination number. For example, some of the La(III) central metals in the La(III)[15-MC_{Cu(II), pheHA-5}](isonicotinate), La(III)[15-MC_{Cu(II), pgHA-5}](isonicotinate), and La(III)[15-MC_{Cu(II), pheHA-5}](ferrocene dicarboxylate) compartments adopt 8-coordinate geometries due to the steric bulk of the guests. Similarly, the Gd(III)[15-MC_{Cu(II), pheHA-5}](isonicotinate) complex likely has a 7-coordinate Gd(III) central metal due to steric effects.

Considering these structures together reveals that the number of encapsulated guests in Ln(III)[15-MC-5] compartments is influenced by steric effects from the length of the side chain, steric effects from compression or elongation of the compartment, and the preferred coordination number of the central lanthanide ion. Due to the flexibility of the host, the compartment volumes can vary significantly from one host-guest complex to another, making the extraction of firm rules difficult. However, these results establish guidelines that larger lanthanide central metals, compressed compartments, and the orientation of inflexible ligands to the periphery of the compartment promote the inclusion of multiple guests.

ESI-MS of Ln(III)[15-MC-5](guest) complexes

There is interest in utilizing Ln(III)[15-MC-5] compartments in solution applications such as supramolecular catalysts or in solution processed materials. ESI-MS can qualitatively characterize monomeric or polymeric host-guest complexes in solution.^{45,46} ESI-MS has previously been used to characterize monomeric Ln(III)[15-MC-5](guest) complexes.^{22,24} While it is a gas-phase technique, experimentally observed ions correspond to species that persist in solution.⁴⁷ ESI-MS spectra of Ln(III)[15-MC-5] complexes with dicarboxylate guests were taken to assess whether dimerization occurs in solution.

Spectra were taken of the crystalline host-guest complexes dissolved in 4:1 methanol/water, or 4:1 DMF/water for La(III)[15-MC_{Cu(II), pheHA-5}](btDC) and injected via a syringe pump at a range of cone-voltages (10-75 mV). For all host-guest complexes, monomeric 1:1 and 1:2 MC-guest species were observed, consistent with previous results. More importantly, dimeric MC-guest species were present for all host-guest complexes. These peaks typically had weaker intensity than the monomeric MC species,

though they were discernible over the background noise. With isonicotinate, 2:3 MC-guest species are observed as +3 cations. 2:2 Ln(III)[15-MC-5](guest) peaks are observed with terephthalate and btDC (figure 2.12). These species correspond to +3 charged MC dimers with two dicarboxylates and one proton. Peaks corresponding to +3 charged MC-dimers with a mixture of dicarboxylate guests and nitrate, hydroxide, or methoxide anions were also observed. In addition, peaks corresponding to +2 charged MC dimers with two completely deprotonated dicarboxylate guests were also observed. The +2 charged 2:2 host-guest species have the same m/z as the +1 charged 1:1 host-guest complex, though the observation of half-integer peaks proves that the +2 2:2 species is present. Reexamination of the previously reported Gd(III)[15-MC_{Cu(II)}, pheHA⁻-5](terephthalate)²³ and Gd(III)[15-MC_{Cu(II)}, pheHA⁻-5](isonicotinate)²⁴ complexes also revealed dimeric MC complexes. ESI-MS spectra of Ln(III)[15-MC_{Cu(II)}-5](NO₃) complexes contain a 2:3 MC-nitrate species. Bridging nitrates have been observed crystallographically across the hydrophilic and hydrophobic faces of the MC.^{32,48} Considering the disparate findings presented herein and from previous ESI-MS studies; it is evident that injection via syringe pump, as opposed to high performance liquid chromatography as was previously utilized, was necessary to observe the dimers. This difference in conditions explains why the dimers were not originally observed.

Unfortunately ESI-MS does not provide structural information on whether the guests bridge across the hydrophobic or hydrophilic faces of the Ln(III)[15-MC-5] dimer. Based on the crystal structures, the simplest explanation is that the isostructural species consisting of dimeric MC compartments bridged across the hydrophobic faces exist in solution. Overall, the ESI-MS data supports that MC dimerization occurs in solution. Therefore, in the development of Ln(III)[15-MC-5] host-guest chemistry, it is appropriate to consider solution applications of the dimeric compartments.

Mesostructured Assemblies of Ln(III)[15-MC-5] Compartments with Unsaturated Dicarboxylate Guests

Crystallographic investigations reveal that dimeric Ln(III)[15-MC-5] compartments are a consistent structural motif that could be useful in preparing functional crystalline materials, such as reaction templates or porous solids. Dr. Choong-Sun Lim synthesized and structurally characterized the complexes of La(III)[15-MC_{Cu(II)},

pheHA-5] with pimelate and suberate, saturated dicarboxylates with straight 7- or 8-carbon chains (figure 2.13).²⁷ Crystal structures of these complexes contain 24 Å solvent channels through the lattices. Given the interest in porous solids in separations, molecular storage, and as reaction media, Dr. Lim and I investigated the guest absorption behavior of these unique complexes. I also undertook a crystallographic study to investigate the structural versatility of the mesostructured motif.

La(III)[15-MC_{Cu(II), pheHA-5}] complexes with pimelate or suberate contain the guest bound to Cu(II) ring metals of four adjacent metallocrowns through each carboxylate oxygen atom (figure 2.14, top left). The hydrophilic faces of the MCs are further bridged by two solvent waters linking two ring coppers on neighbouring MCs. The combination of pimelate and solvent mediated MC connections leads to a concave hydrophilic cluster. Examination of the packing of this tetramer reveals that two concave assemblies interlock to generate an enormous hydrophilic container (figure 2.14, top right). The opening is 8.9 Å wide by 14.6 Å high and grants access to the ~2300 Å³ interior. An even more intricate network is revealed upon consideration of the packing of the hydrophobic faces on these assemblies. As usual, the hydrophobic faces assemble with nearby metallocrowns, forming dimeric compartments (figure 2.14, bottom left). As the MCs in these compartments are components of the octameric assembly, the compartment motif on the exterior of the octamers is repeated six times, generating a large solvent channel (figure 2.14, bottom right). The hexagonal packing of the octameric MC assembly is consistent with the chiral space group P6₂22. The diameter of the solvent channel is 2.4 nm, placing this solid in the mesostructured regime. This complex was only the second example of a chiral mesostructured crystalline solid reported in the literature.⁴⁹ The channel is filled with solvent waters and unbound pimelates. 42.8% of the volume of La(III)[15-MC_{Cu(II), pheHA-5}](pimelate) is accessible to solvent or guest molecules.⁴² Unlike previously reported mesostructured materials, these solids are the result of weak intermolecular forces between building blocks in all directions. The porosity of La(III)[15-MC_{Cu(II), pheHA-5}](pimelate) and La(III)[15-MC_{Cu(II), pheHA-5}](suberate) were measured by Dr. Choong-Sun Lim through N₂ sorption measurements, but neither complex showed permanent porosity. The lack of permanent porosity may be caused by the collapse of the structures upon solvent removal, which was observed by powder X-ray diffraction (pxrd).

Given the lack of permanent porosity, I attempted to access the channels at the solid/liquid interface.⁵⁰⁻⁵⁴ Diffusion experiments were performed where solid La(III)[15-MC_{Cu(II), pheHA-5}](pimelate) was suspended in solutions containing a chromophore guest. Guest inclusion was monitored by UV-VIS absorption spectroscopy. The absorption of a solution of methyl orange sodium salt in acetone decreases after 90 minutes of soaking with the mesostructure (figure 2.15), demonstrating the porosity of the material. Pxd shows La(III)[15-MC_{Cu(II), pheHA-5}](pimelate) loses crystallinity over the course of the diffusion experiment, likely due to the displacement of structurally critical water molecules upon the inclusion of acetone and methyl orange. Though measurements were complicated by visible absorption from dissolution of the MC, the maximum amount of absorbed guest that was observed is 0.1 mmol/g of La(III)[15-MC_{Cu(II), pheHA-5}](pimelate), which was achieved after 18 hours of diffusion. This works out to one molecule of methyl orange per 1.2 octameric compartment, supporting a model where the methyl orange guest diffuses through the 2.4 nm channels and is bound inside the hydrophilic octameric assembly. The guest should easily fit through the octamer's 8.9 x 14.6 Å opening. Framework collapse and the dissolved mesostructure likely prevent a 1:1 guest/octameric compartment ratio from being observed under these conditions. Guests were not absorbed from methylene chloride solutions or with water insoluble guests in acetone, suggesting that solvent miscibility and guest solubility in water are necessary for inclusion. In an attempt to recover the absorbed guest, solid MC isolated from diffusion experiments was submerged in acetone for 18 hours, and no methyl orange diffused out into solution. However, the guest could be recovered by dissolving the mesostructure in methanol and passing the solution through a short pad of silica to remove the La(III)[15-MC_{Cu(II), pheHA-5}].

Given the unique structure and guest absorption behavior, we were interested in exploring the structural versatility of the mesostructured architecture, as different guest absorption behavior and stability could result from different guests, metals, and side chains. The specific aim was to obtain the mesostructured assembly with an MC containing a different side chain or ring metal. Furthermore, there was interest in better understanding the recognition of saturated dicarboxylates by Ln(III)[15-MC_{Cu(II)-5}] compartments. Previous work has shown that all saturated dicarboxylates with a chain

length of up to 6 are excluded from $\text{Ln(III)[15-MC}_{\text{Cu(II), pheHA-5}}$ hydrophobic compartments.²² In contrast, all saturated dicarboxylates are encapsulated by the host. A better understanding of the structural basis of this selectivity could aid in the design of highly discriminating hosts. With these aims, a crystallographic investigation of $\text{Ln(III)[15-MC}_{\text{Cu(II)-5}}$ complexes bearing pheHA, hpheHA, and pgHA side chains with a series of saturated dicarboxylate guests with carbon chain lengths of 6-10 was performed (tables 2.5, 2.6).

First, of all of the host-guest complexes that were investigated, mesostructured assemblies were only seen in the $\text{La(III)[15-MC}_{\text{Cu(II), pheHA-5}}$ clathratocomplexes of pimelate and suberate. Densely packed compartments are observed with MCs bearing pheHA, hpheHA, and pgHA side chains and adipate, pimelate, and suberate guests. Notably, unlike all other $\text{Ln(III)[15-MC}_{\text{Cu(II), pheHA-5}}$ compartments with saturated dicarboxylate guests, the $\text{Dy(III)[15-MC}_{\text{Cu(II), pheHA-5}}$ compartment encapsulates pimelate (figure 2.16). The guest does not fit particularly well within the dimeric host, evidenced by the significant displacement of the MC faces from one another. The pimelate binds bidentate to one Dy(III) ion and monodentate to another. The long, flexible guest is curled, with many Van der Waals contacts with the pheHA side chains. Interestingly, the MC forms a CH-O interaction with the unbound carboxylate oxygen atom.

$\text{Ln(III)[15-MC}_{\text{Cu(II)-5}}$ compartments with hpheHA and pgHA side chains also encapsulate saturated dicarboxylate guests. $\text{Gd(III)[15-MC}_{\text{Cu(II), hpheHA-5}}$ and $\text{La(III)[15-MC}_{\text{Cu(II), pgHA-5}}$ both encapsulate adipate in dimeric compartments (figure 2.17). The $\text{Gd(III)[15-MC}_{\text{Cu(II), hpheHA-5}}$ (adipate) compartment has a height of 12.04 Å. The adipate bridges the Gd(III) ions through bidentate coordination of the carboxylates. In the $\text{La(III)[15-MC}_{\text{Cu(II), pgHA-5}}$ (adipate) structure, two adipate guests are encapsulated in a 12.62 Å tall compartment. Consistent with previous trends, the extra coordination site on La(III) contributes to the binding of additional guests. In both of these structures, CH-O interactions between the phenyl side chains and bound carboxylate oxygen atoms on the guest are observed. It is likely that CH-O interactions cause the differences in saturated guest selectivity afforded by the hpheHA and pgHA compartments versus the pheHA compartment. hpheHA and pgHA side chains can readily engage bound carboxylates in CH-O interactions, while pheHA side chains do not. These interactions likely drive guest

encapsulation, just as π -stacking interactions are the likely driving force for the encapsulation of unsaturated dicarboxylates. Since pheHA does not form CH-O interactions with bound carboxylates, most saturated dicarboxylates, such as adipate, are excluded from the hydrophobic compartment. The one exception is Dy(III)[15-MC_{Cu(II)}, pheHA-5](pimelate). However, this structure reveals a CH-O interaction with the unbound oxygen atom on the monodentate carboxylate.

Numerous other crystal structures were obtained in this investigation. Unfortunately, limited resolution, significant disorder, and possible twinning prevented the location of all atoms or completion of the refinements in most instances. The partial structure solutions reveal networks of densely packed compartments or MCs, and no mesostructured lattice packing. Carboxylates appear to be bound in the hydrophobic cavities of Ln(III)[15-MC_{Cu(II)}-5] hosts with pheHA and hpheHA side chains with suberate, azelate, and sebacate. Though additional details are evident in many of these structures, the accuracy of the structural data can be called into question because appropriate models for the entire complexes could not be obtained.

As a whole, these host-guest complexes with saturated dicarboxylates suggest that the mesostructured assembly is not particularly general. The results serve to reinforce the observations seen with unsaturated carboxylate guests that the side chain and central metal influence the size and selectivity of dimeric La(III)[15-MC_{Cu(II)}-5] compartments. Furthermore, differential guest recognition by the different side chains could be a useful tool in preparing functional solids.

Conclusions

These studies show that Ln(III)[15-MC-5] compartments with pgHA, pheHA, and hpheHA ligands are a series of metalated supramolecular containers with distinct molecular recognition behavior in the solid state. Differences in the size and selectivity of the compartments arise from how the length and flexibility of the phenyl side chains influence host dimerization and the degree that the side chain can converge on a guest. Systematic inclusion of bridging carboxylate guests in these hosts reveals that the compartment height is constrained by the length of the ligand side chain. Longer side chains allow the formation of taller containers that encapsulate longer guests, as hpheHA

ligands can form a 15.2 Å tall compartment. Considering the previously reported 7.70 Å tall Gd(III)[15-MC_{Cu(II), tyrHA}-5] container,⁴⁸ compartment height can be effectively doubled through straightforward modification of the ligand side chain. This work also demonstrates that up to five carboxylate guests can be encapsulated in Ln(III)[15-MC-5] compartments based on considerations of sterics, compartment compression, and the central lanthanide coordination number.

Because Ln(III)[15-MC-5] compartments assemble through supramolecular interactions and recognize guests with flexible side chains, there is significant structural variability between different host-guest complexes. This variability makes the development of definitive rules for predicting these structures unfeasible at this juncture. However, the extensive and systematic structural characterization presented herein, and in previous work, has established some consistent trends in how the guest length, side chain composition, and central metal influence compartment size and guest selectivity. We consider these trends as a theoretical framework one could use to design inclusion complexes of Ln(III)[15-MC-5] compartments.

In the field of molecular encapsulation, there is a trend toward relying on rigid hosts with well defined, permanent cavities to control host size and selectivity. However, these results demonstrate that flexible hosts can generate supramolecular containers with sizes and guest-recognition behavior that is comparable to benchmark rigid systems, albeit in the solid state, while still following clear trends that allow for prediction and design. The ESI-MS data demonstrates that these flexible hosts persist in solution to some degree as well. The theoretical framework for considering factors that influence compartment size and selectivity of Ln(III)[15-MC-5] compartments will guide future investigations of the hosts as reaction vessels, building blocks for porous solids, and in the design of SHG materials. The mesostructured assembly highlights the viability of using Ln(III)[15-MC-5] compartments as building blocks for molecular materials. Considering the compartments for use in SHG materials, a limitation of the current constructs is that visible absorption from the host will limit SHG intensity. As the color originates from the Cu(II) ring metals, one impetus for the work presented in chapter four has focused on preparing optically transparent MCs with Zn(II)

Thinking more broadly to crystal engineering, these results demonstrate how intermolecular interactions can work in concert with dative bonds to generate organized solid state architectures. The cavitand topology in the Ln(III)[15-MC-5] construct relies on peripheral organic substituents to consistently generate dimeric hydrophobic compartments. Importantly, the relationship between side chain length and compartment size and selectivity reveals that secondary sphere interactions can provide a significant amount of control over anion binding and the solid-state assembly of metal complexes. The use of peripheral molecular recognition functionalities to direct substrate binding at a metal center could be a useful tool in the design of molecular materials.

Figures

| Complex | [a] | [b] | [c] | [d] |
|--|---|--|---|--|
| Molecular Formula | GdCu ₅ C ₅₆ H ₈₇ N ₁₀ O ₃₇ | La ₄ Cu ₂ C ₂₃₇ H ₃₈₂ N ₅₀ O _{103.5} S ₁₂ | Gd ₂ Cu ₁₀ C _{154.25} H ₂₂₅ N ₂₈ O _{82.5} | LaCu ₅ C ₆₁ H _{94.5} N ₁₃ O _{29.25} |
| mol. wt [g mol ⁻¹] | 1967.31 | 7698.29 | 4545.88 | 1958.63 |
| crystal system, space group | orthorhombic, P2 ₁ 2 ₁ 2 ₁ | monoclinic, P2 ₁ | monoclinic, P2 ₁ | tetragonal, P4 ₁ 2 ₁ 2 |
| <i>a</i> [Å] | 14.5520(14) | 15.5616(14) | 16.7609(9) | 16.4964(3) |
| <i>b</i> [Å] | 15.9599(15) | 30.839(3) | 35.759(2) | 16.4964(3) |
| <i>c</i> [Å] | 31.340(3) | 30.729(3) | 17.9482(10) | 61.5156(18) |
| α [deg] | 90 | 90 | 90 | 90 |
| β [deg] | 90 | 100.620(7) | 107.712(1) | 90 |
| γ [deg] | 90 | 90 | 90 | 90 |
| volume [Å ³] | 7274.2(12) | 14494(2) | 10247.4(1.0) | 16740.3(7) |
| <i>Z</i> , density, ρ [g cm ⁻³] | 4, 1.796 | 2, 1.764 | 2, 1.473 | 8, 1.554 |
| μ [mm ⁻¹], F (000) | 2.436, 3992 | 2.192, 7764 | 1.795, 4653 | 1.830, 7996 |
| crystal size [mm ³] | 0.15 x 0.14 x 0.14 | 0.11 x 0.03 x 0.01 | 0.36 x 0.30 x 0.18 | 0.21 x 0.17 x 0.03 |
| θ range for data collection [deg] | 1.30 - 28.38 | 0.74 - 29.08 | 1.14 - 29.59 | 1.75 - 25.81 |
| limiting indices | -19 < <i>h</i> < 19 | -19 < <i>h</i> < 19 | -23 < <i>h</i> < 23 | -20 < <i>h</i> < 20 |
| | -21 < <i>k</i> < 21 | -38 < <i>k</i> < 38 | -49 < <i>k</i> < 49 | -20 < <i>k</i> < 20 |
| | -41 < <i>l</i> < 41 | -38 < <i>l</i> < 38 | -24 < <i>l</i> < 24 | -75 < <i>l</i> < 74 |
| measured, independent reflections | 258417, 18148 | 252123, 59688 | 409925, 57566 | 314012, 16062 |
| completeness to θ | 0.998 | 0.997 | 1.000 | 0.998 |
| data/restraints/parameters | 18148 / 12 / 973 | 59688 / 446 / 3775 | 57566 / 2500 / 2741 | 16062 / 820 / 1066 |
| goodness of on F^2 | 1.123 | 0.992 | 1.154 | 1.244 |
| final <i>R</i> indices [$I > 2\sigma(I)$] | $R_1 = 0.0435$, $wR^2 = 0.1263$ | $R_1 = 0.0558$, $wR^2 = 0.1246$ | $R_1 = 0.0550$, $wR^2 = 0.1540$ | $R_1 = 0.0948$, $wR^2 = 0.2034$ |
| <i>R</i> indices (all data) | $R_1 = 0.0540$, $wR^2 = 0.1390$ | $R_1 = 0.1076$, $wR^2 = 0.1610$ | $R_1 = 0.0592$, $wR^2 = 0.1580$ | $R_1 = 0.1051$, $wR^2 = 0.2075$ |
| largest diff. peak and hole [e Å ⁻³] | 1.892 and -1.595 | 2.750 and -1.581 | 2.127 and -1.3933 | 1.119 and -1.550 |

Table 2.1: Crystal structure data for [a] Gd(III)[15-MC_{Cu(II)}, pgHA-5](terephthalate), [b] La(III)[15-MC_{Cu(II)}, pgHA-5](btDC), [c] Gd(III)[15-MC_{Cu(II)}, hpheHA-5](btDC), [d] La(III)[15-MC_{Cu(II)}, hpheHA-5](isonicotinate).

| Complex | [a] | [b] | [c] | [d] |
|--|--|--|--|---|
| Molecular Formula | La ₂ Cu ₅ C ₁₅ H ₁₄₈ N ₂₆ O ₄₉ | La ₂ Cu ₁₀ C ₁₀ H ₁₈₄ N ₂₅ O _{53.58} | La ₂ Cu ₁₀ C ₁₀₆ H ₁₄₉ N ₂₂ O _{54.5} | La ₂ Cu ₁₀ C ₁₃₀ H ₂₁₁ N ₂₀ O _{65.25} |
| mol. wt [g mol ⁻¹] | 3591.81 | 3628.13 | 3516.69 | 4017.92 |
| crystal system, space group | triclinic, P ₁ | orthorhombic, P2 ₁ 2 ₁ 2 ₁ | triclinic, P ₁ | monoclinic, P2 ₁ |
| <i>a</i> [Å] | 15.082(5) | 16.966(3) | 15.1391(12) | 21.897(3) |
| <i>b</i> [Å] | 15.242 (5) | 27.984(4) | 15.5615(12) | 16.761(2) |
| <i>c</i> [Å] | 17.234 (8) | 32.407(5) | 17.1216(14) | 23.454(3) |
| α [deg] | 74.492 (4) | 90 | 72.100(1) | 90 |
| β [deg] | 67.296 (7) | 90 | 77.870(1) | 98.896(2) |
| γ [deg] | 71.961(5) | 90 | 66.827(1) | 90 |
| volume [Å ³] | 3425(2) | 15386(4) | 3510.3(5) | 8519.7(1.8) |
| Z, density, ρ [g cm ⁻³] | 1, 1.741 | 4, 1.566 | 1, 1.664 | 2, 1.566 |
| μ [mm ⁻¹], F (000) | 2.222, 1816 | 1.981, 7410 | 2.168, 1779 | 1.802, 4121 |
| crystal size [mm ³] | 0.25 x 0.17 x 0.09 | 0.28 x 0.24 x 0.20 | 0.38 x 0.22 x 0.03 | 0.40 x 0.34 x 0.09 |
| θ range for data collection [deg] | 1.63-29.71 | 1.74 - 29.58 | 1.83 - 29.64 | 0.88 - 28.38 |
| limiting indices | -20 < h < 20 | -23 < h < 23 | -21 < h < 21 | -29 < h < 29 |
| | -21 < k < 21 | -38 < k < 38 | -21 < k < 21 | -22 < k < 22 |
| | -23 < l < 23 | -44 < l < 44 | -23 < l < 23 | -31 < l < 31 |
| measured, independent reflections | 37707, 37707 | 708432, 43117 | 173395, 39247 | 287865, 42596 |
| completeness to θ | 0.983 | 0.999 | 0.997 | 0.997 |
| data/restraints/parameters | 37707/ 4/ 1829 | 43117/ 335 / 2152 | 39247/ 682 / 2125 | 42596/ 2296 / 2294 |
| goodness of on F^2 | 0.738 | 1.085 | 1.027 | 1.204 |
| final <i>R</i> indices [$I > 2\sigma(I)$] | $R_1 = 0.0571, wR^2 = 0.1758$ | $R_1 = 0.0379, wR^2 = 0.1110$ | $R_1 = 0.0523, wR^2 = 0.1373$ | $R_1 = 0.0482, wR^2 = 0.1324$ |
| <i>R</i> indices (all data) | $R_1 = 0.0640, wR^2 = 0.1839$ | $R_1 = 0.0421, wR^2 = 0.1152$ | $R_1 = 0.0663, wR^2 = 0.1516$ | $R_1 = 0.0518, wR^2 = 0.1364$ |
| largest diff. peak and hole [e Å ⁻³] | 2.389 and -1.878 | 2.469 and -1.761 | 2.062 and -1.289 | 1.466 and -2.119 |

Table 2.2: Crystal structure data for [a] La(III)[15-MC_{Cu(II), pheHA-5}](isonicotinate), [b] La(III)[15-MC_{Cu(II), pgHA-5}](isonicotinate), [c] La(III)[15-MC_{Cu(II), pheHA-5}](terephthalate), [d].

| Complex | [a] | [b] | [c] |
|--|---|---|--|
| Molecular Formula | Gd ₂ Cu ₁₀ C ₁₂₈ H _{183.5} N ₂₀ O _{53.75} | La ₂ Cu ₁₀ C ₁₆₁ H ₂₅₄ N _{23.5} O _{58.75} S | Dy ₂ Cu ₁₀ C ₁₁₁ H ₁₇₈ N ₂₀ O ₅₆ |
| mol. wt [g mol ⁻¹] | 3812.35 | 4564.577 | 3649.16 |
| crystal system, space group | triclinic, P ₁ | triclinic, P ₁ | triclinic, P ₁ |
| <i>a</i> [Å] | 15.4739(6) | 18.9742(12) | 14.8653(10) |
| <i>b</i> [Å] | 15.7235(6) | 19.8779(13) | 17.0643(10) |
| <i>c</i> [Å] | 16.5063(6) | 20.2834(13) | 17.8253(12) |
| α [deg] | 106.389(1) | 93.587(1) | 76.069(1) |
| β [deg] | 99.092(1) | 111.320(1) | 87.087(1) |
| γ [deg] | 98.734(1) | 114.263(1) | 79.311(1) |
| volume [Å ³] | 3721.8(2) | 6291.6(7) | 3807.0(4) |
| Z, density, ρ [g cm ⁻³] | 1, 1.701 | 1, 1.284 | 1, 1.592 |
| μ [mm ⁻¹], F (000) | 2.368, 1940 | 1.283, 2504 | 2.422, 1854 |
| crystal size [mm ³] | 0.31 x 0.26 x 0.22 | 0.35 x 0.18 x 0.08 | 0.34 X 0.20 X 0.11 |
| θ range for data collection [deg] | 2.08 - 31.48 | 1.28 - 28.33 | 1.61 - 28.36 |
| limiting indices | -22 < h < 22 | -25 <= h <= 25 | -19 <= h <= 19 |
| | -23 < k < 23 | -26 <= k <= 26 | -20 <= k <= 20 |
| | -24 < l < 24 | -27 <= l <= 27 | -23 <= l <= 23 |
| measured, independent reflections | 156633, 45283 | 203556, 62188 | 177140, 37759 |
| completeness to θ | 0.947 | 0.998 | 0.999 |
| data/restraints/parameters | 45283/159/1968 | 62188/1749/3169 | 37759/491/1999 |
| goodness of on F^2 | 1.030 | 1.080 | 1.090 |
| final <i>R</i> indices [$I > 2\sigma(I)$] | $R_1 = 0.0364$, $wR^2 = 0.0924$ | $R_1 = 0.0507$, $wR^2 = 0.1396$ | $R_1 = 0.0448$, $wR^2 = 0.1260$ |
| <i>R</i> indices (all data) | $R_1 = 0.0415$, $wR^2 = 0.0967$ | $R_1 = 0.0643$, $wR^2 = 0.1535$ | $R_1 = 0.0508$, $wR^2 = 0.1337$ |
| largest diff. peak and hole [e Å ⁻³] | 1.469 and -0.783 | 1.399 and -0.899 | 1.149 and -0.819 |

Table 2.3: Crystal structure data for [a] Gd(III)[15-MC_{Cu(II)}, hpheHA-5](terephthalate), [b] La(III)[15-MC_{Cu(II)}, pheHA-5](btDC), [c] Dy(III)[15-MC_{Cu(II)}, pheHA-5](pimelate).

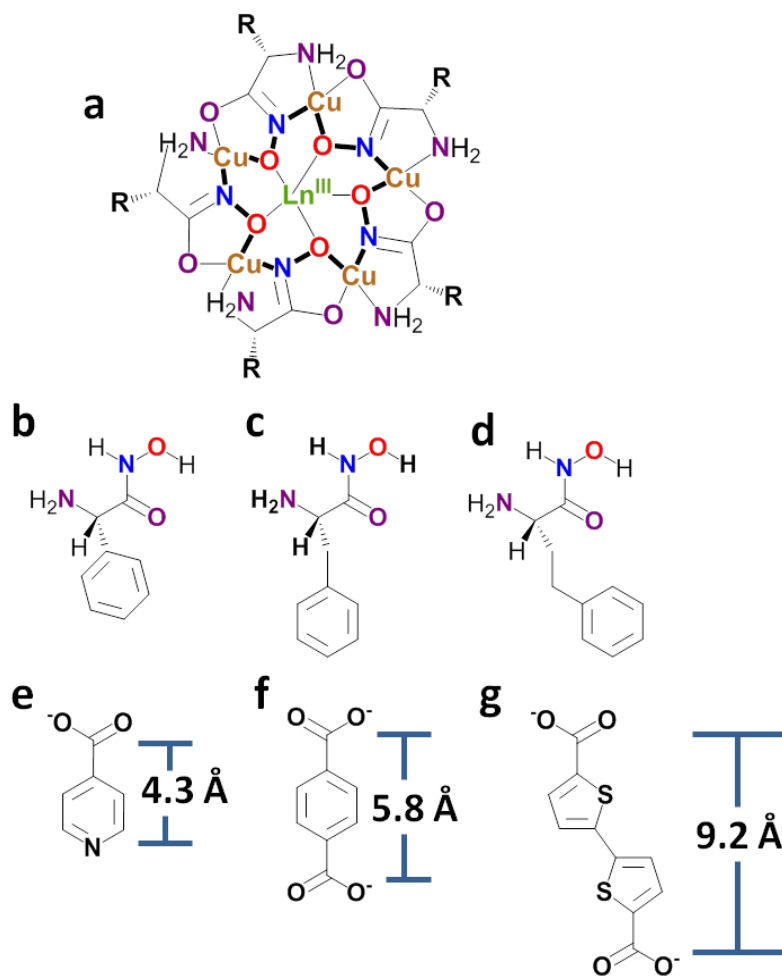


Figure 2.1. Chemdraw diagrams of (a) Ln(III)[15-MC_{Cu(II), S-α-aminoHA-5}], (b) S-pgHA, (c) S-pheHA, (d) S-hpheHA, (e) isonicotinate, (f) terephthalate, (g) btDC. The length of e corresponds to the pyridyl nitrogen to carboxylate-carbon distance, while f and g are the carboxylate-carbon to carboxylate-carbon distances, as determined from crystal structures.

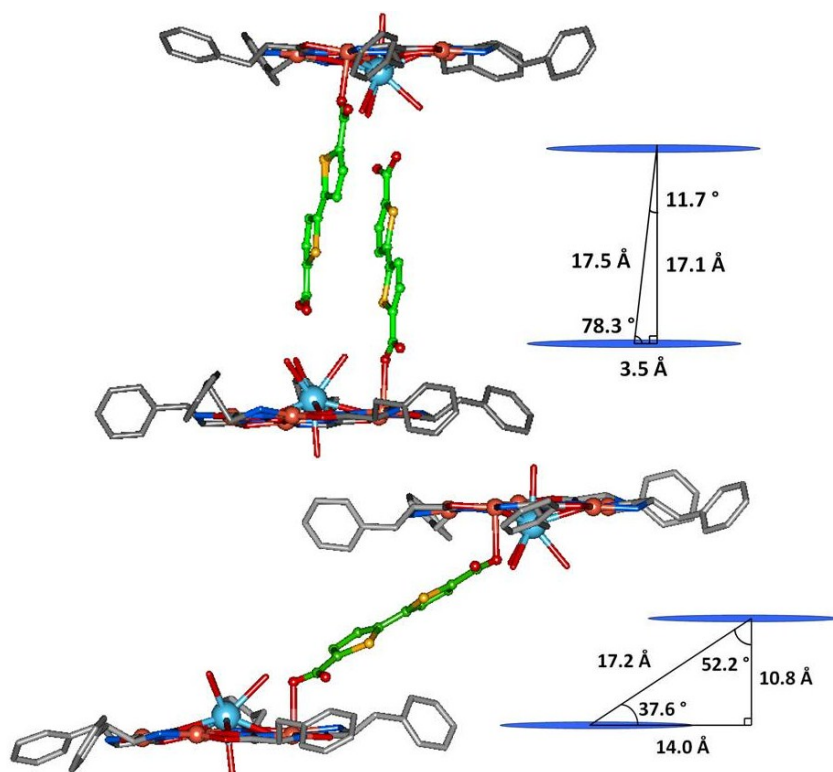


Figure 2.2: Crystal structure and compartment diagrams of La(III)[15-MC_{Cu(II)}, pheHA⁻5](btDC) showing the binding of the *trans*- (top) and *cis*-rotomers (bottom). Color scheme: light blue = La, orange = Cu, red = O, dark blue = N, grey = MC C, green = guest C, yellow = S. Lattice solvent molecules and hydrogen atoms were removed for clarity.

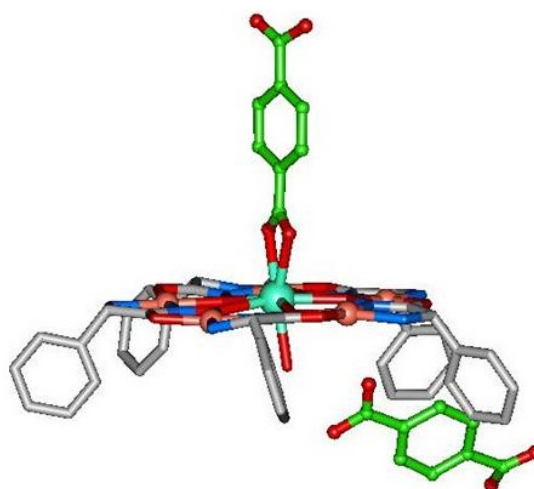


Figure 2.3. Crystal structure of Gd(III)[15-MC_{Cu(II)}, pgHA⁻5](terephthalate). Color scheme: sea green = Gd, orange = Cu, red = O, dark blue = N, grey = MC C, green = guest C. Lattice solvent molecules and hydrogen atoms were removed for clarity.

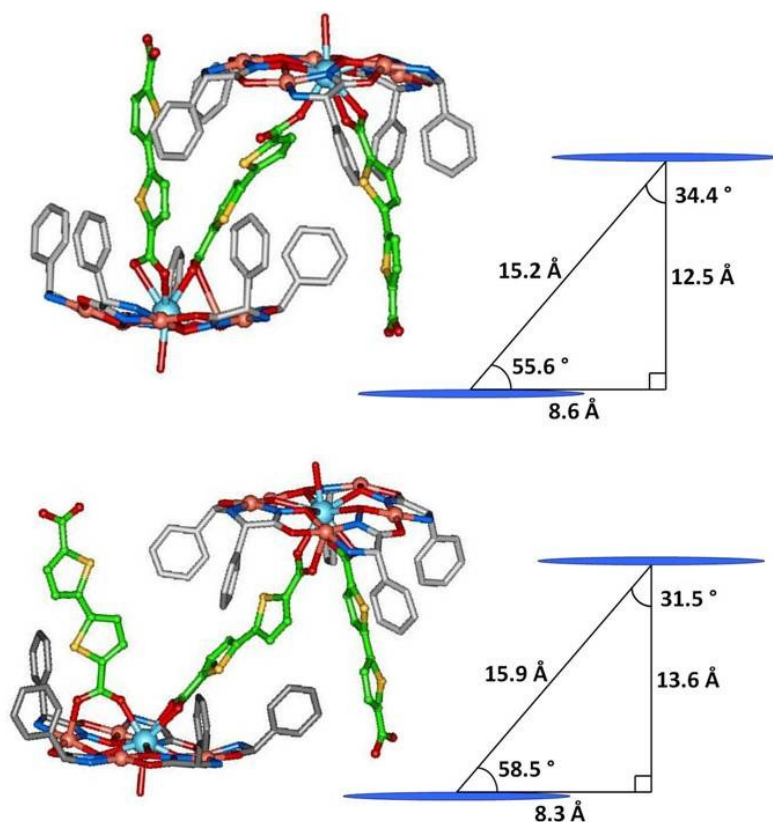


Figure 2.4: Crystal structure and compartment diagrams for $\text{La(III)[15-MC}_{\text{Cu(II)}, \text{pgHA-5}}\text{](btDC)}$ showing the MC dimers bridged by *cis*-btDC (top) and *trans*-btDC (bottom). Crystal structure color scheme: light blue = La, orange = Cu, red = O, dark blue = N, grey = MC C, green = guest C, yellow = sulfur. Solvent molecules and hydrogen atoms were removed for clarity.

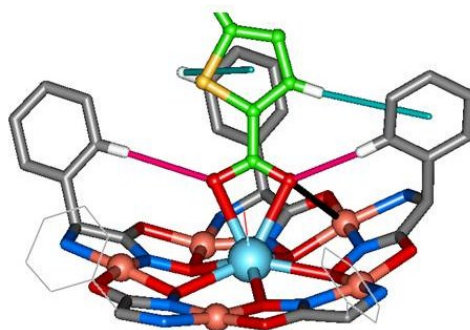


Figure 2.5: Highlight of intermolecular interactions between the pgHA side chains and btDC in the $\text{La(III)[15-MC}_{\text{Cu(II)}, \text{pgHA-5}}\text{](btDC)}$ crystal structure. π -stacking interactions (blue-green line), CH-O interactions (magenta line) and a Cu(II)-O interaction (black line) are highlighted. Crystal structure color scheme: light blue = La, orange = Cu, red = O, dark blue = N, grey = MC C, green = guest C, yellow = sulfur. Solvent molecules and hydrogen atoms were removed for clarity. Two pgHA side chains and a water molecule bound to La(III) are shown as thin lines for clarity.

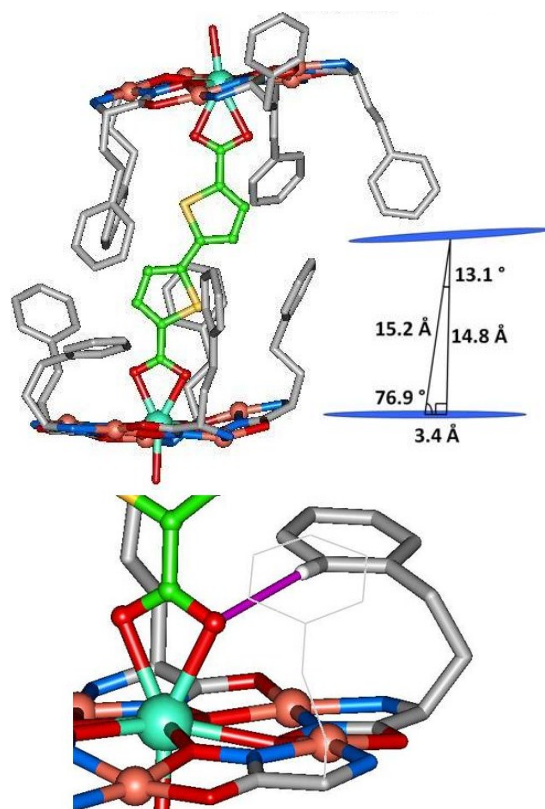


Figure 2.6: Top) Crystal structure and compartment diagram of $\text{Gd(III)[15-MC}_{\text{Cu(II)}}, \text{h}_{\text{pheHA-5}}\text{](btDC)}$, and bottom) highlight of the CH-O interaction between the h_{pheHA} side chain and a carboxylate oxygen on btDC²⁻. Crystal structure color scheme: sea green = Gd, orange = Cu, red = O, dark blue = N, grey = MC C, green = guest C, yellow = S. Guests on the hydrophilic face, unbound counter anions, solvent molecules, and hydrogen atoms were removed for clarity.

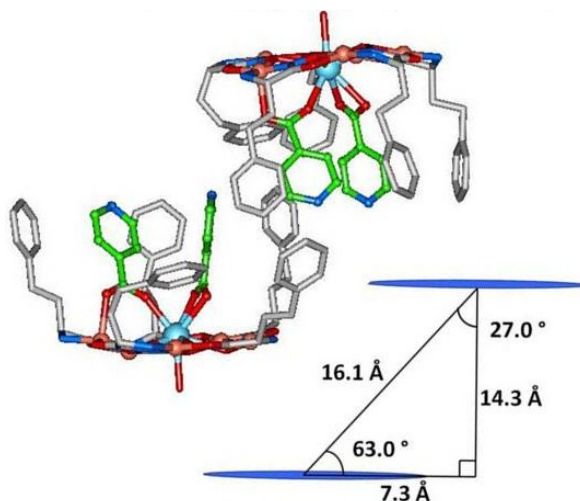


Figure 2.7. Thermal ellipsoid plot and compartment diagram of $\text{La(III)[15-MC}_{\text{Cu(II), hpheHA}^{-5}}\text{] (isonicotinate)}$. Crystal structure color scheme: light blue = La, orange = Cu, red = O, dark blue = N, grey = MC C, green = guest C. Guests on the hydrophilic face, unbound counter anions, solvent molecules, and hydrogen atoms were removed for clarity.

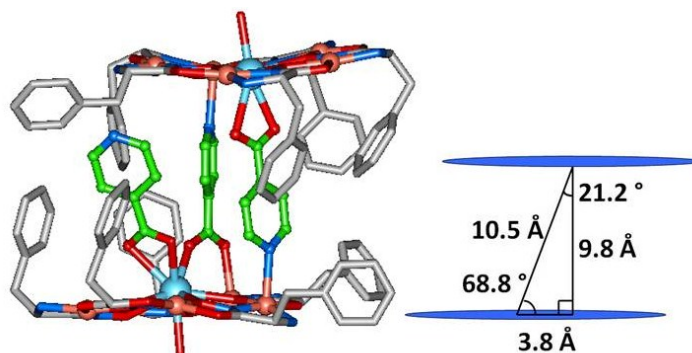


Figure 2.8: Crystal structure and compartment diagram of $\text{La(III)[15-MC}_{\text{Cu(II), pheHA}^{-5}}\text{] (isonicotinate)}$. Crystal structure color scheme: light blue = La, orange = Cu, red = O, dark blue = N, grey = MC C, green = guest C. Guests on the hydrophilic face, unbound counter anions, solvent molecules, and hydrogen atoms were removed for clarity.

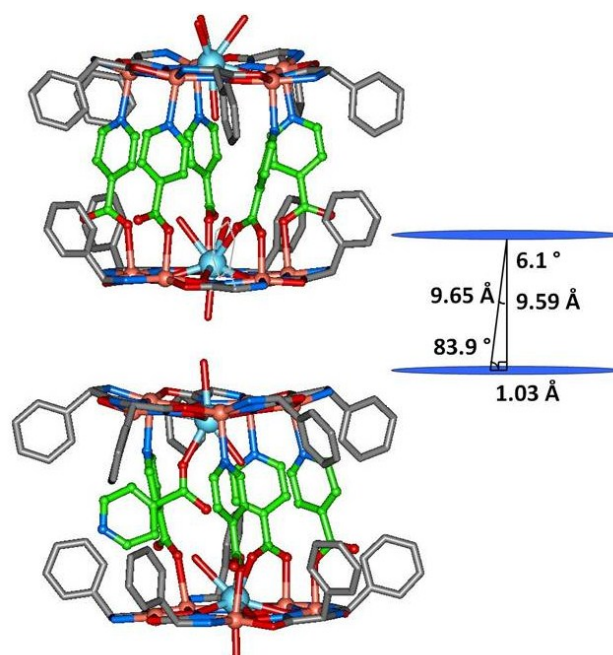


Figure 2.9: Crystal structure and compartment diagram of $\text{La(III)[15-MC}_{\text{Cu(II)}}, \text{pgHA}^{-5}\text{](isonicotinate)}$. The structure is disordered between two compartment orientations, with all isonicotinates aligned (top) and one isonicotinate roughly perpendicular to the others (bottom). Color scheme: light blue = La, orange = Cu, red = O, dark blue = N, grey = MC C, green = guest C. Unbound counter anions, solvent molecules, and hydrogen atoms were removed for clarity.

| MC | Guest | V _{host} (Å ³) | V _{Guest} (Å ³) | P.C. (%) | # Guests | Ln(III) coord. # ^a | Compartment Height (Å) |
|---|---------------|--|---|----------------|----------------|-------------------------------------|---------------------------|
| La(III)[15-MC _{Cu(II),pgHA-5}] | isonicotinate | 710.3 | 463.8 | 65.3 | 5 | 9, 9, 9, 8 | 9.7 |
| La(III)[15-MC _{Cu(II),pheHA-5}] | isonicotinate | 480.3 | 306.3 | 68.5 | 3 | 9, 8 | 10.5 |
| Gd(III)[15-MC _{Cu(II),pheHA-5}] ²⁴ | isonicotinate | 392.0 | 257.6 | 65.7 | 3 | 8, 7 | 10.3 |
| La(III)[15-MC _{Cu(II),hpheHA-5}] ^b | isonicotinate | 292.4 | 171.7 | 58.7 | 2 | 9 | - ^c |
| Gd(III)[15-MC _{Cu(II),pgHA-5}] | terephthalate | - ^d | - ^d | - ^d | 0 | 8 | - ^c |
| La(III)[15-MC _{Cu(II),pheHA-5}] | terephthalate | 380.0 | 175.4 | 48.3 | 1 | 8, 8 | 12.4 |
| Gd(III)[15-MC _{Cu(II),pheHA-5}] ³⁹ | terephthalate | 375.3 | 217.6 | 58.0 | 1 | 8, 8 | 11.9 |
| La(III)[15-MC _{Cu(II),hpheHA-5}] | terephthalate | 526.7 | 325.7 | 61.8 | 2 | 9, 9 | 12.2 |
| Gd(III)[15-MC _{Cu(II),hpheHA-5}] | terephthalate | 277.5 | 170.6 | 61.5 | 1 | 8, 8 | 11.9 |
| La(III)[15-MC _{Cu(II),pgHA-5}] | btDC | - ^d | - ^d | - ^d | 2 ^e | 9, 9, 9, 9 | 15.2, 15.9 |
| La(III)[15-MC _{Cu(II),pheHA-5}] ²⁸ | btDC | - ^d | - ^d | - ^d | 2 ^e | 9, 9 | - ^c |
| Gd(III)[15-MC _{Cu(II),hpheHA-5}] | btDC | 495.7 | 332.5 | 67.1 | 1 | 8, 8 | 15.2 |

Table 2.4. Size and guest inclusion parameters for Ln(III)[15-MC-5] compartments. a) Listed for each distinct MC in the asymmetric unit, b) the volume of the monomeric cavity is reported, c) structure did not contain a formal dimeric MC complex, d) structure did not contain a discrete, complete compartment, e) # of guests bound on the hydrophobic face of each MC.

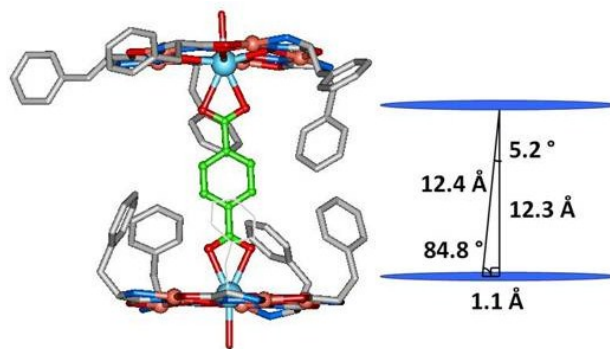


Figure 2.10: Crystal structure and compartment diagram of $\text{La(III)[15-MC}_{\text{Cu(II), pheHA}^{-5}}\text{](terephthalate)}$. Color scheme: light blue = La, orange = Cu, red = O, dark blue = N, grey = MC C, green = guest C. Unbound counter anions, solvent molecules, and hydrogen atoms were removed for clarity. One pheHA side chain is displayed as a thin line for clarity.

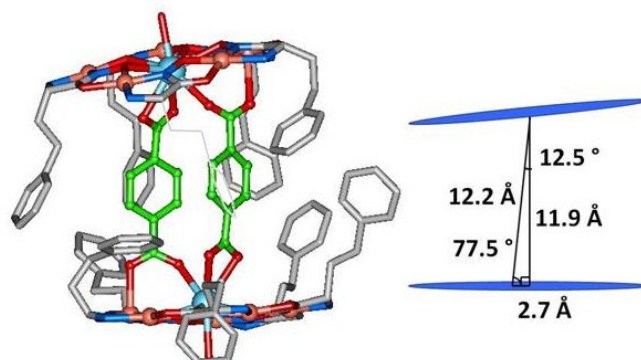
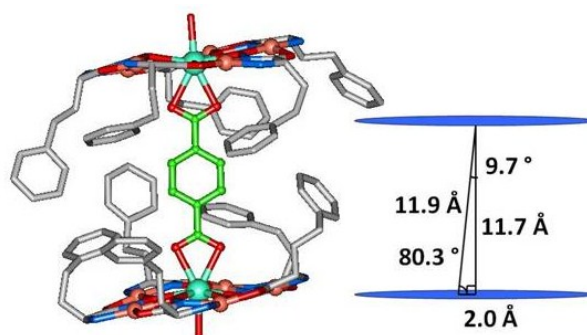


Figure 2.11. Crystal structures and compartment diagrams of top) $\text{Gd(III)[15-MC}_{\text{Cu(II), hpheHA}^{-5}}\text{](terephthalate)}$, and bottom) $\text{La(III)[15-MC}_{\text{Cu(II), hpheHA}^{-5}}\text{](terephthalate)}$. Crystal structure color scheme: sea green = Gd, light blue = La, orange = Cu, red = O, dark blue = N, grey = MC C, green = guest C. Guests on the hydrophilic face, unbound counter anions, solvent molecules, and hydrogen atoms were removed for clarity.

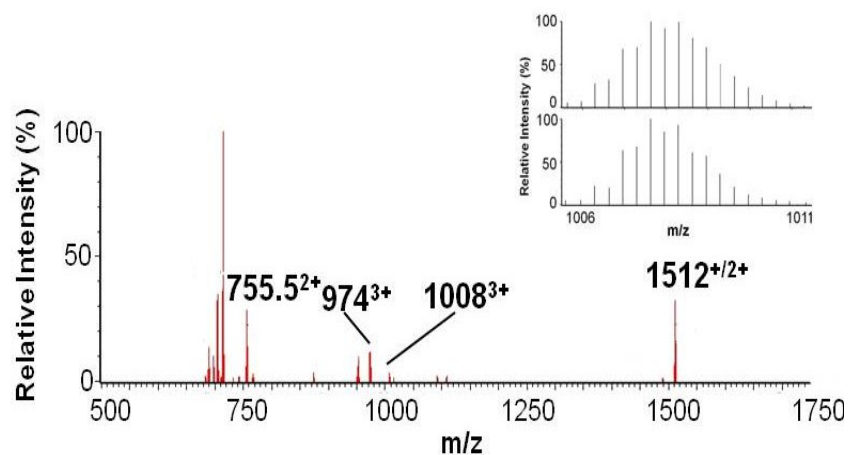


Figure 2.12: Mass spectrum of La(III)[15-MC_{Cu(II), pheHA-5}](terephthalate) taken in 4:1 methanol/water (v/v) injected via syringe pump. Important peaks are observed at m/z = 755.5²⁺: La(III)[15-MC_{Cu(II), pheHA-5}](terephthalateH)₂²⁺, 973.9³⁺: {La(III)[15-MC_{Cu(II), pheHA-5}]₂(terephthalate)(NO₃)³⁺, 1008.0³⁺: {La(III)[15-MC_{Cu(II), pheHA-5}]₂(terephthalate)(terephthalateH)³⁺, 1511.7⁺: La(III)[15-MC_{Cu(II), pheHA-5}](terephthalate)⁺, {La(III)[15-MC_{Cu(II), pheHA-5}]₂(terephthalate)₂²⁺. Inset: Isotope model of the {La(III)[15-MC_{Cu(II), pheHA-5}]₂(terephthalate)(terephthalateH)³⁺ peak at 1008.0³⁺ m/z.

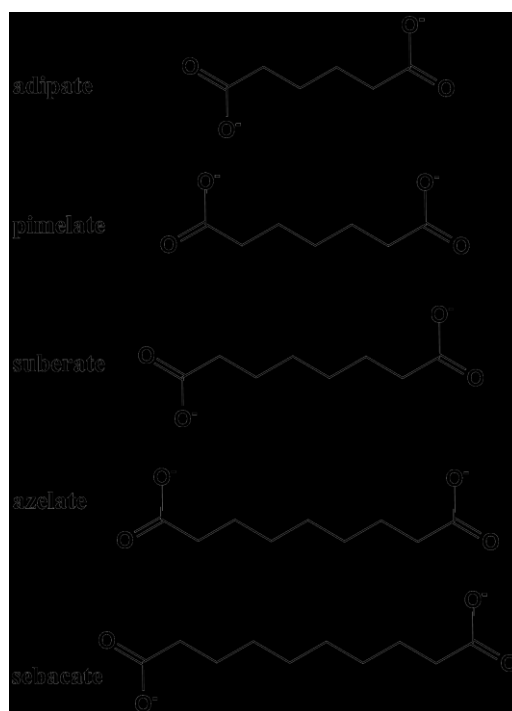


Figure 2.13: Chemdraw diagrams of adipate, pimelate, suberate, azelate, and sebacate.

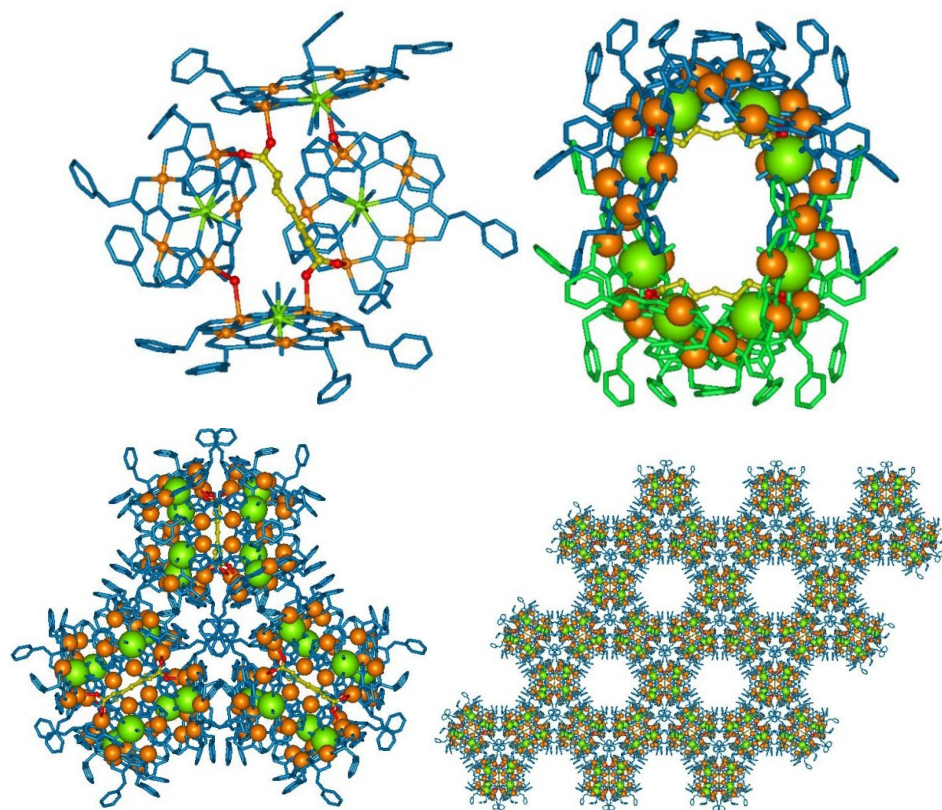


Figure 2.14. Crystal structure images of the $\text{La(III)[15-MC}_{\text{Cu(II), pheHA-5}}\text{](pimelate)}$ complex highlighting different aspect of the mesostructured assembly. Top left) MC tetramer assembled with pimelate, top right) octameric MC hydrophilic compartment highlighting the entrance to the internal cavity, bottom left) assembly of three octameric MC compartments through hydrophobic interactions, bottom right) packing diagram showing the 2.3 nm channels in the lattice. Color scheme: Green = La, orange = Cu, red = pimelate O, dark blue = MC non-metal atoms, yellow = guest C. Unbound counter anions, solvent molecules, and hydrogen atoms were removed for clarity.

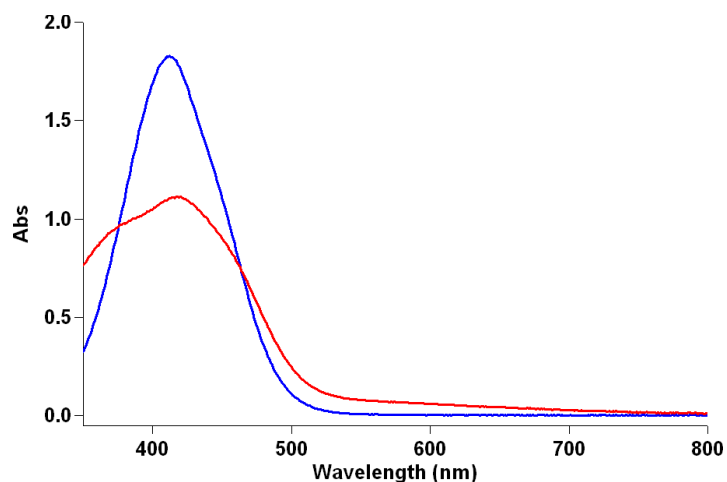


Figure 2.15. UV-VIS absorption spectra from a guest absorption experiment of a 5.8×10^{-5} M methyl orange sodium salt solution in acetone in the absence of the mesostructure (blue) and after soaking with the mesostructure for 18 hours (red). The decreased absorbance indicates guest absorption in the mesostructure. The increased absorption at 375 and 550 nm is due to slight LaMC dissolution.

| MC | a | b | c | d | e | f |
|---------------------|---------|---------|---------|----------|----------|----------|
| A (Å) | 16.2258 | 16.7736 | 15.0407 | 31.6296 | 39.5246 | 20.3902 |
| B (Å) | 28.8381 | 30.4589 | 29.2565 | 16.7149 | 16.7441 | 26.6754 |
| C (Å) | 17.0411 | 17.2669 | 15.7377 | 29.7910 | 33.9964 | 62.8937 |
| α (°) | 90 | 90 | 90 | 90 | 90 | 90 |
| β (°) | 102.657 | 107.854 | 96.336 | 103.501 | 120.892 | 90 |
| λ (°) | 90 | 90 | 90 | 90 | 90 | 90 |
| V (Å ³) | 7780.12 | 8396.90 | 6882.89 | 15314.83 | 19307.22 | 34209.03 |

Table 2.5: Unit cell parameters for Ln(III)[15-MC_{Cu(II)}-5] complexes with adipate and pimelate guests. a) La(III)[15-MC_{Cu(II)}, pgHA-5](adipate), b) La(III)[15-MC_{Cu(II)}, hpheHA-5](adipate), c) Gd(III)[15-MC_{Cu(II)}, hpheHA-5](adipate), d) La(III)[15-MC_{Cu(II)}, hpheHA-5](pimelate), e) La(III)[15-MC_{Cu(II)}, hpheHA-5](suberate), f) Gd(III)[15-MC_{Cu(II)}, hpheHA-5](suberate).

| MC | a | b | c | d |
|---------------------|----------|---------|---------|----------|
| A (Å) | 16.7733 | 16.7529 | 15.4220 | 16.7466 |
| B (Å) | 16.7733 | 18.5478 | 27.9419 | 31.9174 |
| C (Å) | 43.6344 | 18.7839 | 17.0133 | 33.9393 |
| α (°) | 90 | 118.976 | 90 | 90 |
| β (°) | 90 | 105.357 | 94.533 | 90 |
| λ (°) | 120 | 100.366 | 90 | 90 |
| V (Å ³) | 10631.55 | 4583.33 | 7308.44 | 18140.83 |

Table 2.6: Unit cell parameters for Ln(III)[15-MC_{Cu(II)}-5] clathratocomplexes with suberate, azelate, and sebacate guests. a) Dy(III)[15-MC_{Cu(II), pheHA-5}](azelate), b) La(III)[15-MC_{Cu(II), hpheHA-5}](azelate), c) La(III)[15-MC_{Cu(II), pheHA-5}](sebacate), d) La(III)[15-MC_{Cu(II), hpheHA-5}](sebacate).

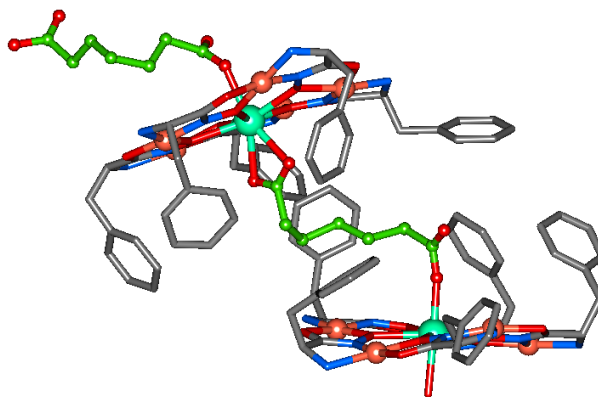


Figure 2.16. Crystal structure of top) Dy(III)[15-MC_{Cu(II), pheHA-5}](pimelate). Crystal structure color scheme: sea green = Dy, orange = Cu, red = O, dark blue = N, grey = MC C, green = guest C. Unbound counter anions, solvent molecules, and hydrogen atoms were removed for clarity.

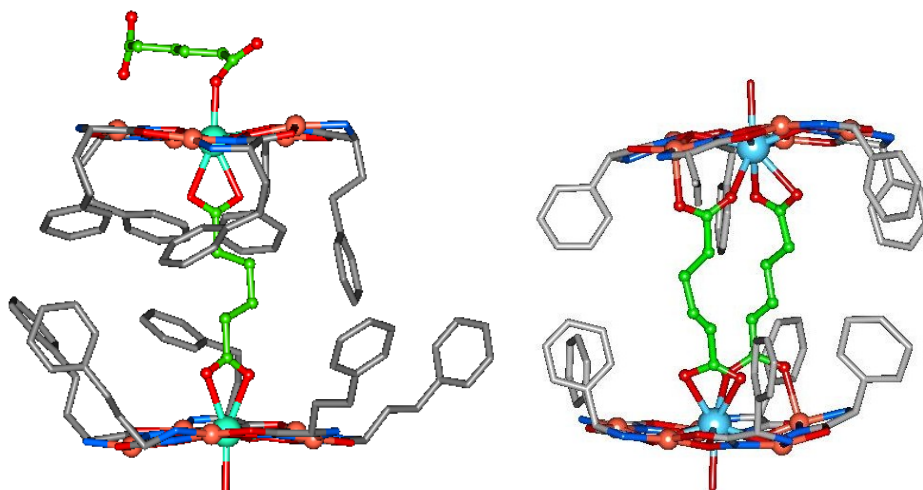


Figure 2.17. Crystal structures of Gd(III)[15-MC_{Cu(II)}, _{hpheHA-5}](adipate) (left) and La(III)[15-MC_{Cu(II)}, _{pgHA-5}](adipate) (right). Color scheme: light blue = La, sea green = Gd, orange = Cu, red = pimelate O, blue = N, grey = MC carbon, green = guest C. Unbound counter anions, solvent molecules, select guests on the hydrophilic faces, and hydrogen atoms were removed for clarity.

References

- (1) Inokuma, Y.; Kawano, M.; Fujita, M. *Nat. Chem.* **2011**, *3*, 349.
- (2) Lee, J.; Farha, O. K.; Roberts, J.; Scheidt, K. A.; Nguyen, S. T.; Hupp, J. T. *Chem. Soc. Rev.* **2009**, *38*, 1450.
- (3) Dinolfo, P. H.; Hupp, J. T. *Chem. Mater.* **2001**, *13*, 3113.
- (4) Ma, L.; Abney, C.; Lin, W. *Chem. Soc. Rev.* **2009**, *38*, 1248.
- (5) MacGillivray, L. R.; Papaefstathiou, G. S.; Friscic, T.; Hamilton, T. D.; Bucar, D.-K.; Chu, Q.; Varshney, D. B.; Georgiev, I. G. *Acc. Chem. Res.* **2008**, *41*, 280.
- (6) Verbiest, T.; Houbrechts, S.; Kauranen, M.; Clays, K.; Persoons, A. *J. Mater. Chem.* **1997**, *7*, 2175.
- (7) Moulton, B.; Zaworotko, M. J. *Chem. Rev.* **2001**, *101*, 1629.
- (8) Wuest, J. D. *Chem. Commun.* **2005**, 5830.
- (9) Evans, O. R.; Xiong, R.-G.; Wang, Z.; Wong, G. K.; Lin, W. *Angew. Chem. Int. Ed.* **1999**, *111*, 557.
- (10) Lin, W.; Ma, L.; Evans, O. R. *Chem. Commun.* **2000**, 2263.
- (11) Evans, O. R.; Lin, W. *Chem. Mater.* **2001**, *13*, 3009.
- (12) Evans, O. R.; Lin, W. *Acc. Chem. Res.* **2002**, *35*, 511.
- (13) Kersting, B.; Lehmann, U. *Adv. Inorg. Chem.* **2009**, *61*, 407.
- (14) Lozan, V.; Loose, C.; Kortus, J.; Kersting, B. *Coord. Chem. Rev.* **2009**, *253*, 2244.
- (15) Klingele, J.; Klingele, M. H.; Baars, O.; Lozan, V.; Buchholz, A.; Leibel, G.; Plass, W.; Meyer, F.; Kersting, B. *Eur. J. Inorg. Chem.* **2007**, *2007*, 5277.
- (16) Lim, C.-S.; Cutland Van Noord, A.; Kampf, J. W.; Pecoraro, V. L. *Eur. J. Inorg. Chem.* **2007**, *2007*, 1347.
- (17) Mezei, G.; Kampf, J. W.; Pan, S.; Poeppelmeier, K. R.; Watkins, B.; Pecoraro, V. L. *Chem. Commun.* **2007**, 1148.
- (18) Zaleski, C. M.; Depperman, E. C.; Kampf, J. W.; Kirk, M. L.; Pecoraro, V. L. *Inorg. Chem.* **2006**, *45*, 10022.
- (19) Zaleski, C. M.; Lim, C. S.; Cutland-Van Noord, A. D.; Kampf, J. W.; Pecoraro, V. L. *Inorg. Chem.* **2011**, *50*, 7707.
- (20) Noord, A. D. C.-V.; Kampf, J. W.; Pecoraro, V. L. *Angew. Chem. Int. Ed.* **2002**, *41*, 4667.
- (21) Cutland, A. D.; Malkani, R. G.; Kampf, J. W.; Pecoraro, V. L. *Angew. Chem. Int. Ed.* **2000**, *39*, 2690.
- (22) Cutland, A. D.; Halfen, J. A.; Kampf, J. W.; Pecoraro, V. L. *J. Am. Chem. Soc.* **2001**, *123*, 6211.
- (23) Lim, C.-S.; Noord, A. D. C.-V.; Kampf, J. W.; Pecoraro, V. L. *Eur. J. Inorg. Chem.* **2007**, 1347.
- (24) G. Mezei; Kampf, J. W.; Pan, S.; Poeppelmeier, K. R.; Watkins, B.; Pecoraro, V. L. *Chem. Commun.* **2007**, *11*, 1148.
- (25) Lim, C. S.; Kampf, J. W.; Pecoraro, V. L. *Inorg. Chem.* **2009**, *48*, 5224.
- (26) Lim, C.-S., *Graduate Thesis*, University of Michigan, 2008.
- (27) Lim, C. S.; Jankolovits, J.; Kampf, J. W.; Pecoraro, V. L. *Chem. Asian. J.* **2010**, *5*, 46.
- (28) Jankolovits, J.; Lim, C.-S.; Kampf, J. W.; Pecoraro, V. L. *Z. Naturforsch.* **2010**, *65b*, 263.
- (29) Jankolovits, J.; Lim, C.-S.; Mezei, G.; Kampf, J. W.; Pecoraro, V. L. *Inorg. Chem.* **2012**, doi:10.1021/ic202347j.
- (30) Tegoni, M.; Furlotti, M.; Tropiano, M.; Lim, C.-S.; Pecoraro, V. L. *Inorg. Chem.* **2010**, *49*, 5190.

- (31) Wynberg, H.; Bantjes, A. *J. Am. Chem. Soc.* **1960**, *82*, 1447.
- (32) Zaleski, C. M.; Lim, C.-S.; Cutland-Van Noord, A. D.; Kampf, J. W.; Pecoraro, V. L. *Inorg. Chem.* **2011**, *50*, 7707.
- (33) *SAINTE Plus*, v. 7.60A; Bruker Analytical X-ray: Madison, WI, 2008.
- (34) Sheldrick, G. M.; *Sadabs*, Program for Empirical Absorption Correction of Area Detector Data, v 2008/1, University of Göttingen, Göttingen, Germany, 2008.
- (35) Sheldrick, G. M. *Acta Cryst.* **2008**, *A64*, 112.
- (36) Sheldrick, G. M. *CELL_NOW* v. 2008/2, Program for Indexing Twins and Other Problem Crystals, University of Göttingen, Göttingen, Germany, 2008.
- (37) S Sheldrick, G. M. *TWINABS* v. 2008/2, Program for Empirical Absorption Correction of Area Detector Data, University of Göttingen, Göttingen, Germany, 2008.
- (38) *SAINTE Plus*, v. 7.60A; Bruker Analytical X-ray: Madison, WI, 2009.
- (39) Cutland, A. D.; Halfen, J. A.; Kampf, J. W.; Pecoraro, V. L. *J. Am. Chem. Soc.* **2001**, *123*, 6211.
- (40) Jankolovits, J.; Kampf, J. W.; Maldonado, S.; Pecoraro, V. L. *Chem. Eur. J.* **2010**, *16*, 6786.
- (41) The centroid of the oxygen-mean plane, meaning the five oxygen atoms in the MC ring, was calculated in Mercury 2.2. Previous work referenced compartment dimensions to the central lanthanides. Conversion between the two scales is complicated by the variable positioning of the central metal in different structures. For previously reported structures discussed in this manuscript, distances are also referenced to the centroids of the oxygen-mean plane.
- (42) Spek, A. L. *J. Appl. Crystallogr.* **2003**, *36*, 7.
- (43) Gerstein, M.; Chothia, C. *Proc. Nat. Acad. Sci.* **1996**, *93*, 10167.
- (44) Mecozzi, S.; J. Rebek, J. *Chem. Eur. J.* **1998**, *4*, 1016.
- (45) Schalley, C. A. *Mass Spectrom. Rev.* **2001**, *20*, 253.
- (46) Schalley, C. A.; Castellano, R. K.; Brody, M. S.; Rudkevich, D. M.; Siuzdak, G.; Rebek, J. *J. Am. Chem. Soc.* **1999**, *121*, 4568.
- (47) Schalley, C. A.; Rivera, J. M.; Martin, T.; Santamaria, J.; Siuzdak, G.; Rebek, J. *J. Org. Chem.* **1999**, 1325.
- (48) Cutland, A. D.; Malkani, R. G.; Kampf, J. W.; Pecoraro, V. L. *Angew. Chem. Int. Ed.* **2000**, *39*, 2689.
- (49) Ma, L.; Lin, W. *J. Am. Chem. Soc.* **2008**, *130*, 13834.
- (50) Choi, H. J.; Lee, T. S.; Suh, M. P. *Angew. Chem. Int. Ed.* **1999**, *38*, 1405.
- (51) Min, K. S.; Suh, M. P. *Chem. Eur. J.* **2001**, *7*, 303.
- (52) Suh, M. P.; Ko, J. W.; Choi, H. J. *J. Am. Chem. Soc.* **2002**, *124*, 10976.
- (53) Metrangolo, P.; Carcenac, Y.; Lahtinen, M.; Pilati, T.; Rissanen, K.; Vij, A.; Resnati, G. *Science* **2009**, *323*, 1461.
- (54) Ananchenko, G. S.; Udachin, K. A.; Dubes, A.; Ripmeester, J. A.; Perrier, T.; Coleman, A. W. *Angew. Chem. Int. Ed.* **2006**, *45*, 1585.

Chapter III

Characterizing the Side Chain Dependent Guest Binding Affinity and Enantioselectivity of Ln(III)[15-Metallacrown-5] Metallocavitands with a Novel Voltammetric Competitive Binding Assay

Introduction

The molecular recognition behavior of many supramolecular hosts makes them useful in separations, catalysis, and materials design.¹⁻⁷ The unique structure of Ln(III)[15-MC-5] metallocavitands can give rise to unique molecular recognition faculties. In particular, the inherent chirality of the MC ring and the multimetallic face of Ln(III)[15-MC-5] complexes⁸⁻¹⁰ differentiate the hosts from most complexes in the literature. Therefore, there is great promise for using these MCs in separations, catalysis, and materials design. Of note, Ln(III) complexes are known to be effective catalysts for¹¹⁻¹³ and give rise to luminescence and magnetic properties.^{14,15} Furthermore, there is promise for synergistic effects between the MC face and the hydrophobic cavity. The cavity can lead to enhanced selectivity through secondary sphere interactions or substrate confinement. There is also the possibility for using the hydrophobic cavity in the design of materials, as highlighted by the crystalline compartments discussed in chapter two and elsewhere.¹⁶⁻¹⁸

To develop Ln(III)[15-MC_{Cu(II)}-5] metallocavitands for separations, catalysis, and materials design, a thorough understanding of their guest recognition behavior is necessary as a foundation. The binding of carboxylate guests has been extensively studied in the solid state¹⁶⁻¹⁸ (see chapter 2). To summarize, crystal structures show that carboxylate guests preferentially bind on the hydrophobic face (figure 3.2). Extensive π -stacking interactions are observed between phenyl side-chains on the Ln(III)[15-MC_{Cu(II)}-5] host and the unsaturated guest. Crystal structures also show that carboxylates typically bind bidentate to the central lanthanide. Gd(III) tends to be 8-coordinate and accommodates one guest. La(III) is typically 9-coordinate. While the solid-state

observations provide a clear picture of how Ln(III)[15-MC_{Cu(II)}-5] metallocavitands recognize guests, they do not provide information on guest affinity. Furthermore, crystal structures are strongly influenced by packing forces. Therefore, they do not necessarily represent the types of complexes, the degree of selectivity, or the predominant guest binding modes in dilute solution at equilibrium. Given these limitations of single crystal X-ray crystallography and the interest in applications of supramolecular hosts in the liquid state, there is a need to understand Ln(III)[15-MC_{Cu(II)}-5] guest recognition in solution.

When considering Ln(III)[15-MC_{Cu(II)}-5] complexes in solution, it is important to note that the *free* metallacrowns have a coordinated hydroxide in neutral aqueous solution. A recent thermodynamic study revealed that the pK_a of water coordinated to the lanthanide on a Ln(III)[15-MC_{Cu(II)}-5] is ~4.5. Therefore, the MC is best formulated as a Ln(III)[15-MC_{Cu(II)}-5](OH)²⁺ cation that also has weakly coordinated solvent molecules or other counterions.¹⁹ To simplify the nomenclature, the hydroxide and other water molecules are implied, and their stoichiometries unspecified, when referring to the free Ln(III)[15-MC_{Cu(II)}-5] host in solution.

NMR spectroscopy is in many ways the most powerful technique for characterizing host-guest interactions.²⁰ Unfortunately, line broadening from the paramagnetic Ln(III)[15-MC_{Cu(II)}-5] precludes characterization with many of the most accessible NMR techniques. The initial measurements of guest affinity to Ln(III)[15-MC_{Cu(II)}-5] hosts utilized ESI-MS, fluorescence and visible absorption spectroscopies, diffusion NMR spectroscopy, and isothermal titration calorimetry. These experiments were limited in scope but established that Ln(III)[15-MC_{Cu(II), pheHA}-5] metallocavitands selectively bind guests in solution.

ESI-MS provided preliminary evidence for complexation between Ln(III)[15-MC-5] hosts and carboxylate guests in solution.¹⁷ Though ESI-MS is a gas-phase technique, species observed by ESI-MS tend to correlate with species that persist in solution.²¹ The first quantitative measurement of guest binding to Ln(III)[15-MC_{Cu(II)}-5] metallocavitands was performed with isothermal titration calorimetry in aqueous buffer.²² Binding affinities for simple carboxylates, such as benzoate, were on the order of 10² - 10³. Stronger guest binding was observed with more Lewis-acidic lanthanides, supporting

the crystallographic observation that carboxylates bind preferentially to the central metal. S- and R-phenylalanine were bound to $\text{Gd(III)[15-MC}_{\text{Cu(II), pheHA-5}}\text{Cl}_3$ with affinities of 89 ± 11 and $57 \pm 11 \text{ M}^{-1}$ respectively, revealing modest enantioselective guest binding by the chiral host.^{23,24} Tegoni et al. reported a thermodynamic investigation of acetate and benzoate binding to $\text{Eu(III)[15-MC}_{\text{Cu(II), pheHA-5}}\text{(NO}_3\text{)}.$ ²⁵ Using a competitive fluorimetry assay in aqueous buffer, binding constants of 389 ± 9 and $98 \pm 3 \text{ M}^{-1}$ were determined for benzoate and acetate, respectively. Notably, the opposite trend is expected based on guest basicity, revealing the strong influence of the hydrophobic cavity.

These previous studies provided a basic description of $\text{Ln(III)[15-MC}_{\text{Cu(II), pheHA-5}}]$ guest affinity, enantioselectivity, and how the host recognizes guests. However, key questions remained pertaining to the development of $\text{Ln(III)[15-MC}_{\text{Cu(II)-5}}]$ metallocavitands for practical applications in solution. Little was known about how functional groups influenced guest affinity. Enantioselective guest binding was very modest and limited to phenylalanine, so there was interest in expanding the substrate scope and developing a strategy for enhancing enantioselectivity. Furthermore, only metallocavitands with pheHA ligands were investigated, so it was not clear how guest binding affinity could be tuned through changes to the $\text{Ln(III)[15-MC}_{\text{Cu(II)-5}}]$ cavity.

This chapter describes investigations on how structural features on the guest or $\text{Ln(III)[15-MC}_{\text{Cu(II)-5}}]$ phenyl side chain influence guest selectivity in solution. These studies were conducted voltammetrically using ferrocene carboxylate as a redox probe. There were three reasons for exploring guest binding with voltammetry. First, voltammetry is an accessible technique that is suitable for the paramagnetic host. Second, voltammetry demonstrates how guest binding could be influenced electrochemically, thus providing a starting point for considering $\text{Ln(III)[15-MC}_{\text{Cu(II)-5}}]$ complexes in redox-responsive devices and materials.²⁶ Third, it was recognized that a new, general method for measuring guest binding thermodynamics could be developed utilizing a voltammetric competition approach.

Voltammetry is frequently used to assess host-guest complexation with redox active substrates.²⁷⁻³¹ The thermodynamics of guest binding to cyclodextrins,³²⁻³⁵ cucurbiturils,³⁶⁻³⁹ calixarenes,^{40,41} and many other systems has been measured voltammetrically.⁴²⁻⁴⁷ In systems where complex dissociation is fast relative to the scan

rate, the observed half-wave potential ($E_{1/2}$) of the redox-active substrate (either host or guest) is perturbed upon binding to another species. Most commonly, the $E_{1/2}$ will shift to positive or negative potentials, which is known as one-way shift behavior. The potential shift is related to the association constant between the redox inactive species and the reduced and oxidized substrate (K_{red} and K_{ox} , respectively) by the Nernst Equation (eq 1).⁴⁸⁻⁵⁰

$$(1) E_C^{0'} = E_f^{0'} + \frac{RT}{F} \ln\left(\frac{1 + K_{red}[MC]_f}{1 + K_{ox}[MC]_f}\right)$$

The novel voltammetric competitive binding assay developed in this chapter measures the binding constant between a redox-inactive host and redox-inactive guest based on the competition with a redox probe. With the $E_{1/2}$ of a redox active guest shifted by a suitable host, titration of a competitive guest displaces the redox active guest, shifting $E_{1/2}$ back toward the free, uncomplexed value. The phenomenon of competitive displacement of a redox active guest was reported separately by Lehn et. al.⁴² and Kaifer et. al.,⁵¹ though no strategy for quantifying the binding constant of the host and competitive guest was reported. A voltammetric competitive binding assay has been reported for polyammonium macrocycles,⁵²⁻⁵⁵ though this technique relied on associated protonation equilibria to quantify competitive guest binding, limiting its applicability. Voltammetric competitive binding assays have also been reported for hosts immobilized on electrode surfaces.⁵⁶⁻⁵⁹ However, this approach is not particularly general as it relies on modified electrodes. Another voltammetric competitive binding assay has been reported that requires the redox probe to be tethered to the host, severely limiting its scope.⁶⁰⁻⁶² The novel assay reported herein is completely homogeneous, does not require modified electrodes or covalent attachment of the host and guest. Therefore, it could be applied to a number of systems that display one-way shift behavior with redox active guests.

After establishing the voltammetric binding assay, this chapter reports the use of the assay to characterize various aspects of Ln(III)[15-MC_{Cu(II)}-5] guest recognition in solution. Enantioselective guest binding is explored with a series of α -amino acid analogs. This study also provides information on how guest affinity is affected by different functional groups on the guest. Such information is relevant to promoting

catalytic turnover and differentiating the roles of the metal ions and hydrophobic cavity. The effect of side-chain variation on guest affinity and selectivity is assessed with Gd(III)[15-MC_{Cu(II)}-5] hosts bearing picoline hydroxamic acid (picHA), pgHA, pheHA, and hpheHA side chains (figure 3.1b-e). These experiments reveal that Ln(III)[15-MC_{Cu(II)}-5] hosts discriminate between guests based on chirality, charge, chemical functionalities, and interactions with the MC side-chains. Importantly, the observation of enhanced guest recognition through side chain substitutions outlines a strategy for tuning selectivity and substrate interactions with the MC. These results will serve as the foundation for developing Ln(III)[15-MC_{Cu(II)}-5] metallocavitands for chiral separations or as supramolecular catalysts. The work presented in this chapter has appeared in two published manuscripts^{23,63} and a third that has been submitted for publication.

Experimental

All reagents were obtained from commercial sources and used as received unless noted otherwise. Distilled, deionized water was used in all experiments. L-pheHA, L-pgHA, and L-hpheHA were synthesized as described in chapter 2. The picHA synthesis is described in chapter 4. Ln(III)[15-MC_{Cu(II),N,L-pheHA-5}]Cl₃ complexes were prepared following either a literature procedure²² or the synthesis described below for the Gd(III) complex. The synthesis described below is recommended as it has better reproducibility, greater yields, and shorter crystallization time. Ln(III)[15-MC_{Cu(II),N,L-pheHA-5}](NO₃) complexes were prepared as previously described.⁶⁴ Cobaltocenium carboxylic acid hexafluorophosphate was prepared following a literature procedure.⁶⁵ Sodium benzoate was obtained from Aldrich. Sodium salts of the remaining guests were prepared by neutralization with an equivalent of sodium bicarbonate or sodium hydroxide and stored in a vacuum desiccator over phosphorous pentoxide. Ferrocene was recrystallized in pentane prior to use. Brockman I activated basic alumina was utilized for MC purification. Sodium hydroxide solutions were standardized by colorimetric titration against dry potassium hydrogen phthalate with a phenolphthalein indicator. ESI-MS was performed on a Micromass LCT-TOF Electrospray Ionization mass spectrometer with a sample cone voltage of 50 V. ESI-MS solutions were injected via syringe pump from the indicated solvents.

Ferrocene carboxylate sodium salt: Ferrocene carboxylic acid (0.2g) dissolved in methanol (5 mL) was added to a solution of 0.05g sodium hydroxide in water. The solvent was removed under vacuum, and the solid dissolved in a minimum amount of methanol (~5 mL). FcC sodium salt was precipitated with ether (75 mL), filtered, washed with an additional ether (25 mL), and air dried. Yield: 0.1445g orange powder, 66%. Elemental analysis calc'd (%) for $C_{11}H_9FeNaO_2$: C 52.42, H 3.60; found: C 52.46, H 3.57.

Synthesis of MC complexes used in titration experiments:

Gd(III)[15-MC_{Cu(II),N,L-pheHA-5}]Cl₃: L-pheHA (0.901 g, 5.00 mmol) was stirred in 35 mL of methanol and deprotonated with two equivalents of 1 M aqueous sodium hydroxide (10.0 mmol). Stirring continued until all of ligand had dissolved. GdCl₃ (0.383 g, 1.03 mmol) and CuCl₂ (0.879 g, 5.16 mmol) were sequentially added, and the solution was stirred overnight. The pH of the solution was adjusted to ~7. After 20 minutes of stirring, the solution was filtered. 5 mL of 0.5 M aqueous sodium chloride was added to the filtrate, and purple crystals of the product formed by slow evaporation of the solvent. The crystals were isolated by filtration, rinsed with 5 mL cold water, and air dried. Yield = 1.4781 g, 86 %. CHN Analysis for $[(C_{45}H_{50}N_{10}O_{10}Cu_5Gd)Cl_3(H_2O)_{14}]$, found (calc'd): C = 31.36 (31.36), H = 4.50 (4.60), N = 8.15 (8.12). ESI-MS (methanol) gave $m/z = 690.9^{2+}$ (691.0^{2+} calc'd for $[GdCu_5(pheHA)_5(OH)]^{2+}$).

Gd(III)[15-MC_{Cu(II),N,L-hpheHA-5}]Cl₃: L-hpheHA (1.00 g, 5.16 mmol) was stirred 30 mL of methanol and deprotonated with two equivalents of 1 M aqueous sodium hydroxide (10.3 mL). Stirring continued until all of ligand had dissolved. GdCl₃ (0.383 g, 1.03 mmol) and CuCl₂ (0.879 g, 5.16 mmol) were sequentially added, and the solution was stirred overnight. The solution was then gravity filtered and passed through a 5 cm tall activated basic alumina shortpad in a 60 mL fine glass fritted funnel. The short pad was further rinsed with ~75 mL of a 3:1 methanol/acetonitrile solution (v/v). The recovered solution was then dried under vacuum. Compound purity was confirmed through CV (see results section and supporting information). Yield = 0.942 g, 43 %. CHN Analysis for $[(C_{50}H_{60}N_{10}O_{10}Cu_5Gd)Cl_3(NaCl)_8(H_2O)_6]$, found (calc'd): C = 28.37 (28.35), H = 3.43 (3.53), N = 6.81 (6.61). ESI-MS (methanol) gave $m/z = 727.4^{2+}$ (727.0^{2+} calc'd for $[GdCu_5(hpheHA)_5(OH)]^{2+}$), 735.0^{2+} (736.0^{2+} calc'd for $[GdCu_5(hpheHA)_5Cl]^{2+}$).

Gd(III)[15-MC_{Cu(II),N,L-pgHA-5}]Cl₃: This compound was prepared following the procedure for 1-hpheHA-Cl, substituting L-phenylglycineHA for L-homopheHA. Yield = 1.14 g, 62.4 %. CHN Analysis for [(C₄₀H₄₀N₁₀O₁₀Cu₅Gd)Cl₃(NaCl)_{5.5}(H₂O)_{9.5}], found (calc'd): C = 25.38 (25.38), H = 3.17 (3.14), N = 7.41 (7.39). ESI-MS (methanol) gave m/z = 656.9²⁺ (655.9²⁺ calc'd for [GdCu₅(pgHA)₅(OH)]²⁺), 664.9²⁺ (665.9 calc'd for [GdCu₅(pgHA)₅Cl]²⁺), 1366.7⁺ (1365.8 calc'd for [GdCu₅(pgHA)₅Cl₂]⁺).

Gd(III)[15-MC_{Cu(II),N,picHA-5}](NO₃)_{1.5}(OH)_{1.5}: PicHA (500 mg, 3.62 mmol), Cu(NO₃)₂ (842 mg, 3.62 mmol) and Gd(NO₃)₃ (326.8 mg, 0.724 mmol) were stirred in a 500 mL flask with 25 of mL dimethylformamide and 8.5 mL of water. 1 M aqueous sodium hydroxide (7.24 mmol) was added and the homogeneous brown solution stirred for one hour. 450 mL of acetone was then added to precipitate the MC. The flask was then stoppered and cooled in a -20 °C freezer. The precipitate was isolated by filtration on a fine glass fritted funnel, rinsed with 30 mL of cold acetone, and dried under vacuum. The purity was confirmed with CV. Yield = 929 mg, 93.4 %. CHN Analysis for [(C₃₀H₂₄N₁₀O₁₀Cu₅Gd) (NO₃)_{1.5}(OH)_{1.5}(H₂O)_{5.5}], found (calc'd): C = 26.20 (26.24), H = 2.48 (2.39), N = 11.93 (11.73). ESI-MS (1:1 water/methanol (v/v)) gave m/z = 585.3²⁺ (585.9²⁺ calc'd for [GdCu₅(picHA)₅(OH)]²⁺), 608.3²⁺ (608.3²⁺ calc'd for [GdCu₅(picHA)₅(NO₃)₂]²⁺), 1278.5⁺ (1277.7⁺ calc'd for [GdCu₅(picHA)₅(NO₃)₂]⁺).

Synthesis of MC-guest complexes:

La(III)(FcC⁻)₂[15-MC_{Cu(II), pheHA-5}](NO₃)₃: La(III)[15-MC_{Cu(II), pheHA-5}](NO₃)₃ (30 mg, 0.018 mmol) and FcC sodium salt (10 mg) was dissolved in a 1:1 mixture of ethanol and acetonitrile (8 mL). Slow evaporation of the solution while protected from light yielded crystals within one month. Yield: 16.5 mg, 43%. Elemental analysis calc'd (%) for LaCu₅C₇₁H₉₈N₁₁O₂₈Fe₂: C 40.19, H 4.66, N 7.26; found C 39.94, H 4.11, N 7.22.

La(III)(FcDC⁻)[15-MC_{Cu(II), pheHA-5}](NO₃)₃: Sodium hydroxide (0.130g) was dissolved in methanol (15 ml). 1,1'-Ferrocene dicarboxylic acid (0.100g) was added and quickly changed from a red color to orange. Ether (100 mL) was added to the solution. The solution was cooled on ice, and filtered to obtain an orange powder of the ferrocene dicarboxylate disodium salt. The powder was washed with ether and air dried. La(III)[15-MC_{Cu(II), pheHA-5}](NO₃)₃ (30 mg, 0.018 mmol) was added to 6 mg of this powder and dissolved in a 1:1 mixture of methanol and water (5 mL). Slow evaporation of the

solution while protected from light yielded crystals within one month. Yield: 20.6 mg. ESI-MS (4:1 methanol/water) gave $[\text{LaCu}_5\text{C}_{45}\text{H}_{50}\text{N}_{10}\text{O}_{10}(\text{FeC}_{12}\text{H}_8\text{O}_4)]^{2+}$ 809 m/z, $[\text{LaCu}_5\text{C}_{45}\text{H}_{50}\text{N}_{10}\text{O}_{10}(\text{FeC}_{12}\text{H}_9\text{O}_4)]^+$ 1620 m/z. Elemental analysis calc'd (%) for $\text{LaCu}_5\text{FeC}_{57.5}\text{H}_{83}\text{N}_{11}\text{O}_{29}$: C 36.26, H 4.39, N 8.09; found C 37.08, H 4.08, N 8.32.

Dy(III)(benzoate)₂[15-MC_{Cu(II), pheHA-5}](benzoate)_{0.75}Cl_{0.25}: A solution of Dy(III) [15-MC_{Cu(II), pheHA-5}]Cl₃ (99.28 mg, 0.063 mmol), sodium benzoate (86.6 mg, 0.601 mmol), and sodium ferrocene carboxylate (1.5 mg, 0.006 mmol) in 1:1 methanol and pH 7.5 0.1 M aq MOPS (10 mL) was slowly evaporated to yield block-shaped crystals. Yield: 0.0981 g. ESI-MS (4:1 methanol/water) gave $[\text{DyCu}_5\text{C}_{45}\text{H}_{50}\text{N}_{10}\text{O}_{10}(\text{C}_7\text{H}_5\text{O}_2)]^{2+}$ 746 m/z, $[\text{DyCu}_5\text{C}_{45}\text{H}_{50}\text{N}_{10}\text{O}_{10}(\text{C}_7\text{H}_5\text{O}_2)_2]^+$ 1613 m/z. Elemental analysis calc'd (%) for $\text{Dy}_2\text{Cu}_{10}\text{C}_{132.25}\text{H}_{174.25}\text{N}_{20}\text{O}_{52.5}\text{Cl}_{0.25}$: C 41.22, H 4.57, N 7.27; found C 42.02, H 4.22, N 7.22.

La(III)(FcC⁻)[15-MC_{Cu(II), hpheHA-5}]: La(III)[15-MC_{Cu(II), hpheHA-5}](NO₃)₃ (30 mg, 0.018 mmol) and FcC sodium salt (10 mg, 0.040 mmol) was dissolved in 6 mL of a 2:1:1 mixture of ethanol, acetonitrile, and water containing 5 mg of tetraethylammonium hexafluorophosphate. Slow evaporation of the solution while protected from light yielded crystals in one month. Yield: 20.0 mg, 43%. Elemental analysis found (calc'd) for $[(\text{LaCu}_5(\text{hpheHA})_5)_2(\text{FcC}^-)_5(\text{NO}_3)(\text{H}_2\text{O})_{15}]$: C = 42.74 (43.17), H = 4.41 (4.56), N = 7.33 (6.82).

Cyclic Voltammetry

CV measurements were performed with a BAS Epsilon potentiostat. The working electrode was a 0.0707 cm² glassy carbon disk that was polished with 0.05 μm polishing alumina on velvet, rinsed, and sonicated in distilled deionized water before each scan. The counter electrode was a platinum wire. The electrochemical cell was water jacketed and held at a constant temperature (25.0 ± 0.1 °C) with a VWR 1145 refrigerated constant temperature controller. *It should be noted that strict temperature control was required for the competition titration experiments.* The cell's exposure to light was limited to prevent FcC⁻ decomposition.⁶⁶ No evidence for decomposition was observed through the course of the experiments. The solution was purged with argon or nitrogen and blanketed with an inert atmosphere during the experiments.

Two different solutions were used for binding constant measurements. For the development of the cyclic voltammetry competitive binding assay and measurement of the series of chiral α -amino acid analogs, electrochemical measurements were performed in 10 mL of a 0.1 M KCl solution containing 50% methanol, 50% 0.1 M aq MOPS buffer solution that had a ξ pH of 7.5.^{67,68} An aqueous 3 M Ag/AgCl (BaSF) reference electrode was employed. No significant changes in the pH were observed through the course of the experiments. The solution resistance was compensated electronically. A scan rate of 200 mV/s was used. For MC binding titrations, the concentration of the MC host was adjusted from 0-12 mM by titration of a solid weighed on a Mettler AT201 balance. For competition titrations, the competitive guest was titrated as a carefully weighed solid to FcC⁻ solutions containing ~ 5-10 equivalents of Ln(III)[15-MC_{Cu(II), pheHA-5}]Cl₃.

For the measurement of guest binding to Ln(III)[15-MC_{Cu(II)-5}] hosts with different side chains, CVs were taken with a scan rate of 50 mV/s and an electronic correction for solution resistance was applied. Measurements were performed at a ξ pH of 8.5 in 8 mL of a 0.1 M sodium triflate solution containing 60% ACN, 40 % 0.1 M aqueous EPPS buffer solution. The pH was measured with a glass electrode calibrated in aqueous solutions and corrected using the reported constant.^{67,69} At this pH the carboxylic acids are deprotonated and EPPS is an effective buffer.⁷⁰ No significant changes in the pH were observed through the course of the experiments. A Ag/Ag⁺ pseudo-reference electrode was employed that was composed of a silver wire in a solution of 0.01 M silver triflate and 0.1 M sodium triflate in 60% ACN, 40% water (v/v). The reference electrode was connected to the cell via a liquid junction containing 0.1M sodium triflate in 60% ACN, 40% water solution (v/v). The reference electrode assembly was wrapped in aluminum foil to protect it from light. The silver wire was polished on fine sandpaper prior to use. The buffer, liquid junction, and silver triflate electrode solutions were prepared fresh daily. The electrode was stored in 0.1M sodium triflate in 60% ACN, 40% water solution (v/v) between uses. All potentials are referenced to the ferrocene/ferrocenium redox couple measured with this electrode. For the titrations, the concentration of FcC⁻ was 0.5 mM. Prior to the experiments, the solution was purged with nitrogen, and the cell was blanketed with nitrogen through the course of the titrations. Titrants were added as a carefully weighed solid up to the endpoint of the

titration or the solubility limit of the MC or guest. For the titration of the MC to FcC^- , up to 20 equivalents of MC were added. For the competition titrations, the MC concentration was ~ 2.3 mM and up to 200 equivalents of guest per FcC^- were titrated.

For all titrations, the shift in the observed $E_{1/2}$ with the change in MC concentration was fit in Origin using equation 1 above and equation 2 below to solve for the concentration of free MC in solution, $[\text{MC}]_f$, where $E_c^{0'}$ and $E_f^{0'}$ are the formal potentials of the free and complexed FcC^- , respectively, R is the gas constant ($8.3145 \text{ J K}^{-1} \text{ mol}^{-1}$), T is the temperature (298.15 K), F is the Faraday constant ($96,485.3 \text{ C mol}^{-1}$), K_{red} and K_{ox} are the association constants between the MC and the reduced and oxidized ferrocene carboxylate, FcC^- and FcC respectively, and $[\text{FcC}^-]_0$ and $[\text{MC}]_0$ are the total concentrations of FcC^- and MC in the solution, respectively.

$$(2) \quad [\text{MC}]_f = \frac{-a + \sqrt{b}}{2K_{\text{red}}}$$

$$a = 1 + K_{\text{red}}[\text{FcC}^-]_0 - K_{\text{red}}[\text{MC}]_0$$

$$b = (1 + K_{\text{red}}[\text{FcC}^-]_0 - K_{\text{red}}[\text{MC}]_0)^2 + 4K_{\text{red}}[\text{MC}]_0$$

For the competition titrations, the shift in the observed $E_{1/2}$ with the change in guest concentration was fit in Origin using equation 1 and equation 3 to solve for $[\text{MC}]_0$ and using K_{red} and K_{ox} determined from the MC binding titrations, where K_{DG} is the dissociation constant between the competitive guest and the MC, K_{Dred} is the dissociation constant between the reduced FcC^- and the MC, and $[\text{G}]_0$ is the total concentration of the competitive guest in solution.

$$(3) \quad [\text{MC}]_f = \frac{a}{3} + \frac{2}{3}\sqrt{(a^2 - 3b)} \cdot \cos\left(\frac{1}{3}\arccos\left(\frac{-2a^3 + 9ab - 27c}{2\sqrt{(a^2 - 3b)^3}}\right)\right)$$

$$a = K_{\text{Dred}} + K_{\text{DG}} + [\text{FcC}^-]_0 + [\text{G}]_0 - [\text{MC}]_0$$

$$b = K_{\text{DG}}([\text{FcC}^-]_0 - [\text{MC}]_0) + K_{\text{Dred}}([\text{G}]_0 - [\text{MC}]_0) + K_{\text{Dred}}K_{\text{DG}}$$

$$c = K_{\text{Dred}}K_{\text{DG}}[\text{MC}]_0$$

All titrations were performed multiple times and the error is reported as the standard deviation.

X-ray Crystallography

Crystallographic data described in this chapter was collected and integrated by the department crystallographer, Jeff W. Kampf. The structures were solved by Jeff W. Kampf or myself. The refinements were largely performed by myself, though Jeff W. Kampf assisted with the treatment of complicated disorder in certain instances.

Crystals were mounted on a standard Bruker SMART-APEX CCD-based X-ray diffractometer equipped with a low temperature device and fine focus Mo-target X-ray tube ($\lambda = 0.71073 \text{ \AA}$) operated at 1500 W power (50 kV, 30 mA). The X-ray intensities were measured at 85(2) K. The detector was placed at a distance 5.055 cm from the crystal. Frames were integrated with the Bruker SAINT⁷¹ software package with a narrow frame algorithm. Analysis of the data showed negligible decay during data collection; the data were processed with SADABS⁷² and corrected for absorption. The structures were solved by direct methods and refined with the Bruker SHELXTL (version 2008/4)⁷³ software package by the full-matrix least-squares method on F^2 . Hydrogen atoms were placed on idealized positions using a riding model.

Crystal data for La(III)(FcC⁻)₂(NO₃)[15-MC_{Cu(II), pheHA -5]}: For a crystal of dimensions 0.45 x 0.30 x 0.22 mm, a total of 4825 frames were collected with a scan width of 0.5° in ω and 0.45° in Φ with an exposure time of 20 s/frame. The structure was solved with formula LaCu₅C₇₁H₉₈N₁₁O₂₈Fe₂, M = 2121.92 g/mol. Orthorhombic space group P2₁2₁2₁, a = 16.3243(11) Å, b = 17.5101(11) Å, c = 30.507(2) Å, V = 8720.1(10) Å³, Z = 4, $\rho_{\text{calcd}} = 1.616 \text{ mg/cm}^3$, $\mu = 2.077 \text{ mm}^{-1}$, max. and min. transmission 0.6579 and 0.4550 respectively, 830 restraints, 1239 parameters, 405792 reflections (R(int) = 0.0421), 24529 independent reflections, for observed data $R_1 = 0.0496$, $wR^2 = 0.1364$, for all data $R_1 = 0.0549$, $wR^2 = 0.1431$, largest diff. peak and hole 3.199 and -1.145 e.Å/cm³.

Crystal data for La(III)(FcDC⁻)[15-MC_{Cu(II), pheHA -5](NO₃)}: For a crystal of dimensions 0.26 x 0.16 x 0.10 mm, A total of 4460 frames were collected with a scan width of 0.5° in ω and 0.45° in Φ with an exposure time of 25 s/frame. The structure was solved with formula LaCu₅FeC_{57.5}H₈₃N₁₁O₂₉, M = 1874.83, orthorhombic space group I2₁2₁2₁, a = 13.8915(9) Å, b = 30.956(2) Å, c = 35.708(2) Å, V = 15355.6(17) Å³, Z = 8, $\rho_{\text{calcd}} = 1.648 \text{ mg/cm}^3$, $\mu = 2.170 \text{ mm}^{-1}$, max. and min. transmission 0.8122 and 0.6022 respectively 322 restraints, 1094 parameters, 302773 reflections (R(int) = 0.0495), 21700

independent reflections, for observed data $R_I = 0.0337$, $wR^2 = 0.0948$, for all data $R_I = 0.0374$, $wR^2 = 0.0982$, largest diff. peak and hole 1.515 and -0.862 e.Å/cm³.

Dy(III)(benzoate)₂[15-MC_{Cu(II), pheHA-5}](benzoate)_{0.75}Cl_{0.25}: For a crystal of dimensions 0.44 x 0.34 x 0.12mm, a total of 5190 frames were collected with a scan width of 0.5° in ω and 0.45° in Φ with an exposure time of 10 s/frame. The structure was solved with formula Dy₂Cu₁₀C_{132.25}H_{174.25}N₂₀O_{52.5}Cl_{0.25}, M = 3853.74 g/mol. Monoclinic space group P2₁, a = 15.5327(7) Å, b = 25.4741(12) Å, c = 19.7410(9) Å, $\beta = 98.379(1)^\circ$, V = 7727.8(6) Å³, Z = 2, $\rho_{\text{calcd}} = 1.656\text{mg/cm}^3$, $\mu = 2.394\text{ mm}^{-1}$, max. and min. transmission 0.6299 and 0.5109 respectively, 555 restraints, 2171 parameters, 299821 reflections (R(int) = 0.0309), 43365 independent reflections, for observed data $R_1 = 0.0353$, $wR^2 = 0.0909$, for all data $R_I = 0.0384$, $wR^2 = 0.0931$, largest diff. peak and hole 1.287 and -0.872 e.Å/cm³.

Results

Establishing the Voltammetric Assay

All MCs used in this chapter were synthesized by the self assembly of one molar equivalent of Ln(III), five equivalents of Cu(II), five equivalents of ligand, and 10 equivalents of base to deprotonate the ligand. Ln(III)[15-MC_{Cu(II), L-pheHA-5}] complexes with Cl⁻ and NO₃⁻ counterions were isolated as a pure solid through crystallization. Gd(III)[15-MC_{Cu(II)-5}]Cl₃ with L-pgHA, L-hpheHA, and picHA could not be crystallized, so they were isolated as crude powders. Inevitably, these solids contained trace Cu(II)-hydroxamate impurities that could not be observed with ESI-MS, CHN analysis, or UV-Vis spectroscopy. The presence of these impurities was evident in the cyclic voltammograms of the compounds. Pure samples of Gd(III)[15-MC_{Cu(II)-5}]Cl₃ show no anodic current from 0 to 250 mV vs Fc/Fc⁺ in 60% ACN, 40 % 0.1 M aqueous ξ pH 8.5 EPPS buffer solution, while the impurities display an irreversible oxidation peak with the current onset at ~100 mV. For Gd(III)[15-MC_{Cu(II), pgHA-5}]Cl₃ and Gd(III)[15-MC_{Cu(II), hpheHA-5}]Cl₃, these impurities were separated by flushing the complexes through a shortpad of basic alumina. Pure Gd(III)[15-MC_{Cu(II), picHA-5}](NO₃) was purified by precipitation from a dimethylformamide-water solution with acetone.

To establish the methodology for measuring guest binding affinities to Ln(III)[15-MC_{Cu(II)}, L-pheHA-5] hosts, CV experiments were performed in a 1:1 mixture of methanol and water. Methanol was necessary to increase MC solubility, while water reduced solution resistance and provided acceptable pH conditions. The KCl electrolyte, chloride MC salts, and MOPS buffer were chosen because they are not known to interact with the Ln(III)[15-MC_{Cu(II)}, L-pheHA-5] lanthanide binding site.¹⁶ The pH values reported for these experimental conditions are the ξ pH, meaning the reported pH was measured in the methanol/water mixture using pH electrodes calibrated in aqueous buffers, and corrected using the reported constants.⁷⁴ The pH of 7.5 was chosen as a suitable pH that ensured FcC⁻ deprotonation and Ln(III)[15-MC_{Cu(II)}, L-pheHA-5] stability. The pK_a's of FcCH and ferrocenium carboxylic acid (FcCH⁺) in water are reported as 4.20 and 1.3, respectively.³² In 50 % methanol, the pK_a of carboxylic acids typically increase 0.75-1 log units.^{75,76} Therefore, the guests should be deprotonated under our conditions. The pK_a of MOPS in a 50% aqueous methanol is 6.77,⁷⁷ thus the pH 7.5 solution is within the buffer range for MOPS.

FcC⁻ undergoes reversible oxidation and reduction in these conditions. Figure 3.3 shows the voltammogram for FcC⁻. The peak separation, ΔE_p , of 70 mV is consistent with observations from previous reports in aqueous solutions.^{32,78} The formal potential of the FcC⁻/FcC couple in the employed electrolytes was estimated from $E_{1/2}$ in the absence of any Ln(III)[15-MC_{Cu(II)}, pheHA-5] and was determined to be 0.337 V vs. Ag/AgCl at 25.0 °C. Upon the addition of Ln(III)[15-MC_{Cu(II)}, pheHA-5]Cl₃ (figure 3.1b), the FcC⁻ wave shifts to more positive potentials with concomitant reduction in peak currents, consistent with complexation of FcC⁻ by Ln(III)[15-MC_{Cu(II)}, pheHA-5]. The positive potential shift results from the MC stabilizing the reduced form of FcC⁻, which is reasonable given that the MC carries a +3 charge, reduced FcC⁻ has a 1⁻ charge, and the oxidized complex FcC is neutral. The decreased peak currents are indicative of slower diffusion of the LnMC-FcC⁻ complex to the electrode surface.

Titration of Ln(III)[15-MC_{Cu(II)}, pheHA-5]Cl₃ with various central metals to 0.6 mM solutions of FcC⁻ were performed. The limited solubility of Ln(III)[15-MC_{Cu(II)}, pheHA-5]Cl₃ allowed the addition of ~10 equivalents of the host. Plots of $E_{1/2}$ vs. MC concentration are shown in figure 3.4. The largest FcC⁻ potential shift is observed with

Dy(III)[15-MC_{Cu(II), pheHA-5}]Cl₃, while titration of the La(III) analog results in a modest shift. The equilibrium between the oxidized and reduced FcC⁻ and the MC is described by a square scheme⁴⁹ (scheme 3.1). K_{red} and K_{ox} represent the association constant for FcC⁻ and FcC, respectively, and $E_f^{0'}$ and $E_c^{0'}$ are the formal potentials of the free and complexed FcC⁻ determined from the voltammetric responses. The change in $E_{1/2}$ with the change in MC concentration can be treated with eq 1.

Examination of this equation reveals that significant potential shifts arise when K_{red} is much larger than K_{ox} . Previous treatments of systems with this behavior operated under the assumption that K_{ox} is negligible.⁴⁸ We felt that this treatment would be an appropriate starting point because the neutral FcC should bind quite weakly to the +3 charged host in comparison to -1 charged FcC⁻. Additionally, ITC studies have revealed association constants of less than 100 M⁻¹ between Ln(III)[15-MC_{Cu(II), pheHA-5}] hosts and the zwitterionic phenylalanine.^{23,24}

Traditional approaches to thermodynamic titrations described by square schemes involve using large excesses of host, and assuming that the concentration of free host in solution is equal to the concentration of host added to solution. However, the limited solubility of L Ln(III)[15-MC_{Cu(II), pheHA-5}]Cl₃ and the high FcC⁻ concentrations required for voltammetry permitted the dissolution of only ~10 equivalents of the MC, making this assumption inappropriate. Therefore, the concentration of free host in solution was solved for explicitly using a previously reported treatment (equation 2).⁴⁸ The change in $E_{1/2}$ with the change in the MC concentration were fit using equations 1 and 2, yielding the association constants shown in table 1. This fitting routine utilized a 1:1 host-guest binding model. While the sequential binding of a second guest to Ln(III)[15-MC_{Cu(II), pheHA-5}] hosts was detected by ITC, this binding strength is very weak ($K_2 = 10\text{-}60\text{ M}^{-1}$). ITC is capable of determining the weak sequential binding of the second guest because it detects complex formation directly by measuring changes in heat. In contrast, the CV assay detects the displacement of the FcC⁻ probe from the host by a competitive guest. Once FcC⁻ is displaced from the host, it can no longer detect the binding of a second guest. Thus the indirect detection of guest binding in the competitive binding assay precludes quantification of the thermodynamics of sequential guest binding. Similarly, the binding of a second guest was not observed in a fluorescence competitive binding assay

or diffusion NMR experiments.²⁵ Furthermore, the high concentration of KCl electrolyte employed in the CV assay could limit guest binding on the hydrophilic face, where chloride has been shown to bind crystallographically.

The CV ferrocene binding titrations were performed for Ln(III)[15-MCCu(II), pheHA-5]Cl₃ metallocavitands, where Ln = La, Nd, Gd, and Dy. The binding constants show stronger association with hosts composed of smaller, more Lewis acidic central metals. A similar trend was previously observed with benzoate.²² La(III)[15-MC_{Cu(II)}, pheHA-5] displays an exceptionally weak association constant of $55 \pm 3 \text{ M}^{-1}$.

Having established the binding affinity of FcC⁻, the development of the competitive binding assay was pursued. A typical competition titration involved the addition of the redox inactive benzoate to a ~10:1 mixture of Ln(III)[15-MC_{Cu(II)}, pheHA-5]Cl₃ and FcC⁻. Addition of the competitive guest displaces FcC⁻ from the host, which increases the concentration of free FcC⁻ in solution and shifts the E_{1/2} back toward the free FcC⁻ value (figure 3.5). The peak currents also return to the free FcC⁻ values. The results of a typical competition titration are shown in figure 3.6, where E_{1/2} is plotted against the redox inactive guest concentration. Nearly complete displacement of the FcC⁻ guest from Dy(III)[15-MC_{Cu(II)}, pheHA-5] was achieved after the addition of 120 equivalents of sodium benzoate under these conditions. Importantly, the addition of benzoate does not alter E⁰_f, indicating that the potential shift is a result of preferential benzoate binding to the host and not merely from changes associated with activity effects or the ionic strength. Additionally, the reversibility of the voltammetric response for FcC⁻, as gauged by ΔE_p, remains constant throughout the competition titration.

A new method for obtaining binding constants based on the competitive displacement of a redox probe was developed. A modified square scheme describes the equilibrium, where the concentration of free Ln(III)[15-MC_{Cu(II)}, pheHA-5] is affected by the competing equilibrium with the redox inactive guest (scheme 3.2). The E_{1/2} is still treated with equation 1, except now the [MC]_f term is solved using equation 3,⁷⁹ where K_{Dred} is the dissociation constant between LnMC and FcC⁻, K_{DG} is the dissociation constant between LnMC and the competitive guest, and [G]₀ is the concentration of the competitive guest added to the solution. The dissociation constant, and not the association constant, is calculated to simplify the fitting equations. An estimate for K_{DG} is obtained

by fitting the competition titration data using equations 1 and 3 in Origin. Binding constants for benzoate to Ln(III)[15-MC_{Cu(II), pheHA-5}] hosts were obtained by the CV competition method and are displayed in table 2. Notably, the values are of a similar magnitude to the previously reported binding constants determined by ITC in aqueous conditions.

The binding constants reported heretofore were calculated under the assumption that K_{ox} is zero. It was necessary to properly assess the veracity of that assumption, as the binding strength of FcC⁻ and FcC have not been determined by an alternative technique. Furthermore, one way $E_{1/2}$ shift behavior does not necessarily indicate a minute K_{ox} value. This is most clearly demonstrated with the case of a cucurbit[7]uril host and a ferrocene derivative guest. The observed $E_{1/2}$ of the ferrocene guest underwent a mere 10 mV shift in the presence of the cucurbit[7]uril. However, ¹H NMR revealed a K_{red} of $3 \times 10^9 \text{ M}^{-1}$ and a similarly large K_{ox} .³⁷ To assess whether K_{ox} is truly negligible with Ln(III)[15-MC_{Cu(II), pheHA-5}] complexes, the interaction between MCs and cobaltocenium carboxylic acid hexafluorophosphate (CocC) was investigated (figure 3.1). CocC is a structural mimic of FcC that is not reduced at the potentials utilized in this study.^{45,80}

The CV competitive binding approach was employed with CocCH·PF₆ as the competitive guest. Modest binding constants of $\sim 100 \text{ M}^{-1}$ were obtained for Gd(III)[15-MC_{Cu(II), pheHA-5}] and Dy(III)[15-MC_{Cu(II), pheHA-5}]. However, the limited solubility of CocC allowed only a small portion of the displacement curve to be generated, so these values have questionable accuracy. However, examination of the potential shift by the guests provides additional information on the CocC binding affinity. Modest shifts in the $E_{1/2}$ of FcC⁻ are observed in the competition titration with CocC, revealing that CocC binds to Ln(III)[15-MC_{Cu(II), pheHA-5}] hosts to a limited extent. A separate competition titration with tetraethylammonium hexafluorophosphate did not shift the $E_{1/2}$, indicating the observed potential shift after addition of CocCH·PF₆ was a result of CocC binding. Comparison with benzoate competition titrations reveals a lesser potential shift with CocC. The $E_{1/2}$ of the $\sim 1:10$ FcC and Dy(III)[15-MC_{Cu(II), pheHA-5}]Cl₃ mixture decreased by 5.5 mV upon adding 11 equivalents of CocC per FcC⁻. A similar 3 mV decrease was observed with La(III)[15-MC_{Cu(II), pheHA-5}]. In contrast, 11 equivalents of benzoate decreased the $E_{1/2}$ 24.5 mV with DyMC (figure 3.3b) and 4.5 mV with LaMC. This

suggests that the binding strength of CocC to Ln(III)[15-MC_{Cu(II), pheHA-5}] is less than benzoate.

Electrospray ionization mass spectrometry (ESI-MS) demonstrated the interaction between Ln(III)[15-MC_{Cu(II), pheHA-5}] and CocC further. Spectra of CocC and Dy(III)[15-MC_{Cu(II), pheHA-5}]Cl₃ or La(III)[15-MC_{Cu(II), pheHA-5}]Cl₃ mixtures revealed low intensity peaks for the Ln(III)[15-MC_{Cu(II), pheHA-5}](CocC) complex. Peaks representing the hydroxide or chloride adducts had comparable or stronger intensity. No peaks were observed with PF₆⁻ bound. In contrast, the spectra of Ln(III)[15-MC_{Cu(II), pheHA-5}]Cl₃ and sodium benzoate mixtures reveal very high intensity peaks for Ln(III)[15-MC_{Cu(II), pheHA-5}](benzoate) complexes, with minute intensity for chloride or hydroxide adducts.

The ESI-MS and electrochemical results with CocC suggest that Ln(III)[15-MC_{Cu(II), pheHA-5}] binds FcC weakly. Also, the association constant for FcC should be smaller than benzoate. Based on these observations, it seems that K₂ is small, but likely not negligible. Therefore, the contribution of K_{ox} was accounted for by solving for K_{red} and K_{ox} simultaneously. Simultaneous fitting of K_{red} and K_{ox} introduces the assumption that the complexation of FcC with the Ln(III)[15-MC_{Cu(II), pheHA-5}] does not appreciably affect the concentration of free LnMC in solution. This is an acceptable assumption given the modest affinity of CocC and that the alternative approach relies on the assumption that K_{ox} is zero. K_{red} and K_{ox} values obtained by simultaneous fitting are displayed in table 1 and the fits are displayed in figure 3.6. Binding constants for benzoate obtained by the competitive CV method were recalculated using the K_{red} and K_{ox} values obtained by simultaneous fitting (table 2).

CVs of FcC⁻ display a decrease in peak height upon titration of Ln(III)[15-MC_{Cu(II), pheHA-5}]Cl₃, a result of slower diffusion of the Ln(III)[15-MC_{Cu(II), pheHA-5}](FcC⁻) complex compared to the free FcC⁻. A previously reported method⁴⁸ was utilized to estimate the apparent diffusion constants for the complex based on the change in the anodic peak height and the K_{red} obtained by simultaneous fitting. These values are listed in table 1. As expected, the values are similar for all lanthanides.

Crystal structures of host-guest complexes were obtained to provide insight guest recognition by Ln(III)[15-MC_{Cu(II), pheHA-5}] metallocavitands. The crystal structure of La(III)[15-MC_{Cu(II), pheHA-5}] with FcC⁻ is shown in figure 3.7. Two FcC⁻ guests are

included in the host's hydrophobic cavity. The bound guests engage in π -stacking interactions with the ligand phenyl rings. The La(III) central metal is nine-coordinate, with bound water molecules on both the hydrophilic and hydrophobic faces filling the remaining coordination sites. Charge balance is achieved with a nitrate coordinated to a Cu(II) ring metal on the hydrophilic face.

The crystal structure of ferrocene dicarboxylate (FcDC^{2-}) bound to $\text{La(III)[15-MC}_{\text{Cu(II), pheHA-5}]}$ is displayed in figure 3.8. The $\text{Gd(III)[15-MC}_{\text{Cu(II), pheHA-5}]}(\text{FcDC}^{2-})$ complex is isostructural. FcDC^{2-} bridges the hydrophilic faces through bidentate coordination to the central metal. FcDC^{2-} is in an anticlinal conformation with a twist angle of 131.3° . FcDC^{2-} also bridges the hydrophobic faces, binding to both the central metal and a Cu(II) ring metal. Thus infinite chains of FcDC^{2-} bridged compartments are observed. The La(III)-La(III) distance is 11.14 \AA , a distance consistent with the compartment size typically observed with $\text{Ln(III)[15-MC}_{\text{Cu(II), pheHA-5}]}$.^{18,81} The encapsulated FcDC^{2-} has a twist angle of 131.7° . This rotation is likely enforced by to maintain a compartment height where π -stacking interactions between the ligand side chains of opposite $\text{Ln(III)[15-MC}_{\text{Cu(II), pheHA-5}]}$ can be maintained. π -stacking interactions between the encapsulated FcDC^{2-} and the ligand side chains are observed, which likely drive the encapsulation of the guest in the compartment.

The crystal structure of benzoate bound to $\text{Dy(III)[15-MC}_{\text{Cu(II), pheHA-5}]}$ is shown in figure 3.9. Benzoate is bound bidentate to an eight coordinate Dy(III) on the hydrophobic face. Guest-ligand π -stacking interactions are again observed in the hydrophobic pocket. On the hydrophilic face, benzoate is bound monodentate to the central metal, and is engaged in a hydrogen bond through the unbound carboxylate to a water coordinated to a copper ring metal. In contrast, the structure reported with an eight coordinate Eu^{III} central metal had benzoate bound monodentate to a copper ring metal^{82, 25}, with the unbound carboxylate hydrogen bonded with a water on the central metal.

Having heretofore successfully developed the CV competitive binding assay, the technique was utilized to explore fundamental aspects of Ln(III)[15-MC-5] guest recognition. First, enantioselective guest binding was assessed with a series of α -amino acid analog guests (figure 3.1). Thermodynamic investigations on these guests allow for preliminary assessment of how factors such as charge, hydrophilicity, and sterics

influence guest binding. These guests possess structural features that contribute to guest binding in Ln(III)[15-MC_{Cu(II)}, L-pheHA-5] hosts, namely a phenyl ring which engages in associative hydrophobic interactions with the pheHA side chains and a carboxylate which preferentially binds to the central lanthanide ion. Second, the effect of side chain substitutions on guest affinity and enantioselectivity was examined with Gd(III)[15-MC_{Cu(II)}-5] complexes bearing L-phenylglycine hydroxamic acid (pgHA), pheHA, L-homophenylalanine hydroxamic acid (hpheHA), and picoline hydroxamic acid (picHA) ligands (figure 3.1). Comparison of guest affinity between MCs with these ligand side chains provides insight on how cavity size and side chain flexibility contributes to guest recognition.

Selective Binding of α -Amino Acid Analogs

Enantioselective guest binding in Ln(III)[15-MC-5] hosts has relevance to the development of the metallocavitand in chiral separations or catalysis. Importantly, the Ln(III)[15-MC-5] topology is significantly different than other chiral compounds in the literature, so it is reasonable to expect novel enantioselectivity from these complexes. Furthermore, chiral selectivity with anionic substrates is generally more challenging than for neutral or cationic substrates. Dr. Choong-Sun Lim performed initial investigations on the chiral selectivity of Ln(III)[15-MC-5] metallocavitands using phenylalanine enantiomers as the guests.^{23,24} Crystal structures of Gd(III)[15-MC_{Cu(II)}, pheHA-5] with phenylalanine Dr. Lim obtained show differential binding of S- and R-phenylalanine (figure 3.11). The structures show the phenylalanine guests bound through a single carboxylate oxygen atom to Gd(III) (figure 3.2a). Two additional unbound nitrates balance the +3 charge of the Gd(III)[15-MC_{Cu(II)}, pheHA-5], demonstrating that S- and R-phenylalanine are bound as zwitterions. The structures differ in the orientation of the ammonium functional group on phenylalanine. For the S-isomer, the ammonium points towards the MC face, associating with a weak hydrogen bond to two ring oxygen atoms (N-O distances = 3.15 Å, 3.30 Å) and a hydroximate nitrogen (N-N distance = 3.2 Å). In the R-phenylalanine structure, the ammonium points away from the MC face.

The solid state structures suggest that S- and R- enantiomers of α -amino acid analogs would be discriminated by Ln(III)[15-MC-5] based on how the substituent at the α -carbon interacts with the MC ring. Dr. Lim also measured the binding affinity of S-

and R-phenylalanine to Gd(III)[15-MC_{Cu(II), pheHA-5}] using ITC. ITC titrations reveal that both enantiomers of phenylalanine bind modestly to Gd(III)[15-MC_{Cu(II), pheHA-5}] with binding constants less than 100 M⁻¹ (table 3). A modest, though significant, thermodynamic preference for S-phenylalanine was observed with the Gd(III)[15-MC_{Cu(II), pheHA-5}]Cl₃ host.

Encouraged by the enantioselectivity displayed with phenylalanine, enantioselective binding of a series of α -amino acid analogs was investigated by Peng Zhao, an undergraduate researcher, and I. We performed an equal number of the titrations and I performed the data interpretation. It was hypothesized that enhanced enantioselectivity could be observed by changing the substituents at the α -carbon. The reasoning was that the weak selectivity was due in part to the weak recognition of the zwitterionic guest. Therefore removing the ammonium would lead to enhanced guest affinity and stronger discrimination of enantiomers. These measurements were performed with CV using the competitive binding assay.⁸³ Measurements were performed under the identical conditions as above, pH of 7.5 in a 0.1 M KCl solution containing 50% methanol, 50% aqueous MOPS solution (v/v). The electrochemical response of FcC⁻ was the same as was observed in the benzoate competition titrations. The CV data were adequately fit with a 1:1 binding model, where the guest is presumed to bind in the hydrophobic cavity.

The association constants between Gd(III)[15-MC_{Cu(II), pheHA-5}]Cl₃ and enantiomers of α -amino acid analogs are shown in table 2. N-acetyl-phenylalanine and methoxyphenylacetate display modest K_a values of approximately 100 M⁻¹ with Gd(III)[15-MC_{Cu(II), pheHA-5}]. In contrast, phenyllactate and mandelate bind much more strongly, with K_a values of over 2000 M⁻¹. Gd(III)[15-MC_{Cu(II), pheHA-5}] only shows statistically significant enantioselectivity towards mandelate, with a 22% preference for the S-enantiomer. The binding strength of phenylalanine could not be measured by the CV competitive binding assay because the guest interacted with FcC⁻, perturbing the potential and reversibility of the redox probe.

Side Chain Dependent Guest Affinity and Selectivity

The appreciable guest affinity and modest enantioselectivity observed with Gd(III)[15-MC_{Cu(II), pheHA-5}] encouraged investigations of the effect of side chain

substitution. The hypothesis was that different side-chain substitutions would interact differently with guest molecules, potentially leading to enhanced guest affinity and selectivity. These experiments were performed with Joseph Grant, an undergraduate researcher. Joseph Grant optimized the pgHA and hpheHA synthesis, performed the majority of the data collection and workup, and contributed to writing the manuscript reporting these results. My contribution was in devising the synthetic methodology and CV experimental setup, data interpretation, performing some titrations, and writing the manuscript.

The effect of the side chain on the topology of the hydrophobic cavity is best depicted by examining crystal structures the metallocavitands. Figure 3.13 contains images that highlight the hydrophobic faces of Gd(III)[15-MC_{Cu(II)}-5] with picHA, pgHA, pheHA, and hpheHA. These representations were generated from structures previously reported structures by removing all bound anions and solvents. The planar Gd(III)[15-MC_{Cu(II)}, picHA-5]⁸⁴ (figure 3.13a) is characterized by two hydrophilic faces and no hydrophobic cavity. Examination of Gd(III)[15-MC_{Cu(II)}-5] complexes with pgHA,⁸¹ pheHA,¹⁸ and hpheHA⁸¹ reveals a hydrophobic cavity generated by the phenyl side chains. pgHA is short, rigid and extends toward the periphery of the MC face, generating a cavity with a modest ~4.6 Å depth. The pheHA side chains are slightly longer (cavity depth is ~ 6.0 Å). Of note, the methylene carbon can orient the pheHA side chain toward the center of the MC where the guests bind preferentially. With a depth of ~7.4 Å, Gd(III)[15-MC_{Cu(II)}, hpheHA-5] exhibits the largest hydrophobic cavity. Such a larger cavity should contribute to greater guest affinity through more extensive associative hydrophobic interactions. The images in figure 3.13 are from crystal structures, therefore the orientation of the side chains are strongly influenced by interactions with proximal MCs in the lattice. It should be noted that the hydrophobic cavities could adopt conformations that differ from these structures in the liquid state. Given the strength of hydrophobic interactions in aqueous solutions however, it is likely that the side chains preferentially associate into hydrophobic cavities.

A crystal structure of FeC⁻ bound to La(III)[15-MC_{Cu(II)}, hpheHA-5] was obtained by the slow evaporation of an ethanol, acetonitrile, water solution (figure 3.14). The structure contains two different monomeric metallocavitands with 9-coordinate La(III)

central metals resting on the hydrophobic face of the MC. In one La(III)[15-MC_{Cu(II)},_{hpheHA}-5], two FcC⁻ anions are encapsulated in the hydrophobic cavity. One FcC⁻ is bidentate to the La(III) ion while the other bridges the La(III) and a Cu(II) ring metal. These FcC⁻ anions are oriented with the ferrocene moiety extended out of the hydrophobic cavity. In the other monomer, one FcC⁻ and one nitrate anion are encapsulated in the hydrophobic cavity. The nitrate is bound bidentate to La(III) while the FcC⁻ bridges the La(III) ion and a Cu(II) ring metal. Extensive π -stacking interactions are observed between the FcC⁻ guests and hpheHA side chains. Unbound FcC⁻ ions observed in the lattice contribute to charge balance. The MCs have water molecules bound on the hydrophilic faces.

Thermodynamic measurements assessing the effect of the Gd(III)[15-MC_{Cu(II)}-5] side chain on guest binding affinity were performed with CV. Previous CV titrations were performed in 50% aqueous methanol conditions.^{63,81} Due to the different solubilities of Gd(III)[15-MC_{Cu(II)}-5]Cl₃ with pgHA and hpheHA side chains, different solution conditions were required. Measurements were performed at a ξ pH of 8.5 in a 0.1 M sodium triflate solution containing 60 % acetonitrile, 40% 100 mM aqueous EPPS (v/v). These conditions were chosen to ensure that FcC⁻ is fully deprotonated⁶⁹ and displays a fully reversible redox wave throughout the titrations, as indicated by the ΔE_p and the ratio of the anodic and cathodic peak currents. The MC and guests are stable and highly soluble in these conditions. The reference electrode was carefully prepared and tested to ensure a stable potential through the course of the experiments. An Ag/Ag⁺ reference electrode with a liquid junction salt bridge, both containing 0.1 M sodium triflate in 60% acetonitrile, 40 % water (v/v), provided the necessary stable potential. Control experiments demonstrate that the $E_{1/2}$ of free FcC⁻ is not affected by the presence of the competitive guest in the absence of an MC, sodium chloride, or by changes in the ionic strength. Furthermore, the addition of excess sodium chloride or sodium triflate do not perturb the observed $E_{1/2}$ in the presence of the MC, suggesting that the presence of these electrolytes do not interfere with guest binding. These controls demonstrate that observed changes in $E_{1/2}$ result entirely from binding interactions of FcC⁻ and the competitive guests with the Gd(III)[15-MC_{Cu(II)}-5] metallocavitand.

In these 40% aqueous acetonitrile conditions, the $E_{1/2}$ of FcC^- undergoes a positive potential shift in the presence of the $\text{Gd(III)[15-MC}_{\text{Cu(II)-5}}\text{]Cl}_3$ (figure 3.15). Association constants between the $\text{Gd(III)[15-MC}_{\text{Cu(II)-5}}\text{]}$ host and FcC^- determined from the MC binding CV titrations (figure 3.16) are listed in table 5. $\text{Gd(III)[15-MC}_{\text{Cu(II), pheHA-5}}\text{]}$ shows a K_a of $4400 \pm 700 \text{ M}^{-1}$ with FcC^- . This is much larger than the value of $1040 \pm 100 \text{ M}^{-1}$ determined in 50% aqueous methanol (*vide supra*). This disparity is attributed to acetonitrile being more polar than methanol, which would to stronger hydrophobic interactions between FcC^- and the hydrophobic cavity on $\text{Gd(III)[15-MC}_{\text{Cu(II), pheHA-5}}\text{]}$. Also, acetonitrile is not a hydrogen bond donor and is a poor ligand, therefore, the carboxylate group on the guest and the metal ions on the ligand are poorly solvated in the acetonitrile solution compared to the methanolic conditions.

The effect of side chain substitution is evident in comparisons of the binding affinities of FcC^- . $\text{Gd(III)[15-MC}_{\text{Cu(II)-5}}\text{]}$ with pgHA and pheHA have the same affinity for FcC^- within error. However, $\text{Gd(III)[15-MC}_{\text{Cu(II), hpheHA-5}}\text{]}$ shows a much greater affinity for FcC^- ($K_a = 12100 \pm 700 \text{ M}^{-1}$), corresponding to a 0.5 kcal/mol enhancement with the longer side chain. T-test analysis confirms a statistically significant difference in the binding strengths between $\text{Gd(III)[15-MC}_{\text{Cu(II), pheHA-5}}\text{]}$ and $\text{Gd(III)[15-MC}_{\text{Cu(II), hpheHA-5}}\text{]}$ (p-value of 0.0005). These MC binding titrations also provide data on the affinity of the oxidized FcC to the host. The binding strength of FcC is weak for hosts with all side-chains relative to the binding of reduced FcC^- , which is reasonable given that the guest is a neutral zwitterion.

Quantitative data was sought on the separate contributions of the cavity and metal ions to guest recognition. It was hoped that comparison of the guest affinity of $\text{Gd(III)[15-MC}_{\text{Cu(II)-5}}\text{]}$ hosts with and without a cavity would provide this information. While the ideal comparison would be to $\text{Gd(III)[15-MC}_{\text{Cu(II)-5}}\text{]}$ with glycine hydroxamic acid or alanine hydroxamic acid ligands, the limited solubility of these MCs in the CV solution prevented the study of these complexes. To overcome solubility limitations, $\text{Gd(III)[15-MC}_{\text{Cu(II), picHA-5}}\text{]}(\text{NO}_3)$ was examined. Though picHA is notably different than the α -amino hydroxamate ligands from the standpoints of electronics and supramolecular topology, the comparison could still be informative. As nitrate salts were necessary for solubility, the binding of FcC^- to $\text{Gd(III)[15-MC}_{\text{Cu(II), pheHA-5}}\text{]}(\text{NO}_3)$ was performed to

assess potential counterion effects. The binding strength to $\text{Gd(III)[15-MC}_{\text{Cu(II), pheHA-5}]}$ with Cl^- and NO_3^- counterions is the same within error (table 5), suggesting that counterion effects are minimal. $\text{Gd(III)[15-MC}_{\text{Cu(II), picHA-5}]}(\text{NO}_3)$ shows a relatively modest binding affinity for FcC^- , with a K_a value of $1900 \pm 100 \text{ M}^{-1}$. This is significantly lower than the value of $4800 \pm 700 \text{ M}^{-1}$ observed with $\text{Gd(III)[15-MC}_{\text{Cu(II), pheHA-5}]}(\text{NO}_3)$.

To expand on these observations with FcC^- and to assess how the side-chain influences enantioselectivity, competitive guest binding titrations were performed to monitor the binding of redox inactive guests. Titration of the redox inactive guest molecule to a mixture of the MC and FcC^- displaces the redox probe, resulting in a negative shift in $E_{1/2}$ back to the value for the free FcC^- . Representative CVs from such titrations can be found in figure 3.17 and titration data is shown in figure 3.18. The binding of benzoate, the prototypical hydrophobic carboxylate, was examined with this competitive binding assay. The results largely parallel the trends observed with FcC^- , suggesting larger cavities lead to greater binding affinities. $\text{Gd(III)[15-MC}_{\text{Cu(II), pgHA-5}]}$ and $\text{Gd(III)[15-MC}_{\text{Cu(II), pheHA-5}]}$ show K_a values of about 800 ± 100 and $1300 \pm 200 \text{ M}^{-1}$, respectively, a statistically significant difference. The binding affinity between $\text{Gd(III)[15-MC}_{\text{Cu(II), hpheHA-5}]}$ and benzoate is again much larger than the other MCs, with a K_a value of $3000 \pm 300 \text{ M}^{-1}$. Competition titrations with $\text{Gd(III)[15-MC}_{\text{Cu(II), picHA-5}]}(\text{NO}_3)$ could not be modeled using the curve fitting routines available to the CV competition assay.

Due to the modest enantioselectivity observed in the aqueous methanol conditions, enantioselective guest binding to MCs with different side chains was assessed with enantiomers of mandelate. The association constants of both S- and R-mandelate between each MC can be found in table 6. A statistically significant preference for the S-mandelate is observed with $\text{Gd(III)[15-MC}_{\text{Cu(II), pgHA-5}]}$ and $\text{Gd(III)[15-MC}_{\text{Cu(II), hpheHA-5}]}$ ($K_S/K_R = 2.2 \pm 0.7$ and 1.5 ± 0.2 respectively, table 7). This enantioselectivity is greater than the modest K_S/K_R observed in aqueous methanol (*vide supra*).^{23 [23]} Enantioselectivity was not observed with $\text{Gd(III)[15-MC}_{\text{Cu(II), pheHA-5}]}$ in these conditions.

Discussion

Establishing the Voltammetric Assay

Prospects of utilizing Ln(III)[15-MC-5] complexes in separations or catalysis have motivated investigations into the guest recognition behavior of the metallocavitand in solution. Preliminary reports demonstrated that Ln(III)[15-MC_{Cu(II), pheHA}-5] hosts selectively bind carboxylate guests with association constants on the order of 10^2 - 10^4 . Trends in the binding affinity suggest that guests bind preferentially to the central lanthanide in the hydrophobic cavity, consistent with crystallographic observations. Modest enantioselectivity was also observed with phenylalanine enantiomers. Further information was sought on how guest binding affinity is influenced by functional groups on the guest and on substitution of the side chain. Importantly, side chain substitutions provide a potential route to improving the enantioselectivity seen with phenylalanine enantiomers. In order to perform these fundamental studies on Ln(III)[15-MC-5] guest recognition, a viable technique was needed.

Voltammetric methods have been integral in the study of molecular inclusion phenomena. Pioneering reports by Peter et al.,^{42,43} Matsue et al.,³² and the Kaifer group²⁶ have firmly established voltammetry as a viable analytical method for host-guest chemistry. CV has been effective quantifying host-guest interactions when redox active hosts or guests are employed. However, the quantitative study of redox inactive guest binding to redox inactive hosts using electrochemical methods was less well developed. This was unfortunate as CV is an accessible technique amenable to paramagnetic systems. It's been realized that competition based experiments with a redox probe could be used to determine the binding strength of redox inactive substrates with CV.^{42,51} Certain electrochemical competitive binding techniques have been established, though they are not especially accessible or general as they require modified electrodes,⁵⁶⁻⁵⁹ hosts with tethered redox active functionalities,⁶⁰⁻⁶² or protonation equilibria associated with guest binding.⁵²⁻⁵⁵ The binding assay developed in this chapter uses standard electrodes, is entirely homogeneous, and does not require a chemically modified host. It can be applied to any host with a redox active guest that exhibits one-way shift behavior. In developing the assay, Wang's mathematical expression⁷⁹ has been applied to relate the binding constant of the redox-inactive guest to the potential shift of the redox probe. Notably, the only previous knowledge this method requires is the binding constant of the redox active guest, which can be determined electrochemically. Thus, the assay allows

for the quantitative study of host-guest complexation using CV exclusively, which makes it highly accessible. The viability of this novel assay was assessed using Ln(III)[15-MC_{Cu(II), pheHA-5}] hosts and benzoate as a guest, which has been studied previously by two groups.^{22,25}

Before performing the competition experiments, the binding affinity of the FcC⁻ redox probe had to be measured. The measurement was performed electrochemically utilizing established methodology.⁴⁸ This methodology relied on the assumption that the binding of the oxidized moiety, FcC, was zero. The veracity of that assumption was assessed by monitoring the affinity of CocC, which is a suitable structural mimic of FcC. CV competition titrations and ESI-MS revealed the CocC binds to Ln(III)[15-MC_{Cu(II), pheHA-5}] hosts with an affinity that is less than benzoate. Therefore, the assumption that K_{ox} is zero is not appropriate for Ln(III)[15-MC_{Cu(II), pheHA-5}] hosts system and K_{red} and K_{ox} were fit simultaneously.

A 1:1 binding model was employed to fit the MC binding titration data. This is justifiable given the reasonable excess of Ln(III)[15-MC_{Cu(II), pheHA-5}] hosts used in the MC binding titrations. Also previous studies with fluorescence spectroscopy, UV-visible spectroscopy, and diffusion NMR spectroscopy did not detect the binding of a second guest.²⁵ ITC detected modest sequential guest binding, with association constants of less than 60 M⁻¹ for the second guest.²² The voltammetric titration data was adequately fit with the 1:1 binding model. The binding constants for FcC⁻ (Table 1) show greater affinity with Ln(III)[15-MC_{Cu(II), pheHA-5}] hosts bearing more Lewis-acidic central metals. This is consistent with the previous ITC experiments and crystallography (figure 3.7 and 9).²² While other coordination modes have been observed in the solid state, such as with the La(III)[15-MC_{Cu(II), pheHA-5}](FcDC²⁻) structure (figure 3.8), these are less common and are often attributed to packing effects.

Having determined the binding constants for FcC⁻, the CV competitive binding assay was used to quantify the binding of benzoate. Association constants measured with this technique closely match the reported values.²² The differences in the conditions between the various techniques should be noted, especially given the high electrolyte concentration and different methanolic solvent employed in the electrochemical measurements. Nevertheless, the similar values support the viability of the competition

technique. Considering the variety of functional groups that can be appended to redox active moieties such as ferrocene, the CV competition approach could be readily generalized to many host systems provided certain conditions are met. First, a detectable dependence of $E_{1/2}$ with concentration of the host is required for this method. This condition is satisfied in systems with disparate affinities for the reduced and oxidized probe. Similarly, competitive binding of the redox-inactive guest must be sufficiently strong to compete with the binding of the redox active guest. This condition is met if the concentration of the redox-inactive competing guest is high and/or its affinity constant with the host is comparable to the affinity constant for the redox probe-host. We estimate that guests with binding strengths within two orders of magnitude of the probe can be measured with this technique. Greater precision could likely be achieved through judicious selection of the conditions and redox probe, and by using a more accurate method for measuring $E_{1/2}$. Lastly, since the assay is a competitive binding technique, sequential guest binding cannot be adequately measured as the probe does not report on guest binding once it is displaced from the host. If these conditions are achievable, the quantitative accuracy of the method is acceptable.

It is worth assessing the binding constants between $\text{Ln(III)[15-MC}_{\text{Cu(II), pheHA-5}}]$ and FcC^- . Though the binding constants follow the expected trend in the Lewis acidity of the central metal, the value for $\text{La(III)[15-MC}_{\text{Cu(II), pheHA-5}}]$ seems exceptionally low. This value is surprising given that ITC determined that the association constant for benzoate to $\text{Dy(III)[15-MC}_{\text{Cu(II), pheHA-5}}]$ is twice the value observed with the La(III) analog.²² A 20-fold difference in the association constants was determined with CV. The primary differences between La(III) and Dy(III) are the increased Lewis-acidity and smaller ionic radius of Dy(III) . While stronger binding is expected with the more acidic metal, electrostatics alone cannot account for the disparity between benzoate and FcC^- . The most significant factor, therefore, is the size of the metal. The larger La(III) is typically nine-coordinate, as is seen for the $\text{La(III)[15-MC}_{\text{Cu(II), pheHA-5}}](\text{FcC}^-)$ complex (figure 3.7), while Dy(III) is typically eight-coordinate, as observed in the $\text{Dy(III)[15-MC}_{\text{Cu(II), pheHA-5}}](\text{benzoate})$ structure (figure 3.9). Such weak FcC^- binding by $\text{La(III)[15-MC}_{\text{Cu(II), pheHA-5}}]$ indicates poor guest recognition when bound to the nine-coordinate metal. Crystal structures of $\text{Ln(III)[15-MC}_{\text{Cu(II), pheHA-5}}]$ hosts with ferrocene carboxylate guests

are especially helpful in revealing the effects of the central metal coordination number. With FcC^- bound to the nine-coordinate lanthanum in the $\text{La(III)[15-MC}_{\text{Cu(II), pheHA-5}}\text{](FcC}^-)$ complex (figure 3.7), the guest is positioned with the hydrophobic ferrocene group extending out of the hydrophobic cavity. This orientation results in minimal hydrophobic contacts with the ligand side chains and poor encapsulation. Such poor guest recognition by the MC with a nine-coordinate metal is reflected in the small binding constant.

Unfortunately, X-ray quality crystals of FcC^- bound to an 8-coordinate $\text{Ln(III)[15-MC}_{\text{Cu(II), pheHA-5}}\text{]}$ could not be obtained. However, a structure of $\text{La(III)[15-MC}_{\text{Cu(II), pheHA-5}}\text{](FcDC}^{2-})$ is illustrative of how FcC^- is bound by an eight-coordinate central metal. Figure 3.10 shows the hydrophobic face of the host and part of the encapsulated FcDC^{2-} guest from the $\text{La(III)[15-MC}_{\text{Cu(II), pheHA-5}}\text{](FcDC}^{2-})$ structure to demonstrate how FcC^- would be positioned in the cavity when bound to an eight-coordinate central metal. The FcDC^{2-} on the hydrophilic face, the second LaMC in the compartment, and the carboxylate group at the 1' position are removed for clarity. In figure 3.10, the carboxylate group on FcDC^{2-} is positioned perpendicular to the MC plane on the hydrophobic face. The perpendicular arrangement of the carboxylate orients the ferrocene group roughly parallel to the MC plane. With this coordination mode, the hydrophobic ferrocene group is held within the hydrophobic cavity, where π -stacking interactions and the hydrophobic effect would significantly contribute to the binding strength. With a bidentate carboxylate, the perpendicular binding can only occur with an 8-coordinate metal. With the nine-coordinate metal, the ferrocene group extends out of the cavity, so binding is weaker.

Such a large difference in the association constants between $\text{La(III)[15-MC}_{\text{Cu(II), pheHA-5}}\text{]}$ or $\text{Dy(III)[15-MC}_{\text{Cu(II), pheHA-5}}\text{]}$ and benzoate was not observed because benzoate has a different hydrophobic topology. The phenyl ring on benzoate is reasonably well encapsulated by the hydrophobic cavity when bound perpendicular to the MC plane with an eight-coordinate metal (figure 3.8). Presumably, the phenyl ring would also be sufficiently included in the cavity when bound at a more acute angle with a 9-coordinate metal. Due to the protruding cyclopentadienyl ring on FcC^- , the extent that the guest is encapsulated in the hydrophobic cavity is highly dependent on how the carboxylate is

oriented relative to the MC plane. Therefore, a more significant difference in binding strength is observed between eight- and nine-coordinate metals with FcC^- . Notably, this demonstrates that significant selectivity can be realized through considerations of the central metal.

Selective Binding of α -Amino Acid Analogs

The CV competitive binding assay has been shown to be a viable method for measuring guest binding affinities to supramolecular hosts. The assay has been utilized to assess how the guest affinity is influenced by guest chirality, functional groups, and the ligand side chain on the host. Previously, $\text{Gd(III)[15-MC}_{\text{Cu(II)}, \text{L-pheHA-5}}$ hosts were shown to differentially bind enantiomers of phenylalanine in the solid state and in solution, with a modest K_S/K_R of 1.6.^{23,24} The crystal structures of $\text{Gd(III)[15-MC}_{\text{Cu(II)}, \text{L-pheHA-5}}$ with S- and R-phenylalanine showed the ammonium group on S-phenylalanine engages in hydrogen bonding interactions with heteroatoms in the MC ring, while the R-enantiomer does not display these interactions. One reason for the modest enantioselectivity observed with phenylalanine enantiomers could be the weak binding strength. Any preference for a particular enantiomer could be tempered by the weak interaction with $\text{Gd(III)[15-MC}_{\text{Cu(II)}, \text{pheHA-5}}$. The weak binding of phenylalanine is partially attributed to its zwitterionic charge state at neutral pH. Thus, to explore enantioselective guest binding further, the inclusion of amino acid analogs substituted at the ammonium group were examined.

Despite their -1 charge, N-acetyl-phenylalanine and methoxyphenylacetate bind quite weakly to $\text{Gd(III)[15-MC}_{\text{Cu(II)}, \text{pheHA-5}}$, with association constants of approximately 10^2 M^{-1} . Unfortunately, no discrimination is observed based on the chirality of these guests, as no statistically significant selectivity is observed at the 5% confidence level (Table 4). Strong binding is observed with phenyllactate. The association constants for S- and R-phenyllactate are 2070 and 2140 M^{-1} , respectively. Again, no enantioselectivity is observed, suggesting the modest chiral discrimination does not arise from the weak binding strength exclusively.

Interestingly, the association constant between S-mandelate and $\text{Gd(III)[15-MC}_{\text{Cu(II)}, \text{pheHA-5}}$ is 22% greater than with R-mandelate. This enantioselectivity cannot be attributed to how the guest is coordinated to the MC face because the enantiomers of

phenyllactate would be expected to bind in the same way. Instead, the chiral recognition likely arises from how the hydrophobic cavity recognizes the alkyl substituent on the guest. Phenyllactate has a phenyl chain while mandelate has a benzyl chain. Likely the aromatic ring on R-mandelate has a mild steric clash with a phenyl side chain on Gd(III)[15-MC_{Cu(II), pheHA-5}], resulting in weaker binding relative to S-mandelate.

The association constants of the α -amino acid analogues with the hydrophobic cavity on Gd(III)[15-MC_{Cu(II), pheHA-5}] allows for comparison of how different guest functionalities impact binding strength. Phenylalanine, N-acetyl-phenylalanine, and phenyllactate are analogs of hydrocinnamate, while mandelate and methoxyphenylacetate are analogs of phenylacetate. The association constants of hydrocinnamate and phenylacetate with Gd(III)[15-MC_{Cu(II), pheHA-5}]Cl₃ were previously measured by ITC in an aqueous pH 7.6 solution at 298 K.²² Despite the different conditions, association constants for hydrocinnamate and phenylacetate determined by the CV competitive binding assay reproduced the corresponding ITC values adequately for K_{a1} , which is attributed to guest binding in the hydrophobic cavity. A similar correlation in the association constants for benzoate determined by the ITC and CV techniques was observed (*vide supra*). Given this empirical correlation between the ITC and CV measurements, approximate comparisons of binding affinities determined with the different techniques are acceptable for guests with disparate association constants. Based on the structure of the Ln(III)[15-MC_{Cu(II), pheHA-5}] hydrophobic cavity, one would expect that the introduction of hydrophilic functionalities on encapsulated guests could influence guest binding in two ways. First, guest binding could be weaker due to steric constraints or the enthalpic penalty of including a hydrophilic residue in a hydrophobic pocket. Secondly, guest affinity could increase due to favorable interactions between the hydrophilic MC face and the guest's hydrophilic functional groups. The affinity of guests with different functional groups can therefore be used to gauge how the metal ions or hydrophobic cavity contribute to guest binding in metallocavitands.

The K_{a1} value determined by ITC between Gd(III)[15-MC_{Cu(II), pheHA-5}] and hydrocinnamate at 298 K is 370 M⁻¹.²² Association constants between Gd(III)[15-MC_{Cu(II), pheHA-5}] and phenylalanine at 298 K are calculated to be 77 M⁻¹ and 64 M⁻¹ for the S- and R-enantiomers respectively.²³ The lower affinity can be attributed in part to the

guest's zwitterionic charge state, though unfavorable interactions between the ammonium group and the hydrophobic cavity likely contribute as well. Considering N-acetyl-phenylalanine, it is evident that the acetyl functionality similarly decreases K_a relative to the unsubstituted analog, hydrocinnamate. Presumably steric factors and unfavorable interactions between the hydrophilic acetyl group with the hydrophobic cavity cause this weak binding affinity.

In contrast, the interaction between the hydroxy-substituted guest phenyllactate and $\text{Gd(III)[15-MC}_{\text{Cu(II), pheHA-5}}$ is much stronger than that observed with hydrocinnamate. Hydroxy-substituted mandelate also has a strong interaction with $\text{Gd(III)[15-MC}_{\text{Cu(II), pheHA-5}}$ when compared to its unsubstituted analog, phenylacetate. This implicates a strong associative interaction between the hydroxyl group on the α -carbon and the MC face. Crystal structures of carboxylates bound to $\text{Gd(III)[15-MC}_{\text{Cu(II), pheHA-5}}$ almost always show the carboxylate bound bidentate to Gd(III) (figure 3.2b). This coordination mode orients the substituents on the α -carbon away from the MC face. The strong binding enhancement observed with the hydroxy-group suggests the guests adopt a bridging mode between a carboxylate oxygen atom and the oxygen off of the α -carbon, forming a five-membered chelate ring (figure 3.2d). Considering the magnitude of the binding constants, the hydroxyl-groups likely undergo a metal-assisted deprotonation in the hydrophobic cavity, resulting in the guests being bound as a dianion. Unfortunately, crystal structures of phenyllactate or mandelate bound to $\text{Gd(III)[15-MC}_{\text{Cu(II), pheHA-5}}$ could not be obtained to confirm this conclusion. However, this binding mode was observed between phenyllactate and $\text{La(III)[15-MC}_{\text{Cu(II), pheHA-5}}$.²⁴ Interestingly, the reported binding constant of $12,800 \pm 300 \text{ M}^{-1}$ for coumarin 343 to $\text{Eu}^{3+}[\text{15-MC}_{\text{Cu(II), L-pheHA-5}}$ is also much greater than the values typically observed for simple carboxylates.²⁵ While coumarin 343 has significant structural differences with phenyllactate and mandelate and the solution conditions are different between the measurements, the guests can all form chelate rings with a Ln(III) central metal through a carboxylate oxygen and another donor oxygen possessing significant electron density. On coumarin 343, this oxygen comes from a carbonyl and not the alkoxide seen with phenyllactate and mandelate, though resonance could place significant electron density at the carbonyl oxygen and enhance binding. Thus, self-consistent binding constants on the

order of 10^3 - 10^4 have been observed for hydrophobic guests that coordinate through two formally negatively charged oxygen atoms to a Ln(III)[15-MC_{Cu(II)}, L-pheHA-5] host.

Metal-assisted deprotonation of phenyllactate and mandelate is further supported by the weak binding of methoxyphenylacetate. Replacing the alcohol group on mandelate with the methoxy group decreases the association constant with Gd(III)[15-MC_{Cu(II)}, pheHA-5] more than twenty-fold. While the ether is sterically bulkier than the alcohol and is a weaker electron donor, these differences are not likely to account for the 20 times smaller K_a . The difference in charge between the -2 charged mandelate and the -1 charged methoxyphenylacetate better accounts for the discrepancy. Methoxyphenylacetate also displays a smaller association constant with Gd(III)[15-MC_{Cu(II)}, pheHA-5] than phenylacetate, further demonstrating that neutral hydrophilic groups on the α -carbon decrease the binding affinity of carboxylate guests. If the association constants of benzoate ($690 \pm 120 \text{ M}^{-1}$), FcC⁻ ($1040 \pm 100 \text{ M}^{-1}$), and FcC ($100 \pm 30 \text{ M}^{-1}$) with Gd(III)[15-MC_{Cu(II)}, pheHA-5] are also considered,⁶³ a trend in guest binding strength emerges. Simple -1 charged carboxylates possess association constants on the order of 10^2 - 10^3 M^{-1} . Association constants of 10^1 to 10^2 M^{-1} are observed for zwitterionic carboxylates and values of 10^3 - 10^4 have been measured for carboxylates substituted with a highly electron rich donor oxygen at the α - or β -carbon.

Side Chain Dependent Guest Affinity and Selectivity

Side-chain variation can potentially provide a facile route to preparing highly selective Ln³⁺[15-MC-5] hosts given their general synthesis through self-assembly reactions. Solid-state studies have implicated the side-chain as an important factor in guest recognition, as the length and flexibility of the phenyl side-chain influence the cavity size and the extent that the host can converge on a bound guest (chapter 2). The data presented herein on the thermodynamics of carboxylate binding to Gd(III)[15-MC_{Cu(II)}-5] with picHA, L-pgHA, L-pheHA, and L-hpheHA side-chains provides the first quantitative demonstration of enhanced guest affinity and enantioselectivity through Ln³⁺[15-MC_{Cu(II)}-5] side chain substitutions.

MC binding titrations reveal that FcC⁻ binds equally to Gd(III)[15-MC_{Cu(II)}, pheHA-5] and Gd(III)[15-MC_{Cu(II)}, pgHA-5], though a significant binding strength enhancement is observed with Gd(III)[15-MC_{Cu(II)}, hpheHA-5]. This difference is attributed to greater

hydrophobic interactions with the longer side-chains on hpheHA, which generate a larger cavity that more completely encapsulates FcC^- . An estimate for the cavity size was obtained from crystal structures of $\text{Gd(III)[15-MC}_{\text{Cu(II)-5}]}$ complexes (figure 3.13).^{18,81,84} These structures show the pgHA side-chain generates a hydrophobic cavity with a depth of ~ 5.1 Å. $\text{Gd(III)[15-MC}_{\text{Cu(II), pheHA-5}]}$ has a ~ 6.0 Å cavity, while $\text{Gd(III)[15-MC}_{\text{Cu(II), hpheHA-5}]}$ has a ~ 7.4 Å cavity. Crystal structures of $\text{La(III)[15-MC}_{\text{Cu(II), pheHA-5}]}(\text{FcC}^-)$ and $\text{La(III)[15-MC}_{\text{Cu(II), pheHA-5}]}(\text{FcDC}^{2-})$ (figures 3.7 and 3.8) suggest that FcC^- would extend over 7.4 Å from the Gd(III) ion. Thus, the larger $\text{Gd(III)[15-MC}_{\text{Cu(II), hpheHA-5}]}$ cavity is better suited for encapsulating FcC^- .

The crystal structure of FcC^- bound to $\text{La(III)[15-MC}_{\text{Cu(II), hpheHA-5}]}$ demonstrates how effectively the hpheHA hydrophobic cavity encapsulates FcC^- (figure 3.14). Though the La(III) ions are 9-coordinate in the structure and Gd(III) is typically 8-coordinate, the structure is still informative. The hpheHA side chains extend above the MC face about as far as FcC^- . Thus, the guest is well encapsulated in the cavity. This encapsulation with hpheHA starkly contrasts the pheHA cavity, where FcC^- extends well beyond the hydrophobic cavity (figure 3.10).

The relatively small binding constant between $\text{Gd(III)[15-MC}_{\text{Cu(II), picHA-5}]}(\text{NO}_3)$ and FcC^- reflects the absence of the hydrophobic cavity. Though a hydrophobic contribution to the binding of FcC^- is conceivable through guest interactions with the aromatic, planar MC, this is expected to be much less than with $\text{Gd(III)[15-MC}_{\text{Cu(II), pheHA-5}]}(\text{NO}_3)$. It was hoped that contribution of the MC face alone to guest recognition in the absence of a cavity could be addressed by measuring guest affinity to $\text{Gd(III)[15-MC}_{\text{Cu(II), picHA-5}]}(\text{NO}_3)$. This value would essentially allow for differentiation of the electrostatic and supramolecular interactions of guests with the metallocavitands. Unfortunately, limited host solubility prevented the study of the most appropriate MCs without cavities, $\text{Gd(III)[15-MC}_{\text{Cu(II)-5}]}$ glycine hydroxamic acid and alanine hydroxamic acid, necessitating analysis of the picHA complexes. Unfortunately, the electronic and structural differences between picHA and the α -aminoHA ligands prevents the direct relation of differences in binding constants to effects of the cavity. The picHA pyridyl group is about 5 log units less basic than the amine on α -aminoHA ligands. Therefore, the $\text{Gd(III)[15-MC}_{\text{Cu(II), picHA-5}]}$ central metal is more Lewis acidic and would have

stronger electrostatic interactions with carboxylate guests. Also, the large pyridyl group on picHA would have a slightly greater hydrophobic interaction with guests than the short two carbon chain on the α -aminoHA ligand backbone. For these reasons, it is likely that 4.5 kcal/mol binding constant with $\text{Gd(III)[15-MC}_{\text{Cu(II), picHA-5}}$ is an overestimation of the electrostatic contribution to guest binding.

Looking at the competition titration data with benzoate, all MCs show a weaker affinity for benzoate than FcC^- . As the pK_a 's of the two guests are effectively the same,^{32,85} the greater affinity for FcC^- is attributed to more extensive hydrophobic interactions with the larger guest. $\text{Gd(III)[15-MC}_{\text{Cu(II), hpheHA-5}}$ again shows significantly greater affinity than the MCs with pheHA and pgHA, a result of the larger cavity. Notably, $\text{Gd(III)[15-MC}_{\text{Cu(II), pheHA-5}}$ shows statistically greater affinity for benzoate than $\text{Gd(III)[15-MC}_{\text{Cu(II), pgHA-5}}$. Such a difference was not observed with FcC^- . This discrepancy likely arises from the relative flexibility of the ligand side chains and the shape of the guests. The pgHA side chain is a rigid phenyl ring that is oriented toward the periphery of the MC face. The pheHA side chain contains a flexible methylene carbon, allowing the phenyl ring to rotate toward the center of the MC (figure 3.13b, 3.12c). The flexibility of the pheHA side chain allows for extensive π -stacking and hydrophobic interactions with benzoate or other guests bound to the Ln(III) ion in the center of the MC. While this is advantageous, the flexibility also introduces a reorganization energy penalty to guest inclusion. The rigid $\text{Gd(III)[15-MC}_{\text{Cu(II), pgHA-5}}$ does not incur this reorganization energy penalty; however, it will have minimal interactions with a carboxylate bound at its center. Thus $\text{Gd(III)[15-MC}_{\text{Cu(II), pheHA-5}}$ likely displays stronger affinity for benzoate because the flexibility of the side-chain allows for more extensive interactions with the guest. The taller $\text{Gd(III)[15-MC}_{\text{Cu(II), pheHA-5}}$ cavity also contributes. With FcC^- , the ferrocene moiety extends toward the periphery of the MC face where it can likely interact with the pgHA side-chains. This effect of guest shape and the smaller reorganization energy involved with $\text{Gd(III)[15-MC}_{\text{Cu(II), pgHA-5}}$ likely cause the lack of discrimination seen with benzoate.

In addition to the enhanced guest binding affinity, variation of the MC side chains can improve enantioselectivity. $\text{Gd(III)[15-MC}_{\text{Cu(II),-5}}$ with pgHA and hpheHA side chains both preferentially bind the S-enantiomer of mandelate. $\text{Gd(III)[15-MC}_{\text{Cu(II), pheHA-5}}$

5] does not display this enantioselectivity. Though a trend is not evident that relates enantioselectivity to chain length or flexibility, these results clearly demonstrate that variation of the side chain provides a route to enhanced enantioselectivity. Impressively the enantioselectivity observed with Gd(III)[15-MC_{Cu(II)}, pgHA-5] is much greater than the modest $1.22 \pm K_S/K_R$ value between Gd(III)[15-MC_{Cu(II)}, pheHA-5] and mandelate determined in 50% aqueous methanol.²³ It is likely that the rigidity of the pgHA side chain contributes to the greater enantioselectivity. The chiral anion selectivity seen with Gd(III)[15-MC_{Cu(II)}, pgHA-5] is not record breaking,^{86,87} though it is on par with the amino acid anion enantioselectivity displayed by certain β -cyclodextrins.⁸⁸ The selectivity is promising for these first-generation ligands, especially considering the dearth of metallamacrocycles that display enantioselective guest binding^{89,90} and the general difficulty of enantioselective *anion* binding.

The lack of chiral discrimination displayed by Gd(III)[15-MC_{Cu(II)}, pheHA-5] is surprising given the modest enantioselectivity observed in 50% aqueous methanol.²³ This difference likely arises from the acetonitrile conditions utilized in this experiment leading to a different binding mode than in the aqueous methanol conditions. Measurements in aqueous methanol showed that the enantiomers of mandelate display statistically significant stronger affinity for Gd(III)[15-MC_{Cu(II)}, pheHA-5] than FcC⁻, which was attributed to the guest being bound via a 5-membered chelate ring through the hydroxyl group and a carboxylate oxygen atom (figure 3.2d). The binding strengths of FcC⁻ and mandelate are more similar in the 60% aqueous acetonitrile conditions, which could be indicative of the guests adopting the same bidentate carboxylate binding mode (figure 3.2b). A different binding mode for mandelate in aqueous methanol and acetonitrile could cause the differences in enantioselectivity. Unfortunately, crystal structures of mandelate bound to Gd(III)[15-MC_{Cu(II)}-5] complexes could not be obtained from any solvent to demonstrate this directly.

Conclusion

The CV competitive binding assay was shown to be an effective approach to measuring association constants between redox inactive substrates. While the technique has its limitations, namely the high substrate and electrolyte concentrations required for

CV and that it is incapable of detecting sequential binding, the approach is applicable to a variety of systems, particularly paramagnetic hosts. The thermodynamic data provided by the CV assay reveals intricate guest recognition by Ln^{3+} [15-MC-5] hosts. Based on the stronger binding observed with more hydrophobic guests and MCs with longer side-chains, it is evident that the phenyl side chains play a significant role in guest recognition. Appreciable enantioselectivity is observed, which is encouraging considering that the side chains investigated herein are simple, first generation constructs. More elaborate side chains will likely lead to enhanced selectivity, which would be a tremendous contribution given the general difficulty of enantioselective anion binding.

Ln^{3+} [15-MC-5] complexes have drawn interest as potential traditional metal-based catalysts or as supramolecular catalysts. The thermodynamic data presented herein has provoking implications for catalysis, as the side chains clearly influence the chemistry occurring at the metal ions. Thus it could be possible to tune catalytic efficiency at the metal ions through secondary coordination sphere interactions with the side chains. Also, the enantioselective guest binding suggests that enantioselective reactions are likely with Ln^{3+} [15-MC-5] complexes.

Ln^{3+} [15-MC-5] complexes are a general platform derived from α -amino hydroxamic acids ligands. These ligands can be synthesized from α -amino acids in short syntheses, typically in 1-2 steps. Given the facile self-assembly of Ln^{3+} [15-MC-5] complexes and the potentially vast ligand libraries that can be derived from the plethora of commercially available, relatively inexpensive chiral α -amino acids, one can envision high throughput screening methodology could be utilized to screen different hosts for their enantioselectivity and reactivity. This approach could enable rapid detection of Ln^{3+} [15-MC-5] metallocavitands suitable for chiral guest resolution or catalysis. The thermodynamic data presented herein describes fundamental aspects of Ln^{3+} [15-MC-5] guest recognition that should encourage such efforts.

Figures

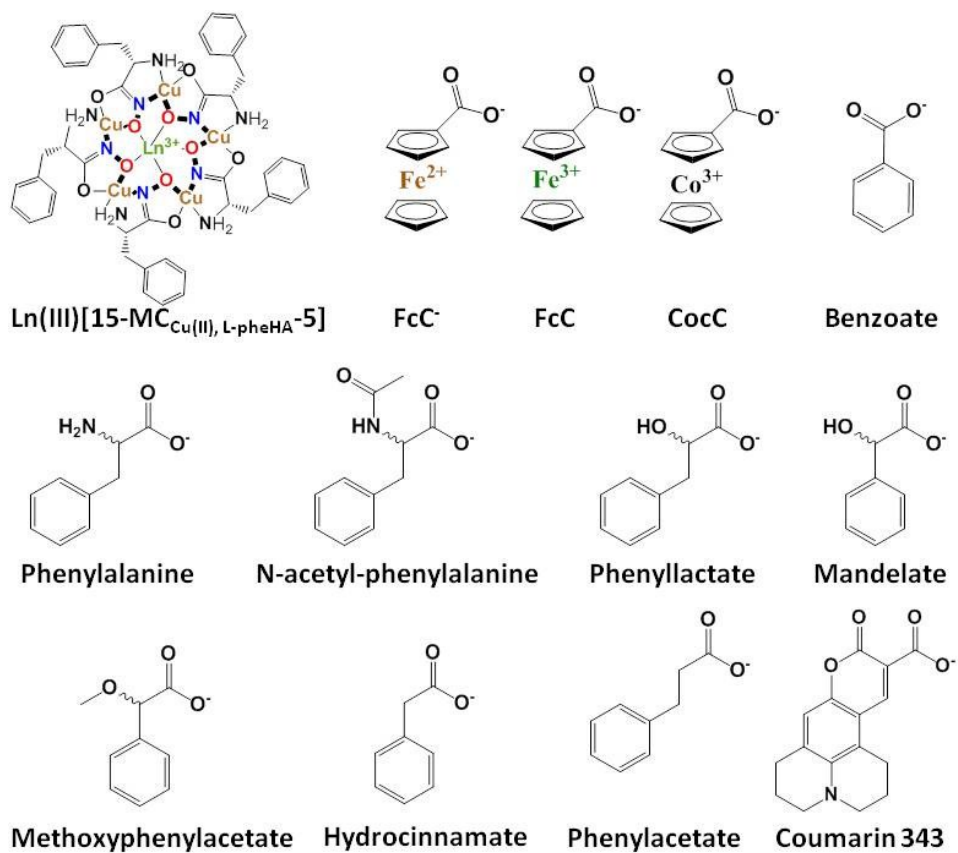


Figure 3.1: Chemdraw diagrams of the $\text{Ln(III)[15-MC}_{\text{Cu(II)}, \text{L-pheHA}^{-5}}$ host and guests discussed in this chapter.

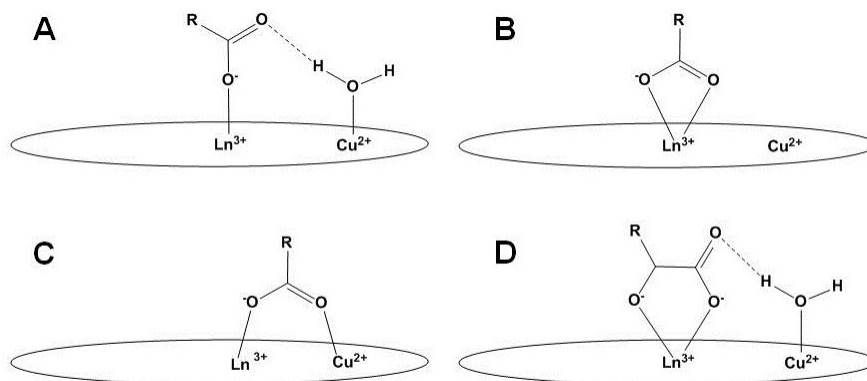


Figure 3.2: Chemdraw diagrams representing the binding modes of carboxylate guests with $\text{Ln(III)[15-MC}_{\text{Cu(II), L-phenHA-5}]$ hosts.

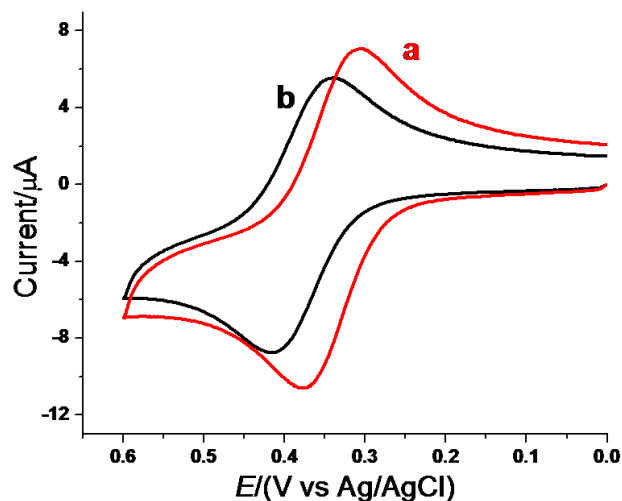
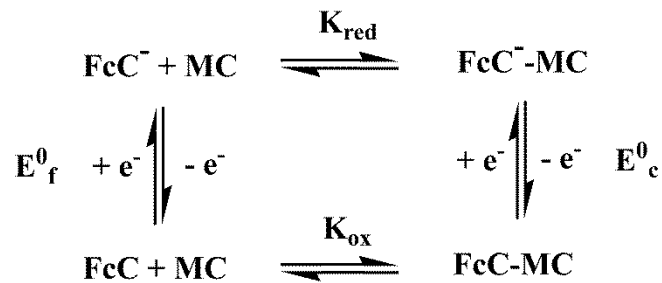


Figure 3.3: Cyclic voltammograms of FcC^- in the absence (a) and presence (b) of 10.7 equivalents of $\text{Dy(III)[15-MC}_{\text{Cu(II), phenHA-5}]Cl_3$ taken in 1:1 methanol and 0.1 M aq MOPS buffer, pH 7.5, 0.1 M KCl, 25 °C. $E_{1/2}$ shifts to greater values due to the host stabilizing the reduced form of FcC^- .



Scheme 3.1: Square scheme depicting the equilibrium between the Ln(III)[15-MC_{Cu(II),pheHA-5}] host, FcC⁻, and FcC.

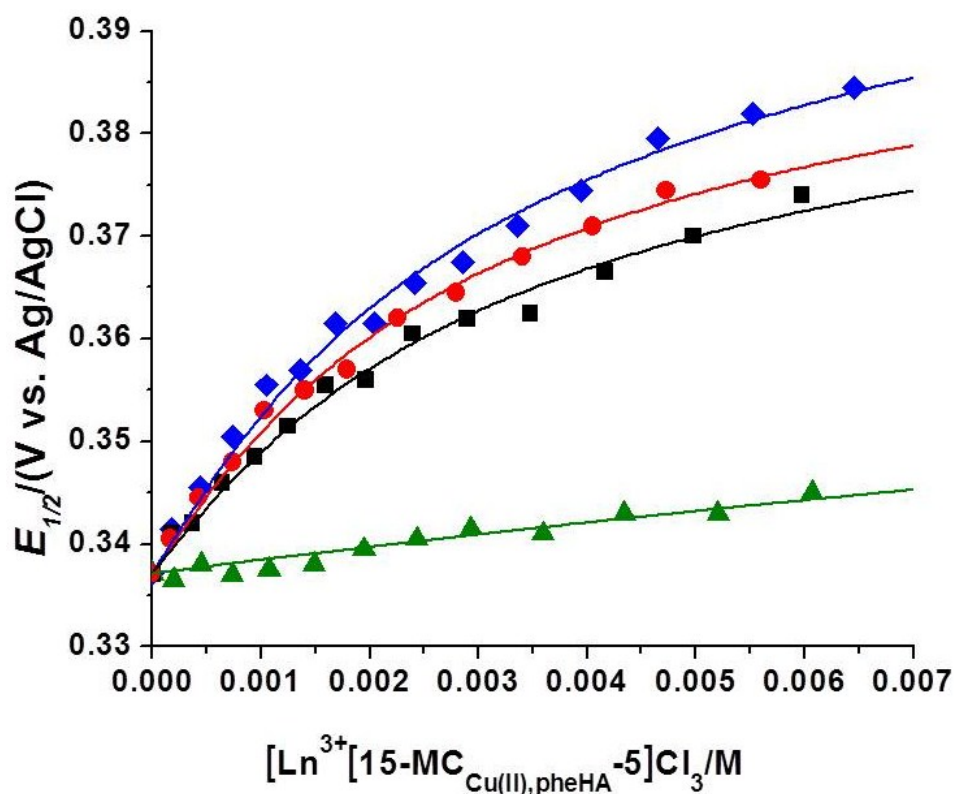


Figure 3.4: Plot of $E_{1/2}$ versus the concentration of Ln(III)[15-MC_{Cu(II),pheHA-5}]Cl₃ from MC binding CV titrations to FcC⁻ in 1:1 methanol and 0.1 M aq MOPS buffer, pH 7.5, 0.1 M KCl, 25 °C. Data points: Blue diamonds - Dy(III)[15-MC_{Cu(II),pheHA-5}]Cl₃, red circles - Gd(III)[15-MC_{Cu(II),pheHA-5}]Cl₃, black squares - Nd(III)[15-MC_{Cu(II),pheHA-5}]Cl₃, green triangles - La(III)[15-MC_{Cu(II),pheHA-5}]Cl₃.

| Ln(III) | $K_{\text{red}}^{[a]}$ (M^{-1}) | $K_{\text{ox}}^{[b]}$ (M^{-1}) | $K_{\text{red}}^{[c]}$ (M^{-1}) | $K_{\text{ox}}^{[c]}$ (M^{-1}) | $D^{[d]}$ ($\times 10^{-6} \text{ cm}^2/\text{s}$) |
|---------|--|---------------------------------------|--|---------------------------------------|---|
| La(III) | 55 ± 3 | - | 60 ± 50 | 0 ± 40 | 1.67 |
| Nd(III) | 600 ± 30 | - | 970 ± 130 | 130 ± 40 | 1.94 |
| Gd(III) | 740 ± 40 | 95 ± 15 | 1040 ± 100 | 100 ± 30 | 1.38 |
| Dy(III) | 940 ± 30 | 120 ± 20 | 1120 ± 100 | 40 ± 30 | 1.54 |

Table 3.1: Binding constants between Ln(III)[15-MC_{Cu(II),pheHA-5}] and FcC⁻ or FcC and the diffusion coefficient for the LnMC-FcC⁻ complex determined in 1:1 methanol and 0.1 M aq MOPS buffer, pH 7.5, 0.1 M KCl, 25 °C.

[a] Calculated based on the assumption that K_{ox} is zero. [b] calculated by a competition titration with CocC. [c] Calculated by simultaneous fitting. [d] Calculated based on the decrease in the anodic peak currents upon titration of the MC and using K_{red} and K_{ox} values determined by simultaneous fitting.

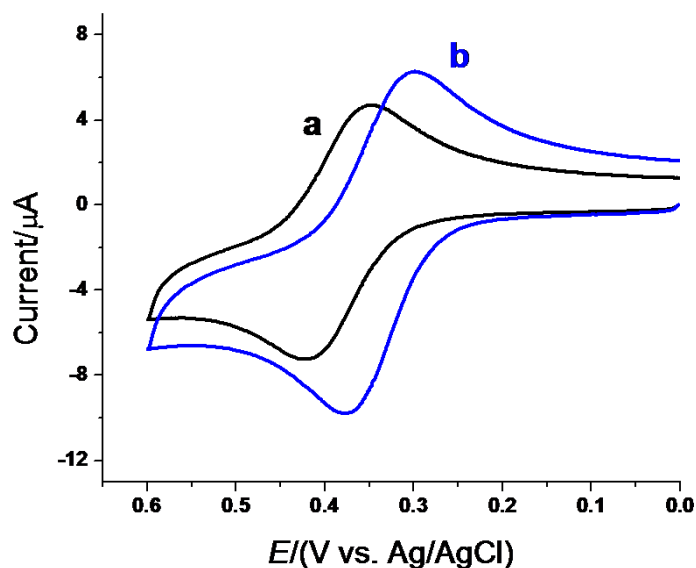


Figure 3.5: CV's from a competition titration of a) FcC⁻ with 10.8 equivalents of Dy(III)[15-MC_{Cu(II),pheHA-5}]Cl₃ and b) after the addition of 170 equivalents of sodium benzoate in 1:1 methanol and 0.1 M aq MOPS buffer, pH 7.5, 0.1 M KCl, 25 °C. $E_{1/2}$ shifts toward the free FcC⁻ potential as the guest is displaced from the host by benzoate.

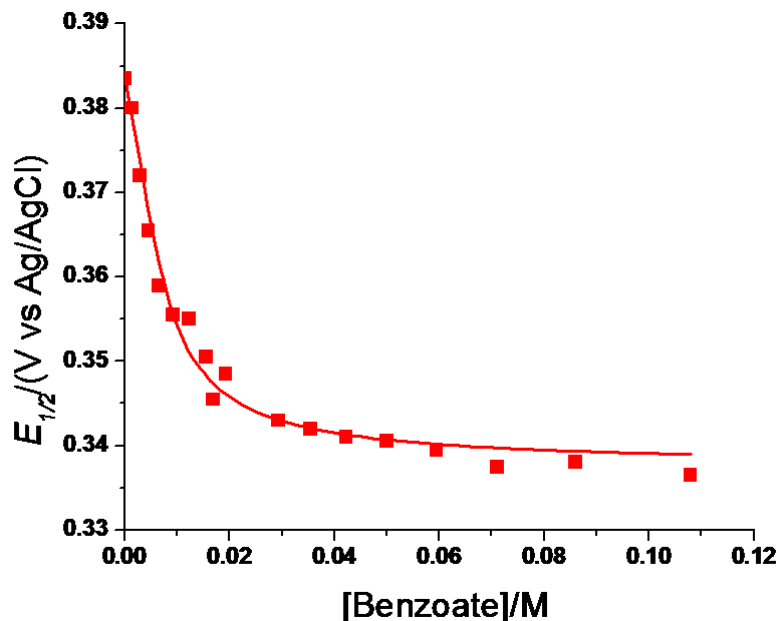


Figure 3.6: Plot of $E_{1/2}$ vs. [benzoate] from a competition titration of the guest to a solution of FcC^- and 10.8 equivalents of $\text{Dy(III)[15-MC}_{\text{Cu(II),pheHA-5}}\text{Cl}_3$ in 1:1 methanol and 0.1 M aq MOPS buffer, pH 7.5, 0.1 M KCl, 25 °C.

| Ln(III) | K_g by CV ^[a] (M^{-1}) | K_g by CV ^[b] (M^{-1}) | K_g by ITC ^[c] (M^{-1}) | K_g Fluorimetry ^[d] (M^{-1}) |
|---------|---|---|--|--|
| La(III) | - | - | 370 ± 20 | - |
| Nd(III) | 510 ± 50 | 680 ± 110 | 550 ± 10 | - |
| Eu(III) | - | - | - | 389 ± 9 |
| Gd(III) | 560 ± 60 | 690 ± 120 | 640 ± 40 | - |
| Dy(III) | 870 ± 80 | 980 ± 40 | 760 ± 20 | - |

Table 3.2: Binding constants between $\text{Ln(III)[15-MC}_{\text{Cu(II),pheHA-5}}\text{]}$ and benzoate determined by the competitive CV assay, ITC,²² and Fluorimetry.²⁵ [a] Calculated using K_{red} obtained from the fitting routine that treats K_{ox} as zero. [b] Calculated using K_{red} and K_{ox} values that were fit simultaneously. CV conditions: 1:1 methanol and 0.1 M aq MOPS buffer, pH 7.5, 0.1 M KCl, 25 °C. [c] ITC conditions: pH 7.6 2mM MOPS in water, 25 °C. The ITC method calculated the binding of a second benzoate, which is not presented here^[23]. [d] Fluorimetry conditions: pH 6.0, 0.02 mM hexamethylenetriamine buffer in water at 25 °C.^[24]

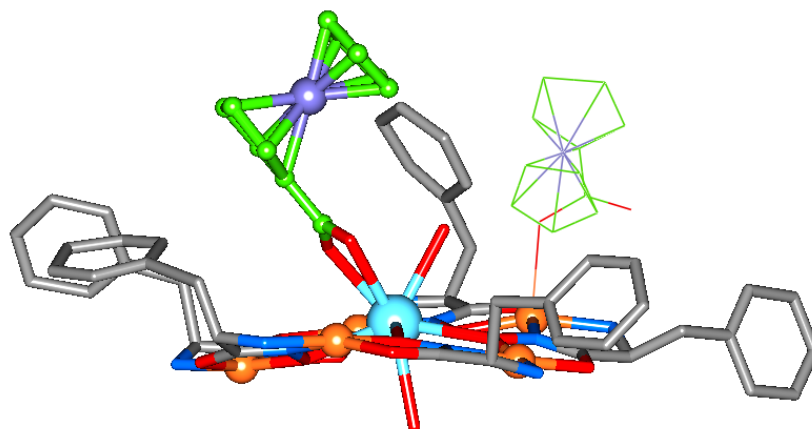


Figure 3.7: Representation of the crystal structure of $\text{La(III)(FcC}^-\text{)}_2[15\text{-MC}_{\text{Cu(II), pheHA}^-5}](\text{NO}_3)$. Unbound or Cu(II)-coordinated solvent, nitrate, and hydrogens were removed for clarity. Color scheme: Grey = MC carbon, green = FcC^- carbon, red = oxygen, blue = nitrogen, orange = copper, light blue = lanthanum. A second FcC^- in the hydrophobic pocket bound to a Cu(II) ion is depicted as a thin line for clarity.

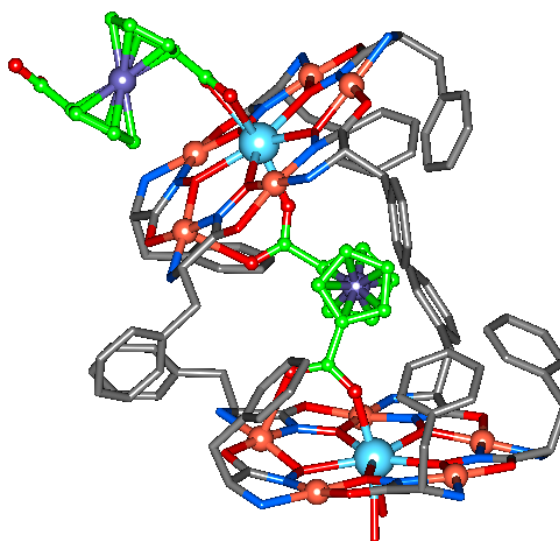


Figure 3.8: Representation of the crystal structure of $\text{La(III)(FcDC}^{2-}\text{)}[15\text{-MC}_{\text{Cu(II), pheHA}^-5}](\text{NO}_3)$. Unbound or Cu(II)-coordinated solvent, nitrate, and hydrogens were removed for clarity. Color scheme: Grey = MC carbon, green = FcC^- carbon, red = oxygen, blue = nitrogen, orange = copper, light blue = lanthanum.

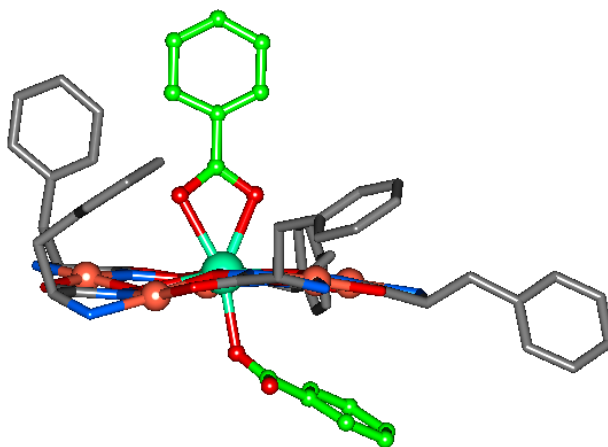


Figure 3.9: Representation of the crystal structure of Dy(III)(benzoate)₂[15-MC_{Cu(II)}, pheHA-5](benzoate)_{0.75}Cl_{0.25}. Unbound or Cu(II)-coordinated solvent, counterions, and hydrogens were removed for clarity. Color scheme: Grey = MC carbon, green = FcC⁻ carbon, red = oxygen, blue = nitrogen, orange = copper, sea green = dysprosium.

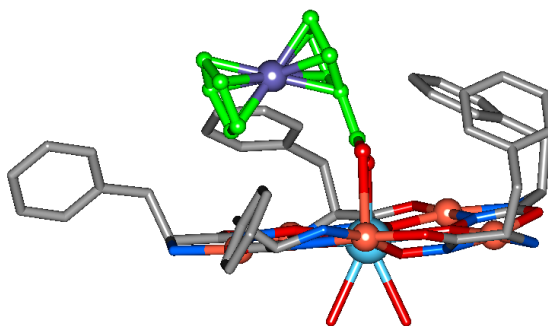


Figure 3.10: Representation of the crystal structure of La(III)(FcDC²⁻)[15-MC_{Cu(II)}, pheHA-5](NO₃) highlighting the orientation of the ferrocene group in the hydrophobic cavity. The additional carboxylate on FcDC²⁻, the other MC in the dimer, lattice solvates, counterions, and hydrogens were removed for clarity. Color scheme: Grey = MC carbon, green = FcC⁻ carbon, red = oxygen, blue = nitrogen, orange = copper, light blue = lanthanum.

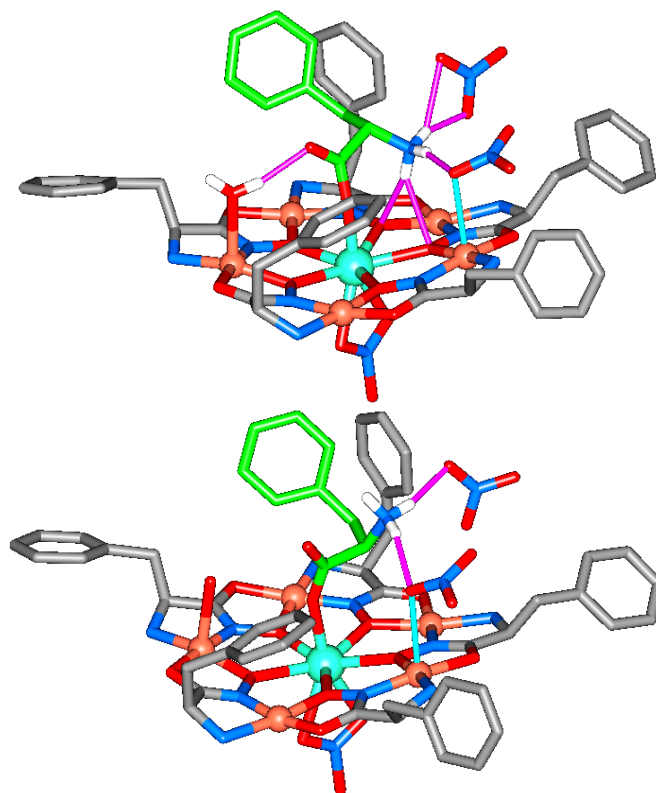


Figure 3.11. Representation of the X-ray crystal structures of $\text{Gd(III)[15-MC}_{\text{Cu(II),pHeHA-5}}$ with S-phenylalanine (top) and R-phenylalanine (bottom) that highlight hydrogen bonding interactions (purple lines). The ammonium on S-phenylalanine engages in hydrogen bonds with heteroatoms in the MC ring, while the ammonium on R-phenylalanine is oriented away from the MC ring. Remaining solvent molecules and hydrogen atoms were removed for clarity. Color scheme: red = oxygen, blue = nitrogen, orange = copper, grey = carbon atoms on the MC, green = carbon atoms on phenylalanine, turquoise = gadolinium, purple line = hydrogen bond, turquoise line = nitrate - copper interaction. These structures were obtained by Dr. Choong-Sun Lim.^{23,24}

| Guest | K_a (M^{-1}) | ΔG^0 (kcal/mol) |
|---|--------------------|-------------------------|
| S-phenylalanine^b | 89 ± 11 | -2.6 ± 0.1 |
| R-phenylalanine^b | 57 ± 11 | -2.3 ± 0.1 |
| N-acetyl-S-phenylalanine^a | 82 ± 16 | -2.6 ± 0.2 |
| N-acetyl-R-phenylalanine^a | 70 ± 7 | -2.5 ± 0.1 |
| S-phenyllactate^a | 2070 ± 140 | -4.52 ± 0.07 |
| R-phenyllactate^a | 2140 ± 110 | -4.54 ± 0.05 |
| S-mandelate^a | 3260 ± 70 | -4.79 ± 0.02 |
| R-mandelate^a | 2680 ± 120 | -4.67 ± 0.04 |
| S-methoxyphenylacetate^a | 140 ± 10 | -2.9 ± 0.1 |
| R-methoxyphenylacetate^a | 120 ± 20 | -2.8 ± 0.2 |
| hydrocinnamate^b | 370 ± 20 | -3.51 ± 0.03 |
| phenylacetate^b | 306 ± 8 | -3.39 ± 0.01 |
| coumarin 343^c | 12,800 ± 300 | -5.60 ± 0.02 |

Table 3.3: Thermodynamic data from competition titrations of Gd(III)[15-MC_{Cu(II),pheHA⁻}5] and α -amino acid analogues. a) Values correspond to association constants determined by the competition CV assay. Solution conditions were 100 mM KCl in 10 mL of a 50% methanol 50% 100 mM aq MOPS buffer, $\text{pH} = 7.5$. Reported errors are the standard deviation of three or more titrations. b) Values correspond to the binding of the first guest as determined by ITC at 298 K in 2mM aqueous MOPS buffer at pH 7.6.⁵³ c) Value was determined by fluorescence in 20 mM aqueous hexamethylenetetramine buffer at pH 6.0.⁵⁴

| Guest | K_S/K_R | p-value ^a |
|------------------------|-------------------|----------------------|
| N-acetyl-phenylalanine | 1.2 ± 0.3 | 0.29 |
| phenyllactate | 0.968 ± 0.082 | 0.526 |
| mandelate | 1.22 ± 0.06 | 0.00207 |
| methoxyphenylacetate | 1.2 ± 0.2 | 0.13 |

Table 3.4: Enantiomeric discrimination of the α -amino acid analog guests by Gd(III)[15-MC_{Cu(II),pheHA}-5]Cl₃. a) The p-value is a two-sided p-value correlating to the null hypothesis that the binding constant of the S-enantiomer is equal to the R-enantiomer.

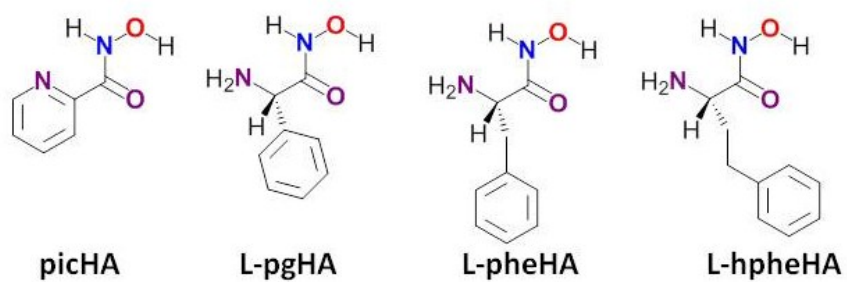


Figure 3.12: Chemdraw diagrams of ligands investigated in the side-chain substitution studies.

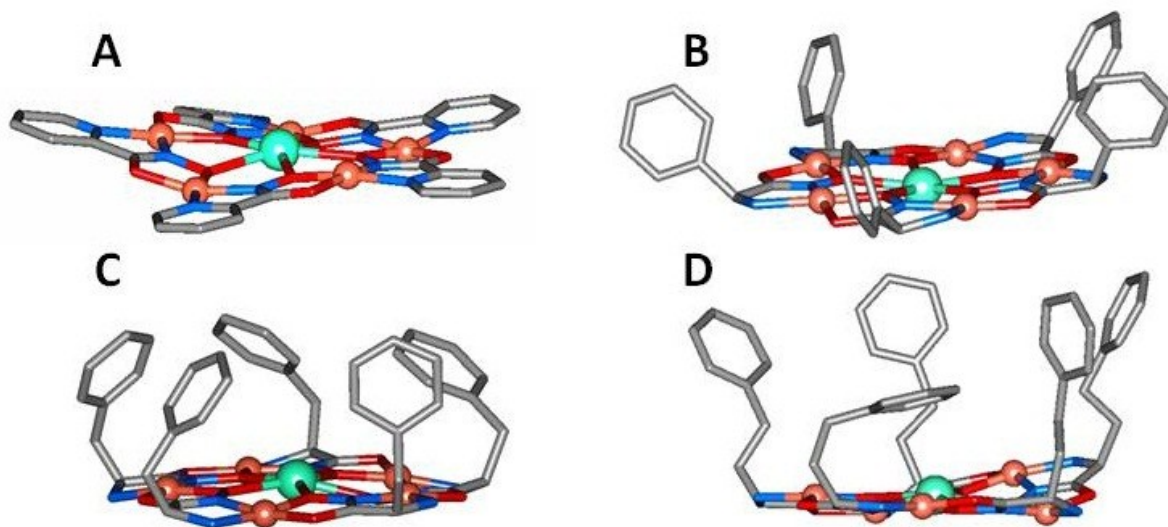


Figure 3.13. Structural representations of A) **1-picHA**, B) **1-pgHA**, C) **1-pheHA**, and D) **1-hpheHA** taken from previously crystal structures. The structures were $\text{Gd(III)[15-MC}_{\text{Cu(II), picHA-5}]\text{(NO}_3\text{)}$,⁸⁴ $\text{Gd(III)[15-MC}_{\text{Cu(II), pgHA-5}]\text{(terephthalate)}$,⁸¹ $\text{Gd(III)[15-MC}_{\text{Cu(II), pheHA-5}]\text{(terephthalate)}$,¹⁸ and $\text{Gd(III)[15-MC}_{\text{Cu(II), hpheHA-5}]\text{(bithiophenedicarboxylate)}$,⁸¹ respectively.

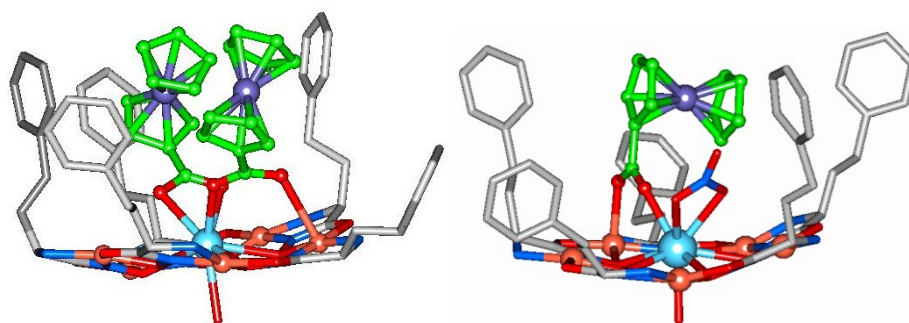


Figure 3.14: Images of the crystal structure of $\text{La(III)[15-MC}_{\text{Cu(II), hpheHA-5}]\text{(FcC}^-\text{)}$ showing the two crystallographically independent monomeric metallocavitands with two FcC^- guests (left) and one FcC^- (right) encapsulated in the hydrophobic cavity. Solvent molecules, hydrogen atoms, and unbound anions were removed for clarity. Color scheme: red = oxygen, blue = nitrogen, orange = copper, grey = carbon atoms on the MC, green = carbon atoms on FcC^- , light blue = lanthanum.

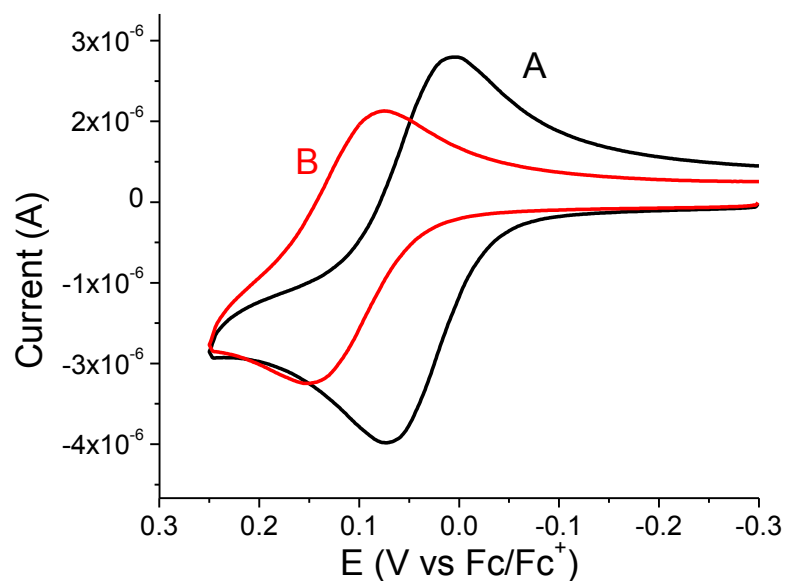


Figure 3.15. CVs from a MC binding titration showing FcC^+ in the presence of 0 equivalents (A) and 10 equivalents (B) of $\text{Gd(III)[15-MC}_{\text{Cu(II), hpheHA-5}}\text{]Cl}_3$ in pH 8.5 0.1 M sodium triflate solution containing 60% ACN, 40 % 0.1 M aqueous EPPS buffer.

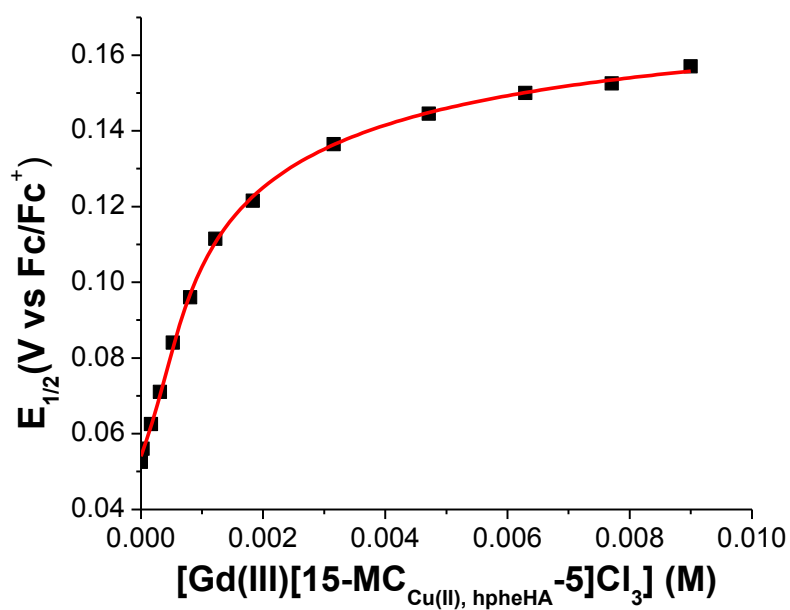


Figure 3.16. Plot of $E_{1/2}$ vs. $[\text{Gd(III)}][15\text{-MC}_{\text{Cu(II)}, \text{hpheHA-5}}]\text{Cl}_3$ from a MC binding CV titration in pH 8.5 0.1 M sodium triflate solution containing 60% ACN, 40 % 0.1 M aqueous EPPS buffer.

| Guest | Ligand | K_a (M^{-1}) | ΔG (kcal/mol) | p-value |
|------------------------|-------------------------|---------------------------|-----------------------|-------------------|
| FcC⁻ | picHA (NO_3) | 1900 ± 100 | 4.47 ± 0.02 | .017 ^a |
| | pgHA | 4800 ± 400 | 5.02 ± 0.05 | .444 ^c |
| | pheHA (NO_3) | 4800 ± 700 | 5.01 ± 0.08 | - |
| | pheHA | 4400 ± 700 | 4.97 ± 0.09 | - |
| | hpheHA | 12100 ± 700 | 5.57 ± 0.03 | .000 ^b |
| FcC | picHA (NO_3) | 35 ± 3 | 2.10 ± 0.05 | .009 ^a |
| | pgHA | 89 ± 4 | 2.66 ± 0.03 | .000 ^b |
| | pheHA (NO_3) | 90 ± 30 | 2.66 ± 0.18 | - |
| | pheHA | 210 ± 30 | 3.18 ± 0.08 | - |
| | hpheHA | 130 ± 40 | 2.89 ± 0.19 | .035 ^b |
| Benzoate | pgHA | 800 ± 100 | 3.96 ± 0.08 | .006 |
| | pheHA | 1300 ± 200 | 4.26 ± 0.09 | - |
| | hpheHA | 3000 ± 300 | 4.74 ± 0.06 | .000 ^b |

Table 3.5. Thermodynamic data for guest binding to $\text{Gd(III)}[15\text{-MC}_{\text{Cu(II)-5}}]$ determined with the CV competitive binding assay in pH 8.5 0.1 M sodium triflate solution containing 60% ACN, 40 % 0.1 M aqueous EPPS buffer.

^aP-value of two-sided t-test corresponding to the null hypothesis that the binding constant of $\text{Gd(III)}[15\text{-MC}_{\text{Cu(II)}, \text{picHA-5}}](\text{NO}_3)$ is equal to that of $\text{Gd(III)}[15\text{-MC}_{\text{Cu(II)}, \text{pheHA-5}}](\text{NO}_3)$.

^bP-value of two-sided t-test corresponding to the null hypothesis that the binding constant of the comparing MC is equal to the binding constant of $\text{Gd(III)}[15\text{-MC}_{\text{Cu(II)}, \text{pheHA-5}}]\text{Cl}_3$.

^cP-value of two-sided t-test corresponding to the null hypothesis that binding constants of $\text{Gd(III)}[15\text{-MC}_{\text{Cu(II)}, \text{pgHA-5}}]$ and $\text{Gd(III)}[15\text{-MC}_{\text{Cu(II)}, \text{pheHA-5}}]$ are equal.

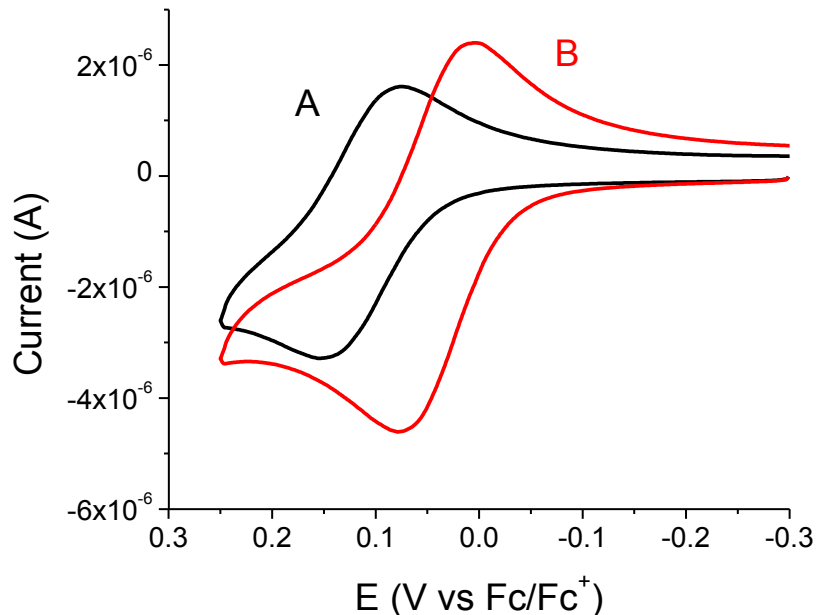


Figure 3.17. CVs of FcC^- from a competitive binding titration in the presence of 4.7 eq $\text{Gd(III)[15-MC}_{\text{Cu(II), hpheHA-5}}\text{]Cl}_3$ and 0 eq (A) and 200 eq (B) of S-mandelate in pH 8.5 0.1 M sodium triflate solution containing 60% ACN, 40 % 0.1 M aqueous EPPS buffer.

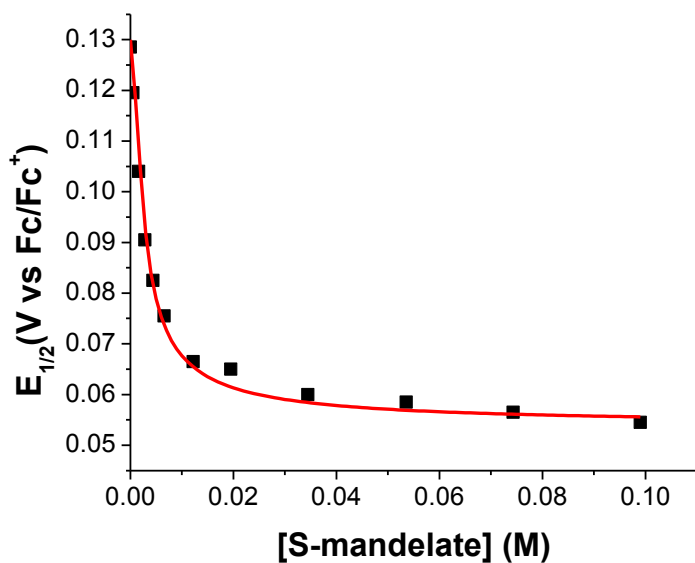


Figure 3.18. Plot of $E_{1/2}$ vs. [S-mandelate] from a competitive binding CV titration performed in pH 8.5 0.1 M sodium triflate solution containing 60% ACN, 40 % 0.1 M aqueous EPPS buffer.

| Guest | Ligand | K_a (M^{-1}) | ΔG (kcal/mol) |
|--------------------------|--------|--------------------|-----------------------|
| S-mandelate (S-5) | pgHA | 5700 ± 1000 | 5.12 ± 0.11 |
| | pheHA | 2800 ± 500 | 4.70 ± 0.10 |
| | hpheHA | 5100 ± 500 | 5.05 ± 0.06 |
| R-mandelate (R-5) | pgHA | 2600 ± 600 | 4.66 ± 0.14 |
| | pheHA | 3000 ± 400 | 4.74 ± 0.08 |
| | hpheHA | 3400 ± 300 | 4.82 ± 0.04 |

Table 3.6. Thermodynamic data on the binding of S- and R-mandelate to Gd(III)[15-MC_{Cu(II)}-5] determined with the competitive binding CV assay in pH 8.5 0.1 M sodium triflate solution containing 60% ACN, 40 % 0.1 M aqueous EPPS buffer.

| Host | K_S/K_R | p-value ^a |
|----------|---------------|----------------------|
| 1-pgHA | 2.2 ± 0.6 | .004 |
| 1-pheHA | 0.9 ± 0.2 | .588 |
| 1-hpheHA | 1.5 ± 0.2 | .001 |

Table 3.7. K_S/K_R values for mandelate binding to Gd(III)[15-MC_{Cu(II)}-5] determined with the competitive binding CV assay in pH 8.5 0.1 M sodium triflate solution containing 60% ACN, 40 % 0.1 M aqueous EPPS buffer.

a) P-value of a two-sided t-test correlating to the null hypothesis that the binding constant of the S-enantiomer is equal to the binding constant of the R-enantiomer.

References

- (1) Yoshizawa, M.; Klosterman, J. K.; Fujita, M. *Angew. Chem. Int. Ed.* **2009**, *48*, 3418.
- (2) *Supramolecular Catalysis*; Leeuwen, P. W. N. M. v., Ed.; Wiley-VCH: Weinheim, 2008.
- (3) Hof, F.; Craig, S. L.; Nuckolls, C.; Rebek, J. J. *Angew. Chem. Int. Ed.* **2002**, *41*, 1488.
- (4) Steed, J. W.; Atwood, J. L. *Supramolecular Chemistry*; John Wiley & Sons, Ltd: West Sussex, 2000.
- (5) Lehn, J. M. *Angew. Chem. Int. Ed. Engl.* **1988**, *87*, 89.
- (6) Cram, D. J. *Angew. Chem. Int. Ed. Engl.* **1988**, *27*, 1009.
- (7) Mallouk, T. E.; Gavin, J. A. *Acc. Chem. Res.* **1998**, *31*, 209.
- (8) Stemmler, A. J.; Barwinski, A.; Baldwin, M. J.; Young, V.; Pecoraro, V. L. *J. Am. Chem. Soc.* **1996**, *118*, 11962.
- (9) Bodwin, J. J.; Cutland, A. D.; Malkani, R. G.; Pecoraro, V. L. *Coord. Chem. Rev.* **2001**, *216-217*, 489.
- (10) Tegoni, M.; Remelli, M. *Coord. Chem. Rev.* **2012**, *256*, 289.
- (11) Kobayashi, S.; Sugiura, M.; Kitigawa, H.; Lam, W. W.-L. *Chem. Rev.* **2002**, *102*, 2227.
- (12) Shibusaki, M.; Yoshikawa, N. *Chem. Rev.* **2002**, *102*, 2187.
- (13) Inanaga, J.; Furuno, H.; Hayano, T. *Chem. Rev.* **2002**, *102*, 2211.
- (14) Bunzli, J. C.-G.; Piguet, C. *Chem. Rev.* **2002**, *102*.
- (15) Eliseeva, S. V.; Bünzli, J.-C. G. *New J. Chem.* **2011**, *35*, 1165.
- (16) Cutland, A. D.; Malkani, R. G.; Kampf, J. W.; Pecoraro, V. L. *Angew. Chem. Int. Ed.* **2000**, *39*, 2690.
- (17) Cutland, A. D.; Halfen, J. A.; Kampf, J. W.; Pecoraro, V. L. *J. Am. Chem. Soc.* **2001**, *123*, 6211.
- (18) Lim, C.-S.; Cutland Van Noord, A.; Kampf, J. W.; Pecoraro, V. L. *Eur. J. Inorg. Chem.* **2007**, *2007*, 1347.
- (19) Dallavalle, F.; Remelli, M.; Sansone, F.; Bacco, D.; Tegoni, M. *Inorg. Chem.* **2010**, *49*, 1761.
- (20) *Analytical Methods in Supramolecular Chemistry*; Schalley, C. A., Ed.; Wiley-VCH: Weinheim, 2007.
- (21) Schalley, C. A. *Mass Spectrom. Rev.* **2001**, *20*, 253.
- (22) Lim, C. S.; Kampf, J. W.; Pecoraro, V. L. *Inorg. Chem.* **2009**, *48*, 5224.
- (23) Lim, C. S.; Jankolovits, J.; Zhao, P.; Kampf, J. W.; Pecoraro, V. L. *Inorg. Chem.* **2011**, *50*, 4832.
- (24) Lim, C.-S., *Graduate Thesis*, University of Michigan, 2008.
- (25) Tegoni, M.; Tropiano, M.; Marchio, L. *Dalton Trans.* **2009**, 6705.
- (26) Kaifer, A. E. *Acc. Chem. Res.* **1999**, *32*, 62.
- (27) Kaifer, A. E.; Gomez-Kaifer, M.; Wiley-VCH: Toronto, 1999.
- (28) Carbo, A. D. In *Supramolecular Chemistry of Anions*; Bianchi, A. Bowman-James, K.; Garcia-Espana, E., Ed.; Wiley-VCH: 1997, p 277.
- (29) Beer, P. D. *Adv. Mater.* **1994**, *6*, 607.
- (30) Boulas, P. L.; Gomez-Kaifer, M.; Echegoyen, L. *Angew. Chem. Int. Ed.* **1998**, *37*, 216.
- (31) Cardona, C. M.; Mendoza, S.; Kaifer, A. E. *Chem. Soc. Rev.* **2000**, *29*, 37.
- (32) Matsue, T.; Evans, D. H.; Osa, T.; Kobayashi, N. *J. Am. Chem. Soc.* **1985**, *107*, 3411.

- (33) Godinez, L. A.; Lin, J.; Munoz, M.; Coleman, A. W.; Kaifer, A. E. *J. Chem. Soc. Faraday Trans.* **1996**, *92*, 645.
- (34) Wang, Y.; Mendoza, S.; Kaifer, A. E. *Inorg. Chem.* **1998**, *37*, 317.
- (35) Isnin, R.; Salam, C.; Kaifer, A. E. *J. Org. Chem.* **1991**, *56*, 35.
- (36) Cui, L.; Gadde, S.; Li, W.; Kaifer, A. E. *Langmuir* **2009**, *25*, 17963.
- (37) Jeon, W. S.; Moon, K.; Park, S. H.; Chun, H.; Ko, Y. H.; Lee, J. Y.; Lee, E. S.; Samal, S.; Selvapalam, N.; Rekharsky, M. V.; Sindelar, V.; Sobransingh, D.; Inoue, Y.; Kaifer, A. E.; Kim, K. *J. Am. Chem. Soc.* **2005**, *127*, 12984.
- (38) Jeon, W. S.; Kim, H.-J.; Lee, C.; Kim, K. *Chem. Commun.* **2002**, 1828.
- (39) Gedde, S.; Kaifer, A. E. *Curr. Org. Chem.* **2011**, *15*, 27.
- (40) Wang, Y. A., Julio; Kaifer, A. E. *Chem. Commun.* **1998**, 1457.
- (41) Sobransingh, D.; Dewal, M. B.; Hiller, J.; Smith, M. D.; Shimizu, L. S. *New J. Chem.* **2008**, *32*, 24.
- (42) Gross, F. P. H., M. W.; Lehn, J. M.; Sessions, R. B. *J. Chem. Soc. Chem. Commun.* **1981**, 1067.
- (43) Peter, F.; Gross, M.; Hosseini, M. W.; Lehn, J. M. *J. Electroanal. Chem.* **1983**, *144*, 279.
- (44) Podkosielnny, D.; Hooley, R. J.; Rebek, J.; Kaifer, A. E. *Org. Lett.* **2008**, *10*, 2865.
- (45) Philip, I.; Kaifer, A. E. *J. Org. Chem.* **2005**, *70*, 1558.
- (46) Philip, I. E.; Kaifer, A. E. *J. Am. Chem. Soc.* **2002**, *124*, 12678.
- (47) Carter, M. T.; Rodriguez, M.; Bard, A. J. *J. Am. Chem. Soc.* **1989**, *111*, 8901.
- (48) Mendoza, S.; Castaño, E.; Meas, Y.; Godinez, L. A.; Kaifer, A. E. *Electroanalysis* **2004**, *16*, 1469.
- (49) Laviron, E.; Roullier, L. *J. Electroanal. Chem.* **1985**, *186*, 1.
- (50) Addison, A. W.; Carpenter, M.; Lau, L. K. M.; Wicholas, M. *Inorg. Chem.* **1978**, *17*, 1545.
- (51) Godinez, L. A.; Lin, J.; Coleman, A. W.; Kaifer, A. E. *Electroanalysis* **1996**, *8*, 1072.
- (52) Bianchi, A.; Domenech, A.; Garcia-Espana, E.; Luis, S. V. *Anal. Chem.* **1993**, *65*, 3137.
- (53) Andres, A.; Arago, J.; Bencini, A.; Bianchi, A.; Domenech, A.; Fusi, V.; Garcia-Espana, E.; Paoletti, P.; Ramirez, J. A. *Inorg. Chem.* **1993**, *32*, 3418.
- (54) Doménech, A.; García-España, E.; Ramírez, J. A. *Talanta* **1995**, *42*, 1663.
- (55) Bencini, A. B., A.; Burguete, M. I.; Dapporto, P.; Domenech, Antonio; Garcia-Espana, Enrique; Luis, Santiago V.; Paoli, P.; Ramirez, Jose A. *J. Chem. Soc. Perkin Trans. 2* **1994**, 569.
- (56) Sugawara, K.; Tanaka, S.; Nakamura, H. *Anal. Chem.* **2002**, *67*, 299.
- (57) Rojas, M. T.; Koeniger, R.; Stoddart, J. F.; Kaifer, A. E. *J. Am. Chem. Soc.* **1995**, *117*, 336.
- (58) Sugawara, K.; Kamiya, N.; Hirabayashi, G.; Kuramitz, H. *Anal. Sci.* **2005**, *21*, 897.
- (59) Yang, Y.; Yang, X.; Yang, H.; Liu, Z.; Liu, Y.; Shen, G.; Yu, R. *Anal Chim Acta* **2005**, *528*, 135.
- (60) Casas-Solvas, J. M.; Ortiz-Salmeron, E.; Fernandez, I.; Garcia-Fuentes, L.; Santoyo-Gonzalez, F.; Vargas-Berenguel, A. *Chem. Eur. J.* **2009**, *15*, 8146.
- (61) Sato, S.; Nojima, T.; Takenaka, S. *J. Organomet. Chem.* **2004**, *689*, 4722.
- (62) Mirzoian, A.; Kaifer, A. E. *Chem. Commun.* **1999**, 1603.
- (63) Jankolovits, J.; Kampf, J. W.; Maldonado, S.; Pecoraro, V. L. *Chem. Eur. J.* **2010**, *16*, 6786.

- (64) Zaleski, C. M.; Lim, C. S.; Cutland-Van Noord, A. D.; Kampf, J. W.; Pecoraro, V. L. *Inorg. Chem.* **2011**, *50*, 7707.
- (65) Sheats, J. E.; Rausch, M. D. *J. Org. Chem.* **1970**, *35*, 3245.
- (66) Ali, L. A. C., A.; Kemp, T. J.; *J. Chem. Soc. Dalton Trans.* **1973**, 1468.
- (67) Perrin, D. D.; Dempsey, B. *Buffers for pH and Metal Ion Control*; Chapman and Hall: London, 1979.
- (68) Subirats, X.; Roses, M.; Bosch, E. *Separ. Purif. Rev.* **2007**, *36*, 231.
- (69) Espinosa, S.; Bosch, E.; Roses, M. *Anal. Chem.* **2000**, *72*, 5193.
- (70) Azab, H. A.; Nour, K. M. A. *J. Chem. Eng. Data* **1999**, *44*, 678.
- (71) *SAINT Plus*, v. 7.60A; Bruker Analytical X-ray: Madison, WI, **2009**.
- (72) Sheldrick, G. M.; *SADABS: Program for Empirical Absorption Correction of Area Detector Data*: Gottingen, Germany, **2008**.
- (73) Sheldrick, G. M. *Acta Cryst.* **2008**, *A64*, 112.
- (74) Canals, I.; Portal, J. A.; Bosch, E.; Roses, M. *Anal. Chem.* **2000**, *72*, 1802.
- (75) Rived, F.; Rosés, M.; Bosch, E. *Anal. Chim. Acta* **1998**, *374*, 309.
- (76) H. A. Azab, M. R. Mahmoud, *J. Chem. Eng. Data*, **1995**, *40*, 523.
- (77) Azab, H. A.; Orabi, A. S.; El-Salam, E. T. A. *J. Chem. Eng. Data* **1998**, *43*, 703.
- (78) McCormack, S.; Russell, N. R.; Cassidy, J. F. *Electrochim. Acta* **1992**, *37*, 1939.
- (79) Wang, Z.-X. *FEBS Lett.* **1995**, *360*, 111.
- (80) Wang, Y.; Mendoza, S.; Kaifer, A. E. *Inorg. Chem.* **1998**, *37*, 317.
- (81) Jankolovits, J.; Lim, C.-S.; Mezei, G.; Kampf, J. W.; Pecoraro, V. L. *Inorg. Chem.* **2012**, doi:10.1021/ic202347j.
- (82) Tegoni, M.; Tropiano, M.; Marchio, L. *Dalton Trans.* **2009**, 6705.
- (83) Jankolovits, J.; Kampf, J. W.; Maldonado, S.; Pecoraro, V. L. *Chem. Eur. J.* **2010**, *16*, 6786.
- (84) Stemmler, A. J.; Kampf, J. W.; Kirk, M. L.; Atasi, B. H.; Pecoraro, V. L. *Inorg. Chem.* **1999**, *38*, 2807.
- (85) Azab, H. A.; Ahmed, I. T.; Mahmoud, M. R. *J. Chem. Eng. Data* **1995**, *40*, 523.
- (86) Siracusa, L.; Hurley, F. M.; Dresen, S.; Lawless, L. J.; Pérez-Payán, M. N.; Davis, A. P. *Org. Lett.* **2002**, *4*, 4639.
- (87) Sirikulajorn, A.; Tuntulani, T.; Ruangpornvisuti, V.; Tomapatnaget, B.; Davis, A. P. *Tetrahedron* **2010**, *66*, 7423.
- (88) Easton, C. J.; Lincoln, S. F. *Chem. Soc. Rev.* **1996**, 163.
- (89) Fiedler, D.; Leung, D. H.; Bergman, R. G.; Raymond, K. N. *J. Am. Chem. Soc.* **2004**, *126*, 3674.
- (90) Brumaghim, J. L.; Michels, M.; Raymond, K. N. *Eur. J. Org. Chem.* **2004**, *22*, 4552.

Chapter IV

Solvent Directed Assembly of Luminescent Lanthanide Metallacrowns from Building Blocks with Incompatible Symmetry Preferences and Open Coordination Sites

Introduction

Dative bonds are used widely in the assembly of discrete supramolecular edifices, such as molecular polygons, polyhedral, and helices.¹⁻³ The diverse architectures and physical properties of discrete coordination driven assemblies are increasingly utilized in functional applications of broad interest. Interior cavities in many assemblies bind guests and facilitate catalytic transformations of encapsulated guests,^{4,5} enhances the reactivity of encapsulated organometallic catalysts,⁶⁻⁹ and can perturb the physical properties of responsive guests for sensing applications.¹⁰⁻¹² Coordination driven assemblies also serve as building blocks for the construction of porous solids, nanofibers, and liquid crystalline columnar phases.¹³⁻¹⁷ Additionally, metal ions in coordination driven assemblies can generate catalytic, optical, magnetic, and electrochemical functionality.¹⁸⁻²²

Numerous strategies for the synthesis of discrete coordination driven assemblies have been developed.^{1,2} Assembly in solution is emphasized to differentiate these complexes from clusters that tend to form spontaneously upon crystallization. Importantly, complexes that assemble in solution have some degree of solution stability. Also, solution phase assembly suggests the building blocks can be derivatized and still assemble the same complex. Such behavior might not be expected for complexes that assemble upon crystallization as subtle structural changes can drastically alter the crystallization process. The most reliable strategies for preparing metal-based molecular assemblies employ molecular building blocks possessing symmetry elements found in the self-assembled complex. Combining building blocks with different symmetry elements found in the supramolecular complex (symmetry compatible building blocks) leads to the formation of the complex through self-assembly. One such strategy, the molecular library

approach,²³ is exemplified by Fujita's M_4L_4 molecular square.²⁴ The complex contains C_2 symmetric 4,4'-bipyridyl ligands that generate straight edges and square planar Pd(ethylenediamine) metal centers to arrange the bridging ligands at 90° angles. Thus, four C_2 symmetric linkers and four 90° Pd(ethylenediamine) vertices assemble to form the molecular square. Another symmetry based approach is the symmetry interaction model,²⁵ best exemplified by Raymond's T_d symmetric M_4L_6 cluster.²⁶ The design employs a C_2 symmetric dicatechol ligand and C_3 symmetric octahedral metal ions to reproduce the symmetry elements found in the tetrahedron. Furthermore, the approach angle of the dicatechol ligands with the metal ions is considered to enforce the appropriate relative orientations of the symmetry axes in the building blocks. In these examples, formation of the discrete, high symmetry assembly is driven by the formation of a maximum number of stable dative bonds.

For coordination driven assemblies, multiple complexes can often form in solution through distortions in the geometry of the metal ions and guests.²⁷ For example, Fujita's M_4L_4 molecular square rearranges to an M_3L_3 at low concentrations.²⁸ Flexible ligands have also been shown to lead to the formation of different complexes.²⁹ Significant effort has been devoted to controlling the assembly of different complexes from the same building blocks. One of the most elegant is the weak-link approach, where ligand coordination to a metal ion reversibly shifts the topology of the macrocycle.¹² Assemblies have also been prepared that selectively form different complexes through the encapsulation of a guest in the central cavity of the complex.^{21,30-34}

In certain instances, the solvent can selectively direct the assembly of metal ions and bridging ligands into different macrocycles in solution. The Severin group has recently reported a ruthenium assembly that forms a tetranuclear complex in chloroform, but octanuclear complexes in dichloromethane.³⁵ A number of other solvent controlled macrocyclic assemblies have been reported.³⁶⁻³⁸ Importantly, the complexes in these examples assemble in solution, demonstrating that the solvent dependence is not merely a crystallization phenomenon. In these examples, differences in the energies of solvation are thought to direct the assembly. While the solvent-directed approach has significant promise, there is little understanding of how to *design* building blocks whose assembly is dependent on the solvent. As novel architectures can give rise to distinct properties and

functionality, influence over the structural motif through a simple variable like the solvent would be powerful in the search for metal-based assemblies that address areas of need.

In this chapter, a novel design strategy for realizing solvent-dependent coordination driven assemblies is presented. The approach relies on symmetry incompatible building blocks with open coordination sites to direct the assembly of different structural motifs. Symmetry incompatible building blocks possess symmetry elements that are not complementary with a single self-assembled structure, so each building block directs the assembly toward different constructs. Furthermore, metal ions with open metal sites are utilized so that solvent coordination, or solvation, at these positions can selectively direct the assembly toward one of the different possible constructs. The viability of this approach is demonstrated by the solvent directed assembly of multiple lanthanide metallocrowns (LnMCs)³⁹ in solution from identical building blocks.

The MC design strategy used in this work relies on ligands that form fused chelate rings to generate the vertices of a macrocyclic molecular polygon.^{40,41} Ligands that form fused 5-membered and 6-membered chelate rings, such as salicylhydroxamic acid, orient metal ions at 90° angles. Furthermore, the *trans*-arrangement of the chelate rings generates a linear edge. Thus propagation of this chelate motif four times completes the 360° macrocycle and generates a square-shaped 12-MC-4 (figure 4.1). Ligands with two fused 5-membered chelate rings, such as picolinehydroximate (picHA, figure 4.1, 4.2), generate a 72° angle between metal ions in the MC ring. With the appropriate ring metals and central metal (such as a lanthanide ion), the building blocks complete the 360° rotation and generate a pentagonal 15-MC-5. An important aspect of the fused chelate ring design is that a planar arrangement of the bidentate ligands is necessary to generate the planar macrocyclic polygon. Jahn-Teller distorted ring metals, such as Cu(II), are particularly effective in this regard because ring strain prevents the formation of octahedral *cis*-isomers. Notably, the only Ln-MCs obtained from the reaction of picHA, a Ln(III) ion, and either Cu(II) or Ni(II) are Ln(III)[15-MC-5] complexes.^{42,43}

While MCs have been widely studied for their single-molecule magnetic behavior, anion recognition chemistry, and as building blocks for porous solids,³⁹

luminescent LnMCs have not been reported. Emission from the excited state of a lanthanide ion through $f-f$ transitions is known as luminescence.⁴⁴ Importantly, the contraction of Ln(III) f -orbitals leads to narrow line widths for $f-f$ transitions, as broadening from ligand vibrations is avoided. Furthermore, Ln(III) luminescence has lifetimes of up to milliseconds. $f-f$ transitions are Laporte-forbidden, which leads to low extinction coefficients of $\sim 1 \text{ M}^{-1}\text{cm}^{-1}$ that makes direct excitation of the Ln(III) ions impractical. Therefore, the antenna effect is exploited in Ln(III) luminescence, where the Ln(III) ion is sensitized through energy transfer from the excited state of a ligand. Notably, the antenna effect leads to large Stokes shifts of hundreds of nm. The long lifetimes, narrow line widths, and large Stokes shifts make Ln(III) luminescence a unique spectroscopic feature for biomedical imaging and optical devices.⁴⁵ Ln(III) ions that emit in the near-infrared (NIR) region draw particular interest for telecommunications applications and for biomedical imaging due to the transparency of biological tissue in the NIR. NIR emitting Ln(III) complexes typically display short lifetimes on the order of microseconds and quantum yields of less than 0.5% due to vibrational quenching.^{46,47} 100% quantum yields and millisecond lifetimes are theoretically possible for these complexes. Vibrational quenching is caused by high energy N-H, O-H, and C-H oscillators. Uniquely, the inorganic MC macrocycle mitigates vibrational quenching by removing C-H bonds from the vicinity of the lanthanide ion. The promise of highly efficient luminescent complexes, particularly in the NIR, has motivated the synthesis of lanthanide MCs with Zn(II) ring metals. Zn(II) was necessary because $d-d$ transitions are known to provide a quenching pathway in Ln complexes with Cu(II) or other metal ions.⁴⁸ The d^{10} Zn(II) ring metal eliminates potential quenching caused by $d-d$ transitions. These studies were also motivated by the promise of preparing MCs with diamagnetic ring metals for their single-ion magnetism properties and optically transparent MCs for developing new materials exhibiting second harmonic generation.

From the standpoint of symmetry-based design, it is important to note that Zn(II) typically forms tetrahedral, 5-coordinate, or octahedral complexes. Tetrahedral, trigonal bipyramidal, and distorted square pyramidal geometries lead to non-planar arrangements of bidentate ligands. Therefore, the symmetry preference of Zn(II) is incompatible with the design of planar MCs, such as the Ln(III)[15-MC-5]. In addition, the 5- and 6-

coordinate ions will have open coordination sites when coordinated with two bidentate ligands. These aspects of Zn(II) coordination chemistry suggest that unlike Cu(II) or Ni(II), the reaction of Zn(II), picHA, and Ln(III) could be directed by the solvent to form a variety of Ln-MCs. Likewise, the large coordination number (commonly 8-9) of lanthanide ions could increase the role of the solvent in MC assembly further. Thus, the synthesis of LnMCs with Zn(II) provides the ideal system for demonstrating how solvent dependence can be incorporated into coordination-driven assemblies by using symmetry incompatible building blocks with open coordination sites. The viability of this approach is demonstrated herein with the solvent dependent assembly of Zn(II), picHA, and Ln(III) ions. Eight structurally distinct MCs were found to assemble based on the solvent. Six of these MCs have been structurally characterized and their solution stability is discussed. The luminescence properties of one of these complexes are also provided. The structure, solution behavior, and luminescence of one LnMC in this series, a $\text{Ln}^{3+}[\text{12-MC}_{\text{Zn(II), picHA-4}}]_2[\text{24-MC}_{\text{Zn(II), picHA-8}}]_2^{3+}$ complex ($\text{LnZn}_{16}\text{L}_{16}$) has recently been reported.⁴⁹

Experimental

All reagents were obtained from commercially available sources and used as received unless otherwise described. Methylene chloride used in picHA synthesis was purified on a Glass Contour solvent system prior to use. Methanol was dried where specified by distillation over magnesium. The $\text{Eu(III)[15-MC}_{\text{Ni(II),picHA-5}}\text{](NO}_3\text{)}_3$ was prepared following the reported procedure for the Sm(III) analog,⁴³ substituting $\text{Eu(NO}_3\text{)}_3$ for $\text{Sm(NO}_3\text{)}_3$. Electrospray ionization mass spectrometry (ESI-MS) was performed with a Micromass LCT time of flight electrospray ionization mass spectrometer at 150 °C at cone voltages of 50 V. Samples were injected via syringe pump as ~50 μM solutions. ESI-MS data was processed with MassLynx 4.0 software. NMR was performed on 400 or 500 MHz Varian spectrometers and the chemical shifts referenced to residual solvent signals or tetramethylsilane (TMS). ^1H Diffusion NMR was performed using a the DOSY gradient compensated stimulated echo with spin lock and convection compensation (DgcsteSL_cc) pulse sequence at temperatures of 293 K in pyridine- D_5 and 293 or 298 K in methanol- D_4 . A diffusion delay of 150 ms, diffusion gradient length of 3.0 ms, and a gradient strength array of 15-30 increments were used. The gradient field strength was

calibrated with D₂O by the University of Michigan NMR facility staff. The data was fit according to equation the equation $\ln(I/I_0) = -\gamma^2 \delta^2 G^2 (\Delta - \delta/3) D$ to solve for the diffusion coefficient (D), where I = intensity or integral of the peak at a given G, I₀ = intensity or integral of the peak at G = 0, γ = magnetogyric constant of the nucleus (for ¹H, $g = 2.675 \times 10^8 \text{ T}^{-1} \text{ s}^{-1}$), δ = diffusion gradient length, Δ = diffusion delay, G = gradient field strength. Cyclic voltammetry was performed on a BAS Epsilon potentiostat in 0.1 M aqueous potassium chloride. The working electrode was a 0.0707 cm² glassy carbon disk and a platinum wire counter electrode was employed. A BAS Ag/AgCl reference electrode was utilized. The electrochemical cell was water jacketed and held at a constant temperature (25.0 ± 0.1 °C) with a VWR 1145 refrigerated constant temperature controller. Thermogravimetric analysis was performed on a Perkin-Elmer TGA-7 thermogravimetric analyzer using a temperature ramp rate of 20 °C per minute.

Picoline hydroxamic acid: Following a modified literature method⁵⁰, picolinic acid (5 g, 40.6 mmol) and N-methylmorpholine (5.80 mL, 52.8 mmol) were mixed under nitrogen in 100 mL of dry dichloromethane at 0 °C. Ethyl chloroformate (4.64 mL, 48.7 mmol) was added dropwise via syringe, and the mixture was stirred for ten minutes. Separately, 100 mL of methanol was sparged with nitrogen for ten minutes. In separate flasks, hydroxylamine hydrochloride (4.23 g, 60.9 mmol) and 85% potassium hydroxide (3.93 g, 60.9 mmol) were each dissolved in 50 mL of the sparged methanol. The solutions were combined and cooled at 0 °C under a stream of nitrogen for ten minutes to precipitate potassium chloride. Under an ambient atmosphere, both solutions were vacuum filtered, combined, and sealed under a nitrogen atmosphere. After stirring for one hour at room temperature, the solvent was removed under vacuum, and the residue was taken up in 150 mL of water and washed with methylene chloride (2 x 50 mL). The aqueous layer was dried under vacuum, and the solid was recrystallized in ~15 mL of hot water, with white needles precipitating upon cooling in an ice bath. This solid was then recrystallized in ~75 mL of 1:1 tetrahydrofuran/dichloromethane (v/v) and filtered hot if necessary. To this hot solution, ~20 mL of hexanes was added to the cloudiness point. Homogeneity was restored with a few drops of dichloromethane, and the solution was cooled at -20 °C to yield white to faint pink needles. The product was isolated by vacuum filtration, ground into a fine powder, and thoroughly dried under vacuum. Yield = 3.13 g, 56%.

m.p. 116.5 °C (dec. Above 121 °C). ^1H NMR [$(\text{CD}_3)_2\text{SO}$, 500 Mhz, TMS], δ 11.45 (br, 1H) 9.11 (br, 1H), 8.60 (d, $^3\text{J}(\text{H,H})=6$ Hz, 1H, ph), 7.98(m, 2H, ph), 7.58 ppm (m, 1H, ph), ^{13}C NMR [$(\text{CD}_3)_2\text{SO}$, 100 Mhz, $(\text{CD}_3)_2\text{SO}$] δ 161.4, 150.1, 148.5, 137.6, 126.3, 121.8 ppm. IR (KBr): $\nu = 3173$ (b, O-H, N-H), 2860 (m, C-C), 1657 (s, C=O) 1591 (m), 1570 (m), 1495 (m), 1431 (m), 1178 (w), 1026 (w), 1000 (w), 823 (w), 703 (w), 624 cm^{-1} (w). CHN found (calc'd for $\text{C}_6\text{H}_6\text{N}_2\text{O}_2$) C: 52.10 (52.17), H: 4.34 (4.38), N: 20.32 (20.28).

Quinaldic hydroxamic acid: In a dry 250 mL flask, Quinaldic acid (6g, 0.0319 mol) was mixed with 100 mL dry methanol under N_2 in an ice bath. Thionyl chloride (0.0478 mol, 3.46 mL) was added dropwise, making the solution homogeneous. The solution was refluxed for 20 hours, cooled to room temperature, and evaporated to dryness under vacuum, yielding quinaldic acid methyl ester hydrochloride as an off-white powder. This solid was dissolved in 30 mL of degassed methanol, combined with a solution of potassium hydroxide (0.0319 mol, 2.06 g) in 30 mL of degassed methanol under a stream of N_2 , and cooled in an ice bath for fifteen minutes. Separately, solutions of hydroxylamine hydrochloride (0.0957 mol, 6.65 g) and potassium hydroxide (0.0957 mol, 6.19 g) in degassed methanol were prepared under a stream of N_2 , combined, and cooled in an ice bath for 15 minutes. The ester and hydroxylamine solutions were filtered to remove the white potassium chloride precipitate. The filtrates were combined, flushed with N_2 , stoppered, and stirred for two days at room temperature. Three additional equivalents of hydroxylamine were prepared from hydroxylamine hydrochloride and potassium hydroxide as described above and added to the reaction mixture. After 2 more days, the reaction mixture was concentrated to a volume of ~50 mL and the solid was triturated to break up and dissolve the yellow solid, though colorless solid (potassium chloride) remained. 425 mL of water was slowly added, leading to the precipitation of quinaldic hydroxamic acid as white needles and dissolution of potassium chloride. The solution was cooled in an ice bath and the solid was collected by vacuum filtration and rinsed with cold water. The white solid was ground to a fine powder and thoroughly dried in a vacuum desiccator over P_2O_5 . Yield = 4.90 g, 82%. mp = 144 °C (dec.); ^1H NMR δ (ppm) (400 mHz, CD_3OD), 8.38 (d, 1H, J = 8 Hz), 8.06 (m, 2H), 7.90 (d, 1H, J = 8 Hz), 7.74 (td, 1H), 7.60 (td, 1H); ^{13}C NMR δ (ppm) (100 mHz): 163.0, 149.3, 146.6, 137.4,

130.0, 129.3, 129.2, 127.6, 127.6, 118.1; IR (cm⁻¹): 3416 (O-H, br), 3135 (N-H, br), 2861 (C-H), 1664 (s), 1648 (s), 1625 (s), 1504 (s), 1424 (w), 1043 (m), 918 (m), 769 (w), 626 (w); CHN analysis found (calc'd for C₁₀H₈N₂O₂): C = 63.95 (63.83), H = 4.18 (4.29), N = 14.87 (14.89).

Zn(II)[12-MC_{Zn(II)}, picHA-4](OTf)₂: PicHA (1.086 mmol, 150.0 mg) and zinc triflate (1.358 mmol, 493.5 mg) were mixed with 10 mL of methanol and 1 mL of pyridine in a 125 mL Erlenmeyer flask. Triethylamine (2.172 mmol, 302.9 μL) was added and the solution was stirred for one hour. Ether (75 mL) was added all at once, resulting in a yellow-white precipitate. The flask was covered and faintly yellow crystals formed after sitting overnight. The crystals were isolated by filtration, ground to a fine powder, rinsed with 3 mL of -20° C methanol, and air dried. Addition of another 75 mL of ether to the filtrate and letting the solution sit led to the formation of additional crystals. Yield = 262.4 mg, 58%. ¹H NMR δ (ppm) (500 MHz, pyridine-D₅), 8.87 (d, 1H, J = 5 Hz), 8.39 (d, J = 8 Hz, 1H), 8.04 (t, 1H, J = 8 Hz), ESI-MS (methanol) gave m/z = 434.8²⁺ (434.9²⁺ calc'd for [Zn₅(picHA)₄]²⁺), 1018.5⁺ (1017.7⁺ calc'd for [Zn₅(picHA)₄(OTf)]⁺). CHN Analysis for [(Zn₅(C₆H₄N₂O₂)₄(OTf)₂(C₅H₅N)₅(H₂O)₅], found (calc'd): C = 36.89 (37.01), H = 2.84 (3.11), N = 10.94 (11.00).

Zn(II)[12-MC_{Zn(II)}, quinHA-4](NO₃)₂: QuinHA (0.399 mmol, 75.0 mg) and zinc nitrate hexahydrate (0.498 mmol, 148.2 mg) were mixed in 10 mL of a 4:1 methanol and pyridine mixture (v/v). Triethylamine (0.797 mmol, 111.2 μL) was added and the solution was stirred overnight. The solution was transferred to a 50 mL beaker and the beaker was placed in a wide-mouth jar containing ether (~75 mL). Yellow-orange crystals formed by ether vapor diffusion. The crystals were isolated by filtration. Yield = 131.2 mg, 85%. ¹H NMR δ (ppm) (400 MHz, CD₃OD), 8.77 (d, 1H, J = 9 Hz), 8.67 (d, J = 6 Hz, 1H), 8.32 (d, J = 8, 3H), 8.06 (d, 1H, J = 8 Hz), 8.01 (t, 1H, J = 8 Hz), 7.33 (t, 1H, J = 7 Hz), ESI-MS (methanol) gave m/z = 535.1²⁺ (535.9⁺ calc'd for [Zn₅(quinHA)₄]²⁺), 1132.2⁺ (1132.8⁺ calc'd for [Zn₅(quinHA)₄(NO₃)]⁺). CHN Analysis for [(Zn₅(C₁₀H₆N₂O₂)₄(NO₃)₂(C₅H₅N)₄(H₂O)_{2.5}], found (calc'd): C = 46.18 (46.28), H = 3.09 (3.17), N = 12.59 (12.59).

Zn(II)[12-MC_{Zn(II)}, quinHA-4](BF₄)₂: QuinHA (0.399 mmol, 75.0 mg) and zinc tetrafluoroborate hydrate (0.498 mmol, 128.0 mg) were mixed in 10 mL of a 4:1

methanol and pyridine mixture (v/v). Triethylamine (0.797 mmol, 111.2 μ L) was added and the solution was stirred overnight. The solution was transferred to a 50 mL beaker and placed in a wide-mouth jar containing ether (~75 mL). Long yellow needles crystallized upon ether vapor diffusion and were isolated by filtration, rinsed with -20 $^{\circ}$ C methanol, and air dried. Yield = 86.1 mg, 51%, ESI-MS (methanol) gave $m/z = 534.9^{2+}$ (535.9^{+} calc'd for $[\text{Zn}_5(\text{quinHA})_4]^{2+}$). CHN Analysis for $[(\text{Zn}_5(\text{C}_{10}\text{H}_6\text{N}_2\text{O}_2)_4(\text{BF}_4)_2(\text{C}_5\text{H}_5\text{N})_{5.5})]$, found (calc'd): C = 48.42 (48.25), H = 3.28 (3.09), N = 11.27 (11.25).

LnZn₅(picHA)₅: A general synthesis for the LnZn₅(picHA)₅ is described below for the Eu(III) analog. Analogues of other lanthanides were prepared by substituting the appropriate lanthanide ion for Eu(III). Characterizations of all isolated complexes are provided after the synthetic exemplar.

Eu(III)(NO₃)₃[15-MC_{Zn(II)}, picHA-5]: PicHA (0.724 mmol, 100.0 mg), zinc nitrate hexahydrate (0.724 mmol, 215.4 mg), and europium nitrate pentahydrate (0.145 mmol, 62.0 mg) were combined in 12 mL of a premixed solution of 4:1 methanol and pyridine (v/v). Triethylamine (1.45 mmol, 202.0 μ L) was added and the solution was stirred overnight. The solution was transferred to a 50 mL beaker and crystallized by ether vapor diffusion in a wide-mouth jar containing ~75 mL of ether. The yellow crystals were isolated by filtration. Yield = 140.5 mg, 56%. ESI-MS (pyridine) gave $m/z = 587.9^{2+}$ (587.8^{2+} calc'd for $[\text{EuZn}_5(\text{picHA})_5(\text{OH})]^{2+}$), 610.4^{2+} (610.3^{2+} calc'd for $[\text{EuZn}_5(\text{picHA})_5(\text{NO}_3)]^{2+}$). CHN Analysis for $[(\text{EuZn}_5(\text{C}_6\text{H}_4\text{N}_2\text{O}_2)_5(\text{NO}_3)_3(\text{C}_5\text{H}_5\text{N})_4(\text{H}_2\text{O})_4)]$, found (calc'd): C = 34.78 (34.64), H = 2.63 (2.79), N = 13.85 (13.73).

La(III)(NO₃)₃[15-MC_{Zn(II)}, picHA-5]: Yield = 155.5 mg, 62%. ¹H NMR δ (ppm) (500 mHz, pyridine-D₅), 8.79 (d, 1H, J = 5 Hz), 8.30 (d, J = 8 Hz, 1H), 7.88 (t, 1H, J = 8 Hz), 7.39 (t, 1H, J = 6 Hz), ESI-MS (pyridine) gave $m/z = 580.9^{2+}$ (580.8^{2+} calc'd for $[\text{LaZn}_5(\text{picHA})_5(\text{OH})]^{2+}$), 620.9^{2+} (620.4^{2+} calc'd for $[\text{LaZn}_5(\text{picHA})_5(\text{OH})(\text{pyridine})]^{2+}$). CHN Analysis for $[(\text{LaZn}_5(\text{C}_6\text{H}_4\text{N}_2\text{O}_2)_5(\text{NO}_3)_3(\text{C}_5\text{H}_5\text{N})_4(\text{H}_2\text{O})_4)]$, found (calc'd): C = 34.79 (34.90), H = 2.68 (2.81), N = 13.94 (13.84).

Nd(III)(NO₃)₃[15-MC_{Zn(II)}, picHA-5]: Yield = 143.4 mg, 58%. ESI-MS (pyridine) gave $m/z = 584.4^{2+}$ (584.3^{2+} calc'd for $[\text{NdZn}_5(\text{picHA})_5(\text{OH})]^{2+}$), 606.9^{2+} (606.8^{2+} calc'd for

[NdZn₅(picHA)₅(NO₃)₂]²⁺. CHN Analysis for [(NdZn₅(C₆H₄N₂O₂)₅(NO₃)₃(C₅H₅N)₄(H₂O)₃], found (calc'd): C = 35.07 (35.16), H = 2.66 (2.71), N = 13.75 (13.62).

Gd(III)(NO₃)₃[15-MC_{Zn(II), picHA-5}]: Yield = 136.9 mg, 54%. ESI-MS (pyridine) gave m/z = 590.4⁺ (590.4⁺ calc'd for [GdZn₅(picHA)₅(OH)]²⁺), 612.8²⁺ (612.8²⁺ calc'd for [GdZn₅(picHA)₅(NO₃)₂]²⁺). CHN Analysis for [(GdZn₅(C₆H₄N₂O₂)₅(NO₃)₃(C₅H₅N)₄(H₂O)_{4.5}], found (calc'd): C = 34.30 (34.35), H = 2.64 (2.83), N = 13.97 (13.94).

LnZn₅(quinHA)₅: A general synthesis for these compounds is described below for the Dy(III) analog. Complexes with other lanthanides were prepared by substituting the appropriate lanthanide ion for Dy(III). Characterizations of all isolated complexes are provided after the synthetic exemplar.

Dy(III)(NO₃)₂[15-MC_{Zn(II), quinHA-5}](NO₃): QuinHA (0.425 mmol, 80.0 mg), zinc nitrate hexahydrate (0.425 mmol, 126.4 mg), and dysprosium nitrate hexahydrate (0.085 mmol, 37.3 mg) were combined in 15 mL of pyridine. Triethylamine (0.850 mmol, 118.6 μL) was added and the solution was stirred overnight. The solution was transferred to a 50 mL beaker and crystallized by ether vapor diffusion in a wide-mouth jar containing ~75 mL of ether. The yellow-orange crystals were isolated by filtration, rinsed with -20° C pyridine, and air dried. Yield = 135.7 mg, 76%. ESI-MS (pyridine) gave m/z = 740.8²⁺ (740.9⁺ calc'd for [DyZn₅(quinHA)₅(NO₃)₂]²⁺). CHN Analysis for [(DyZn₅(C₁₀H₆N₂O₂)₅(NO₃)₃(C₅H₅N)₆(H₂O)]₃, found (calc'd): C = 45.29 (45.78), H = 3.06 (2.98), N = 12.75 (12.68).

Tb(III)(NO₃)₂[15-MC_{Zn(II), quinHA-5}](NO₃): Yield = 136.0 mg, 75%. ESI-MS (pyridine) gave m/z = 738.3²⁺ (739.4²⁺ calc'd for [TbZn₅(quinHA)₅(NO₃)₂]²⁺), 1540.7⁺ (1539.7⁺ calc'd for [TbZn₅(quinHA)₅(NO₃)₂]⁺). CHN Analysis for [(TbZn₅(C₁₀H₆N₂O₂)₅(NO₃)₃(C₅H₅N)₆(H₂O)₃], found (calc'd): C = 44.97 (45.08), H = 2.85 (2.89), N = 12.37 (12.63).

Y(III)(NO₃)₂[15-MC_{Zn(II), quinHA-5}](NO₃): Yield = 101.7 mg, 63%. ¹H NMR δ (ppm) (500 MHz, pyridine-D₅), 9.27 (d, 1H, J = 9 Hz), 8.78 (d, J = 8 Hz, 1H), 8.62 (d, 1H, J = 9 Hz), 7.99 (m, 2H), 7.63 (t, 1H, J = 7 Hz), ESI-MS (pyridine) gave m/z = 703.3²⁺ (704.4²⁺ calc'd for [YZn₅(quinHA)₅(NO₃)₂]²⁺). CHN Analysis for

$[(Y\text{Zn}_5(\text{C}_{10}\text{H}_6\text{N}_2\text{O}_2)_5(\text{NO}_3)_3(\text{C}_5\text{H}_5\text{N})_4(\text{H}_2\text{O})_2]$, found (calc'd): C = 44.51 (44.60), H = 2.84 (2.89), N = 12.64 (12.63).

Er(III)(NO₃)₂[15-MC_{Zn(II), quinHA-5}](NO₃): Yield = 122.3 mg, 74%. ESI-MS (pyridine) gave $m/z = 742.9^{2+}$ (742.9^{2+} calc'd for $[\text{ErZn}_5(\text{quinHA})_5(\text{NO}_3)]^{2+}$). CHN Analysis for $[(\text{ErZn}_5(\text{C}_{10}\text{H}_6\text{N}_2\text{O}_2)_5(\text{NO}_3)_3(\text{C}_5\text{H}_5\text{N})_4(\text{H}_2\text{O})_{1.5}]$, found (calc'd): C = 43.00 (43.02), H = 2.69 (2.73), N = 12.24 (12.18).

Nd(III)(NO₃)₂[15-MC_{Zn(II), quinHA-5}](NO₃): Yield = 136.3 mg, 79%. ESI-MS (pyridine) gave $m/z = 731.9^{2+}$ (731.9^{2+} calc'd for $[\text{NdZn}_5(\text{quinHA})_5(\text{NO}_3)]^{2+}$). CHN Analysis for $[(\text{NdZn}_5(\text{C}_{10}\text{H}_6\text{N}_2\text{O}_2)_5(\text{NO}_3)_3(\text{C}_5\text{H}_5\text{N})_5(\text{H}_2\text{O})_3]$, found (calc'd): C = 44.18 (44.21), H = 2.74 (3.02), N = 12.47 (12.37).

Ho(III)(NO₃)₂[15-MC_{Zn(II), quinHA-5}](NO₃): Yield = 156.1 mg, 92%. ESI-MS (pyridine) gave $m/z = 742.4^{2+}$ (742.4^{2+} calc'd for $[\text{HoZn}_5(\text{quinHA})_5(\text{NO}_3)]^{2+}$). CHN Analysis for $[(\text{HoZn}_5(\text{C}_{10}\text{H}_6\text{N}_2\text{O}_2)_5(\text{NO}_3)_3(\text{C}_5\text{H}_5\text{N})_5(\text{H}_2\text{O})_2]$, found (calc'd): C = 43.42 (43.51), H = 2.76 (2.85), N = 12.30 (12.25).

LnZn₄(quinHA)₄: A general synthesis for these compounds is described below for the Dy(III) analog. Complexes with other lanthanides were prepared by substituting the appropriate lanthanide ion for Dy(III). Characterizations of all isolated complexes are provided after the synthetic exemplar.

Dy(III)[12-MC_{Zn(II), quinHA-4}](NO₃)₃: QuinHA (0.133 mmol, 25.0 mg), zinc nitrate hexahydrate (0.133 mmol, 39.5 mg), and dysprosium nitrate hexahydrate (0.33 mmol, 14.6 mg) were combined in 3 mL of a 4:1 mixture of methanol and pyridine (v/v). Triethylamine (0.266 mmol, 37.1 μL) was added followed by the addition of 3 mL of dimethylformamide (DMF). Once homogeneous, the solution was immediately transferred to a 50 mL beaker and crystallized by ether vapor diffusion in a wide-mouth jar containing ~ 75 mL of ether. The yellow-orange crystals were isolated by filtration, rinsed with -20°C pyridine, and air dried. Yield = 49.4 mg, 72%. ESI-MS (pyridine) gave $m/z = 614.9^{2+}$ (614.9^{2+} calc'd for $[\text{DyZn}_4(\text{quinHA})_4(\text{NO}_3)]^{2+}$), 1290.8^+ (1291.7^+ calc'd for $[\text{DyZn}_4(\text{quinHA})_4(\text{NO}_3)_2]^+$). CHN Analysis for $[(\text{DyZn}_4(\text{C}_{10}\text{H}_6\text{N}_2\text{O}_2)_4(\text{NO}_3)_3(\text{C}_5\text{H}_5\text{N})_4(\text{DMF})_4(\text{H}_2\text{O})_5]$, found (calc'd): C = 41.81 (42.11), H = 3.63 (4.03), N = 12.98 (12.96).

Y(III)[12-MC_{Zn(II), quinHA-4}](NO₃)₃: Yield = 43.1 mg, 65%. ESI-MS (pyridine) gave m/z = 577.4²⁺ (578.4²⁺ calc'd for [YZn₄(quinHA)₄(NO₃)₂]²⁺), 1216.7⁺ (1217.8⁺ calc'd for [YZn₄(quinHA)₄(NO₃)₂]⁺). CHN Analysis for [(YZn₄(C₁₀H₆N₂O₂)₄(NO₃)₃(C₅H₅N)₄(DMF)₄(H₂O)_{6.5}], found (calc'd): C = 42.90 (43.09), H = 3.59 (4.27), N = 13.24 (13.26).

Tb(III)[12-MC_{Zn(II), quinHA-4}](NO₃)₃: Yield = 39.7 mg, 27%. ESI-MS (9:1 DMF/pyridine (v/v)) gave m/z = 613.5²⁺ (613.4⁺ calc'd for [TbZn₄(quinHA)₄(NO₃)₂]²⁺). CHN Analysis for [(TbZn₄(C₁₀H₆N₂O₂)₄(NO₃)₃(C₅H₅N)₄(DMF)₄(H₂O)₇], found (calc'd): C = 41.22 (41.46), H = 3.39 (4.16), N = 12.80 (12.76).

Er(III)[12-MC_{Zn(II), quinHA-4}](NO₃)₃: Yield = 79.6 mg, 57%. ESI-MS (9:1 DMF/pyridine (v/v)) gave m/z = 617.0²⁺ (617.9²⁺ calc'd for [ErZn₄(quinHA)₄(NO₃)₂]²⁺). CHN Analysis for [(ErZn₄(C₁₀H₆N₂O₂)₄(NO₃)₃(C₅H₅N)₄(DMF)₄(H₂O)_{6.5}], found (calc'd): C = 41.31 (41.47), H = 3.49 (4.11), N = 12.65 (12.76).

LnZn₈(picHA)₈

La(III)[12-MC_{Zn(II), picHA-4}]₂Cl₃: PicHA (100 mg, 0.724 mmol), zinc chloride (128.3 mg, 0.941 mmol), and La(NO₃)₃ hexahydrate (62.7 mg, 0.145 mmol) were mixed in 15 mL of a 9:1 water/pyridine mixture (v/v). After stirring overnight, the solution was set to slowly evaporate, yielding yellow crystals within two weeks. The crystals were isolated by filtration and rinsed with a -20 °C solution of 4:1 water/pyridine. Yield = 60.0 mg, 16% based on picHA. ESI-MS (4:1 water/pyridine): 583.5³⁺ (583.5³⁺ calc'd for [LaZn₈(C₆H₄N₂O₂)₈]³⁺), 882.8²⁺ (883.8²⁺ calc'd for [LaZn₈(C₆H₄N₂O₂)₈(OH)]²⁺), 893.8²⁺ (892.8²⁺ calc'd for [LaZn₈(C₆H₄N₂O₂)₈Cl]²⁺). CHN: found (calc'd for LaZn₈(C₆H₄N₂O₂)₈(C₅H₅N)_{6.5}Cl₃(H₂O)_{8.5}) C: 38.55 (38.30), H: 3.10 (3.25), N: 11.91 (11.48).

Dy(III)[12-MC_{Zn(II), picHA-4}]₂(OH)₃: PicHA (100 mg, 0.724 mmol), zinc carbonate basic (79.5 mg, 0.724 mmol), and dysprosium carbonate (69.6 mg, 2.41 mmol) were mixed in 10 mL of a 9:1 water/pyridine mixture (v/v). After stirring overnight, the solution was filtered through a fine glass frit. The filtrate was set to crystallize by THF vapor diffusion. After two days, the solution was filtered to remove white precipitate and again set to crystallize by THF vapor diffusion. Yellow crystals formed within two weeks and were isolated by filtration and rinsed with a -20 °C solution of 4:1 water/pyridine. Yield

= 28.6 mg, 14% based on picHA. ESI-MS (4:1 water/pyridine): 895.2²⁺ (895.3²⁺ calc'd for DyZn₈(C₆H₄N₂O₂)₈(OH)]²⁺). CHN: found (calc'd for DyZn₈(C₆H₄N₂O₂)₈(C₅H₅N)₂(OH)₃(H₂O)_{1.5}) C: 31.08 (30.91), H: 2.83 (3.35), N: 10.59 (11.19).

Nd(III)[12-MC_{Zn(II)}, picHA-4]₂(OH)₃: The NdZn₈(picHA)₈(OH)₃ was synthesized following the procedure for DyZn₈(picHA)₈(OH)₃, substituting neodymium carbonate for dysprosium carbonate. Yield = 18.3 mg, 10% based on picHA. ESI-MS (4:1 water/pyridine): 585.9³⁺ (585.2³⁺ calc'd for NdZn₈(C₆H₄N₂O₂)₈]³⁺), 886.3²⁺ (886.3²⁺ calc'd for NdZn₈(C₆H₄N₂O₂)₈(OH)]²⁺). CHN: found (calc'd for NdZn₈(C₆H₄N₂O₂)₈(C₅H₅N)₂(OH)₃(H₂O)_{6.5}) C: 33.66 (33.45), H: 2.65 (2.81), N: 11.55 (12.11).

LnZn₁₆(picHA)₁₆: Two general syntheses were developed that are described below for TbZn₁₆L₁₆ and YbZn₁₆L₁₆. The procedure for TbZn₁₆(picHA)₁₆ yields larger crystals suitable for crystal structure determination and is more effective for larger lanthanides such as La(III). The procedure for YbZn₁₆(picHA)₁₆ is more effective for smaller lanthanides and tends to yield higher purity material, though the crystals are typically too small for structure determination and it is less effective with large lanthanide ions. Triethylamine can be substituted for sodium hydroxide in both procedures. Characterizations of all isolated complexes are provided after the two synthetic exemplars.

Tb(III)[12-MC_{Zn(II)}, quinHA-4]₂[24-MC_{Zn(II)}, quinHA-8](OTf)₃: PicHA (150 mg, 1.09 mmol) and sodium hydroxide (86.9 mg, 2.17 mmol) were stirred in 20 mL of methanol. Once dissolved, zinc trifluoromethanesulfonate (395 mg, 1.09 mmol) was added, turning the solution cloudy. Terbium nitrate (29.5 mg, 0.068 mmol) was then added and the solution gradually clarified. After twenty minutes, 5 mL of pyridine was added. After stirring overnight, the solution was gravity filtered and set to slowly evaporate, yielding yellow crystals within two weeks. Occasionally a second filtration is required after about two days to remove a white precipitate. Yield = 115.2 mg, 36%. ESI-MS (methanol): 1127.2³⁺ (1127.4³⁺ calc'd for [TbZn₁₆(C₆H₄N₂O₂)₁₆]³⁺). CHN: found (calc'd for TbZn₁₆(C₆H₄N₂O₂)₁₆(C₅H₅N)₈(CF₃SO₃)₃(H₂O)₁₂(CH₃OH)) C: 35.22 (35.69), H: 2.38 (2.82), N: 11.57 (11.89).

Yb(III)[12-MC_{Zn(II), quinHA-4}]₂[24-MC_{Zn(II), quinHA-8}](OTf)₃: PicHA (150 mg, 1.09 mmol), sodium hydroxide (2.186 mL of a 0.9937 M solution in methanol, 2.17 mmol), zinc trifluoromethanesulfonate (395 mg, 1.09 mmol), and ytterbium nitrate (30.5 mg, 0.068 mmol) were stirred in 20 mL of methanol for twenty minutes. 5 mL of pyridine was added. After another 20 minutes, 5 mL of water was added. After another twenty minutes, the solution was gravity filtered and set to slowly evaporate, yielding yellow crystals within two weeks. Yield = 22.9 mg, 7%. ESI-MS (methanol): 1132.5³⁺ [1132.4³⁺ calc'd. For YbZn₁₆(C₆H₄N₂O₂)₁₆³⁺]. CHN found (calc'd for YbZn₁₆(C₆H₄N₂O₂)₁₆(C₅H₅N)₈(CF₃SO₃)₃(H₂O)₂(CH₄O)₄) C: 37.40 (37.01), H: 2.50 (2.69), N: 11.85 (12.07).

La(III)[12-MC_{Zn(II), quinHA-4}]₂[24-MC_{Zn(II), quinHA-8}](OTf)₃. Yield = 51.7 mg, 16%. ¹H NMR δ (ppm) (500 mHz, CD₃OD), 8.13 (d, 1H, J = 6 Hz), 7.96 (d, J = 9 Hz, 1H), 7.78 (m, 3H), 7.46 (d, 1H, J = 10 Hz), 7.31 (t, 1H, J = 8 Hz), 6.84 (t, 1H, J = 8 Hz), ESI-MS (methanol): 1120.8³⁺ [1120.7³⁺ calc'd. For LaZn₁₆(C₆H₄N₂O₂)₁₆³⁺]. CHN found (calc'd for LaZn₁₆(C₆H₄N₂O₂)₁₆(C₅H₅N)₈(CF₃SO₃)₃(H₂O)₄(CH₄O)) C: 37.09 (37.00), H: 2.40 (2.78), N: 12.36 (12.07).

Nd(III)[12-MC_{Zn(II), quinHA-4}]₂[24-MC_{Zn(II), quinHA-8}](OTf)₃. Yield = 144.0 mg, 47%. ESI-MS (methanol): 1122.4³⁺ [1122.4³⁺ calc'd. For NdZn₁₆(C₆H₄N₂O₂)₁₆³⁺]. CHN found (calc'd for NdZn₁₆(picHA)₁₆(py)₈(OTf)₃(H₂O)₄) C: 37.02 (36.93), H: 2.37 (2.50), N: 12.20 (12.39).

Sm(III)[12-MC_{Zn(II), quinHA-4}]₂[24-MC_{Zn(II), quinHA-8}](OTf)₃. Yield = 159.7 mg, 50%. ESI-MS (methanol): 1124.3³⁺ [1124.4³⁺ calc'd. For SmZn₁₆(C₆H₄N₂O₂)₁₆³⁺]. CHN found (calc'd for SmZn₁₆(C₆H₄N₂O₂)₁₆(C₅H₅N)₈(CF₃SO₃)₃(H₂O)₁₂) C: 35.49 (35.75), H: 2.26 (2.76), N: 12.00 (11.83).

Eu(III)[12-MC_{Zn(II), quinHA-4}]₂[24-MC_{Zn(II), quinHA-8}](OTf)₃. Yield = 62.9 mg, 20%. ESI-MS (methanol): 1125.2³⁺ [1125.4³⁺ calc'd. For EuZn₁₆(C₆H₄N₂O₂)₁₆³⁺]. CHN found (calc'd for EuZn₁₆(C₆H₄N₂O₂)₁₆(C₅H₅N)₈(CF₃SO₃)₃(H₂O)₉) C: 35.95 (36.15), H: 2.44 (2.66), N: 11.94 (12.13).

Gd(III)[12-MC_{Zn(II), quinHA-4}]₂[24-MC_{Zn(II), quinHA-8}](OTf)₃. Yield = 155.0 mg, 49%. ESI-MS (methanol): 1126.8³⁺ [1127.1³⁺ calc'd. For GdZn₁₆(C₆H₄N₂O₂)₁₆³⁺]. CHN found

(calc'd for $\text{GdZn}_{16}(\text{C}_6\text{H}_4\text{N}_2\text{O}_2)_{16}(\text{C}_5\text{H}_5\text{N})_8(\text{CF}_3\text{SO}_3)_3(\text{H}_2\text{O})_9$) C: 35.81 (35.99), H: 2.58 (2.83), N: 11.75 (11.91).

Dy(III)[12-MC_{Zn(II), quinHA-4}]₂[24-MC_{Zn(II), quinHA-8}](OTf)₃. Yield = 99.3 mg, 31%. ESI-MS (methanol): 1128.5³⁺ [1128.7³⁺ calc'd. For $\text{DyZn}_{16}(\text{C}_6\text{H}_4\text{N}_2\text{O}_2)_{16}^{3+}$]. CHN found (calc'd for $\text{DyZn}_{16}(\text{C}_6\text{H}_4\text{N}_2\text{O}_2)_{16}(\text{C}_5\text{H}_5\text{N})_8(\text{CF}_3\text{SO}_3)_3(\text{H}_2\text{O})_{10}(\text{CH}_3\text{OH})_2$) C: 35.66 (35.79), H: 2.41 (2.72), N: 11.81 (12.01).

Ho(III)[12-MC_{Zn(II), quinHA-4}]₂[24-MC_{Zn(II), quinHA-8}](OTf)₃. Yield = 117.7 mg, 36%. ESI-MS (methanol): 1129.1³⁺ [1129.4³⁺ calc'd. For $\text{HoZn}_{16}(\text{C}_6\text{H}_4\text{N}_2\text{O}_2)_{16}^{3+}$]. CHN found (calc'd for $\text{HoZn}_{16}(\text{C}_6\text{H}_4\text{N}_2\text{O}_2)_{16}(\text{C}_5\text{H}_5\text{N})_8(\text{CF}_3\text{SO}_3)_3(\text{H}_2\text{O})_{20}$) C: 34.52 (34.57), H: 2.62 (3.01), N: 11.38 (11.60).

Er(III)[12-MC_{Zn(II), quinHA-4}]₂[24-MC_{Zn(II), quinHA-8}](OTf)₃. Yield = 152.3 mg, 47%. ESI-MS (methanol): 1129.8³⁺ [1130.4³⁺ calc'd. For $\text{ErZn}_{16}(\text{C}_6\text{H}_4\text{N}_2\text{O}_2)_{16}^{3+}$]. CHN found (calc'd for $\text{ErZn}_{16}(\text{C}_6\text{H}_4\text{N}_2\text{O}_2)_{16}(\text{C}_5\text{H}_5\text{N})_8(\text{CF}_3\text{SO}_3)_3(\text{H}_2\text{O})_{16}$) C: 35.30 (35.08), H: 2.71 (2.88), N: 11.47 (11.77).

Tm(III)[12-MC_{Zn(II), quinHA-4}]₂[24-MC_{Zn(II), quinHA-8}](OTf)₃. Yield = 52.1 mg, 16%. ESI-MS (methanol): 1130.1³⁺ [1130.7³⁺ calc'd. For $\text{TmZn}_{16}(\text{C}_6\text{H}_4\text{N}_2\text{O}_2)_{16}^{3+}$]. CHN found (calc'd for $\text{TmZn}_{16}(\text{C}_6\text{H}_4\text{N}_2\text{O}_2)_{16}(\text{C}_5\text{H}_5\text{N})_8(\text{CF}_3\text{SO}_3)_3(\text{H}_2\text{O})_6(\text{CH}_3\text{OH})_3$) C: 37.27 (37.12), H: 2.88 (2.82), N: 12.02 (12.07).

Y(III)[12-MC_{Zn(II), quinHA-4}]₂[24-MC_{Zn(II), quinHA-8}](OTf)₃. Yield = 155.4 mg, 50%. ¹H NMR δ (ppm) (500 mHz, CD₃OD), 8.14 (d, J = 5 Hz, 1H), 7.96 (d, J = 8 Hz, 1H), 7.77 (m, 3H), 7.50 (d, J = 8 Hz, 1H), 7.32 (t, 1H, J = 6 Hz), 6.80 (t, 1H, J = 6 Hz), ESI-MS (methanol): 1103.4³⁺ [1104.1³⁺ calc'd. For $\text{YZn}_{16}(\text{C}_6\text{H}_4\text{N}_2\text{O}_2)_{16}^{3+}$]. CHN found (calc'd for $\text{YZn}_{16}(\text{C}_6\text{H}_4\text{N}_2\text{O}_2)_{16}(\text{C}_5\text{H}_5\text{N})_8(\text{CF}_3\text{SO}_3)_3(\text{H}_2\text{O})_9(\text{CH}_3\text{OH})_2$) C: 36.61 (36.66), H: 2.74 (2.84), N: 11.99 (12.13).

Ln₂Zn₉(quinHA)₁₀: A general synthesis for these compounds is described below for the Dy(III) analog. Complexes with other lanthanides were prepared by substituting the appropriate lanthanide ion for Dy(III). Characterizations of all isolated complexes are provided after synthetic exemplar.

Dy₂Zn₉(quinHA)₁₀(OH)(NO₃)₂Cl : QuinHA (0.664 mmol, 125.0 mg), zinc chloride (0.531 mmol, 72.5 mg), triethylamine (1.33 mmol, 185 μL), and dysprosium nitrate hexahydrate (0.133 mmol, 58.2 mg) were stirred in 20 mL of a 1:1 mixture of water and

pyridine (v/v). Once homogeneous, the solution was immediately transferred to a 50 mL beaker and crystallized by benzene vapor diffusion in a wide-mouth jar containing ~75 mL of benzene. Yellow-orange crystals were isolated by filtration, rinsed with a 4° C 4:1 mixture of water and pyridine (v/v), and air dried. Yield = 166.1 mg, 67% based on H₂quinHA. ESI-MS (4:1 water/pyridine (v/v)) gave m/z = 930.5³⁺ (930.3³⁺ calc'd for [Dy₂Zn₉(quinHA)₁₀(OH)]³⁺), CHN Analysis for [(Dy₂Zn₉(C₁₀H₆N₂O₂)₁₀(OH)Cl(NO₃)₂(C₅H₅N)₈(H₂O)_{9.5}], found (calc'd): C = 44.60 (44.77), H = 3.00 (3.22), N = 11.28 (11.19).

Tb₂Zn₉(quinHA)₁₀(OH)(NO₃)_{2.5}Cl_{0.5}: Yield = 158.5 mg, 63% based on H₂quinHA. ESI-MS (4:1 water/pyridine (v/v)) gave m/z = 928.4³⁺ (928.2³⁺ calc'd for [Tb₂Zn₉(quinHA)₁₀(OH)]³⁺), CHN Analysis for [(Tb₂Zn₉(C₁₀H₆N₂O₂)₁₀(OH)Cl(NO₃)₂(C₅H₅N)₈(H₂O)_{9.5}], found (calc'd): C = 44.02 (44.17), H = 2.84 (3.31), N = 11.26 (11.08).

Eu₂Zn₉(quinHA)₁₀(OH)(NO₃)_{2.5}Cl_{0.5}: Yield = 168.5 mg, 68% based on H₂quinHA. ESI-MS (4:1 water/pyridine (v/v)) gave m/z = 923.4³⁺ (923.5³⁺ calc'd for [Tb₂Zn₉(quinHA)₁₀(OH)]³⁺), CHN Analysis for [(Tb₂Zn₉(C₁₀H₆N₂O₂)₁₀(OH)Cl(NO₃)₂(C₅H₅N)₈(H₂O)_{9.5}], found (calc'd): C = 44.80 (44.76), H = 2.85 (3.25), N = 11.43 (11.37).

Zn₄(picHA)₂(acetate)₄(DMF)₂: Picoline hydroxamic acid (0.724 mmol, 100 mg), zinc acetate dihydrate (0.724 mmol, 158.9 mg), and europium nitrate pentahydrate (0.145 mmol, 62.1 mg) were stirred in 15 mL of methanol overnight. 3 mL of DMF was added, and the solution was set aside to crystallize by slow evaporation. In two weeks, the faintly yellow crystals that formed were isolated by vacuum filtration and rinsed with -20 °C methanol. Yield = 37.2 mg, 22 % based on Zn(II), CHN Analysis for [Zn₄(C₆H₄N₂O₂)₂(C₂H₃O₂)₂(C₃H₇NO)₂], found (calc'd): C = 34.19 (34.09), H = 3.75 (3.74), N = 9.28 (9.17).

LnZn₄(quinHA)₄(12-crown-4): A general synthesis for these compounds is described below for the Dy(III) analog. Complexes with other lanthanides were prepared by substituting the appropriate lanthanide ion for Dy(III). Characterizations of all isolated complexes are provided after the synthetic exemplar.

Dy(III)[12-MC_{Zn(II), quinHA-4}](12-crown-4)(OTf)₃: QuinHA (0.638 mmol, 120 mg), zinc triflate (0.638 mmol, 231.8 mg), and dysprosium triflate (0.159 mmol, 102.9 mg) were combined in 12 mL pyridine. Triethylamine (1.275 mmol, 177.9 μ L) was added followed by the addition of 12-crown-4 (0.478 mmol, 77.4 μ L). The solution was stirred overnight, transferred to a 50 mL beaker and crystallized by benzene vapor diffusion in a wide-mouth jar containing \sim 75 mL of benzene. The yellow-orange crystals were isolated by filtration, rinsed with -20 $^{\circ}$ C pyridine, and air dried. Yield = 190.8 mg, 54%. CHN Analysis for [DyZn₄(C₁₀H₆N₂O₂)₄(C₈H₁₂O₄)₃(C₅H₅N)₅(C₆H₆)_{0.5}(CF₃SO₃)₃], found (calc'd): C = 42.68 (42.61), H = 3.13 (3.08), N = 8.16 (8.18).

Tb(III)[12-MC_{Zn(II), quinHA-4}](12-crown-4)(OTf)₃: Yield = 318.1 mg, 86%. CHN Analysis for [TbZn₄(C₁₀H₆N₂O₂)₄(C₈H₁₂O₄)₃(C₅H₅N)_{5.5}(C₆H₆)_{0.5}(CF₃SO₃)₃(H₂O)_{2.5}], found (calc'd): C = 42.48 (42.42), H = 3.01 (3.30), N = 8.34 (8.19).

Er(III)[12-MC_{Zn(II), quinHA-4}](12-crown-4)(OTf)₃: Yield = 304.0 mg, 86%. CHN Analysis for [ErZn₄(C₁₀H₆N₂O₂)₄(C₈H₁₂O₄)₃(C₅H₅N)₅(C₆H₆)(CF₃SO₃)₃(H₂O)_{2.5}], found (calc'd): C = 42.38 (42.53), H = 3.02 (3.31), N = 8.06 (7.86).

Yb(III)[12-MC_{Zn(II), quinHA-4}](12-crown-4)(OTf)₃: Yield = 278.6 mg, 76%. CHN Analysis for [YbZn₄(C₁₀H₆N₂O₂)₄(C₈H₁₂O₄)₃(C₅H₅N)₅(C₆H₆)(CF₃SO₃)₃(H₂O)₂], found (calc'd): C = 42.69 (42.59), H = 3.09 (3.27), N = 7.97 (7.88).

Y(III)[12-MC_{Zn(II), quinHA-4}](12-crown-4)(OTf)₃: Yield = 299.6 mg, 85%. CHN Analysis for [YZn₄(C₁₀H₆N₂O₂)₄(C₈H₁₂O₄)₃(C₅H₅N)_{5.5}(C₆H₆)_{0.5}(CF₃SO₃)₃(H₂O)_{1.5}], found (calc'd): C = 44.20 (44.10), H = 3.26 (3.34), N = 8.43 (8.52).

Photophysical Procedures: All photophysical data presented in this chapter was collected by Dr. Christopher M. Andolina in the laboratory of Prof. Kenneth N. Raymond at the University of California, Berkeley. Stock solutions of the complexes were made using *ca.* 5.0 mg of sample in 5 mL of dry HPLC grade methanol. Typical sample concentrations for absorption and fluorescence measurements were *ca.* 3×10^{-7} to 5×10^{-6} M. Measurements were collected 1.0 cm cells in quartz Spectrosil[®] or equivalent (Starna Cells, Inc.). UV-Visible absorption spectra were recorded on a HP 8542 diode array absorption spectrometer equipped with a temperature controller at 25.0 $^{\circ}$ C. Emission spectra were acquired on a HORIBA Jobin Yvon IBH FluoroLog-3 spectrofluorometer equipped with a temperature controller at 25.0 $^{\circ}$ C. Spectra were

reference corrected for both the excitation light source variation (lamp and grating) and the emission spectral response (detector and grating). Quantum yields were determined by the optically dilute method using the following equation;

$$\frac{\Phi_x}{\Phi_r} = \left[\frac{A_r(\lambda_r)}{A_x(\lambda_x)} \right] \left[\frac{I(\lambda_r)}{I(\lambda_x)} \right] \left[\frac{n_x^2}{n_r^2} \right] \left[\frac{D_x}{D_r} \right]$$

where A is the absorbance at the excitation wavelength (λ), I is the intensity of the excitation light at the same wavelength, n is the refractive index and D is the integrated luminescence intensity (900-1100 nm). The subscripts 'x' and 'r' refer to the sample and reference, respectively. A quantum yield standard, Yb(dipicolinate)₃³⁻, in 0.1 M TRIS buffer pH = 7.4 ($\Phi_r = 0.015 \pm 0.02$ %) was used as a reference⁵¹ and prepared according to the literature.⁵²

Luminescence lifetimes were determined with a HORIBA Jobin Yvon IBH FluoroLog-3 spectrofluorometer, adapted for time-resolved measurements. For steady-state emission spectroscopy a 450 W Xenon lamp was used as the excitation source. A thermoelectrically cooled single photon detection module (Hamamatsu, Inc. H9170-75 NIR PMT) at -61°C and -900 V was used as the detector. Spectral selection of the emission was achieved by passage through a double grating emission monochromator (600 grooves/mm) blazed at 1 μ m, the observed emission signals were not corrected for the efficiency of the grating.

For time-resolved luminescent lifetime measurements, either a sub-microsecond Xenon flash lamp (Jobin Yvon, 5000XeF) or a Sirah Cobra Stretch dye laser (CSTR-LG24, Plasmatechnik GmbH) pumped by a QuantaRay INDI-HG Nd:YAG (SpectraPhysics, Inc.) were used as the excitation sources for the Yb(III) and Nd(III) complexes, respectively. The Xenon flash lamp was coupled to a double grating excitation monochromator for spectral selection. The Xenon flash lamp was coupled to a double grating excitation monochromator for spectral selection. The input pulse energy (100 nF discharge capacitance) was *ca.* 50 mJ, yielding an optical pulse duration of less than 300 ns at FWHM for the Xenon flash lamp. The dye laser pulse 8-10 ns, with an approximate energy of 10 mJ/pulse ($\lambda_{EX} = 376$, Exalite 376 Dye), was routed directly into the sample chamber of the Fluorolog. A portion of this excitation was sampled with a 10% beam splitter, which was focused onto the entrance of a UV-sensitive photodiode

(DET210, Thor Laboratories). The small amplitude analogue output from the photodiode was processed into a TAC Start signal (NIM) using a TB-01 pulse converter module from IBH. The output signal from the PMT was processed using a TB-02 0.5 GHz preamplifier module from IBH, and a 100 MHz Constant Fraction Discriminator (CFD) (Model 6915, Phillips Scientific), yielding appropriate TAC Stop signals (NIM). These were acquired using a 2 ns PCI Multi Channel Scaling (MCS) card (Model P7888-1E, FAST ComTec GmbH) Signals were acquired using an IBH DataStation Hub photon counting module and data analysis was performed using the commercially available DAS 6 decay analysis software package from HORIBA Jobin Yvon IBH. Goodness of fit was assessed by minimizing the reduced chi squared function, χ^2 , and a visual inspection of the weighted residuals. Each trace contained at least 10,000 points and the reported lifetime values result from at least three independent measurements.

X-ray Crystallography

All complexes described in this chapter were prepared by myself. Diffraction data was collected and processed by the department crystallographer, Jeff W. Kampf. The structures were solved and refined primarily by myself. Jeff W. Kampf lent his expertise in handling non-routine instances of twinning, disorder, or other complications. Jeff W. Kampf also critiqued and made modifications to models at the final stages of refinement.

Intensity data for all other samples were collected at 85(2) K on a standard Bruker SMART-APEX CCD-based X-ray diffractometer equipped with a low temperature device and fine focus Mo-target X-ray tube ($\lambda = 0.71073 \text{ \AA}$) operated at 1500 W power (50 kV, 30 mA). The frames were integrated with the Bruker SAINT⁵³ software package with a narrow frame algorithm. The data were processed with SADABS⁵⁴ and corrected for absorption. The structures were solved and refined with the Bruker SHELXTL (version 2008/4) software package.⁵⁵

Intensity data for all other samples were collected at 85(2) K on an AFC10K Saturn 944+ CCD-based X-ray diffractometer equipped with a low temperature device and Micromax-007HF Cu-target micro-focus rotating anode ($\lambda = 1.54187 \text{ \AA}$). operated at 0.20 kW power (20 kV, 10 mA), $\mu = 4.510 \text{ mm}^{-1}$. The data were processed with CrystalClear 2.0⁵⁶ and corrected for absorption. The structures were solved and refined

with the SHELXTL (version 2008/4) software package.⁵⁷ All other experimental details are presented in table 4.1 and 4.2.

Results

Assembly and Structures with Zn(II) and picHA

The strategy for assembling 12-MC-4 and 15-MC-5 complexes from Zn(II) and picHA was based on previous work with Cu(II) and Ni(II) ions. M_5L_4 complexes were found to assemble in water and polar organic solvents, which are presumed to be a $M(II)[12-MC-4]$.^{33,58-62} The formation of the M_5L_4 was demonstrated with ESI-MS and 1H NMR. These complexes have limited solution stability, and tend to persist with a variety of mononuclear complexes. The addition of a lanthanide ion leads to the conversion to a $Ln(III)[15-MC-5]$ complex.³⁴ These $Ln(III)[15-MC-5]$ complexes have been extensively characterized by X-ray crystallography, ESI-MS, 1H NMR spectroscopy, and UV-Vis spectroscopy.^{42,43,63}

As a starting point, the reaction between Zn(II) and picHA was examined in the absence of a Ln(III) ion. Similar to the Cu(II) and Ni(II) chemistry, ESI-MS of a 1:1 mixture of Zn(II) and picHA in pyridine revealed a $Zn_5L_4^{2+}$ species at 434.9²⁺, along with $Zn_5L_4(\text{anion})^+$ complexes (figure 4.3, table 4.3). Similar observations were made in 4:1 water/pyridine and 9:1 DMF/pyridine mixtures (v/v). The Zn_5L_4 was crystallized from a methanol/pyridine/ether solution. X-ray crystallography revealed a $Zn(II)[12-MC_{Zn(II),picHA-4}](py)_5(OTf)_2$ complex (figure 4.4). The picHA ligands form fused five-membered chelate rings, coordinating bidentate through the carbonyl and hydroximate oxygens at one position and bidentate through the hydroximate and pyridyl nitrogens at the other. The Zn(II) ions are five-coordinate with an axially bound pyridine. Tao values⁶⁴ were measured to assess whether the Zn(II) ions are square pyramidal or trigonal bipyramidal, where 0 represents pure square pyramidal and 1 indicates pure trigonal bipyramidal geometries (table 4.4). The tao values range from 0.04 to 0.41, revealing that the Zn(II) ions have distorted square-pyramidal geometries. A crystal structure of the $Zn(II)[12-MC_{Zn(II)-4}]$ was also obtained with quinaldic hydroxamic acid (quinHA, 4.2) with tetrafluoroborate (BF_4^-) counterions (figure 4.5). Quinaldic acid is a derivative of picHA with an appended phenyl ring. The complex shows effectively the same structural

motif as the $Zn_5(picHA)_4$ complex. The Zn(II) ions again have square pyramidal geometry ($\tau = 0.04 - 0.30$) with axially bound pyridine ligands. Bond lengths fall within the expected values (table 4.4), though the Zn(II)-N_{quinHA-pyridine} bond length is slightly elongated (2.16 Å). The cavity radius of the $Zn_5(quinHA)_4$ is 0.646 Å, again providing a reasonable fit for the Zn(II) ion (ionic radius = 0.68 Å).

To this point, MCs assembled with Zn(II) match those observed with Cu(II) and Ni(II). However, the mass spectrum of a 1:2:1 solution of picHA, triethylamine, and $Zn(NO_3)_2$ in methanol revealed peaks at $m/z = 860.7^{3+}$ and 1307.5^{2+} , corresponding to a $Zn_{14}(picHA)_{12}(methoxide)^{3+}$ and $Zn_{14}(picHA)_{12}(methoxide)(NO_3)^{2+}$, respectively. Low intensity peaks for $Zn_{13}(picHA)_{11}$ and $Zn_{15}(picHA)_{13}$ species were also observed. Similar peaks were seen when the assembly was performed in DMF, though with lower intensity relative to the Zn_5L_4 peaks. Unfortunately, these complexes have not been crystallographically characterized yet. Observation of such a large cluster is not unprecedented as a $Cu_{28}(\alpha\text{-aminoHA})_{20}$ helicate has been isolated previously.⁶⁵

Assembly and Structures of Ln(III)[15-MC-5] complexes

Encouraged that the M_5L_4 complex forms with Zn(II), the synthesis of the Ln(III)[15-MC_{Zn(II), picHA-5}] was pursued. ESI-MS analysis of a 5:10:5:1 picHA, triethylamine, Zn(II), La(III) reaction mixture in pyridine reveals peaks for a $LaZn_5(picHA)_5$ species at $m/z = 603.3^{2+}$ (figure 4.6). Low intensity peaks for the Zn_5L_4 and a $LaZn_4L_4$ species are also present. The $LaZn_5(picHA)_5$ also assembles in methanol, DMF, and 9:1 DMF/pyridine. The $LaZn_5(picHA)_5$ persists in pyridine and 9:1 DMF/pyridine even upon heating the assembly reaction mixtures at 65 °C for 24 hours (figure 4.7). A crystal structure was obtained of $Eu(III)[15-MC_{Zn(II),picHA-5}](NO_3)_3(py)_4$ that shows this $LnZn_5(picHA)_5$ species displays the archetypal Ln(III)[15-MC-5] (figure 4.8). A fifteen-membered macrocycle is observed with a Eu(III) ion bound in the center by five hydroximate oxygen atoms. The nine-coordinate Eu(III) ion is capped by bidentate nitrates on both faces of the MC. The 1.06 Å radius of the [15-MC-5] cavity provides a good fit for the 1.12 Å radius Eu(III) ion, thus the central metal fits in the center of the oxygen mean plane (merely a 0.31 Å displacement). The Zn(II) ions are again five-coordinate. Tao values ranging from 0.03 to 0.51 show that the Zn(II) ions vary from being square pyramidal to about halfway between square pyramidal and

trigonal bipyramidal. Four of the Zn(II) ions have axially bound pyridines, while one has a monodentate nitrate. The MC face is severely ruffled, which is attributed to the 5-coordinate Zn(II) ions that arrange the bidentate picHA ligands in a non-planar fashion. The Zn(II)-N_{picHA-pyridyl} bond lengths are slightly elongated (2.145 Å) due to ring strain from the ruffling of the MC face. All other metal-ligand bond lengths fall within the expected ranges. This LnZn₅(picHA)₅(NO₃)₃ was also isolated with La(III), Nd(III), and Gd(III).

The synthesis of the LnZn₅(picHA)₅ was pursued with smaller lanthanides. These ions tend to be more interesting for luminescence and single-ion magnetism. Unfortunately, attempts to isolate the LnZn₅(picHA)₅ with smaller lanthanide ions has been unsuccessful. ESI-MS of the assembly reaction mixture with Y(III) in pyridine reveals that the Zn₅L₄ species is more prevalent than with La(III). Low intensity peaks for a YZn₅L₅ and YZn₄L₄ are observed at room temperature (figure 4.9), though these peaks are more intense after heating at 65 °C for 24 hours (figure 4.10). Ln(III)[15-MC_{Cu(II)}-5] complexes are thermodynamically less stable with smaller lanthanide ions⁶⁶ and more difficult to crystallize, so similar effects could be a factor here as well. Nevertheless, the Ln[15-MC_{Zn(II)}-5] structure type was crystallized with small lanthanides with quinHA ligands (figure 4.11) The LnZn₅(quinHA)₅ was isolated with Nd(III), Tb(III), Dy(III), Ho(III), Er(III), Y(III), though it could not be obtained with Yb(III). The crystal structure of the Dy(III)[15-MC_{Zn(II),quinHA}-5](NO₃)₃(pyridine)₆ complex shows the typical 15-MC-5 motif. A nine-coordinate Dy(III) ion is bound in the center with coordinated bidentate nitrates. An unbound nitrate in the lattice provides charge balance. The MC is highly ruffled again due to four Zn(II) ring ions ($\tau = 0.10 - 0.64$), though an octahedral Zn(II) ion gives one fifth of the MC a planar topology. Bond distances are again within the expected ranges except for the slightly elongated Zn(II)-N_{quinHA pyridyl} distance of 2.201 Å (table 4.4).

Solvent Dependent Assembly and Structures of other LnMCs

The solvent dependence in MCs assembled with Ln(III) ions was investigated. A solvent dependent assembly is reasonable considering that the 5-coordinate Zn(II) ions and large Ln(III) ions contain open coordination sites. The assembly could be directed by the solvation of these ions. The mass spectrum of the assembly reactions in pyridine

reveals low intensity LnZn_4L_4 species. Knowing that Ln(III) ions prefer oxygen-donor atoms, the assembly was performed in dimethylformamide/pyridine mixtures. The DMF/pyridine solvent led to a notable increase in the LnZn_4L_4 intensity relative to the Zn_5L_4 and LnZn_5L_5 with both La(III) and Y(III) (figures 4.6, 4.7, 4.9, 4.10). The LnZn_4L_4 intensity is modest with La(III), though it dominates the spectrum with Y(III). The LnZn_4L_4 could not be crystallized with picHA, but suitable crystals were obtained with quinHA. The crystal structure shows the LnZn_4L_4 to be a $\text{Dy(III)[12-MC}_{\text{Zn(II),quinHA}^-4}](\text{DMF})_4(\text{NO}_3)_3$ complex (figure 4.12). The DyZn_4L_4 is a concave twelve-membered macrocycle, resembling the Zn_5L_4 . Each Zn(II) ion is square pyramidal ($\tau = 0.08 - 0.22$) with pyridine ligands bound axially and the Zn(II) ions resting above the ligand plane by 0.564 Å on average. Elongated Zn(II)-N_{picHA-pyridyl} bond distances of 2.21 Å are observed. The central cavity on the [12-MC-4] has a radius of merely 0.64 Å, too small for the 1.027 Å radius of Dy(III). Therefore, the Dy(III) ion sits 1.19 Å above the oxygen mean plane. The Dy(III) is 8-coordinate, with four coordinated DMF molecules. The Dy-O_{hydroximate} bond distances are slightly shorter than the Dy-O_{DMF} distances (2.330 and 2.406 Å, respectively). Three unbound nitrate anions in the lattice provide charge balance.

Encouraged by the LnZn_4L_4 that preferentially assembles in DMF/pyridine mixtures, the assembly reaction was performed in aqueous pyridine. ESI-MS of 5:10:5:1 mixtures of picHA, triethylamine, $\text{Zn}(\text{NO}_3)_2$, and $\text{Ln}(\text{NO}_3)_3$ salts in 4:1 water/pyridine reveal a variety of novel species with high intensity peaks (figures 4.6, 4.7, 4.9, 4.10). An LnZn_8L_8 assembles preferentially with larger lanthanide ions such as La(III), while dilanthanide complexes, such as $\text{Ln}_2\text{Zn}_8\text{L}_{10}$, $\text{Ln}_2\text{Zn}_8\text{L}_9$, and $\text{Ln}_2\text{Zn}_9\text{L}_{10}$, form preferentially with smaller lanthanides, such as Y(III). However, these complexes assemble with both La(III) and Y(III). Two crystal structures of the LnZn_8L_8 were obtained that both show a $\text{Ln(III)[12-MC}_{\text{Zn(II), picHA}^-4}]_2^{3+}$ sandwich complex. The structures differ in the anions bound axially to Zn(II) ring metals. A $\text{La(III)[12-MC}_{\text{Zn(II), picHA}^-4}]_2(\text{Cl})_2(\text{py})_6$ complex was crystallized from an aqueous pyridine solution (figure 4.13). The complex shows two concave [12-MC-4] subunits sandwiching an eight-coordinate La(III) ion. Thus this complex can be viewed as the LnZn_4L_4 capped with a tetradentate [12-MC-4] instead of the four DMF ligands. The La(III) ion sits 1.315 Å

above the oxygen mean planes of the [12-MC-4] subunits. The Zn(II) ions are again five-coordinate with long Zn-N_{picHA-pyridyl} bond distances. Six pyridines and two chlorides are bound axially to the Zn(II) ring metals. There is an unsymmetrical pitch to the 12-MC-4 rings. This distortion is not so pronounced in the LnZn₄ or Zn₅L₄, and is attributed to the different axial ligands on the Zn(II) ring ions.

Another crystal structure of the LnZn₈L₈ was obtained from a sample grown in aqueous pyridine using carbonate salts of Zn(II) and Dy(III). This structure shows the Dy(III)[12-MC_{Zn(II), picHA-4}]₂³⁺ sandwich complex with three μ₂-oxygen atoms bridging the axial positions of Zn(II) ring metals (figure 4.14). The average Zn-O-Zn angle of 108° is more consistent with the sp³ hybridization expected for water. These bridging oxygens are assigned as hydroxides based on the acidity of the two Zn(II) ions, requirements for charge neutrality, and the somewhat short Zn-O bond lengths (avg. = 1.981 Å). The two Zn(II) ions without hydroxide ligands are adjacent to each other and have axially bound pyridines. Similar to the LaZn₈(picHA)₈Cl₂(py)₆ sandwich complex structure, the pitch of the picHA ligands varies around the ring, which is reflected in the range of τ-values for the Zn(II) ions (0.01 - 0.76).

As sandwich complexes of the Ln(III)[12-MC-4] were obtained with a second 12-MC-4 unit, a sandwich complex with a 12-crown-4 was sought. Such a LnZn₄L₄ complex with macrocyclic ligands was pursued to generate high symmetry Ln(III) complexes for their single-ion magnetic properties. A crystal structure of the Dy(III)[12-MC_{Zn(II), quinHA-4}](12-crown-4)(pyridine)₄(OTf)₃ was obtained from a pyridine solution by benzene vapor diffusion (figure 4.15). The complex shows an eight-coordinate Dy(III) ion sandwiched between the 12-crown-4 and 12-MC-4. The distance from the Ln(III) ion to the oxygen mean plane of the MC (1.031 Å) is over 0.5 Å shorter than the Ln(III)-12-crown-4 distance (1.588 Å), which can be attributed in part to the larger cavity size of the MC (0.663 and 0.551 Å, respectively). The Dy(III)-(12-crown-4) and Dy(III)-(12-MC-4) bond distances average 2.465 Å and 2.271 Å, respectively. The Zn(II) ring metals on the 12-MC-4 are square pyramidal (τ = 0.08 - 0.22) with pyridine ligands in the axial position.

A crystal structure of a dilanthanide complex that also assembles in aqueous pyridine was obtained with quinHA. This structure showed a

$\text{Ln}_2\text{Zn}_9(\text{quinHA})_{10}(\text{OH})(\text{py})_9$ complex (figure 4.16). The other dilanthanide complexes observed via mass spectrometry are presumed to have somewhat similar structures given their similar formula. Two 8-coordinate Dy(III) ions in the center of the $\text{Dy}_2\text{Zn}_9\text{L}_{10}$ are bridged by three $\mu_2\text{-O}_{\text{hydroximate}}$ atoms. The MC repeat unit propagates irregularly around this core. The complex appears as two planar Ln-MCs that have collided at a 90° angle relative to the other. On one, a distinct Dy(III)[14-MC-5] motif is observed with one Dy(III) ring metal and a hydroxide bridge. Such a Dy(III)[14-MC-5] motif was recently reported with Mn(III) ring metals and shi ligands (figure 4.17).⁶⁷ The bridging oxygen is thought to be a hydroxide based on the charge balance requirements for the +4 charged cluster, as only three anions were located in the lattice. ESI-MS of the complex also consistently shows a hydroxide adduct. The 1.99 and 1.95 Å Zn-O bond distances and 101.5° Zn-O-Zn bond angles does not clarify whether the oxygen is from a water or hydroxide. Hydrogen bond acceptors surrounding the oxygen atom demonstrate that the oxygen is protonated, however the assignment as a hydroxide or water based on the orientation of the hydrogen bond acceptors is not possible due to disorder. From this evidence, the oxygen atom is tentatively assigned as a hydroxide, though formulation as a water is possible. The other quinHA ligand plane in the $\text{Dy}_2\text{Zn}_9\text{L}_{10}$ structure could be described as a split open Dy(III)[15-MC-5] (figure 4.17). Four Zn(II) ions and four quinHA ligands propagate the prototypical MC motif. However, a Dy(III) ion occupies the position of the fifth zinc, disrupting the 15-MC-5. The fourth Zn(II) ion is four-coordinate, binding the fifth quinHA ligand in the with the reverse directionality of the other ligands. The O, O'-chelate of this quinHA ligand binds to an additional Zn(II)-quinHA subunit, which altogether caps the axial metal sites on the Dy(III)[14-MC-5].

The assembly reaction of picHA, $\text{Zn}(\text{NO}_3)_2$, and $\text{La}(\text{NO}_3)_3$ was also performed in methanol. ESI-MS analysis reveals prominent peaks for two LnMCs, the LaZn_5L_5 and the $\text{LaZn}_{16}\text{L}_{16}$ complex. The assembly with smaller lanthanide ions, such as Y(III) shows the $\text{YZn}_{16}\text{L}_{16}$ as the predominant LnMC along with a $\text{Y}_2\text{Zn}_3(\text{picHA})_4$ species (figures 4.7, 4.9). Performing the assembly reaction at 65°C does not alter the spectra of the assembly with La(III), though $\text{Y}_4\text{Zn}_4\text{L}_8$ and $\text{Y}_4\text{Zn}_4\text{L}_9$ clusters are observed for the assembly reaction with Y(III) (figure 4.6, 4.9). The tetralanthanide clusters have not been crystallographically characterized. Crystal structures of the $\text{TbZn}_{16}\text{L}_{16}$, $\text{DyZn}_{16}\text{L}_{16}$, and

ErZn₁₆L₁₆ were obtained by slow evaporation of a methanol solution containing pyridine, which all showed an Ln(III)[12-MC_{Zn(II),picHA-4}]₂[24-MC_{Zn(II),picHA-8}](OTf)₃(py)₈ complex. The TbZn₁₆L₁₆ structure is described in detail here (figure 4.18). The structure contains the Tb(III)[12-MC_{Zn(II),picHA-4}]₂ sandwich complex encapsulated in the cavity of a [24-MC_{Zn(II),picHA-8}] ring (figure 4.19). The TbZn₁₆L₁₆ has overall S₈ symmetry. Charge balance is achieved with three unbound triflate counterions. The [24-MC-8] ring is assembled with octahedral Zn(II) ions that possess alternating Λ and Δ absolute stereochemical configuration (figure 4.19).

The TbZn₈L₈ subunit closely resembles the LnZn₈L₈ structures. Long Zn(II)-N_{pyridyl} bond distances (avg. =2.17 Å) are observed, while the Zn(II)-O_{hydroximate} and Zn(II)-N_{hydroximate} distances fall within the expected range (2.00-2.07 Å). The Zn(II)-O_{carbonyl} distances are long (avg = 2.14 Å) because the oxygen atom also coordinates to a [24-MC-8] Zn(II) ion. The [12-MC-4] units in the TbZn₁₆L₁₆ complex bind an eight-coordinate Tb(III) ion with average Tb-O bond lengths of 2.35 Å. The [24-MC-8] binds the Tb(III)[12-MC-4]₂ sandwich through coordination of its hydroximate oxygen atom to the axial position of each Zn(II) ion on the [12-MC-4] units (avg. bond length = 1.98 Å). Additionally, each Zn(II) ion on the [24-MC-8] coordinates to a picHA carbonyl oxygen atom on the [12-MC-4] unit (avg. bond length = 2.27 Å). The octahedral Zn(II) ions on the [24-MC-8] also coordinate an *O,O*-picHA, *N,N'*-picHA, and a pyridine molecule (figure 4.19). The [24-MC-8] and Tb(III)[12-MC-4]₂ further associate through π -stacking interactions between the picHA rings.

In the course these crystallizations, a Zn₄(picHA)₂(acetate)₄(DMF)₂ complex was obtained by slow evaporation of a methanol solution (figure 4.20). This complex is characterized as a [6-MC-2] ring system in the chair orientation. Each Zn(II) ion is five-coordinate, with two monodentate acetate ligands that both bridge with an adjacent Zn(II). The acetate bridged Zn(II) ions are further bridged by an O_{hydroximate} atom in the 6-MC-2 ring. Two trigonal bipyramidal Zn(II) ions ($\tau = 0.65$) have a bidentate O, O'-picHA ligands and a coordinated DMF molecule. The other Zn(II) ions are square pyramidal ($\tau = 0.30$), with a bidentate coordinated N, N'-picHA ligand. The Zn-N_{picHA} pyridyl bond distances are 2.14 Å. This complex has also been crystallized with pyridine in place of the DMF molecule.⁶⁸ Synthetically, this complex was frequently obtained during

crystallizations with acetate, underscoring the need to avoid carboxylates to isolate many of these Zn(II)-MCs. A similar 6-MC-2 has been observed in a $\text{Cu}_2(\text{di-2-pyridyl ketone oxime})_4$ complex.⁶⁹

The assembly reaction was also performed in DMF. At room temperature with La(III), peaks for the Zn_5L_4 , LaZn_5L_5 , and LaZn_8L_8 are prominent (figure 4.6). Upon heating the solution at 65°C for 24 hours, however, the LaZn_8L_8 peaks are lost and peaks for the $\text{LaZn}_{16}\text{L}_{16}$, as well as a new $\text{LaZn}_{12}\text{L}_{12}$ species are observed (figure 4.7). With Y(III), the room temperature assembly shows a mixture of a variety of species: Zn_5L_4 , YZn_4L_4 , YZn_8L_8 , $\text{YZn}_{12}\text{L}_{12}$, and $\text{Y}_2\text{Zn}_3\text{L}_4$ (figure 4.9). Heating the solution changes the spectrum so that the $\text{YZn}_{12}\text{L}_{12}$ peaks are predominant and $\text{YZn}_{16}\text{L}_{16}$ is also present (figure 4.10). The $\text{LnZn}_{12}\text{L}_{12}$ and $\text{Ln}_2\text{Zn}_3\text{L}_4$ complexes have not been crystallographically characterized yet.

Solution Integrity of MCs with Zn(II) Ring Ions

Having crystallographically characterized this series of MCs with Zn(II) ring metals, information on their solution stability was sought. Pure $\text{Zn}_5(\text{picHA})_4(\text{OTf})_2(\text{py})_5$ samples were dissolved in a variety of solvents at room temperature. Based on ESI-MS analysis, the $\text{Zn}_5(\text{picHA})_4$ is stable in methanol, acetonitrile, pyridine, 4:1 water, and 9:1 DMF/pyridine as the $\text{Zn}_5(\text{picHA})_4$ peaks are retained and no new peaks grow in after 24 hours (figure 4.21). In DMF and water (unbuffered), partial decomposition is observed after 24 hours as peaks for $\text{Zn}_{14}(\text{picHA})_{12}$ species and related complexes are seen. The ^1H NMR spectrum of the Zn_5L_4 was collected in pyridine- D_5 (figure 4.22). The spectrum contains four resonances in the phenyl region from the MC and three resonances from pyridine. The two doublets and two triplets with 1:1:1:1 integral ratios is consistent with the C_4 symmetric $\text{Zn}_5(\text{picHA})_4$ complex, which has four chemically distinct protons from the picHA ligand. Further evidence for the solution integrity of the Zn_5L_4 was obtained from diffusion NMR experiments, which measures the diffusion coefficient of a complex.⁷⁰ The Stokes-Einstein equation (eqn. 1, below) relates the diffusion coefficient (D) can be related to the hydrodynamic radius of the complex (r_H), where k_b is the Boltzman constant (1.3806×10^{-23}), T is the temperature in Kelvin, and η is the viscosity of the solution at that temperature in $\text{kg m}^{-1}\text{s}^{-1}$.

$$(1) \quad \Gamma_H = \frac{k_b T}{6\pi\eta D}$$

A limitation of this technique is that the Stokes-Einstein equation relies on the assumption that the molecule diffusing in solution is a perfect sphere. As this assumption is not accurate for these MCs, the accuracy of the technique is limited. Also, the Stokes-Einstein equation calculates the hydrodynamic radius of the complex, so the values are expected to be larger than the molecular radius from the crystal structure. Nevertheless, the hydrodynamic radius measured by diffusion NMR supports the proposition that the complex in the crystal structure is stable in solution.

Diffusion NMR analysis of the $Zn_5(picHA)_4(OTf)_2$ gave a diffusion coefficient of $2.8 \pm 0.1 \times 10^{-10} \text{ m}^2\text{s}^{-1}$ in methanol- D_4 , corresponding to a hydrodynamic radius of $7.9 \pm 0.3 \text{ \AA}$. The distance from the central Zn(II) to the furthest hydrogen on the picHA and pyridine ligands are 8.4 and 7.7 \AA , respectively. Thus, the diffusion NMR experiment also supports that the $Zn_5(picHA)_4$ complex is stable in solution. The $Zn_5(quinHA)_4(NO_3)_2$ complex was also characterized in methanol. ESI-MS showed peaks for the $Zn_5(quinHA)_4$ only. ^1H NMR showed six resonances in the phenyl region for the complex, consistent with the C_4 symmetric complex. The diffusion coefficient of $4.02 \pm 0.04 \times 10^{-10} \text{ m}^2\text{s}^{-1}$ in methanol- D_4 gave a hydrodynamic radius of $10.3 \pm 0.1 \text{ \AA}$, which is consistent with the crystal structure (7.8 - 10.1 \AA).

Ligand exchange experiments were performed to further assess the stability of the Zn_5L_4 . The $Zn_5(picHA)_4$ was mixed with four equivalents of $H_2quinHA$ in methanol and pyridine, making the picHA:quinHA ratio 1:1. ESI-MS analysis reveals complete ligand exchange in methanol and pyridine after 25 hours (figure 4.23). Species for the Zn(II)[12-MC-4] are centered at the 3:2 and 2:3 picHA:quinHA ratios.

ESI-MS shows that the $LnZn_5(picHA)_5$ and $LnZn_5(quinHA)_5$ complexes are relatively stable in pyridine (figure 4.21) and methanol. Over short periods of time (1 day or so), the ESI-MS spectrum contains peaks for only the $LnZn_5L_5$ complex. However, the complexes show evidence for rearranging in solution, as peaks for the Zn_5L_4 , $LnZn_{16}L_{16}$, and dinuclear Ln_2 clusters appear over two weeks. In 4:1 water/pyridine, the $LnZn_5L_5$ complexes rapidly convert to the $LnZn_8L_8$ and Ln_2 clusters within two hours. ^1H NMR of the $LaZn_5(picHA)_5(NO_3)_3$ in pyridine- D_5 shows four proton resonances in the phenyl

region that are upfield of the $Zn_5(picHA)_4$ peaks (figure 4.22). The spectrum is appropriate as each picHA ligand is related by a C_5 symmetry axis. In addition, residual pyridine resonances from the solvent are observed. Diffusion NMR at 293 K gave a diffusion coefficient of $2.55 \pm 0.02 \times 10^{-10} \text{ m}^2\text{s}^{-1}$ and hydrodynamic radius of $8.67 \pm 0.06 \text{ \AA}$. In the crystal structure of the $EuZn_5(picHA)_5(NO_3)_3$, the distance from the central Ln(III) to the furthest picHA proton is 8.9 \AA . Considering the planarity of the $LnZn_5(picHA)_5$, the hydrodynamic radius of $8.67 \pm 0.06 \text{ \AA}$ is reasonable.

The exciting host-guest chemistry of $Ln(III)[15-MC_{Cu(II),pheHA-5}]$ complexes prompted the investigation of the stability of the $LnZn_5(picHA)_5$ in the presence of carboxylates. Carboxylate binding is a possible route to enhancing the luminescence of these complexes or preparing soft solids, such as NLO materials using the LnMCs as building blocks. The stability of the $LnZn_5(picHA)_5$ was called into doubt by the crystal structure of the $Zn_4(picHA)_2(acetate)_4$ complex (figure 4.20). The titration of triethylammonium acetate to the $LaZn_5(picHA)_5(NO_3)_3$ in pyridine shows the complete loss of the $LaZn_5(picHA)_5$ resonances with five equivalents of acetate. No peaks for MC ions are observed by ESI-MS, suggesting that this complex is unstable with respect to carboxylates. However, ESI-MS shows that the $LaZn_5(picHA)_5$ peak is maintained with 15 equivalents of *p*-toluenesulfonate.

The $LnZn_4(quinHA)_4$ partially converts to the $LnZn_5(quinHA)_5$ and $Zn_5(quinHA)_4$ in 9:1 DMF/pyridine. ESI-MS shows peaks for these species upon dissolution of the complex. No evidence for the $LnZn_4(quinHA)_4(12\text{-crown-}4)$ was found with mass spectrometry. The $LaZn_8(picHA)_8$ is not completely stable in solution. Upon dissolution, ESI-MS of the $LaZn_8(picHA)_8$ contains prominent peaks for the complex (figure 4.21), though $Zn_5(picHA)_4$ peaks are evident after 24 hours. However, no other LnMCs are present. The ^1H NMR spectrum shows two distinct MC resonances at 8.65 and 8.10 ppm with relative integrals of 1:2 (figure 4.24). The two dimensional ^1H COSY spectrum shows that the remaining resonance overlaps with the residual pyridine peak at 7.65 ppm. In methanol, the complex completely rearranges to form the $LaZn_5(picHA)_5$ and $LaZn_{16}(picHA)_{16}$ after 24 hours. Slight conversion to the $LaZn_5(picHA)_5$ is seen in pyridine or to the $LaZn_{16}(picHA)_{16}$ in 9:1 DMF/pyridine and DMF. The $Ln_2Zn_9(quinHA)_{10}$ shows limited solution stability as well. The mass spectrum shows

only peaks for the complex in 4:1 water pyridine (figure 4.21), though peaks for the Zn_5L_4 grow in within 24 hours at room temperature. The complex rearranges to other dilanthanide species in methanol after 24 hours at room temperature, though little rearrangement is seen in pyridine or 9:1 DMF/pyridine.

LnZn₁₆L₁₆ Solution Integrity

The $LnZn_{16}(picHA)_{16}$ shows exceptional solution stability. ESI-MS of $LnZn_{16}(picHA)_{16}(OTf)_3$ complexes dissolved in methanol at room temperature exclusively display peaks for the $LnZn_{16}(picHA)_{16}$, with the +3 peak ~ 1104 - 1135 m/z being most prominent (figure 4.21). Based on ESI-MS, $EuZn_{16}(picHA)_{16}$ is also stable in acetonitrile, DMF, dimethylsulfoxide, and methanol/pyridine mixtures. In pyridine at room temperature, the $LaZn_{16}(picHA)_{16}$, and $YbZn_{16}(picHA)_{16}$ to a lesser extent, give rise to $Zn_5(picHA)_4$ after 90 minutes, and faint peaks for the $LaZn_5(picHA)_5$ can be observed after 6 weeks. The $LnZn_{16}(picHA)_{16}$ seems to be more stable in 9:1 DMF/pyridine, as $Zn_5(picHA)_4$ species do not grow in with Eu(III), Y(III), or Yb(III). In 4:1 water/pyridine, the $LnZn_{16}(picHA)_{16}$ converts to the $LnZn_8(picHA)_8$. This rearrangement is faster with La(III) than Y(III). The 1H NMR spectrum of $YZn_{16}(picHA)_{16}(OTf)_3$ grown with pyridine- D_5 further supports the solution stability (figure 4.25). Six peaks are observed in the aromatic region. Based on the relative integrals, these peaks are five individual proton resonances and a peak consisting of three overlapping proton resonances at 7.8 ppm. This fits the expected spectrum for $YZn_{16}(picHA)_{16}$, which should contain eight proton resonances from the two chemically distinct picHA rings. The coupling in the spectrum matches the expected four doublets and four triplets. Two dimensional 1H COSY NMR demonstrates that two chemically distinct picHA ligands are present. Furthermore, the diffusion coefficient measured with diffusion NMR was $3.48 \pm 0.01 \times 10^{-10}$ m²/s. Using the Stokes-Einstein equation, the hydrodynamic radius of the complex was found to be 11.6 ± 0.2 Å, which matches the 10.7 Å radius measured in the crystal structures of the $LnZn_{16}(picHA)_{16}(OTf)_3$ complexes reasonably.

The 1H NMR spectrum of the $LaZn_{16}(picHA)_{16}$ shows seven predominant peaks in the phenyl region, one consisting of two overlapping resonances, and a number of low intensity peaks (figure 4.26). The chemical shifts of the major peaks are slightly different than the $YZn_{16}(picHA)_{16}$. The low intensity peaks are best explained by ligand

dissociation, which would break the symmetry of the complex and increase the number of peaks resonances in the spectrum. Ligand dissociation is supported by mass spectra of the $\text{LnZn}_{16}\text{L}_{16}$, which occasionally show +3 and +4 peaks for complexes with dissociated ligands. Elemental analysis demonstrates that the $\text{LaZn}_{16}(\text{picHA})_{16}(\text{OTf})_3$ sample is pure, so ligand dissociation best accounts for the difference. Consistent with the ligand dissociation hypothesis, the $\text{LnZn}_{16}(\text{picHA})_{16}$ complexes undergo ligand exchange. Ligand substitution is observed by ESI-MS upon the addition of 32 equivalents of quinHA to the $\text{LnZn}_{16}(\text{picHA})_{16}(\text{OTf})$ in methanol (figure 4.27). After 6.5 hours, ESI-MS shows peaks for $\text{YZn}_{16}(\text{picHA})_{15}(\text{quinHA})$ and $\text{YZn}_{16}(\text{picHA})_{14}(\text{quinHA})_2$, revealing that limited ligand exchange has occurred. With the La(III) complex, a statistical distribution of peaks is observed centered at the $\text{LaZn}_{16}(\text{picHA})_5(\text{quinHA})_{11}^{3+}$. This array of $\text{LaZn}_{16}(\text{picHA})_x(\text{quinHA})_{16-x}$ peaks roughly fits what would be expected for the peak distribution at equilibrium. These spectra demonstrates that ligand exchange occurs with the $\text{LnZn}_{16}\text{L}_{16}$ complexes and that exchange is much faster with La(III) than Y(III). These observations further support that ligand dissociation leads to the many low intensity peaks in the $\text{LaZn}_{16}(\text{picHA})_{16}(\text{OTf})_3$ ^1H NMR spectrum and explains why such peaks are not as prevalent with $\text{YZn}_{16}(\text{picHA})_{16}(\text{OTf})_3$.

To address whether the $\text{LnZn}_{16}(\text{picHA})_{16}$ is stable or merely persistent in solution, lanthanide exchange was monitored by adding a 10-fold excess of $\text{Ln}(\text{NO}_3)_3$ ($\text{Ln} = \text{La}(\text{III}), \text{Y}(\text{III})$) to $\text{EuZn}_{16}(\text{picHA})_{16}(\text{OTf})_3$ in methanol. ESI-MS showed no peaks for La-1 or Y-1 after two weeks at room temperature. The $\text{LaZn}_{16}(\text{picHA})_{16}(\text{OTf})$ also showed no evidence for Y(III) exchange by ESI-MS and ^1H NMR. Likewise the Y(III) ion in $\text{Y}(\text{III})\text{Zn}_{16}(\text{picHA})_{16}(\text{OTf})$ did not exchange for La(III). The addition of excess Ln(III) increased the intensity of the weak ligand dissociation peaks, consistent with the cation promoting ligand dissociation by binding dissociated picHA ligands. As a whole, these results suggest the central lanthanide in the $\text{LnZn}_{16}(\text{picHA})_{16}$ is kinetically stable in methanol over seven days at room temperature.

The aqueous stability of the $\text{LnZn}_{16}(\text{picHA})_{16}$ was examined. The $\text{LaZn}_{16}(\text{picHA})_{16}(\text{OTf})_3$ decomposes in water, giving rise to an insoluble white precipitate that is consistent with Zn(II) or La(III) hydrolysis. The $\text{YZn}_{16}(\text{picHA})_{16}$ and $\text{YbZn}_{16}(\text{picHA})_{16}$ were stable in water. No new LnMCs were observed in the ESI-MS

spectra (figure 4.28), and no lanthanide exchange was observed. The $\text{YbZn}_{16}(\text{picHA})_{16}(\text{OTf})_3$ was also stable in HEPES buffer (20 mM pH 7.4 HEPES, 0.1 M NaCl). ^1H NMR of the $\text{YZn}_{16}(\text{picHA})_{16}(\text{OTf})_3(\text{pyridine-}D_5)_8$ was taken in D_2O (figure 4.27). The low solubility of the complex (~ 0.2 mM) required 375 scans to observe the spectrum. Four peaks are observed with relative integrals of 1:4:2:1, consistent with the 8 resonances in the complex. Numerous low intensity peaks are observed as well, suggesting that the complex is stable in water, though ligand dissociation is more prevalent. Based on this aqueous stability, the assembly reaction was performed in water. ESI-MS revealed that the $\text{YZn}_{16}(\text{picHA})_{16}$ assembles in water, giving rise to the $\text{YZn}_{16}(\text{picHA})_{16}$ peak at 1104.1^{3+} . The $\text{LaZn}_{16}(\text{picHA})_{16}$ has not been observed to assemble in water.

Zn₅L₄ Conversion to LnMCs

The assembly of the LnMCs was probed further by examining the conversion of the $\text{Zn}_5(\text{picHA})_4$ in the presence of a Ln(III) ion. It was hoped that these experiments would provide insights into the kinetic stability of the different complexes in different solvents, and also on the possible role of the $\text{Zn}_5(\text{picHA})_4$ as an intermediate in the assembly of the LnMCs. The reactions were performed by adding 0.8 equivalents of either $\text{La}(\text{NO}_3)_3$ or $\text{Y}(\text{NO}_3)_3$ to the $\text{Zn}_5(\text{picHA})_4(\text{OTf})_2$, which gives a 5:6.26:1 ratio of picHA, Zn(II), and the Ln(III). ^1H NMR and ESI-MS were collected after 24 hours at room temperature and 24 hours of heating at 65 °C. The spectra were unchanged after additional heating. The titration of La(III) to the $\text{Zn}_5(\text{picHA})_4(\text{OTf})_2$ in pyridine (figure 4.22) shows the $\text{Zn}_5(\text{picHA})_4$ resonances are almost completely replaced by four new peaks with lower chemical shifts. Heating the solution does not change the spectra. The spectra of isolated $\text{LaZn}_5(\text{picHA})_5(\text{NO}_3)_3$ in pyridine has the same appearance but slightly different chemical shifts. ESI-MS confirms that the $\text{LaZn}_5(\text{picHA})_5$ is the product of the reaction. Thus, the $\text{Zn}_5(\text{picHA})_4$ cleanly converts to the $\text{LaZn}_5(\text{picHA})_5$ in the presence of $\text{La}(\text{NO}_3)_3$ in pyridine at room temperature. Differences in the chemical shifts could possibly arise from counterion effects. With Y(III), a number of low intensity peaks appear in the ^1H NMR spectrum upon the addition of $\text{Y}(\text{NO}_3)_3$ (figure 4.29). The $\text{Zn}_5(\text{picHA})_4$ resonances are still prominent, and no changes are evident after heating the solution. ESI-MS shows a variety of species are present, including the $\text{Zn}_5(\text{picHA})_4$,

$\text{YZn}_4(\text{picHA})_4$, and $\text{YZn}_5(\text{picHA})_5$. So the conversion with Y(III) is not as complete or selective as the reaction with La(III), though it still proceeds at room temperature.

In 9:1 DMF/pyridine, conversion of the $\text{Zn}_5(\text{picHA})_4$ to LnMCs occurs quite rapidly at room temperature. With La(III), ESI-MS shows the $\text{LaZn}_5(\text{picHA})_5$ is the primary product of the reaction (figure 4.30). Four downfield resonances grow into the spectrum at room temperature, though the $\text{Zn}_5(\text{picHA})_4$ is still present. No changes are observed upon heating the spectrum. With Y(III), the $\text{YZn}_4(\text{picHA})_4$ is the primary product based on ESI-MS (figure 4.31). In the ^1H NMR spectrum, The $\text{YZn}_4(\text{picHA})_4$ resonances are slightly upfield of the $\text{Zn}_5(\text{picHA})_4$. The $\text{Zn}_5(\text{picHA})_4$ is still present with 0.8 equivalents of Y(III). These data show that there is no significant energy barrier inhibiting $\text{Zn}_5(\text{picHA})_4$ conversion to the $\text{LaZn}_5(\text{picHA})_5$ and $\text{YZn}_4(\text{picHA})_4$.

In 4:1 water/pyridine, very little conversion of the $\text{Zn}_5(\text{picHA})_4$ to the $\text{LaZn}_8(\text{picHA})_8$ occurs with the addition of 0.8 equivalents of $\text{La}(\text{NO}_3)_3$ (figure 4.24). The ^1H NMR spectrum shows slight changes to the $\text{Zn}_5(\text{picHA})_4$ chemical shifts upon the addition of La(III), and very low intensity peaks grow in at ~ 8.5 and 8.1 ppm that are consistent with the spectrum of isolated $\text{LaZn}_8(\text{picHA})_8$. Heating the reaction mixture does not change the spectrum. ESI-MS reveals low intensity peaks for the $\text{LaZn}_8(\text{picHA})_8$, supporting that limited conversion occurs. The titration of Y(III) results in the near complete loss of the $\text{Zn}_5(\text{picHA})_4$ resonances and the appearance of a variety of peaks with very low, near baseline intensity (figure 4.32). ESI-MS reveals peaks for the $\text{Zn}_5(\text{picHA})_4$, $\text{YZn}_8(\text{picHA})_8$, and Y_2 clusters. The low intensity of the resonances in the ^1H NMR spectrum could be due to the low concentration of the different species in solution or exchange processes. However, this titration shows solvent-based selectivity for the conversion of the $\text{Zn}_5(\text{picHA})_4$ to $\text{LnZn}_8(\text{picHA})_8$ and Ln_2 species, as different complexes assemble in pyridine.

In methanol, ^1H NMR and ESI-MS demonstrate that the $\text{Zn}_5(\text{picHA})_4$ reacts with the Ln(III) ions to form LnMCs. With La(III), both the $\text{LaZn}_5(\text{picHA})_5$ and the $\text{LaZn}_{16}(\text{picHA})_{16}$ can be observed (figure 4.26). Upon reacting at room temperature, the $\text{LaZn}_5(\text{picHA})_5$ peaks are most prominent, though weak $\text{LaZn}_{16}(\text{picHA})_{16}$ resonances are present in the ^1H NMR and mass spectra. Heating the reaction leads to the growth of the $\text{LaZn}_{16}(\text{picHA})_{16}$ peaks. With Y(III), only very weak peaks for the $\text{YZn}_{16}(\text{picHA})_{16}$ are

observed after reacting at room temperature in the ESI-MS and ^1H NMR spectra (figure 4.25). However, the $\text{YZn}_{16}(\text{picHA})_{16}$ peaks dominate the spectra upon heating the reaction mixture, though the $\text{Zn}_5(\text{picHA})_4$ is still present. Furthermore, the ESI-MS and ^1H NMR spectra show no evidence for the $\text{YZn}_5(\text{picHA})_5$. Thus the reaction of the $\text{Zn}_5(\text{picHA})_4$ with Y(III) in methanol proceeds selectively to the $\text{LnZn}_{16}(\text{picHA})_{16}$, though the $\text{LaZn}_5(\text{picHA})_5$ also forms with La(III). The $\text{Zn}_5(\text{picHA})_4$ seems to have a reasonable amount of kinetic and thermodynamic stability, as the conversion is driven by heat and does not proceed to conversion, even with an excess of Ln(III) relative to picHA.

In DMF, there are four resonances for the $\text{Zn}_5(\text{picHA})_4$. Upon the addition of 0.8 equivalents of $\text{La}(\text{NO}_3)_3$, four downfield resonances are present after twenty four hours (figure 4.33). The Zn_5L_4 resonances are still present with slightly lower integrals as the new peaks. ESI-MS suggests this new species is the $\text{LaZn}_5(\text{picHA})_5$, and the four resonances are consistent with the roughly D_{5h} symmetric complex. Upon heating the solution, a variety of low intensity peaks grow in to the ^1H NMR spectrum. The $\text{Zn}_5(\text{picHA})_4$ to $\text{LaZn}_5(\text{picHA})_5$ integral ratios stay roughly the same. ESI-MS shows the $\text{LaZn}_{12}(\text{picHA})_{12}$ species grows in upon heating. This shows that the Zn_5L_4 converts to the $\text{LaZn}_5(\text{picHA})_5$ at room temperature, though $\text{LaZn}_{12}(\text{picHA})_{12}$ formation has a higher activation barrier. The addition $\text{Y}(\text{NO}_3)_3$ to the $\text{Zn}_5(\text{picHA})_4$ leads to significant changes to the ^1H NMR spectrum (figure 4.34). Though peak overlap obscures the spectrum, it is evident that the $\text{Zn}_5(\text{picHA})_4$ resonance at 8.75 ppm decreases in intensity and a strong resonance at 8.65 ppm appears. ESI-MS suggests that this species is the $\text{YZn}_4(\text{picHA})_4$, though low intensity peaks for the $\text{YZn}_8(\text{picHA})_8$ and $\text{YZn}_{16}(\text{picHA})_{16}$ are also observed. Upon heating, the ^1H NMR spectrum shows a nearly complete loss of the $\text{Zn}_5(\text{picHA})_4$. The $\text{YZn}_4(\text{picHA})_4$ also loses intensity, and new resonances appear from 6.8 - 9.2 ppm. ESI-MS reveals that these new resonances originate from the $\text{YZn}_{12}(\text{picHA})_{12}$ and $\text{YZn}_{16}(\text{picHA})_{16}$. So the conversion of the $\text{Zn}_5(\text{picHA})_4$ to the $\text{YZn}_4(\text{picHA})_4$ proceeds at room temperature, though the formation of larger MCs requires heating. Also, all species are stable for long periods of time at room temperature once formed.

Luminescence of the $\text{LnZn}_{16}\text{L}_{16}$

One of the motivations for synthesizing LnMCs with Zn(II) ring metals was to explore their luminescence properties. The MC topology effectively excludes C-H

oscillators from the proximity of the central metal, which suggests that LnMCs can lead to efficient luminescence by mitigating vibrational quenching. Considering the structures of all of the LnMCs, the luminescence of the $\text{LnZn}_{16}(\text{picHA})_{16}$ is particularly promising because the complex does not coordinate solvent molecules near the Ln(III) ion, thus vibrational quenching from pyridines or other ligands is minimized. The nearest C-H oscillator in the $\text{LnZn}_{16}(\text{picHA})_{16}$ located over 6.7 Å from the Ln(III) ion. Also, there is no solvent bound to the central Ln(III). The absorption spectrum of $\text{YbZn}_{16}(\text{picHA})_{16}(\text{OTf})_3$ in methanol (figure 4.35) shows picHA ligand absorptions between 200-400 nm with apparent maxima at 284 and 325 nm. Both Yb(III) and Nd(III) are readily sensitized by the $\text{LnZn}_{16}(\text{picHA})_{16}$ in methanol and acetonitrile upon excitation of the picHA absorption bands. The characteristic ${}^5\text{F}_{5/2} \rightarrow {}^5\text{F}_{7/2}$ transition is observed in the emission spectrum of $\text{YbZn}_{16}(\text{picHA})_{16}(\text{OTf})_3$ (figure 34), while $\text{NdZn}_{16}(\text{picHA})_{16}(\text{OTf})_3$ displays ${}^4\text{F}_{3/2} \rightarrow {}^4\text{I}_{11/2}$ and ${}^4\text{F}_{3/2} \rightarrow {}^4\text{I}_{13/2}$ transitions. Using $\text{Yb}(\text{dipicolinate})_3^{3-}$ as a reference ($\Phi = 0.015 \pm 0.02\%$)⁷¹, a quantum yield of $0.89 \pm 0.18\%$ was measured in methanol. The time-resolved photoluminescence lifetime of $\text{YbZn}_{16}(\text{picHA})_{16}(\text{OTf})_3$ is 14 μs in methanol at 25.0 °C. The lifetime is extended to 33 μs in acetonitrile. The photoluminescence lifetime of $\text{NdZn}_{16}(\text{picHA})_{16}(\text{OTf})_3$ is over 1 μs in acetonitrile. The number of methanol molecules bound in the inner-sphere of Yb(III) and Nd(III), q , was estimated by comparing the luminescent lifetimes in methanol and methanol- D_4 (figure 4.36).⁷² The q number in methanol gave values of 0.03 and 0.09 for the Yb(III) and Nd(III) complexes, respectively, revealing that no methanol molecules are directly coordinated to the central Ln(III) in solution. This observation is consistent with the crystal structure of the $\text{LnZn}_{16}(\text{picHA})_{16}$.

Discussion

Synthesis

The assembly of picHA, Zn(II), and Ln(III) building blocks was motivated by the promising spectroscopic and magnetic properties of LnMCs with d^{10} ring metals. Furthermore, these building blocks have incompatible symmetry preferences and open coordination sites, promoting the formation of a variety of MCs whose assembly can be directed by the solvent choice. This work establishes a design strategy for realizing self-

assembled complexes that selectively assemble based on the solvent. A variety of MCs were found to assemble in solution, and six of these different motifs have been structurally characterized.

Isolation of each MC presented in this work was relatively straightforward once the appropriate crystallization conditions were established. It should be noted that though all MCs assemble in solution with both La(III) and Y(III) based on ESI-MS, they could not necessarily be crystallized with all Ln(III) ions. The $Zn_5(picHA)_4$ could only be crystallized with triflate counterions, though $Zn_5(quinHA)_4$ complexes with NO_3^- , Cl^- , and BF_4^- counterions were crystallized. The $LnZn_5(picHA)_5$ could only be crystallized with La(III)-Gd(III). Crystallization of the $LnZn_5L_5$ complexes with smaller lanthanide ions was only achieved with quinHA. For the crystallization of the $LnZn_{16}L_{16}$ with small lanthanides, the addition of water to the mother liquor assisted crystallization, though it led to smaller crystals. However, the presence of water in the mother liquor tended to enhance the purity of the $LnZn_{16}L_{16}$. The $LnZn_8L_8$ proved to be the most temperamental complex to crystallize because these crystallizations often yielded the $LnZn_{16}L_{16}$. An excess of Ln(III) was needed to prevent $LnZn_{16}L_{16}$ crystallization. Also, solutions of the $LnZn_8L_8$ frequently precipitated white powder (presumably hydrolyzed metal ions). For the chloride adduct, this precipitation could be mitigated by using by using excess Zn(II), though co-precipitation of Zn_5L_4 impurities was an unfortunate consequence of such an approach.

Structural Aspects of Ln(III)[15-MC_{Zn(II)}-5] Complexes

The MCs presented in this work can be divided into three structural categories: 15-MC-5 motifs, 12-MC-4 motifs, and a dilanthanide cluster. Ln(III)[15-MC-5] complexes with picHA ligands are known with Cu(II) and Ni(II) ligands (figure 4.37).^{42,43} Ln(III)[15-MC-5] complexes are also known to assemble with α -aminoHA ligands and Cu(II) or Ni(II), though they have only been crystallographically characterized with Cu(II).⁴² PicHA is closely related to the α -aminoHA ligands as they both have nitrogen donor atoms off of the α -carbon and form fused five-membered chelate rings. The formation of pentagonal shaped Ln(III)[15-MC-5] complexes was expected based on the geometry of the picHA fused chelate rings (figure 4.1). Eu(III)[15-MC_{picHA}-5] complexes form relatively planar complexes with Cu(II) and Ni(II) (figure

4.37). The $\text{Eu(III)[15-MC}_{\text{Ni(II),picHA-5}}$ complex has octahedral and square planar ring ions, while the $\text{Eu(III)[15-MC}_{\text{Cu(II),picHA-5}}$ complex has square planar or square pyramidal Cu(II) ions that sit within the ligand plane (table 4.5). These metal ion geometries align the equatorial picHA ligands within the same plane, leading to a fairly planar MC (figure 4.37). In contrast, the $\text{Eu(III)[15-MC}_{\text{Zn(II),picHA-5}}$ is severely ruffled. This ruffled topology is attributed to the square pyramidal and trigonal bipyramidal Zn(II) ions, which enforce a non-planar arrangement of the equatorial picHA ligands. The orientation of the picHA ligands alternate from one face to the other through the 15-membered macrocycle, which causes the ruffled topology. Compared to the $\text{EuCu}_5(\text{picHA})_5$ and $\text{EuCu}_5(\text{picHA})_5$ complexes, the $\text{EuZn}_5(\text{picHA})_5$ has elongated $\text{Zn(II)-N}_{\text{picHA-py}}$ distances and more twisting in the angles between picHA and the ring metals (Table 4.5). Notably, crystallographic and thermodynamic studies of $\text{Ln(III)[15-MC}_{\text{Cu(II),}\alpha\text{-aminoHA-5}}$ complexes found a correlation between the planarity of the MC and its stability. More planar MCs were generated with larger Ln(III) ions, while smaller Ln(III) central ions led to more ruffled, less stable complexes. The ruffled $\text{Eu(III)[15-MC}_{\text{Zn(II),picHA-5}}$ topology can be an indicator of relatively low solution stability.

Despite the severe ruffling of the MC face seen in the $\text{EuZn}_5(\text{picHA})_5$ structure, most structural parameters of the $\text{Ln(III)[15-MC}_{\text{M(II),picHA-5}}$ complex are consistent through the Ni(II) , Cu(II) , and Zn(II) series. In particular, the environment of the Eu(III) ion is fairly consistent through the series. The cavity radii and $\text{Eu(III)-O}_{\text{hydroximate}}$ distances are nearly the same. The similarity in the $\text{Eu(III)-O}_{\text{hydroximate}}$ distances is surprising as the $\text{EuNi}_5(\text{picHA})_5$ has an eight-coordinate Eu(III) , while the Cu(II) and Zn(II) complexes have nine-coordinate Eu(III) central ions. The nine-coordinate Eu(III) ion should have longer bond distances as its ionic radius is 0.054 Å larger. However, this effect is not observed for the bonds from the MC. Considering the coordinated nitrates, it is surprising to see the $\text{Eu(III)-O}_{\text{NO}_3}$ bond distances are similar for the bidentate nitrates. However, the $\text{Eu(III)-O}_{\text{NO}_3}$ bond distance for the monodentate nitrate in the $\text{EuNi}_5(\text{picHA})_5$ is more than 0.2 Å shorter than the bidentate nitrate. As a whole, the different 15-MC-5 complexes provide similar Eu(III) coordination environments despite significant differences in the MC ring.

Structural Aspects of Complexes with [12-MC_{Zn(II)-4] Motifs}

A variety of novel MCs with 12-MC_{Zn(II),picHA}-4 motifs were also crystallized, with the Zn₅L₄ being an exemplar. Notably, the analogous Cu₅L₄ and Ni₅L₄ complexes have been extensively studied in solution for their role as intermediates in the assembly of Ln(III)[15-MC-5] complexes.^{33,34,58,59,61,73} The crystal structures of these complexes have not been reported. Calculations by Tegoni et al. suggested that the complex has a concave topology.⁶⁰ The concave topology of the Zn₅(picHA)₄(OTf)₂ and Zn₅(quinHA)₄(BF₄)₂ structures confirm this prediction (figures 4.3, 4.4).

Structurally, these complexes are provocative because the geometry of the picHA and α -aminoHA ligands promote the pentagonal 15-MC-5 motif. The square shaped 12-MC-4 must inherently orient the metal ions at 90° angles. As the corresponding angles in the pentagonal 15-MC-5 are 108°, the Zn₅L₄ tolerates an 18° perturbation in the relative orientation of the Zn(II) ions. Analysis of the Zn₅(quinHA)₄ crystal structure reveals a number of prominent distortions. The average angle between the centroid of the O₂O⁻-picHA chelate, Zn(II), and the axial pyridyl nitrogen in the Zn₅L₄ is 111.1°, while the ideal planar complex would have a 90° angle. The Zn-O_{hydroximate}-N_{hydroximate}-Zn torsion angle is 162.9° in the Zn₅(quinHA)₄, compared to 180° in the ideal planar pentagon. Also, there is an increase in the Zn(II)-N_{picHA-pyridyl} bond distance to over 2.15 Å. The average ring metal-N_{picHA pyridyl} bond distance in the crystal structures of the Eu(III)[15-MC_{Cu(II),picHA}-5](NO₃)₃⁴² and Eu(III)[15-MC_{Ni(II),picHA}-5](NO₃)₃ are 1.991 and 2.050 Å, respectively (table 4.5). These parameters reveal that the square shaped macrocycle is generated through bending at the ring ions, twisting of the picHA face, and an elongation in the Zn(II)-N_{picHA-pyridyl} bond distance. In effect, the concavity of the 12-MC-4 motif eliminates the influence of the picHA chelate ring geometry.

The concavity of the Zn₅L₄ contrasts the planar 12-MC-4 complexes that are known with shi³⁻ and other ligands. Notably, the concave topology could generate different functionality. First, only one face of the concave Zn₅L₄ has open coordination sites. This is important when considering assemblies or networks of these MCs. For planar 12-MC-4 complexes, bridging guests coordinate to both faces of the complex, leading to the formations of infinite chains or networks.^{74,75} Similarly, the Ln(III)[15-MC_{Cu(II), α -aminoHA}-5] compartments and monomeric metallocavitands discussed in previous chapters bind anionic guests to both the hydrophobic and hydrophilic faces. The

concave 12-MC-4 motifs can only bind Lewis bases to one face. This face differentiation will promote the formation of *discrete* assemblies. Thus, the concave MC topology broadens the scope of assemblies that can be designed with MC building blocks. For example, David Chou, a graduate student in the Pecoraro group, has exploited the concave structure of Fe(III)[9-MC_{Fe(III),shi}-3] complexes to prepare discrete dimers with bridging 1,3-benzene dicarboxylate ligands.

Beyond differences in Lewis Base recognition, the concave 12-MC-4 will also have different cation recognition behavior from planar 12-MC-4 complexes. A number of planar 12-MC-4 complexes bind cations on both faces of the MC. This phenomenon is observed in the Na(I)₃[12-MC_{Ga(III),shi}-4]₂ metallacryptate (figure 1.13),⁷⁶ as well as monomeric [12-MC_{Mn(III),shi}-4] complexes.⁷⁷ Such molecular recognition is facilitated by the orientation of the oxygen-donor atoms in the planar MCs. The oxygen lone pairs are oriented above and below the MC plane. In contrast, the lone pairs on the concave Zn₅L₄ are both oriented to the *same* face of the MC. One is pointed towards the center of the MC, while the other is oriented upward and toward the periphery of the MC. Thus, the concave 12-MC-4 should be *incapable* of binding cations on the concave face, so only one central cation should be possible.

The molecular recognition capabilities of the concave face of the [12-MC_{Zn(II),picHA}-4] complexes is also promising. The concave face has a cavitand topology, similar to a calixarene or resorcinarene (figure 1.4). It is likely that the concave MC will exhibit similar molecular recognition chemistry for neutral, organic guests as these benchmark hosts. For example, the concave cavity of the Zn₅L₄ is appropriately sized for binding C₆₀. The recognition of neutral, organic guests would be a new area for MC host-guest chemistry, which has heretofore focused primarily on Lewis acids and bases.

Another unique feature of the concave 12-MC-4 motif is that the complex possesses inherent chirality. Inherently chiral molecules are enantiomers that are chiral in the rotational sense of substituents on the *entire* complex and not because of a single chiral center. Importantly, inherently chiral molecules do not possess a mirror plane of symmetry parallel to the rotation axis. The inherent chirality of the 12-MC-4 originates from the rotational directionality of the [M-N-O] repeat unit in the MC ring and the concave topology that eliminates the mirror plane of symmetry through the ring (figure

4.38). The Zn_5L_4 assembles and crystallizes as a racemic mixture, though resolution of the complex could be possible. To the authors knowledge, the only inherently chiral metallamacrocycles that have been resolved are $Ln(III)[15-MC_{Cu(II),\alpha\text{-aminoHA-5}}]^{78}$ and $Cu(II)[12-MC_{Cu(II),\beta\text{-aminoHA-4}}]^{79}$ complexes. These complexes were resolved through the use of resolved enantiomeric ligands. Importantly, inherently chiral complexes are promising for their chiral recognition capabilities. One potential problem of $Ln(III)[15-MC_{Cu(II),\alpha\text{-aminoHA-5}}$ and $Cu(II)[12-MC_{Cu(II),\beta\text{-aminoHA-4}}$ complexes from a chiral recognition standpoint is that the hydrophobic face possesses the opposite inherent chirality of the hydrophilic face. Thus, chiral discrimination could potentially be low with these complexes due to substrate interaction on either face. The concave 12-MC-4 complexes obviate this issue as substrates can interact with the metal ions on only one face of the complex.

The 12-MC-4 motif is also observed in the $LnZn_4L_4$, $LnZn_8L_8$, and $LnZn_{16}L_{16}$. The $\sim 0.64\text{-}0.74$ Å central cavity of the 12-MC-4 is too small for the $Ln(III)$ ions (ionic radii = 0.977 -1.160 Å). Therefore, the $Ln(III)$ ions rest far above the plane. A similar effect is seen in crown ether complexes^{80,81} and MCs^{76,77,82} where the guest cation is too large for the macrocycle. Notably, the positioning of the large $Ln(III)$ ion far above the oxygen mean-plane (OMP) leaves four open coordination sites on the *same* face. This contrasts the $Ln(III)[15-MC-5]$ complexes, where the $Ln(III)$ ion has coordination sites above and below the plane. The four open coordination sites in close proximity create exciting possibilities for molecular recognition chemistry, as tetradentate ligands can bind to the system to tune the chemistry of the $Ln(III)$ ion. This could be useful to tune the luminescence properties by appending ligands that can act as antennae. Furthermore, high symmetry monolanthanide complexes can be prepared with C_4 symmetric macrocycles, which are interesting for single-ion magnetism. The $Tb(\text{phthalocyanine})_2$ sandwich complex has one of the highest reported experimental blocking temperatures (11.7 K at 997 Hz)⁸³, so related complexes could also have interesting magnetic properties. As a proof-of-concept that the four open coordination sites on the $LnZn_4L_4$ can bind other ligands, the $LnZn_4L_4$ was crystallized with a 12-crown-4 (figure 4.15). The complex would only be crystallized in the absence of DMF and nitrate. DMF in the solvent leads to the crystallization of the $LnZn_4(\text{quinHA})_4$, while nitrate leads to the $LnZn_5(\text{quinHA})_5$.

The 12-crown-4 nests tightly in the narrow space between the pyridine ligands. It is likely that larger macrocycles might not fit effectively without displacing the pyridine ligands or replacing them with smaller substrates. Notwithstanding these potential problems, it is likely that a similar synthetic approach could be applied to preparing high symmetry $\text{LnZn}_4(\text{picHA})_4$ complexes in the future. The advantage of this approach from the SMM perspective is that small changes to the coordination geometry of the lanthanide can be systematically varied, which could have profound effects on the SMM behavior. For example, the Ln(III)-O distance is over 0.2 Å longer for the 12-crown-4 than the 12-MC-4 in the $\text{DyZn}_4(\text{quinHA})_4(12\text{-crown-4})$ complex. There is only a 0.08 Å difference in the $\text{DyZn}_4(\text{quinHA})_4(\text{DMF})_4$ complex. Comparison of the LnZn_4 , LnZn_8 , and LnZn_{16} complexes reveals that parameters such as the twist angles, plane-plane distances, and ligand-field symmetry are systematically varied in these complexes. Greater variation in these parameters could be achieved by changing the macrocycles or pyridine ligands to subtly influence the Ln(III) ion geometry. These differences are described in detail in the graduate thesis of Thaddeus Boron. It would be much more difficult to engineer such structural differences with traditional organic ligands, which do not necessarily respond to structural changes to the extent that these MCs do. The particular appeal of combining organic macrocycles with MCs is that the donor atoms in the organic macrocycle can be readily changed and be made asymmetric. For example, the aza-12-crown-4 could be studied, which has four nitrogen donor atoms, to assess the effects of nitrogen versus oxygen donors. 12-crown-4 complexes with mixed oxygen/nitrogen ligands are also known and could provide further insight into this phenomenon.

Since the LnZn_4L_4 binds a 12-crown-4, the formation of a 12-MC-4 sandwich complex was expected. Also, 12-crown-4 complexes are known to form sandwich complexes with lanthanide ions.^{80,81} The LnZn_8L_8 sandwich complexes (figures 4.13, 4.14) can be considered an extension of these complexes. A select group of MC sandwich complexes have been reported previously.^{76,84-87} The $\text{Na}(\text{I})_3[12\text{-MC}_{\text{Ga(III),shi-4}}]_2(\text{OH})_4$ metallacryptate (figure 1.13)⁷⁶ is the most similar MC with a sandwich motif. In the $\text{Na}(\text{I})_3[12\text{-MC}_{\text{Ga(III),shi-4}}]_2(\text{OH})_4$, four μ_2 -hydroxides bridge the two 12-MC-4 units through coordination to the Ga(III) ring metals. The two 12-MC-4 units sandwich a sodium cation in the center, and each MC also binds a sodium cation on the opposite

face. The $\text{DyZn}_8(\text{picHA})_8(\text{OH})_3$ similarly has μ_2 -hydroxide groups that bridge the axial sites on the ring metals. The notable difference between these complexes is that the $\text{Na}(\text{I})_3[12\text{-MC}_{\text{Ga}(\text{III}),\text{shi-4}}]_2(\text{OH})_4$ has a fourth hydroxide. It is worth considering whether a fourth bridging hydroxide would be possible on the LnZn_8L_8 . While adding a fourth hydroxide would give the LnZn_8L_8 a -1 charge, this is likely not an issue as the $\text{Na}(\text{I})_3[12\text{-MC}_{\text{Ga}(\text{III}),\text{shi-4}}]_2(\text{OH})_4$ also has a -1 charge. Another concern is that the distance between the 12-MC-4 units is too great for a fourth hydroxide to bind. However, the 12-MC-4 units in the $\text{DyZn}_8(\text{picHA})_8(\text{OH})_3$ are actually closer together than in the $\text{Na}(\text{I})_3[12\text{-MC}_{\text{Ga}(\text{III}),\text{shi-4}}]_2(\text{OH})_4$. The distance between Ga(III) ions on opposite MCs is 3.54 Å, while the hydroxide bridged Zn(II) ions are on average 3.21 Å apart. So there is nothing inherent to the separation of the two 12-MC $_{\text{Zn}(\text{II}),\text{picHA-4}}$ units that prevent a fourth hydroxide. The remaining issue is the pitch of the MC. It is possible that the three bridging hydroxides make the 12-MC-4 to adopt a flatter pitch in one portion, which could cause a steeper pitch on one picHA ligand. This is likely not the limitation either. Overlaying 12-MC-4 units from the $\text{DyZn}_8(\text{picHA})_8$ and $\text{LaZn}_8(\text{picHA})_8$ shows that each picHA on the $\text{DyZn}_8(\text{picHA})_8$ has a shallower pitch than on the $\text{LaZn}_8(\text{picHA})_8$ (figure 4.39). If the pitch of each individual picHA ligand was coupled, then the $\text{LaZn}_8(\text{picHA})_8$ would have some picHA ligands that are less concave than the $\text{DyZn}_8(\text{picHA})_8$. The steeper pitch in the $\text{LaZn}_8(\text{picHA})_8$ likely does not arise from the larger La(III) cation because the $\text{Zn}_5(\text{quinHA})_4$ is as concave as the $\text{DyZn}_4(\text{quinHA})_4$. Likely, the pitch of the picHA ligands is primarily dictated by the axially bound ligands. In order to alleviate steric clashes, more concave 12-MC-4 units form with bulkier axial ligands. As the pitch of the picHA ligands are not necessarily coupled, the shallow pitch necessary for binding a fourth hydroxide should be feasible. The presence of pyridine ligands and not a fourth μ_2 -hydroxide in the complex is likely a result of the crystallization process. Likely the pyridine bound complex is less soluble. Analysis of the structure suggests the axially bound pyridine ligands are sterically confined. Use of a bulkier pyridine derivative, such as 3,5-dimethylpyridine could limit Zn(II) coordination and lead to crystallization of the $\text{LnZn}_8(\text{picHA})_8(\text{OH})_4$. Such a complex would be a noteworthy analogue of the $\text{Na}(\text{I})_3[12\text{-MC}_{\text{Ga}(\text{III}),\text{shi-4}}]_2(\text{OH})_4$ metallacryptate because, unlike sodium, the lanthanide central metal could have novel magnetic and spectroscopic properties.

The $\text{LnZn}_{16}(\text{picHA})_{16}$ is the largest and most extraordinary MC with a 12-MC-4 motif discovered in this work. This complex contains a $\text{LnZn}_8(\text{picHA})_8$ sandwich motif encapsulated within the interior of a 24-MC-8. As the sandwich complex is considered a host-guest complex, the $\text{LnZn}_{16}(\text{picHA})_{16}$ is a host(host-guest) complex. MCs as large as the 24-MC-8 are known but not particularly common. Notably, the alternating Δ , Λ octahedral chirality of the Zn(II) ions in the 24-MC-8 (figure 4.19) is consistent with the coordination seen in other large MC rings.^{88,89} As the $\text{LnZn}_{16}\text{L}_{16}$ complex contains an integral concave Ln(III)[12-MC-4] motif, it is interesting to consider whether the concave Fe(III)[9-MC_{Fe(III), shi}-3] could form an analogous structure. The 9-MC-3 would have to be encapsulated in an 18-MC-6, but such an $\text{Fe}_{13}\text{L}_{12}$ complex seems feasible.

Structural Aspects of the Ln_2 Cluster

This work also presented a novel dilanthanide cluster, $\text{Ln}_2\text{Zn}_9(\text{quinHA})_{10}(\text{OH})$. This cluster does not possess a typical MC motif throughout the whole macrocycle. Instead, the complex contains fragments that resemble previously reported complexes (figure 4.17). The structure itself contains two perpendicular fragments. One fragment is a $\text{Ln}_2\text{Zn}_4(\text{picHA})_4(\text{OH})$ structure with a Ln(III)[14-MC-5] topology. A related Ln(III)[14-MC_{Mn(III), shi}-5] was recently isolated independently.⁶⁷ However, this Dy(III)[14-MC_{Zn(II), quinHA}-5] motif has a saddled structure and, therefore, lacks the C_2 symmetry of the Mn(III) complex (figure 4.17). The Dy(III)[14-MC_{Zn(II), quinHA}-5] also has different ligands coordinated axially and to the peripheral Dy(III) since it is a component of a larger cluster. It should be noted that no $\text{Ln}_2\text{Zn}_4(\text{picHA})_4$ complexes have been observed in the assembly of these MC complexes. The other fragment of the $\text{Ln}_2\text{Zn}_9(\text{quinHA})_{10}(\text{OH})$ can be viewed as a split open Ln(III)[15-MC-5] complex. Figure 4.17 clearly demonstrates the structural similarities of the cluster and the isolated Ln(III)[15-MC-5].

While this $\text{Ln}_2\text{Zn}_9(\text{quinHA})_{10}(\text{OH})$ is the only dilanthanide cluster that was crystallographically characterized, a number of other clusters were observed by ESI-MS, such as the $\text{Ln}_2\text{Zn}_7\text{L}_8$, $\text{Ln}_2\text{Zn}_8\text{L}_9(\text{OH})$ and $\text{Ln}_2\text{Zn}_8\text{L}_{10}$. When considering the formation of coordination driven assemblies, one can envision a number of possible intermediates. Furthermore, kinetic mistakes are possible, where the assembly of the building blocks forms a complex that is kinetically stable, though not the thermodynamic product.

Typically, the assembly process is too fast to observe or isolate these intermediates and mistakes. The work on the assembly and stability of these dilanthanide clusters are not intermediates as they persist even upon heating the solutions. However, it is possible that they are kinetic mistakes as the clusters could have exceptional stability in certain solvent conditions that contributes to their persistence at 65 °C. Interestingly, the $\text{Ln}_2\text{Zn}_9(\text{quinHA})_{10}$ contains structural motifs that resemble other known MCs. This observation suggests that the dilanthanide clusters could be kinetic mistakes in the assembly of LnMCs, and the structures could provide glimpses of intermediates in MC assembly processes. For example, one might envision that the synthesis of the LnZn_5L_5 involves the incorporation of the Ln(III) ion into the center of a Zn_5L_4 , followed by the flattening and opening of the 12-MC-4. This intermediate would possess a split open motif, and incorporation of an exogenous ligand would complete the LnZn_5L_5 . The split open Ln[15-MC-5] motif in the $\text{Ln}_2\text{Zn}_9(\text{quinHA})_{10}$ could be a glimpse at this intermediate. Alternatively, the fragments in these clusters could be the result of a reaction of MC with another, which is supported by the $\text{Ln}_2\text{Zn}_4\text{L}_4(\text{OH})$ motif in the $\text{Ln}_2\text{Zn}_9(\text{quinHA})_{10}$. With these concepts of kinetic mistakes, intermediates, and intermetallacrown reactions in mind, it is interesting to consider possible structures of the $\text{Ln}_2\text{Zn}_7\text{L}_8$, $\text{Ln}_2\text{Zn}_8\text{L}_9(\text{OH})$ and $\text{Ln}_2\text{Zn}_8\text{L}_{10}$ species observed via ESI-MS. For example, the $\text{Ln}_2\text{Zn}_8\text{L}_9(\text{OH})$ could be formulated as an Ln(III)[12-MC-4] that reacts with another Ln(III)[12-MC-4] and an exogenous picHA ligand. Crystal structures of these remaining dilanthanide complexes could provide useful insight into the assembly of LnMCs.

So far, 6 distinct structural motifs containing Zn(II), picHA, and Ln(III) building blocks have been crystallographically characterized. These complexes have been discussed separately based on their different structural motifs. Promisingly, the different structures could generate different molecular recognition behavior, solid state architectures, and physical properties. The concave 12-MC-4 topologies are particularly exciting as they are completely face differentiated. The possibilities for utilizing these different structure types are dependent in part on the intricacies of their assembly and their solution stability. Such aspects of the chemistry of these MCs are discussed below.

Given the diverse series of complexes assembled from Zn(II), picHA, and Ln(III), questions arise pertaining to how these building blocks assemble. Such questions are

particularly pertinent as the monolanthanide MCs contain similar structural motifs. During the assembly process, do the Zn(II) ions and hydroximates assemble around the central Ln(III) ion, or does the Ln(III) ion react with the Zn_5L_4 , displacing the central Zn(II) to form a Ln(III)[12-MC $_{Zn(II), picHA}$ -4] complex? Considering the progression of monolanthanide MCs prepared in this work, the latter scenario seems more likely. The following thought experiment provides a rationale for how these complexes relate (figure 4.40). The reaction of the Zn_5L_4 with a Ln(III) ion could displace the central Zn(II) ion, forming a Ln(III)[12-MC $_{Zn(II), picHA}$ -4]. Or, the approach of the Ln(III) ion could split open the 12-MC-4 ring, pushing the central Zn(II) ion into ring. This intermediate could incorporate an exogenous picHA ligand to form the Ln(III)[15-MC-5]. This concept is supported by the observation of the split-open Ln(III)[15-MC-5] motif in the $Dy_2Zn_9(quinHA)_{10}(OH)$ structure. Thus, the $LnZn_4L_4$ and $LnZn_5L_5$ could be viewed as products of two different pathways for the reaction of the Zn_5L_4 with a Ln(III) ion. The $LnZn_4L_4$ could react with a Zn_5L_4 , displacing the central Zn(II) ion to form the $LnZn_8L_8$ sandwich complex. Lastly, this $LnZn_8L_8$ sandwich complex could take eight ligands and eight Zn(II) ions from two Zn_5L_4 complexes to generate the 24-MC-8 motif and form the $LnZn_{16}L_{16}$. In such a scenario, the solvent could selectively stabilize these different intermediates, preventing the reactions from proceeding to completion and allowing for their isolation and characterization. These possibilities are discussed below in light of the solution assembly and stability data.

Theoretical Framework for Solvent Directed Assemblies with Symmetry Incompatible Building Blocks

The assembly of discrete macrocyclic complexes through metal ion coordination is thermodynamically driven by the formation of a maximum number of strong metal-ligand interactions upon completion of the ring and entropic effects. Extensive research has shown that stable macrocycles assemble from symmetry compatible building blocks, meaning that the symmetry elements in each individual building block introduce integral symmetry elements in the assembled complex.^{1,27} The Ln(III)[15-MC $_{Cu(II), picHA}$ -5] exemplifies a self-assembled system composed of symmetry compatible building blocks.^{40,41} The picHA chelate ring geometry introduces vertices with 72° external angles needed for the pentagonal macrocycle (figure 4.1). The Cu(II) ion arranges the picHA

ligands in the equatorial plane, enforcing the planarity of the pentagonal macrocycle and forming a linear bridge between the 72° vertices. Lastly, the Ln(III) central metal can accept the electron density in the central cavity and form complexes with C_5 rotational symmetry. Thus, the picHA ligand, Cu(II) ring ion, and central Ln(III) ion are symmetry compatible as they all introduce symmetry elements that are integral to the pentagonal Ln(III)[15-MC_{Cu(II),picHA-5}] macrocycle. The symmetry compatible building blocks help account for the significant solution stability of the complex, as the maximum number of thermodynamically stable dative bonds are formed upon completion of the macrocycle. Notably, the Ln(III)[15-MC_{picHA-5}] with Ni(II) and Cu(II) ring metals are so stable that no other LnMCs have been observed to assemble in solution. Also, the equilibrium between the M_5L_4 and LnM_5L_5 is completely driven to the LnM_5L_5 and no rearrangement to the M_5L_4 is observed in solution upon dissolution.⁷³ Lastly, Ln(III)[15-MC_{picHA-5}] with Ni(II) and Cu(II) show no solvent dependence despite possessing numerous open coordination sites.

This work explores the use of symmetry incompatible building blocks with open coordination sites as a strategy to realize coordination driven assemblies that are directed by the solvent selection. Symmetry incompatible building blocks have symmetry elements that are not complementary with the symmetry of a single self-assembled complex, *exclusively*. PicHA generates the vertex of a planar pentagon. However, Zn(II) forms 5-coordinate complexes with non-planar structures. Cu(II) also forms five-coordinate square-pyramidal complexes in LnCu₅L₅ complexes. However, the Cu(II), resides within the equatorial ligand plane. In contrast, square pyramidal Zn(II) ions reside over 0.5 Å above the equatorial ligand plane, causing the ligands to deviate from planarity. Thus, the two building blocks are symmetry incompatible because they introduce symmetry elements found in *different* assemblies. Moreover, the Ln(III) is highly flexible as it can adopt coordination environments with a variety of symmetry elements, such as C_3 , C_4 , and C_5 rotation axes. Thus, these symmetry incompatible building blocks are not programmed to form one complex *exclusively*. Since the Zn(II) and Ln(III) ions have open coordination sites, the assembly can proceed selectively to one particular complex based on the coordination of solvent molecules. The advantage of this synthetic approach is that multiple complexes can *selectively* assemble from the same

components by simply changing the solvent. It should be noted that the solvent is also acting as a ligand in these complexes, so the effects of solvation and coordination to the open metal sites cannot be separated. Importantly, these complexes could have unique structural features or physical properties that can be applied in areas of need.

Solvent Directed Assembly of PicHA, Zn(II), and Ln(III)

ESI-MS provides the strongest evidence for the selectivity imposed by the solvent. By simply mixing H₂picHA, 2 equivalents of triethylamine, and 1.25 equivalents of Zn(NO₃)₂, two distinct MC structural motifs are observed to assemble in solution (figure 4.3): the Zn₅L₄ and clusters with approximately Zn₁₄L₁₂ stoichiometry. Upon mixing 5 equivalents of H₂picHA, 10 equivalents of triethylamine, 5 equivalents of Zn(NO₃)₂, and 1 equivalent of a Ln(NO₃)₃ salt, eight distinct LnMC motifs have been identified that assemble in solution (figures 4.6, 4.7, 4.9, 4.10): LnZn₄L₄, LnZn₅L₅, LnZn₈L₈, LnZn₁₂L₁₂, LnZn₁₆L₁₆, Ln₂Zn₃L₄, Ln₂Zn₇₋₉L₈₋₁₀, and Ln₄Zn₄₋₅L₈₋₉. Such an intricate solvent dependence has not been obtained in any other chemical system, supporting the viability of the symmetry incompatible building blocks with open-coordination sites approach. All complexes, except the Ln₂Zn₃L₄, persist after heating the solutions at 65 °C for over 24 hours. As described above, six of these MCs have been isolated and crystallographically characterized: Zn(II)[12-MC-4], Ln(III)[12-MC-4], Ln(III)[15-MC-5], Ln(III)[12-MC-4]₂, Ln(III)[12-MC-4]₂[24-MC-8], and the Ln₂Zn₉L₁₀ cluster.

The geometry of the fused chelate rings on picHA promotes the formation of a pentagonal 15-MC-5 motif (figure 4.1). In contrast, the distorted square pyramidal Zn(II) ring metals promote the formation of concave 12-MC-4 topologies. Additionally, it can be surmised that aqueous pyridine mixtures lead to bridging waters or hydroxides, which can disrupt the traditional symmetry of MCs and lead to elaborate Ln₂ clusters (figure 4.16). For these reasons, the LnZn₅L₅ assembly is directed by the ligand, while the LnZn₄L₄, LnZn₈L₈, Ln₂ clusters, LnZn₁₂L₁₂, and LnZn₁₆L₁₆ are promoted by the solvent. As the LnZn₅L₅ is primarily directed by the ligand, its assembly shows very limited solvent dependence (table 4.3). The LaZn₅L₅ assembles in all solvents, albeit to varying extents. The YZn₅L₅ is more selective, assembling in pyridine and 9:1 DMF/pyridine exclusively.

The assembly of the LnMCs with 12-MC-4 topologies and the Ln₂ clusters is directed by selective interactions between the solvent and the open metal sites on the Zn(II) and Ln(III) ions. Figure 4.41 relates the solvent to the LnMCs that selectively assemble in those conditions. The LnZn₅L₅ was omitted from this chart as its assembly shows a limited solvent dependence. It is evident that pyridine containing solvents lead to the formation of complexes with solvent exposed Zn(II) ions, such as the LnZn₄L₄ and LnZn₈L₈. This trend likely arises from soft Zn(II) ring metal having a high affinity for pyridine, a soft ligand. Hydroxide, and presumably water as well, can act as a bridging ligand between two Zn(II) ions. Therefore, the assembly in 4:1 water/pyridine generates MCs with solvent-exposed Zn(II) ring metals and bridging hydroxides. This selectivity is reflected in the crystal structures of the LnZn₈(picHA)₈ complexes (figure 4.13, 4.14), which contain Zn(II) ions with pyridine ligands, or hydroxides, in the axial positions.

The Ln(III) ions are more oxophilic than Zn(II) and seem to prefer being solvated by DMF containing solvents. This preference for DMF is reflected in the preferential assembly of the LnZn₄L₄ in 9:1 DMF/pyridine. The Ln(III) ions are open to the DMF molecules while the Zn(II) ring metals are free to interact with pyridine. The DMF ligands on the Dy(III) ion in the DyZn₄(quinHA)₄ crystal structure are consistent with this trend (figure 4.12). In 4:1 water/pyridine, the absence of DMF likely contributes to the formation of a sandwich complex. As there is no DMF to solvate the exposed Ln(III) sites in the LnZn₄L₄, a sandwich motif is generated to saturate the coordination sphere central ion. The assembly of the LnZn₁₆L₁₆ in methanol, which contains a sandwich motif, further supports this idea. Furthermore, the 24-MC-8 motif in the LnZn₁₆L₁₆ can be attributed to the absence of pyridine during its assembly. As the Zn(II) ions are not solvated by pyridine, the 24-MC-8 assembles to bind to the Zn(II) axial coordination sites. So DMF solvates the Ln(III) coordination sites and prevents the formation of sandwich complexes. Pyridine solvates the axial Zn(II) sites and blocks the formation of 24-MC-8 motifs on the Ln(III)[12-MC-4] motif.

Based on these trends in the solvent dependent assembly, the LnZn₁₂L₁₂ complex that assembles in DMF likely has a Ln(III)[12-MC-4][24-MC-8](DMF)₄ structure. A model of this proposed structure is displayed in figure 4.42. The proposed structure contains a Ln(III)[12-MC_{Zn(II),picHA}-4] motif with four DMF ligands coordinated to the

Ln(III) ion, just as in the $\text{DyZn}_4(\text{quinHA})_4$ structure. A 24-MC-8 would be bound to the Zn(II) ions of the 12-MC-4 since there is no pyridine to solvate the axial coordination sites on the ring metals. This proposed complex possesses the formula $\text{LnZn}_{12}\text{L}_{12}$ and is consistent with the solvent dependent assembly that has been observed heretofore.

It is also worth considering the $\text{Zn}_{14}\text{L}_{12}$ complex that assembles in methanol and DMF, but not in pyridine containing solvents. Considering that a 24-MC-8 seems to assemble on $\text{M}[12\text{-MC-4}]$ platforms in the absence of pyridine, it is possible that this $\text{Zn}_{14}\text{L}_{12}$ is a $\text{Zn(II)}[12\text{-MC-4}][24\text{-MC-8}]$. This complex would have a $\text{Zn}_{13}\text{L}_{12}$ stoichiometry. While a species with this stoichiometry has not been observed by ESI-MS, it is possible that the species can only be ionized with an exogenous Zn(II) to form the $\text{Zn}_{14}\text{L}_{12}$, or by losing a ligand to form the $\text{Zn}_{13}\text{L}_{11}$.

The strategy of realizing solvent directed assemblies through the use of symmetry incompatible building blocks with open coordination sites provides a novel approach to assembling a diverse array of complexes. The approach expands on the powerful symmetry-based design strategies that have been established,¹ potentially giving rise to a number of different complexes from the same building blocks through a simple change in the solvent. Such a variety of complexes is exciting as different structures can give rise to unique functionality or physical properties. For the LnMCs presented in this work, different luminescence and magnetic properties are expected due to the different Ln(III) coordination environments. Also, the inherently chiral Zn_5L_4 and LnZn_4L_4 , concave LnZn_8L_8 and $\text{LnZn}_{16}\text{L}_{16}$ sandwich complexes, and bifacial LnZn_5L_5 should have vastly different molecular recognition capabilities and template different assemblies and networks. The strategy of using symmetry incompatible building blocks with open coordination sites should be quite general because similar symmetry considerations dictate the assembly of most MCs and other coordination driven assemblies. However, it should be noted that the variety of complexes realized in this work is influenced by solvation of both the Zn(II) and Ln(III) ions. As many coordination driven assemblies utilize only one metal, the scope of complexes obtained could be limited. Furthermore, the variety of LnMCs is also promoted by the *different* solvation preferences of Zn(II) and Ln(III). As Zn(II) is soft and Ln(III) is a hard oxophilic cation, the assembly is directed by the presence of both pyridine, a soft ligand, and DMF. If both metal ions had

similar hardness or softness, they would have similar solvation behavior. Thus, the assembly would respond to fewer solvents and the number of complexes that assemble could be limited.

Solution Integrity of MCs with Zn(II) Ring Ions

The structures of the six MCs that have been isolated from picHA, Zn(II), and Ln(III) building blocks suggest promise for luminescence, single molecules magnetism, and molecular recognition. In all of these areas, solution stability can be important. Luminescent lanthanide compounds used in biomedical assays must be kinetically stable in water to prevent leaching of the toxic Ln(III) ion from the ligand.⁹⁰ For processing compounds into optical devices, molecular materials, or onto surfaces for magnetic characterization, varying degrees of kinetic or thermodynamic stability are required. Coordination driven assemblies with symmetry compatible building blocks often possess notable stability in solution. Assemblies with flexible ligands, or assemblies that change their topology in response to different substrates, often persist as mixtures of complexes in equilibrium with each other. Thus, the thermodynamic and kinetic stability of the complexes prepared from the symmetry incompatible building blocks is a potential concern. The stability of the six isolated MCs was assessed to gain insight into their viability for different applications. Varying degrees of solution stability were observed.

Zn₅L₄ Stability

The Zn₅L₄ is stable in pyridine, 9:1 DMF/pyridine, 4:1 water/pyridine, acetonitrile, and methanol at room temperature for 24 hours. The ESI-MS and ¹H NMR spectra are consistent with these species (figures 4.21, 4.22), and no new peaks grow in to the spectra over 24 hours. This stability suggests promise for utilizing the Zn₅L₄ in molecular recognition applications. Also, the resolution of the Zn₅L₄ enantiomers seems feasible based on this limited data. There is evidence for partial rearrangement in water and DMF to the Zn₁₄L₁₂ and other related clusters. To gain further insight into the kinetic and thermodynamic stability of the Zn₅L₄, the complex was reacted with 0.8 equivalents of Ln(NO₃)₃ in different solvents. ¹H NMR and ESI-MS suggest that the conversion to the LnZn₄(picHA)₄, LnZn₅(picHA)₅, and LnZn₈(picHA)₈ proceed effectively at room temperature. This is true in any solvent, as the LnZn₄(picHA)₄ appears after 24 hours at room temperature in DMF and 9:1 DMF/pyridine (figures 4.30, 4.31). Likewise the

$\text{LnZn}_5(\text{picHA})_5$ appears in DMF, methanol, and DMF/pyridine upon reacting at room temperature. In contrast, the conversion to the $\text{LnZn}_{12}(\text{picHA})_{12}$ and $\text{LnZn}_{16}(\text{picHA})_{16}$ requires heating to reach equilibrium (figures 4.33, 4.34, 4.25, 4.26).

These differences suggest that there is a reasonably large activation energy for forming the $\text{LnZn}_{12}\text{L}_{12}$ and $\text{LnZn}_{16}\text{L}_{16}$ that is not present for the LnZn_4L_4 , LnZn_5L_5 , or LnZn_8L_8 . Based on the crystal structure of the $\text{LnZn}_{16}\text{L}_{16}$ and the proposed structure of the $\text{LnZn}_{12}\text{L}_{12}$, this activation energy is likely for the formation of the 24-MC-8 ring. Returning to the proposed mechanism for the assembly of the monolanthanide MCs from the Zn_5L_4 discussed above and in figure 4.40, the reactions involve two types of transformations. A substitution of the central metal ion is required in the conversion of the Zn_5L_4 to the LnZn_5L_5 or LnZn_5L_4 , and for the converting the LnZn_4L_4 to the LnZn_8L_8 . Based on the conversion of the Zn_5L_4 to the LnZn_4L_4 , LnZn_5L_5 , or LnZn_8L_8 at room temperature, this reaction likely has a modest activation energy. The second reaction type in the proposed mechanism would involve the 24-MC-8 assembling around the exposed Zn(II) ring metals of a concave Ln(III)[12-MC-4]. As the Zn(II) and ligands in the 24-MC-8 originate from the Zn_5L_4 , formation of the 24-MC-8 requires decomposition of the Zn_5L_4 . The kinetic barrier to Zn_5L_4 decomposition should be greater than central metal substitution. It should be noted that no evidence has been obtained demonstrating that a 24-MC-8 species persists in the absence of the LnZn_4L_4 or LnZn_8L_8 complexes. Overall, these kinetic trends in reactivity suggest that the Zn_5L_4 complex as a whole is kinetically stable at room temperature, though the central metal is not.

Consideration of the thermal barrier to Zn_5L_4 decomposition in the formation of the 24-MC-8 adds a layer of complexity to the solvent dependent assembly that arises from differences in the solvation of the metal ions. Regarding $\text{LnZn}_{12}\text{L}_{12}$ and $\text{LnZn}_{16}\text{L}_{16}$ formation specifically, the absence of pyridine leads to the assembly of the 24-MC-8 on the axial coordination sites on the Ln(III)[12-MC-4] units. However, the thermal barrier to 24-MC-8 formation through Zn_5L_4 decomposition could also be influenced by the solvent. Specifically, the Zn_5L_4 could be more kinetically stable in pyridine-containing solvents. The solvent dependence seen in the $\text{Zn}_{14}\text{L}_{12}$ species supports this notion. The $\text{Zn}_{14}\text{L}_{12}$ complex only assembles in methanol and DMF based on ESI-MS. No $\text{Zn}_{14}\text{L}_{12}$ is seen in 9:1 DMF/pyridine, pyridine, or 4:1 water/pyridine. Also, partial decomposition of

the Zn_5L_4 to the $Zn_{14}L_{12}$ is evident in DMF, not in 9:1 DMF/pyridine, pyridine, or 4:1 water/pyridine. Likely, pyridine containing solvents prevent $LnZn_{12}L_{12}$ and $LnZn_{16}L_{16}$ formation by coordinating to the axial sites on the Zn(II) ring metals and stabilizing the Zn_5L_4 or $LnZn_4L_4$.

The titrations of $Ln(NO_3)_3$ to Zn_5L_4 also show that the Zn_5L_4 has a similar thermodynamic stability as the LnMCs. This stability is evident in the significant amount of Zn_5L_4 that remains once the $Ln(NO_3)_3$ is added, especially considering that there is an excess of $Ln(NO_3)_3$ for most of these titrations. In 4:1 water/pyridine, the $LnZn_8(picHA)_8$ and Ln_2 clusters are minor species at equilibrium (figures 4.24, 4.32). In methanol and DMF, the LnMCs are major species, though the $Zn_5(picHA)_4$ is still present. The conversion to the $LaZn_5(picHA)_5$ is nearly complete in pyridine, though faint peaks for the $Zn_5(picHA)_4$ remain with one equivalent of $La(NO_3)_3$. The conversion is much more limited with Y(III). This greater thermodynamic stability with larger lanthanides is consistent with the trends in $Ln(III)[15-MC_{Cu(II),pheHA-5}]$ complexes in aqueous conditions.⁶⁶ For the conversion to the $YZn_4(picHA)_4$ in 9:1 DMF/pyridine, there is a shortage of Y(III), and the integrals suggest nearly complete conversion to the $YZn_4(picHA)_4$.

Based on these titrations, the $Zn_5(picHA)_4$ should be present at equilibrium to some extent upon dissolution of all LnMCs. Also, the relative thermodynamic stabilities of the preferred LnMC and Zn_5L_4 vary in the different solutions. Based on the cation recognition chemistry of organic macrocycles, this trend is likely dictated in part by the solvation energy of the cations in the different solvents. Solvents that solvate certain ions more strongly will favor MCs where these ions are unbound. So the instability of LnMCs in 4:1 water/pyridine could result from the strong solvation of the Ln(III) ion in water. Likewise, the strong relative stability of the $LnZn_5L_5$ compared to the Zn_5L_4 in pyridine could be due to the poor solvation of free Ln(III) and strong solvation of free Zn(II) by pyridine.

Such thermodynamic and kinetic stability for the Zn_5L_4 contrasts the behavior of the Cu_5L_4 and Ni_5L_4 . Thermodynamic investigations of these systems with α -aminoHA ligands in aqueous conditions have shown the Cu_5L_4 and Ni_5L_4 to possess modest thermodynamic stability, persisting at equilibrium with a variety of mononuclear species

from pH 4-6.^{60,61} The NMR and ESI-MS spectra of the $Zn_5(picHA)_4$ and $Zn_5(quinHA)_4$ suggest the complexes are the only species in pyridine containing solvents and methanol at room temperature. So the M_5L_4 seems to be most stable with Zn(II). This can be rationalized based on the preferred geometries of the ions. As the M_5L_4 is a concave structure, it requires metal ions with distorted square pyramidal geometries. As ligand field effects promote square pyramidal and octahedral geometries in Cu(II) and Ni(II), the M_5L_4 is less stable with these metal ions. Notably, the $Cu_5(pheHA)_4$ is much less stable than the corresponding $LnCu_5(pheHA)_5$. Effectively no $Cu_5(pheHA)_4$ is present at equilibrium upon dissolution of the $LaCu_5(pheHA)_5$. In contrast, some $Zn_5(picHA)_4$ persists at equilibrium. Therefore, the difference in the relative stabilities of the MCs is greater with Cu(II) than with Zn(II). This could be due to both the greater stability of the Zn_5L_4 relative to the Cu_5L_4 and the lower stability of the $LnZn_5L_5$ relative to the $LnCu_5L_5$. Presumably both are true, as the preferred square-pyramidal Zn(II) coordination geometry is complementary with the 12-MC-4 structure but not with the 15-MC-5. Likewise, the square-pyramidal preference of Cu(II) complements the 15-MC-5, but not the 12-MC-4. It would be worthwhile to gain a better understanding of the assembly of these Zn(II) MCs through quantitative measurements.

LnMC Stability

Consistent with the Zn_5L_4 conversion reactions above, the LnMCs undergo rearrangements to the Zn_5L_4 over time. With the $LnZn_4L_4$, this conversion appears to proceed rapidly upon dissolution, and the $LnZn_5L_5$ forms as well. The $LnZn_5L_5$, $LnZn_8L_8$, and $Ln_2Zn_9L_{10}$ undergo slower rearrangements at room temperature. Since the complexes rearrange to the Zn_5L_4 , the central Ln(III) ion must be kinetically unstable in these LnMCs at room temperature. Importantly, as the rearrangement to the Zn_5L_4 is relatively slow, it is evident that the MCs have reasonable kinetic stabilities that allow for their isolation and solution characterization. Furthermore, solution processing of the complexes and incorporation into ordered assemblies and networks should also be feasible. However, the $LnZn_5L_5$ is unstable with respect to carboxylates. Presumably acetate bridged Zn(II) complex are generated, such as the $Zn_4(picHA)_2(acetate)_4$ complex (figure 4.20). Therefore, the carboxylate binding chemistry presented in chapters 2 and 3

will not be possible with the LnZn_5L_5 . Fortunately, the LnZn_5L_5 appears to be stable with sulfonates, so sulfonate recognition chemistry could be pursued.

Unlike the other LnMCs, the $\text{LnZn}_{16}\text{L}_{16}$ complexes with middle to late Ln(III) ions, such as Y(III), are stable kinetically in a variety of organic solvents and water at room temperature. No Zn_5L_4 is observed by ESI-MS in methanol or pyridine over many days. This stability is impressive considering that most other MCs with large rings are unstable in solution. With the very large or very small Ln(III) ions such as La(III) and Yb(III), some Zn_5L_4 grows in over time in pyridine, demonstrating partial decomposition. Importantly, the central Ln(III) ion in the $\text{LnZn}_{16}\text{L}_{16}$ is kinetically stable, as no lanthanide exchange was observed over one week in methanol or in water. However, the $\text{LaZn}_{16}(\text{picHA})_{16}$ decomposes in water. The kinetic stability of the central Ln(III) ion in the $\text{LnZn}_{16}\text{L}_{16}$ suggests promise for biomedical assays. The kinetic stability of the $\text{LnZn}_{16}\text{L}_{16}$ relative to the other LnMCs likely arises from the large number of chelate rings in its structure. The LnZn_4L_4 and LnZn_5L_5 have 12 and 15 five-membered chelate rings, respectively, while the $\text{LnZn}_{16}\text{L}_{16}$ contains 48. For the central Ln(III) to be removed from the $\text{LnZn}_{16}\text{L}_{16}$, a much larger number of chelate rings and dative bonds would have to be broken compared to the other LnMCs.

It should be noted, however, that there was evidence for ligand dissociation in the $\text{LnZn}_{16}\text{L}_{16}$ complexes (figure 4.27). Ligand dissociation was more prevalent with larger Ln(III) central metals and in water. Ligand exchange unfortunately complicates potential applications in biomedical assays. However, it advantageously provides a straightforward route to functionalization of the complexes. The $\text{LnZn}_{16}\text{L}_{16}$ could be attached to a surface or polymer by exchanging a picHA ligand for a functionalized picHA tethered to the support. Potentially, chromophores could be incorporated into the $\text{LnZn}_{16}\text{L}_{16}$ complex that could serve as antenna for sensitizing the Ln(III) ion for luminescence. Ligand exchange should also be possible with the other LnMCs.

One major challenge in self-assembled systems is the preparation of unsymmetrical complexes. A noteworthy example of this are the class of mixed ligand and mixed ring-metal MCs.⁹¹ Unsymmetrical LnMCs would be a novel demonstration, but also allow for unprecedented control in the design of materials using functionalized ligands or the covalent attachment of the complexes to supports. In this regard, it was

exciting to observe that certain LnMCs undergo rearrangement to different complexes once dissolved in a different solvent. For example, the LaZn_8L_8 rearranges to the $\text{LaZn}_{16}\text{L}_{16}$ in methanol. It was hoped that by performing this solvent induced rearrangement in the presence of a different ligand, mixed ligand MCs could be isolated. For example, mixing $\text{LaZn}_8(\text{picHA})_8$, 8 Zn(II), and 8 quinHA ligands in methanol could generate an $\text{La(III)}[12\text{-MC}_{\text{Zn(II),picHA-4}}]_2[24\text{-MC}_{\text{Zn(II),quinHA-8}}]$. Unfortunately, ligand exchange eliminated any selectivity in these transformations. Ligand exchange was faster than the rearrangement of the MC, so site selectivity could not be realized. Furthermore, even if a site selective mixed ligand LnMC were prepared, it would undergo ligand exchange once dissolved in solution.

The kinetic stability of all of these LnMCs is impressive considering the size of the assemblies and that Zn(II) and Ln(III) are particularly labile metal ions. Importantly, kinetic stability will allow for the characterization of their properties, and possibly the attachment of the complexes onto solid supports. The stability of the $\text{LnZn}_{16}\text{L}_{16}$ is particularly promising for biomedical luminescence assays. However, ligand dissociation with the $\text{LnZn}_{16}\text{L}_{16}$ could be problematic. Notably, the stability of these complexes could likely be enhanced by employing tethered or macrocyclic ligands. This approach should minimize ligand dissociation and enhance the thermodynamic stability of the complex if the ligand were properly designed.

Luminescence of the $\text{LnZn}_{16}\text{L}_{16}$

As Ln(III) luminescence is used widely in optical devices and biomedical assays,⁹² information on the luminescence of the LnMCs was sought. In particular, the exclusion of high energy C-H oscillators from the proximity of the Ln(III) ion in LnMCs was expected to lead to efficient emission from the NIR emitting lanthanides, which typically suffer from vibrational quenching. Initial measurements were performed on the $\text{LnZn}_{16}\text{L}_{16}$ complexes, which have been shown to be stable in solution. Also, the crystal structures suggest that no solvent can coordinate to the Ln(III) ions or Zn(II) ions near the central metal, vibrational quenching should be strongly reduced in this complex. The $\text{YbZn}_{16}(\text{picHA})_{16}(\text{OTf})_3$ and $\text{NdZn}_{16}(\text{picHA})_{16}(\text{OTf})_3$ show efficient lanthanide centered luminescence in the NIR upon excitation of the ligand absorption bands in the ultraviolet region of the electromagnetic spectrum. The magnitude of the quantum yield and

luminescence lifetime of a lanthanide complex is dependent in part on the proximity of C-H oscillators that non-radiatively quench the Ln(III) excited state.^{46,47} Traditional organic ligand scaffolds do not effectively remove C-H oscillators from the proximity of the lanthanide without employing cumbersome and expensive deuteration or halogenation steps during the ligand synthesis. In contrast, the C-H oscillators on the MC itself are over 6.7 Å from the Ln(III) ion on the LnMCs presented herein. The YbZn₁₆(picHA)₁₆(OTf)₃ and NdZn₁₆(picHA)₁₆(OTf)₃ are the first luminescent LnMCs to be reported (figure 4.35).⁴⁹ The YbZn₁₆(picHA)₁₆(OTf)₃ has a quantum yield of 0.89 % in methanol upon excitation at 325 nm, meaning that 0.89% of the photons absorbed by the ligands in the complex are emitted from the Yb(III) at 980 nm. Time resolved measurements show the luminescence lifetime is 14 μs. This is the most efficient NIR emitting luminescent lanthanide complex in protic solvents. The luminescence of the YbZn₁₆(picHA)₁₆ is slightly better in acetonitrile due to reduced vibrational quenching from the solvent, and compares rather well to the very best luminescent complexes with non-deuterated or fluorinated ligands in non-deuterated solvents.^{19,93-95} The luminescence of the NdZn₁₆(picHA)₁₆ also compares well with the best complexes in the literature.

As vibrational quenching also effects the luminescence of the visible emitting Eu(III), Dy(III), and Sm(III) ions, the MC approach should be effective for these ions as well. The LnZn₁₆(picHA)₁₆ complexes did not exhibit lanthanide centered emission for the visible emitting lanthanides. To address whether the lack of visible emission was due to the energy of the ligand triplet state being too low to sensitize the lanthanide, attempts were made to measure the triplet state energy using the GdZn₁₆(picHA)₁₆(OTf) complex. Upon excitation of the complex at 280 or 340 nm in a frozen 1:4 methanol/ethanol matrix at 77 K, a broad band centered at 490 nm is observed, consistent with the ligand phosphorescence (figure 4.43). However, no band was observed upon application of a 100 μs delay, suggesting rapid quenching of this electronic state. Such rapid quenching is most consistent with a photoinduced intramolecular charge transfer process. It has been proposed that NIR emitting lanthanides can be sensitized through photoinduced intramolecular charge transfer processes, where charge recombination can result in energy transfer to the Ln(III) ion excited state. Such mechanisms rely on Yb(III) ion

reduction,⁹⁶ or a ligand reduction process.^{97,98} Importantly, these charge transfer states are thought to be too low in energy to sensitize the visible emitting Ln(III) ions, though suitable for the NIR emitting complexes.

For the LnZn₁₆L₁₆, a charge transfer process involving ligand reduction is most likely, as the rapid quenching of the GdZn₁₆(picHA)₁₆ and NdZn₁₆(picHA)₁₆ emission would not be observed if Ln(III) reduction was required. The reduction potentials of these Ln(III) ions are too large. A reduction of the pyridine group in picHA is more likely. The reduction potential of pyridinium in pyridine is about -1.6 V vs. 1 M AgNO₃/Ag at 40 °C.⁹⁹ The Rehm-Weller equation^{100,101} is used to estimate the driving force for a photoinduced charge transfer process, where e_0 is the elementary electronic charge, E_{ox} is the oxidation potential of the complex, E_{red} is the reduction potential of the complex, E_d is the singlet state energy of the complex, and w is a factor for the coulombic interaction (estimated as 0.1 eV).

$$\Delta G = e_0(E_{ox} - E_{red}) - E_d - w$$

The EuZn₁₆(picHA)₁₆ and GdZn₁₆(picHA)₁₆ both show irreversible oxidations at 0.88 V versus Ag/AgCl in 0.1 M aqueous KCl at 25 °C (figure 4.43), which likely originates from oxidation of the hydroximate. The reduction potential of pyridinium (-1.6 V) is an acceptable estimate of the reduction potential of the picHA pyridine bound to Zn(II) in the LnZn₁₆(picHA)₁₆. With the E_d at 325 nm of 3.815 eV, the driving force for the photoinduced charge transfer process in the LnZn₁₆(picHA)₁₆ can be roughly estimated as -1.44 eV. This means the energy of the photoinduced charge transfer state is 1.44 eV above the ground state. Given the crude estimates used in the calculations, this value likely has limited accuracy. However, the number is informative. The Eu(III) ⁵D₀ emissive state is 2.14 eV above the ground state,⁹⁶ meaning the LnZn₁₆(picHA)₁₆ charge transfer state is too low in energy to sensitize the Eu(III) ion. The Yb(III) ²F_{5/2} emissive state energy is 1.27 eV, so the YbZn₁₆(picHA)₁₆ charge transfer state is sufficiently high in energy for sensitizing the Yb(III) ion. These values support, but do not prove, that Ln(III) sensitization proceeds via a photoinduced charge transfer process. They also suggest that to sensitize the visible emitting Ln(III) ions, ligands with more positive reduction potentials are needed. Ligands with more positive reduction potentials could be realized by adding electron withdrawing functionalities or by incorporating donor-

acceptor functionalities into the ligand scaffold.⁹³ These possibilities are discussed in greater detail in chapter 5.

Overall, the synthetic work presented earlier in the chapter gave rise to LnMCs with Zn(II) ring ions, which importantly avoided excited state quenching through the *d-d* transitions of Cu(II) and Ni(II). These complexes possess enough solution stability, particularly the LnZn₁₆L₁₆, to allow for the characterization of their luminescence properties in solution. Luminescence studies of the LnZn₁₆(picHA)₁₆ have resulted in the first reported luminescent LnMC.⁴⁹ Importantly, these results also establish the general strategy for achieving bright NIR emitting luminescent lanthanide complexes by using LnMCs, or other metallamacrocycles, to mitigate vibrational quenching. The YbZn₁₆(picHA)₁₆ is the brightest complex with protonated ligands in protic solvents, proving the viability of this approach. It is possible that more efficient NIR luminescence, or visible emission, could be achieved in LnZn₁₆(picHA)₁₆ complexes by enhancing the efficiency of the energy transfer process. As energy transfer likely proceeds through a photoinduced charge transfer process, incorporating electron donor and acceptor groups into the ligand could enhance the luminescence properties.

Prospects for MCs with Zn(II) Ring Ions in Second Harmonic Generation Applications

An important impetus for the synthesis of MCs with Zn(II) ring metals was to prepare optically transparent MCs for second harmonic generation (SHG). Previously, Ln(III)[15-MC_{Cu(II),pheHA-5}] compartments were shown to effectively bind and orient the dipolar guest isonicotinate in the solid state such that there was a net dipole moment through the crystal. This result was impressive because it demonstrated that MC compartments can assist in overcoming the biggest challenge in preparing solid-state SHG materials: the requirement that chromophores be aligned to create a net dipole through the lattice. Analysis of the structure suggests that the chirality of the LnCu₅(pheHA)₅ ensures crystallization in a non-centrosymmetric space group, while the binding of isonicotinate guests on the hydrophilic and hydrophobic face of the host promotes a net dipole through 1-dimensional chains of the host-guest complex. Unfortunately, visible absorption from the Cu(II) ring metals scatters frequency-doubled light, so the SHG efficiency was low. Optically transparent MCs with Zn(II) ring metals

would overcome this issue. These initial studies focused on the achiral picHA ligand family. It was recognized that these achiral ligands would allow crystallization in centrosymmetric space groups. However, it was expected that the syntheses and properties of MCs with these achiral ligands would inform studies with the chiral α -aminoHA ligands. Highlights of initial work on MCs with Zn(II) ring metals and chiral ligands are presented in chapter 5. The different chapters of this thesis are tied together in part by the prospect of applying the guest recognition chemistry developed in chapters two and three with the Zn(II)-MCs from chapter four to develop SHG materials.

An important goal in the development of SHG materials with MCs, the preparation of the LnZn_5L_5 , was accomplished. The variety of other MCs that can be synthesized with Zn(II) and picHA create additional opportunities for preparing SHG materials, as the different concave and planar topologies of these MCs should generate vastly different assemblies and guest recognition behavior. These MCs should have sufficient solution stability for crystal engineering of frequency doubling crystalline host guest complexes. While these LnMCs are unstable with respect to carboxylates, dipolar sulfonates should be suitable guests for these studies. Moreover, the concave face of the 12-MC-4 can likely be used to bind substrates with organic topologies through Van der Waals interactions.

An important requirement of crystalline SHG complexes is thermal stability due to the operating temperatures of over 200 °C. Thermogravimetric analysis of the $\text{YZn}_4(\text{quinHA})_4$, $\text{LaZn}_8(\text{picHA})_8\text{Cl}_3$, and $\text{DyZn}_5(\text{quinHA})_5(\text{NO})_3$ were performed to assess the thermal stability of the complexes (figure 4.44). All of the LnMCs showed a gradual mass loss of lattice solvent molecules and coordinated pyridine ligands through about 340° C, though the MC seems stable at those temperatures. Above ~340° C, significant mass loss reveals MC decomposition. Thus, the LnMCs with Zn(II) ring metals show acceptable thermal stability for SHG applications. Future efforts to develop SHG materials using MCs should focus on preparing chiral Zn(II)-MCs with α -aminoHA ligands. Alternatively, resolution of the inherently chiral Zn_5L_4 could generate a chiral host that will enforce the noncentrosymmetric organization required for SHG. These prospects are discussed in greater detail in chapter five.

Conclusion

This chapter sought to establish that intricate solvent directed assemblies can be realized from symmetry incompatible building blocks with open coordination sites. Furthermore, the aim was to isolate Ln(III) MCs with optically transparent, diamagnetic ring metals for Ln(III) luminescence, second-order NLO, and single-ion magnetism. The synthesis and characterization of luminescent LnMCs was a primary goal meant to establish that MCs and other metallamacrocycles mitigate vibrational quenching and therefore, provide a general strategy for achieving efficient luminescent Ln(III) complexes. As part of the thesis objectives of utilizing MC structural versatility to tune MC assembly and physical properties, this chapter focused on the assembly of LnMCs using Zn(II) ring ions in place of Cu(II) and Ni(II)

This chapter reported the assembly of eight distinct LnMC motifs in solution. Six LnMCs have been isolated, crystallographically characterized, and assessed for solution stability. The selective assembly of so many complexes *in solution* from the same building blocks is unprecedented, establishing the syntax design strategy for solvent directed assemblies. This approach should be applicable to other systems and allow for an expansion in the diversity of MCs and coordination driven assemblies that can be assembled. Key synthetic targets for MC chemistry were isolated with Zn(II), the Ln(III)[15-MC_{M(II),picHA}-5] and M(II)[12-MC_{Zn(II),picHA}-4]. Furthermore, a variety of LnMC were isolated that vastly expand the structural topologies in these complexes. A variety of perturbations to the ligand bond distances and angles allow MCs to adapt to different central metals and ring metals.

The stability of the LnMCs provides insight into how to design stable complexes. Importantly, the thermodynamic stability of the Ln(III)[15-MC_{Cu(II), α -aminoHA}-5] complexes can be attributed in part to the instability of the Cu₅L₄ intermediate. Importantly, the limited thermodynamic stability of the LnMCs with Zn(II) is due to the significant stability of the Zn₅L₄. This trend shows that to prepare thermodynamically stable LnMCs, the ligand and ring metal must be designed based on symmetry arguments such that stable MCs can't assemble without a Ln(III) ion.

The MCs with Zn(II) ring metals developed in this chapter show groundbreaking luminescence properties and exhibit promise for novel functionality in magnetism, NLO,

and as molecular building blocks. The $\text{YbZn}_{16}(\text{picHA})_{16}$ in particular displays record setting NIR luminescence, establishing LnMCs as one of the only effective strategies for mitigating vibrational quenching in NIR emitting Ln(III) coordination complexes. Also, the highly symmetrical monolanthanide MCs provides a platform for correlating subtle changes to the Ln(III) ligand field to single-ion magnet behavior.¹⁰² Additionally, these LnMCs absorb visible light minimally, which is promising for second harmonic generation. The distinct topologies of the planar LnZn_5L_5 , concave Zn_5L_4 , and LnZn_8L_8 and $\text{LnZn}_{16}\text{L}_{16}$ sandwiches should show different molecular recognition behavior and template vastly different assemblies.

These results advance MCs toward the long term goal of multifunctional materials. LnMCs were known previously to be effective supramolecular hosts, building blocks for crystalline solids, and single molecule magnets. This work demonstrates that LnMCs can be tuned through ring metal substitutions for luminescence, optical transparency, or different magnetic properties and structural topologies. The versatility of the MC platform allows for structural changes to the building blocks to tune the structure and functionality, while still generating familiar complexes. Future studies will be able to apply the complexes and insights from this work in the development complexes with diverse functionality. These possibilities are discussed in the following chapter.

Figures

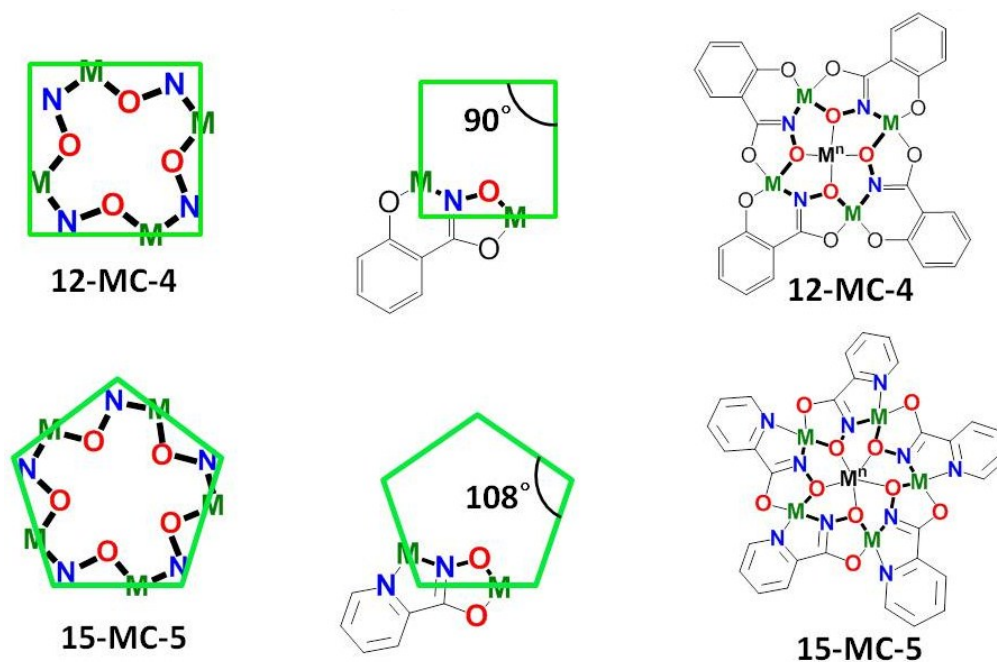


Figure 4.1: Diagrams displaying the design strategy for MCs based on the chelate ring geometry. The square-shaped 12-MC-4 is generated from ligands that form fused 5- and 6-membered chelate rings, such as salicylhydroximate (top). The pentagonal 15-MC-5 is generated from ligands that form fused 5-membered chelate rings, such as picHA (bottom).

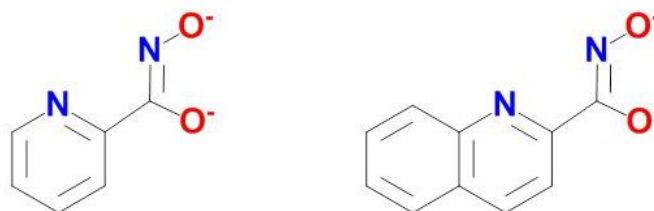


Figure 4.2: Chemdraw representations of picHA (left) and quinHA (right).

| Complex | DyZn ₄ (quinHA) ₄ (DMF) ₄ (NO ₃) ₃ | TbZn ₁₆ (picHA) ₁₆ (OTf) ₃ | ErZn ₁₆ (picHA) ₁₆ (OTf) ₃ | Zn ₄ (picHA) ₂ (acetate) ₂ (DMF) ₂ |
|---|--|---|--|--|
| Molecular Formula | Dy _{0.5} Zn ₂ C _{37.5} H ₄₅ N _{0.5} O _{13.5} | TbZn ₁₆ C ₁₃₈ H ₁₅₀ N ₄₀ O ₂₅ F ₆ | Er _{0.25} Zn ₄ C _{37.5} H _{45.25} F _{2.25} N _{10.5} O _{18.88} S _{0.75} | Zn ₄ C ₂₆ H ₃₄ N ₆ O ₁₄ |
| mol. wt [g mol⁻¹] | 1056.82 | 4743.94 | 1312.18 | 916.15 |
| crystal system / space group | orthorhombic, P2 ₁ 2 ₁ 2 | tetragonal, P4/ncc | tetragonal, P4/ncc | triclinic, P-1 |
| a [Å] | 19.5887(5) | 27.3594(4) | 29.8991 (4) | 7.9774 (2) |
| b [Å] | 22.7717(7) | 27.3594(4) | 29.8991 (4) | 10.4943 (3) |
| c [Å] | 10.1759(3) | 28.025(2) | 23.6731 (17) | 1036971 (3) |
| α [deg] | 90 | 90 | 90 | 80.681 (1) |
| β [deg] | 90 | 90 | 90 | 77.535 (1) |
| γ [deg] | 90 | 90 | 90 | 79.547 (1) |
| volume [Å³] | 4539.1(1) | 20977.6 (1.6) | 21163 (2) | 852.85 (4) |
| Z / density, ρ [g cm⁻³] | 4 / 1.546 | 4 / 1.502 | 16 / 1.647 | 1 / 1.784 |
| μ [mm⁻¹], F (000) | 6.220 / 2150 | 4.510 / 9540 | 3.789 / 10600 | 2.853 / 464 |
| crystal size [mm³] | 0.13 x 0.10 x 0.08 | 0.23 x 0.20 x 0.13 | 0.21 x 0.02 x 0.02 | 0.34 x 0.20 x 0.20 |
| θ range for data collection [deg] | 2.98 - 68.23 | 3.23 - 68.26 | 4.02 - 61.76 | 1.97 - 30.52 |
| limiting indices | -23 <= h <= 23 | -32 <= h <= 32 | -34 <= h <= 34 | -11 <= h <= 11 |
| | -27 <= k <= 27 | -32 <= k <= 32 | -34 <= k <= 34 | -14 <= k <= 14 |
| | -12 <= l <= 12 | -12 <= l <= 12 | -26 <= l <= 26 | -15 <= l <= 15 |
| measured/unique reflections | 97529 / 8302 | 28153 / 9625 | 252937 / 8278 | 34139 / 5208 |
| completeness to θ [%] | 99.9 | 99.9 | 99.9 | 99.9 |
| data/restraints/parameters | 8302 / 166 / 628 | 9625 / 126 / 742 | 8278 / 146 / 742 | 5208 / 0 / 230 |
| goodness of fit on F² | 1.102 | 1.090 | 1.126 | 1.044 |
| final R indices [I > 2σ(I)] | r ₁ = 0.0662, wR ² = 0.1831 | r ₁ = 0.0535, wR ² = 0.1729 | r ₁ = 0.0854 wR ² = 0.2559 | r ₁ = 0.0225, wR ² = 0.0594 |
| R indices (all data) | r ₁ = 0.0704, wR ² = 0.1865 | r ₁ = 0.0550, wR ² = 0.1744 | r ₁ = 0.0911, wR ² = 0.2637 | r ₁ = 0.0260, wR ² = 0.0612 |
| largest diff. peak and hole [e Å⁻³] | 1.165 and -1.076 | 0.910 and -0.843 | 1.046 and -5.300 | 0.684 and -0.289 |

Table 4.1: Crystallographic data for DyZn₄(quinHA)₄(DMF)₄(NO₃)₃, TbZn₁₆(picHA)₁₆(OTf)₃, ErZn₁₆(picHA)₁₆(OTf)₃, Zn₄(picHA)₂(acetate)₂(DMF)₂.

| Complex | DyZn ₄ (quinHA) ₄ (12-crown-4)(OTf) ₃ | DyZn ₅ (quinHA) ₅ (NO ₃) ₃ | EuZn ₅ (picHA) ₅ (NO ₃) ₃ | DyZn ₁₆ (picHA) ₁₆ (OTf) ₃ |
|--|--|---|---|---|
| Molecular Formula | DyZn ₄ C ₁₀₁ H ₉₀ N ₁₈ O ₂₁ F ₉ S ₃ | DyZn ₅ C _{109.41} H _{93.77} N _{24.41} O ₂₀ | EuZn ₅ C ₉₀ H ₄₄ N ₁₇ O ₂₁ | DyZn ₁₆ C ₁₄₉ H ₁₅₄ N ₆₀ O ₆₁ S ₃ F |
| mol. wt [g mol ⁻¹] | 2583.07 | 2559.87 | 1697.83 | 5278.95 |
| crystal system / space group | orthorhombic, P2 ₁ 2 ₁ 2 ₁ | orthorhombic, Pca2 ₁ | tetragonal, I4 ₁ /a | tetragonal, P4/ncc |
| <i>a</i> [Å] | 19.3892 (14) | 35.696 (3) | 45.3648 (6) | 29.903(3) |
| <i>b</i> [Å] | 19.7342 (14) | 13.3057 (2) | 45.3648 (6) | 29.903(3) |
| <i>c</i> [Å] | 27.959 (2) | 22.7159 (4) | 12.0304 (9) | 23.649(2) |
| α [deg] | 90 | 90 | 90 | 90 |
| β [deg] | 90 | 90 | 90 | 90 |
| γ [deg] | 90 | 90 | 90 | 90 |
| volume [Å ³] | 10698 (1) | 10789.2 (8) | 24758 (2) | 21147(3) |
| <i>Z</i> / density, ρ [g cm ⁻³] | 4 / 1.604 | 4 / 1.576 | 16 / 1.822 | 4 / 1.658 |
| μ [mm ⁻¹], <i>F</i> (000) | 1.726, 5220 | 5.537, 5188 | 10.036 / 13504 | 4.931 / 10608 |
| crystal size [mm ³] | 0.36 x 0.18 x 0.12 | 0.23 x 0.15 x 0.18 | 0.18 x 0.18 x 0.18 | 0.25 x 0.12 x 0.11 |
| θ range for data collection [deg] | 1.79 - 28.30 | 2.48 - 68.24 | 3.8 - 68.24 | 1.87 - 68.20 |
| limiting indices | -25 <= <i>h</i> <= 25 | -43 <= <i>h</i> <= 43 | -54 <= <i>h</i> <= 54 | -25 <= <i>h</i> <= 25 |
| | -26 <= <i>k</i> <= 26 | -15 <= <i>k</i> <= 13 | -54 <= <i>k</i> <= 54 | -36 <= <i>k</i> <= 36 |
| | -36 <= <i>l</i> <= 37 | -27 <= <i>l</i> <= 27 | -14 <= <i>l</i> <= 14 | -28 <= <i>l</i> <= 28 |
| measured/unique reflections | 120476 / 26538 | 135044 / 19572 | 148290 / 11345 | 14229 / 9683 |
| completeness to θ [%] | 99.9 | 99.5 | 100.0 | 99.9 |
| data/restraints/parameters | 26538 / 140 / 1540 | 19572 / 344 / 1533 | 11345 / 663 / 1047 | 9683 / 62 / 652 |
| goodness of fit on <i>F</i> ² | 1.019 | 1.082 | 1.084 | 0.851 |
| final <i>R</i> indices [<i>I</i> > 2 σ (<i>I</i>)] | <i>r</i> ₁ = 0.0442, <i>wR</i> ² = 0.0888 | <i>r</i> ₁ = 0.0534, <i>wR</i> ² = 0.1409 | <i>r</i> ₁ = 0.0560, <i>wR</i> ² = 0.1608 | <i>r</i> ₁ = 0.0558, <i>wR</i> ² = 0.1665 |
| <i>R</i> indices (all data) | <i>r</i> ₁ = 0.0652, <i>wR</i> ² = 0.0975 | <i>r</i> ₁ = 0.0573, <i>wR</i> ² = 0.1448 | <i>r</i> ₁ = 0.0607, <i>wR</i> ² = 0.1648 | <i>r</i> ₁ = 0.0592, <i>wR</i> ² = 0.1705 |
| largest diff. peak and hole [e Å ⁻³] | 2.564 and -0.932 | 0.861 and -1.567 | 1.283 and -1.399 | 1.576 amd -1.290 |

Table 4.2: Crystallographic data for DyZn₄(quinHA)₄(12-crown-4)(OTf)₃, DyZn₅(quinHA)₅(NO₃)₃, EuZn₅(picHA)₅(NO₃)₃, DyZn₁₆(picHA)₁₆(OTf)₃.

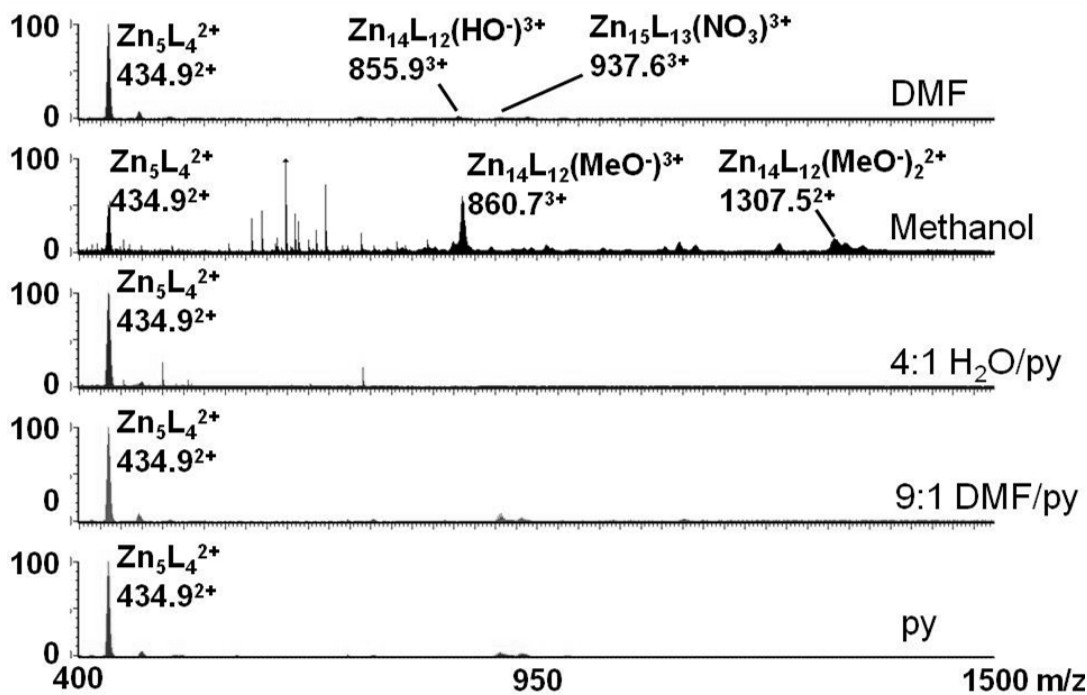


Figure 4.3: Mass spectra of the assembly of 1:2:1 H₂picHA, triethylamine, and Zn(NO₃)₂ in the indicated solvents at room temperature after 24 hours.

| Solvent | MCs w/o Ln(III) | La(III) MCs | Y(III) MCs |
|--------------------|----------------------------------|---|--|
| Pyridine | Zn ₅ L ₄ | LaZn ₄ L ₄ | YZn₄L₄ |
| | | LaZn₅L₅ | YZn₅L₅ |
| 9:1 DMF/pyridine | Zn ₅ L ₄ | LaZn ₄ L ₄ | YZn₄L₄ |
| | | LaZn₅L₅ | YZn ₅ L ₅ |
| 4:1 water/pyridine | Zn ₅ L ₄ | LaZn ₅ L ₅ | YZn ₈ L ₈ |
| | | LaZn₈L₈ | Y ₂ Zn ₇ L ₈ |
| | | La ₂ Zn ₉ L ₁₀ | Y₂Zn₈L₉ |
| | | | Y₂Zn₈L₁₀ |
| | | | Y₂Zn₉L₁₀ |
| methanol | Zn ₅ L ₄ | LaZn₅L₅ | YZn₁₆L₁₆ |
| | Zn ₁₃ L ₁₁ | LaZn₁₆L₁₆ | Y ₄ Zn ₄ L ₈ |
| | Zn ₁₄ L ₁₂ | | Y ₄ Zn ₅ L ₉ |
| DMF | Zn ₅ L ₄ | LaZn ₄ L ₄ | YZn ₄ L ₄ |
| | Zn ₁₄ L ₁₂ | LaZn₅L₅ | YZn ₈ L ₈ |
| | Zn ₁₅ L ₁₃ | LaZn ₈ L ₈ | YZn₁₂L₁₂ |
| | | LaZn₁₂L₁₂ | YZn ₁₆ L ₁₆ |
| | | LaZn₁₆L₁₆ | Y ₂ Zn ₃ L ₄ |

Table 4.3: MC species observed by ESI-MS for the reaction of H₂picHA, triethylamine, Zn(NO₃)₂, and Ln(NO₃)₃ (5:10:5:1 ratio) in the indicated solvent. The major LnMC species in the mass spectrum (based on relative intensities) are displayed in bold.

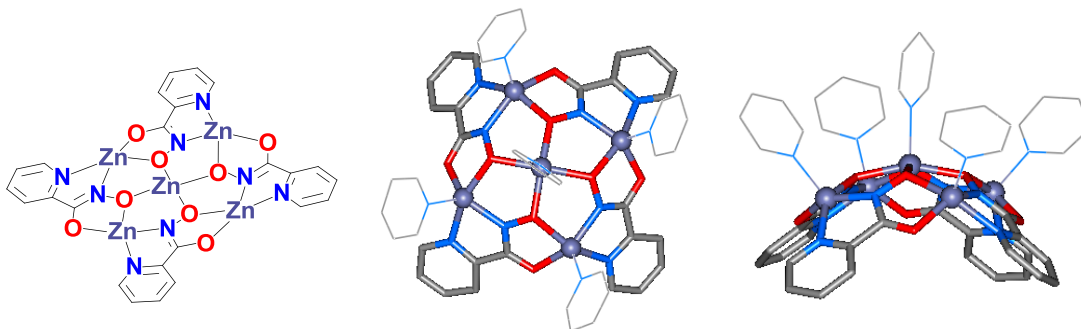


Figure 4.4: Chemdraw diagram (left) and crystal structure images of the $\text{Zn}_5(\text{picHA})_4(\text{OTf})_2$ complex viewed down the convex face (center) and from the side (right). Color scheme: Grey = carbon, red = oxygen, blue = nitrogen, grey-purple = zinc. Coordinated pyridine ligands are displayed as thin lines for clarity.

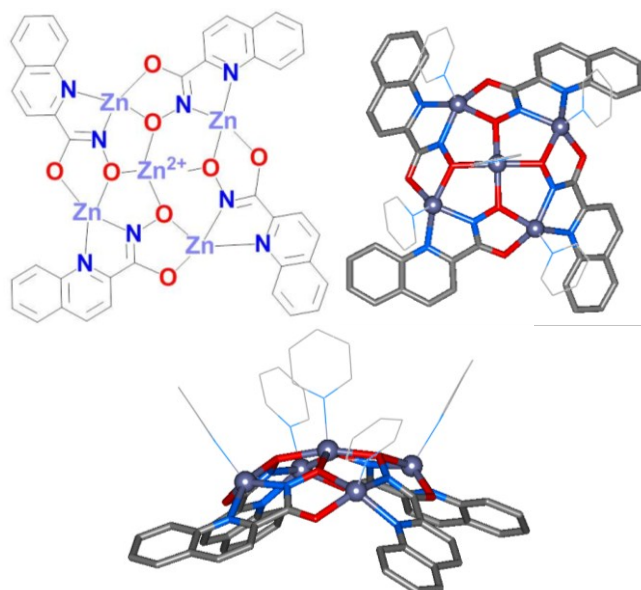


Figure 4.5: Chemdraw diagram (top left) and crystal structure images of the $\text{Zn}_5(\text{quinHA})_4(\text{BF}_4)_2$ complex viewed down the convex face (top right) and from the side (bottom). Color scheme: Grey = carbon, red = oxygen, blue = nitrogen, grey-purple = zinc. Coordinated pyridine ligands are displayed as thin lines for clarity.

| MC | Zn ₅ L ₄ ^d | DyZn ₅ L ₅ ^d | DyZn ₄ L ₄ ^{d,f} | DyZn ₈ L ₈ ^e | DyZn ₁₆ L ₁₆ ^{e,g} |
|---|---|---|---|---|---|
| Ring M coord. # | 5 | 5,5,5,5,6 | 5 | 5 | 5 |
| avg. τ | 0.19 | 0.24 | 0.16 | 0.34 | 0.06 |
| range τ | 0.04 - 0.30 | 0.10 - 0.64 | 0.15 - 0.17 | 0.02 - 0.77 | 0.00 - 0.01 |
| avg. Zn _{ring} -LMP ^a (Å) | 0.534 | 0.514 | 0.564 | 0.617 | 0.665 |
| avg. Zn-O _{hydroximate} (Å) | 2.068 | 2.079 | 2.084 | 2.040 | 2.019 |
| avg. Zn-O _{carbonyl} (Å) | 2.006 | 1.992 | 1.993 | 2.056 | 2.134 |
| avg. Zn-N _{hydroximate} (Å) | 2.021 | 1.998 | 1.997 | 2.041 | 2.066 |
| avg. Zn-N _{L-py} (Å) | 2.162 | 2.201 | 2.208 | 2.157 | 2.181 |
| avg. Zn _{ring} -L _{axial} (Å) | 2.041 | 2.123 | 2.060 | 2.060 | 1.987 |
| avg. Zn _{ring} -Zn _{ring} (Å) | 4.822 | 4.837 | 4.816 | 4.825 | 4.879 |
| avg. Zn _{ring} -OMP ^b (Å) | 0.682 | 0.224 | 0.677 | 0.588 | 0.556 |
| range Zn _{ring} -OMP ^b (Å) | 0.478 - 0.849 | -0.681 - 1.253 | 0.648 - 0.706 | 0.234 - 1.296 | 0.530 - 0.582 |
| Central M coord. # | 5 | 9 | 8 | 8 | 8 |
| avg. Central M-O _{hydroximate} (Å) | 2.041 | 2.426 | 2.330 | 2.369 | 2.340 |
| avg. Central M-OMP _{MC} (Å) | 0.375 | 0.014 | 1.289 | 1.229 | 1.073 |
| central cavity radius ^c (Å) | 0.65 | 1.04 | 0.66 | 0.64 | 0.72 |

Table 4.4: Selected geometric parameters for selected MCs with Zn(II) ring metals. a) Ligand mean plane for 5-coordinated ions, b) oxygen mean plane for the atoms in the central cavity, c) cavity radius is calculated as the average distance from the oxygen atom to the centroids of the OMP minus the radius of an oxygen atom (1.36 Å), d) L = quinHA, e) L = picHA, f) 12-MC-4 values only.

| Ring Metal | Ni(II) | Cu(II) | Zn(II) |
|--|-----------|-----------|-----------|
| Eu(III) coord. # | 8 | 9 | 9 |
| avg. Eu-O_{hydroximate} (Å) | 2.44 | 2.43 | 2.42 |
| avg. Eu-O_{NO3-top} (Å) | 2.538 | 2.518 | 2.521 |
| avg. Eu-O_{NO3-bottom} (Å) | 2.303 | 2.517 | 2.537 |
| cavity radius^a | 1.077 | 1.065 | 1.061 |
| Eu(III)-OMP (Å) | 0.147 | 0.040 | 0.031 |
| Ring metal coord. # | 4,6,6,6,6 | 4,5,5,5,5 | 5,5,5,5,5 |
| avg. M-O_{hydroximate} (Å) | 1.999 | 1.942 | 2.053 |
| avg. M-O_{carbonyl} (Å) | 2.001 | 1.933 | 1.998 |
| avg. M-N_{hydroximate} (Å) | 1.963 | 1.938 | 2.014 |
| avg. M-N_{picHA-py} (Å) | 2.038 | 1.991 | 2.145 |
| avg. M-axial ligand | 2.149 | 2.300 | 2.068 |
| avg. M-picHA mean plane | 0.022 | 0.156 | 0.510 |
| avg. M-OMP (Å) | 0.192 | 0.176 | 0.502 |
| avg. M-M (Å) | 4.668 | 4.584 | 4.757 |
| avg. O_{centroid}-M-axial ligand (°) | 90.76 | 97.53 | 110.99 |
| avg. N_{centroid}-M-axial ligand | 90.01 | 97.56 | 107.26 |
| avg. M-O_{hydroximate}-N_{hydroximate} (°) | 106.83 | 106.26 | 107.03 |
| avg. picHA O_{hydroximate}-N_{hydroximate}-C-O_{carbonyl} (°) | 1.043 | 1.60 | 0.76 |
| avg. picHA N_{hydroximate}-C-C-N_{picHA-py} (°) | 6.271 | 4.23 | 5.20 |
| avg. M-O_{hydroximate}-N_{hydroximate}-M (°) | 174.711 | 171.18 | 166.67 |
| avg. O_{carbonyl}-O_{hydroximate}-M-axial ligand (°) | 90.76 | 94.10 | 101.96 |
| avg. N_{hydroximate}-N_{picHA-py}-M-axial ligand (°) | 91.83 | 99.42 | 106.60 |

Table 4.5: Selected bond lengths and angles in Eu(III)[15-MC_{M(II),picHA-5}](NO₃)₃ complexes where M = Ni, Cu, Zn. All parameters are reported as their absolute values. Parameters emphasizing effects of the ruffling of the MC face are displayed in bold. a) The cavity radius was calculated as the difference in the distance from the centroids of the five donor oxygens (measured with Mercury) and the ionic radius of a 3-coordinate -2 charged oxygen atom (1.36 Å)¹⁰³. Previous cavity radius calculations utilized the ionic radius of the hydroximate oxygens of 1.30 Å. The previous calculations also used a more elaborate method for calculating the oxygen-centroid distance, those the values are effectively the same as those measured with Mercury.

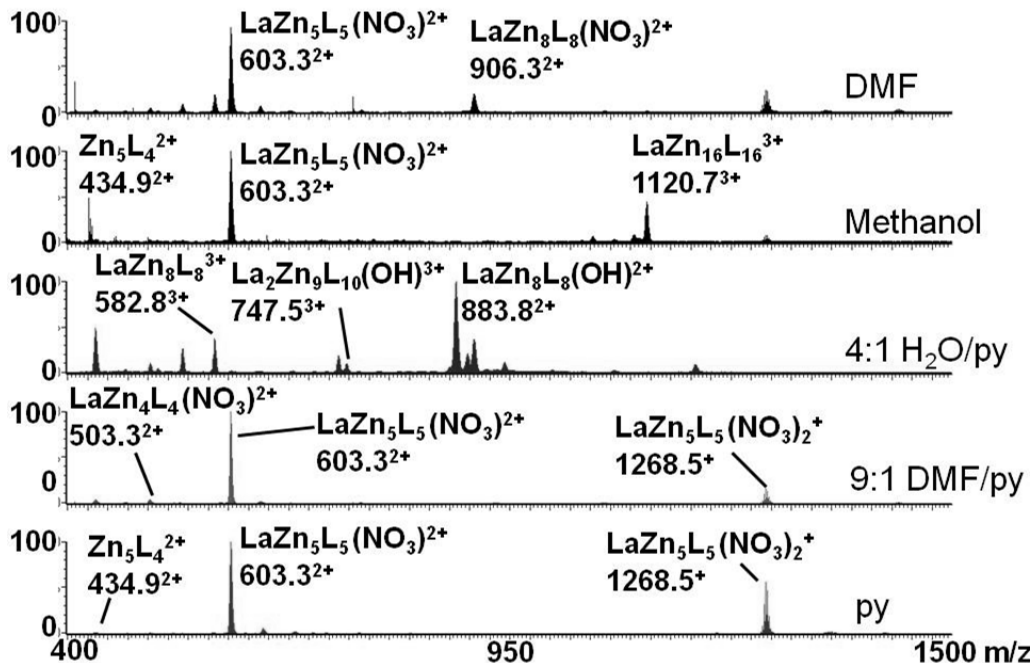


Figure 4.6: Mass spectra of assembly reactions at room temperature of 5:10:5:1 H₂picHA, triethylamine, Zn(NO₃)₂, and La(NO₃)₃ in the indicated solvents after 24 hours.

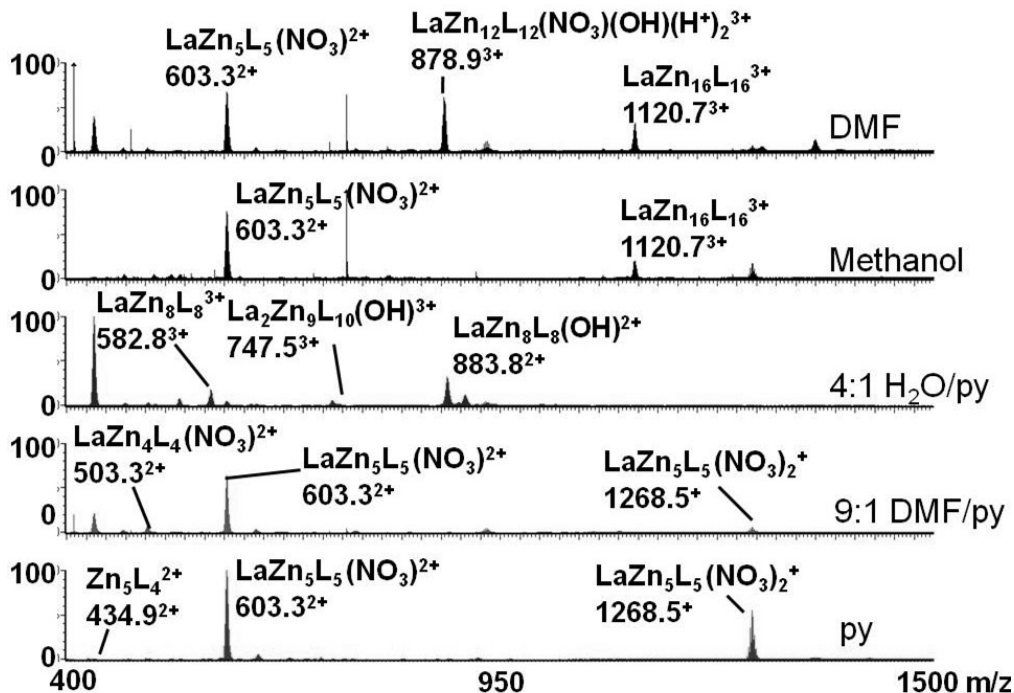


Figure 4.7: Mass spectra of assembly reactions performed at 65 °C of 5:10:5:1 H₂picHA, triethylamine, Zn(NO₃)₂, and La(NO₃)₃ in the indicated solvents after 24 hours.

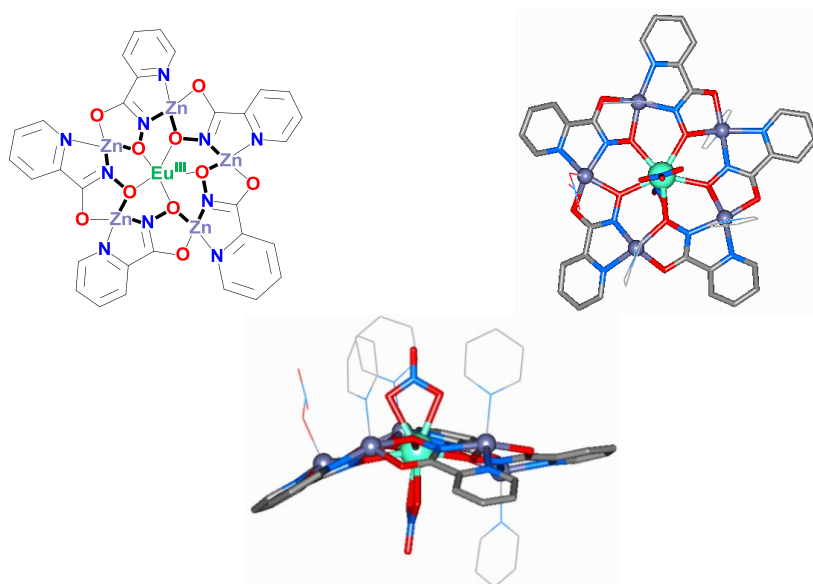


Figure 4.8: Chemdraw diagram (top left) and crystal structure images of the $\text{EuZn}_5(\text{picHA})_5(\text{NO}_3)_3$ complex highlighting the 15-MC-5 motif (top right) and ruffled topology (bottom). Color scheme: Grey = carbon, red = oxygen, blue = nitrogen, grey-purple = zinc, sea green = europium. Coordinated pyridine ligands are displayed as thin lines for clarity.

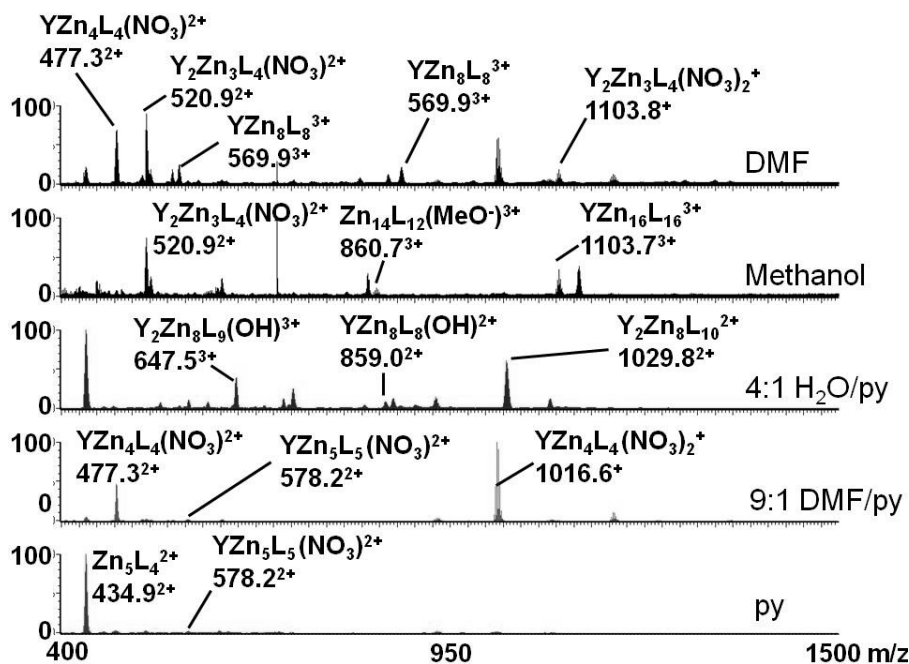


Figure 4.9: Mass spectra of assembly reactions at room temperature of 5:10:5:1 H_2picHA , triethylamine, $\text{Zn}(\text{NO}_3)_2$, and $\text{Y}(\text{NO}_3)_3$ in the indicated solvents after 24 hours.

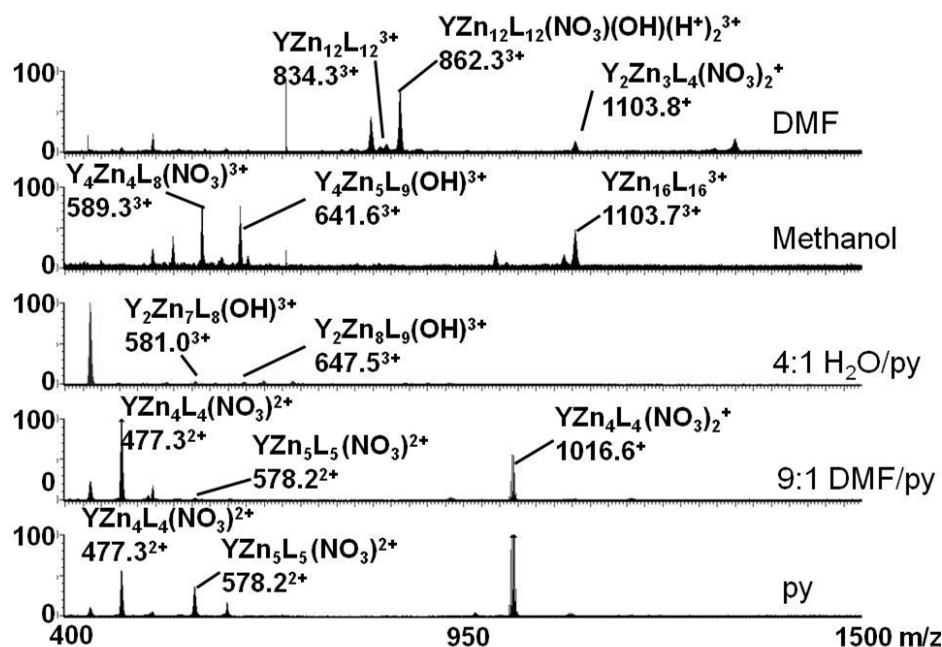


Figure 4.10: Mass spectra of assembly reactions performed at 65 °C of 5:10:5:1 H₂picHA, triethylamine, Zn(NO₃)₂, and Y(NO₃)₃ in the indicated solvents after 24 hours.

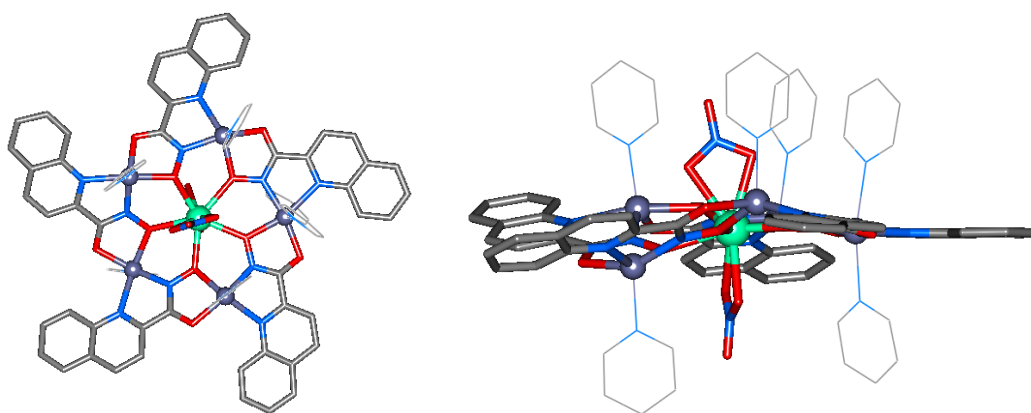


Figure 4.11: Chemdraw diagram (left) and crystal structure images of the DyZn₅(quinHA)₅(NO₃)₃ complex highlighting the 15-MC-5 motif (left) and ruffled topology (right). Color scheme: Grey = carbon, red = oxygen, blue = nitrogen, grey-purple = zinc, green = dysprosium. Coordinated pyridine ligands are displayed as thin lines for clarity.

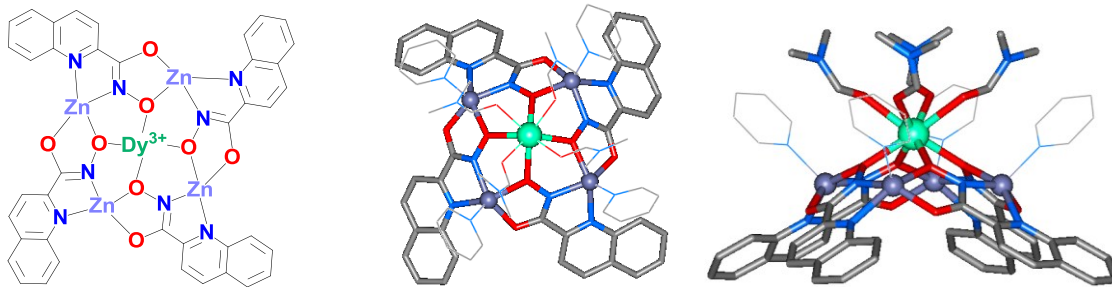


Figure 4.12: Chemdraw diagram (left) and crystal structure images of the $\text{DyZn}_4(\text{quinHA})_4(\text{DMF})_4(\text{NO}_3)_3$ complex. Color scheme: Grey = carbon, red = oxygen, blue = nitrogen, grey-purple = zinc, green = dysprosium. Coordinated pyridine and DMF (center only) ligands are displayed as thin lines for clarity.

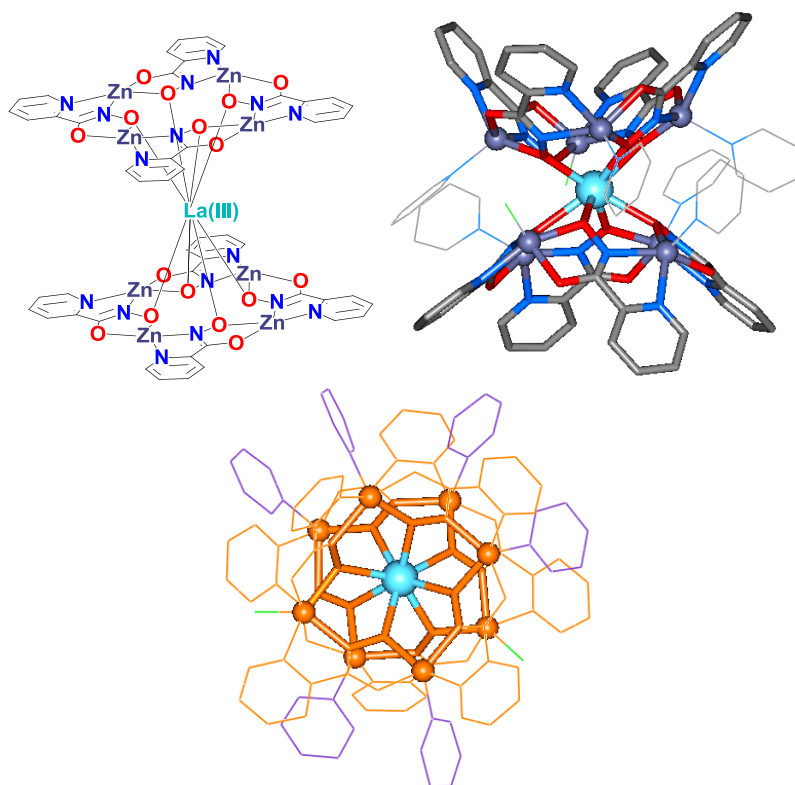


Figure 4.13: Chemdraw diagram (left) and crystal structure images of the $\text{LaZn}_8(\text{picHA})_8\text{Cl}_2$ complex viewed perpendicular to the concave 12-MC-4 units (right). The crystal structure image on the bottom highlights the MC motif (bold lines) in the sandwich complex (orange). Color scheme: Grey = carbon, red = oxygen, blue = nitrogen, grey-purple = zinc, light blue = lanthanum, purple = pyridine ligands in the right figure. Coordinated pyridine chloride ligands are displayed as thin lines for clarity.

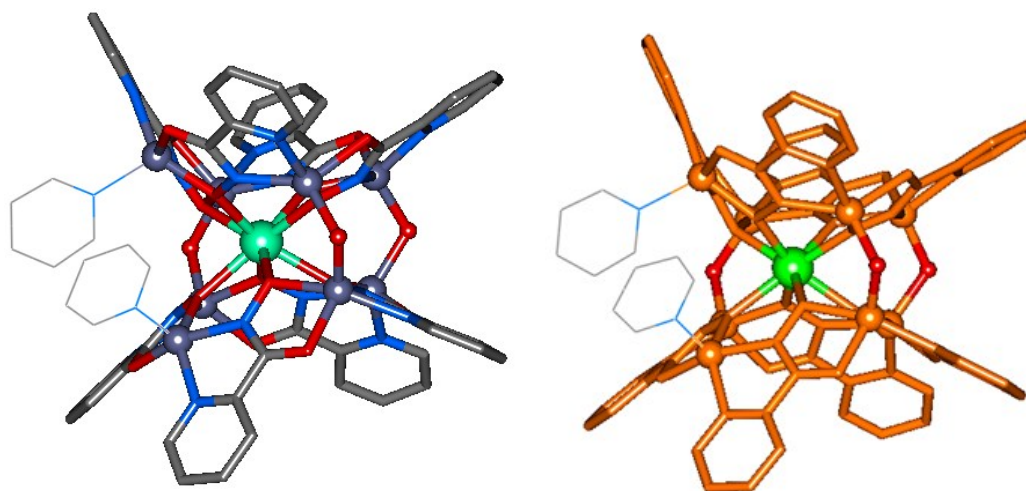


Figure 4.14: Crystal structure images of the $\text{DyZn}_8(\text{quinHA})_8(\text{OH})_3$ complex shown with elemental colors and in orange to highlight the 12-MC-4 units. Color scheme: Grey = carbon, red = oxygen, blue = nitrogen, grey-purple = zinc, sea green, green = dysprosium, orange = atoms in the 12-MC-4. Coordinated pyridine ligands are displayed as thin lines for clarity.

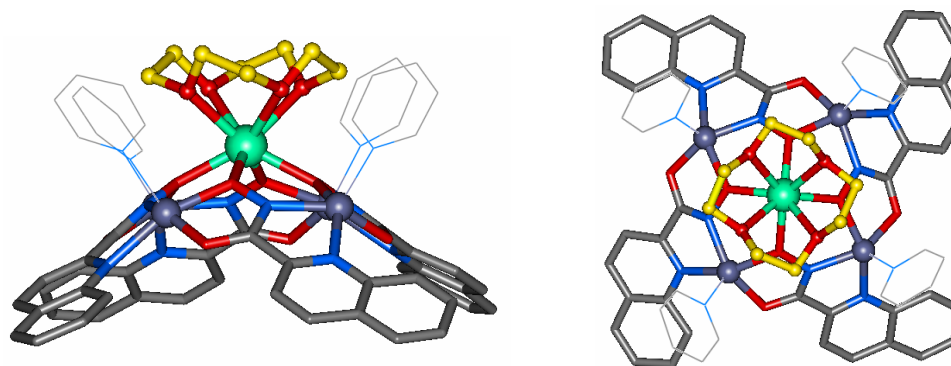


Figure 4.15: Crystal structure images of the $\text{DyZn}_4(\text{quinHA})_4(12\text{-crown-4})(\text{py})_4$. Color scheme: Grey = MC carbon, yellow = 12-crown-4 carbon, red = oxygen, blue = nitrogen, grey-purple = zinc, sea green = dysprosium. Coordinated pyridine ligands are displayed as thin lines for clarity.

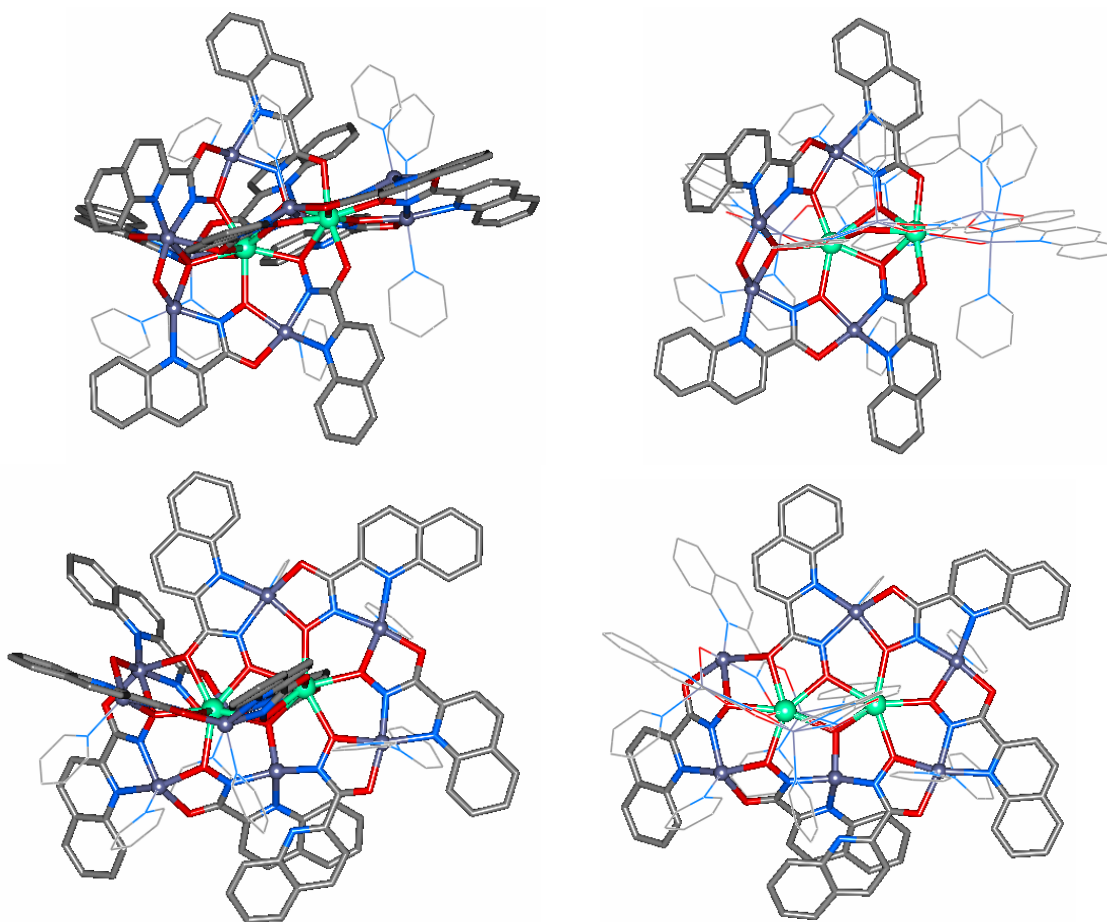


Figure 4.16: Crystal structure images of the $\text{Dy}_2\text{Zn}_9(\text{quinHA})_{10}$ complex. The complex is displayed from two different angles to highlight the 14-MC-5 (top) and split 15-MC-5 (bottom) motifs. The structures are displayed with stick representations (left) or stick and line representations (right) to enhance clarity. Color scheme: Grey = carbon, red = oxygen, blue = nitrogen, grey-purple = zinc, sea green = dysprosium. Coordinated pyridine ligands are displayed as thin lines for clarity.

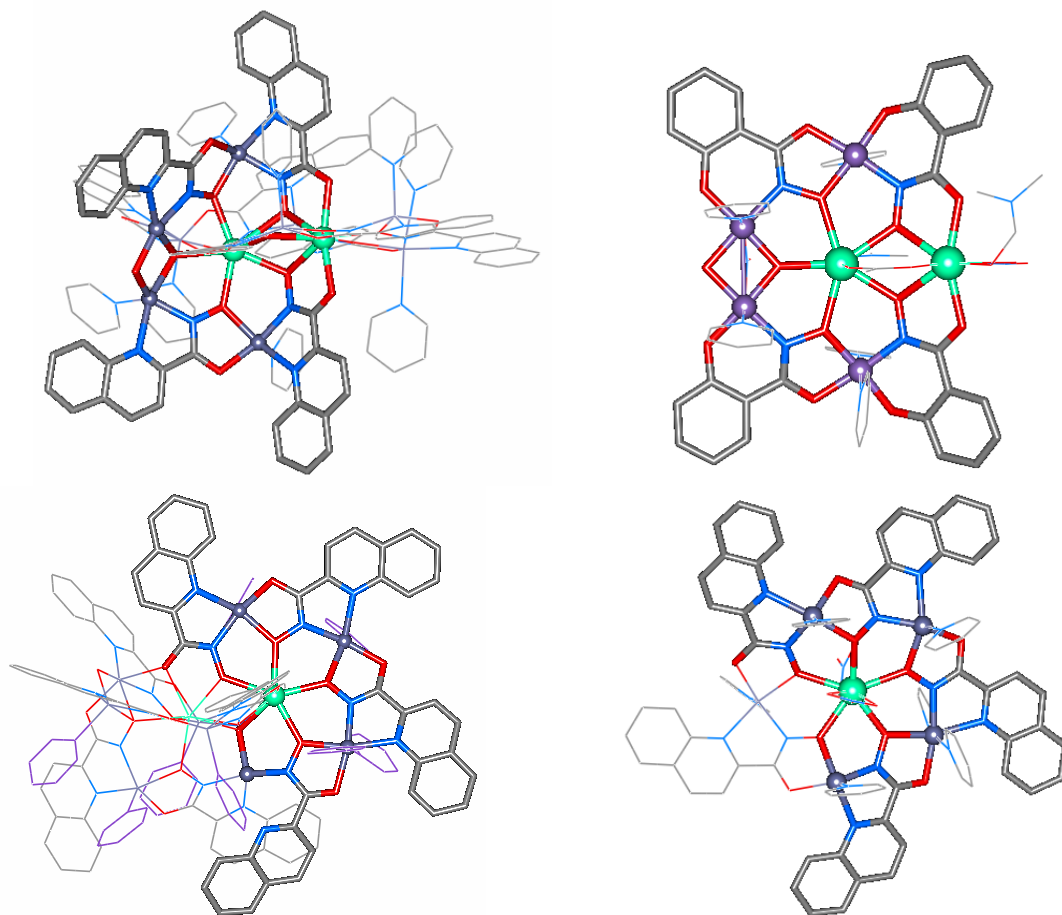


Figure 4.17: Comparisons of the different structural motifs in the $\text{Dy}_2\text{Zn}_9(\text{quinHA})_{10}(\text{OH})$ cluster (top left, bottom left) with the $\text{Ln}(\text{III})[14\text{-MC}_{\text{Mn}(\text{III}),\text{shi}^-5}(\text{OH})]$ (top right) and $\text{Dy}(\text{III})[15\text{-MC}_{\text{Zn}(\text{II}),\text{quinHA}-5}]$ (bottom right) complexes. Axial ligands and other aspects of the structure are displayed as thin lines to highlight the relevant structural motifs. Color scheme: Grey = carbon, red = oxygen, blue = nitrogen, grey-purple = zinc, sea green = dysprosium, purple = manganese.

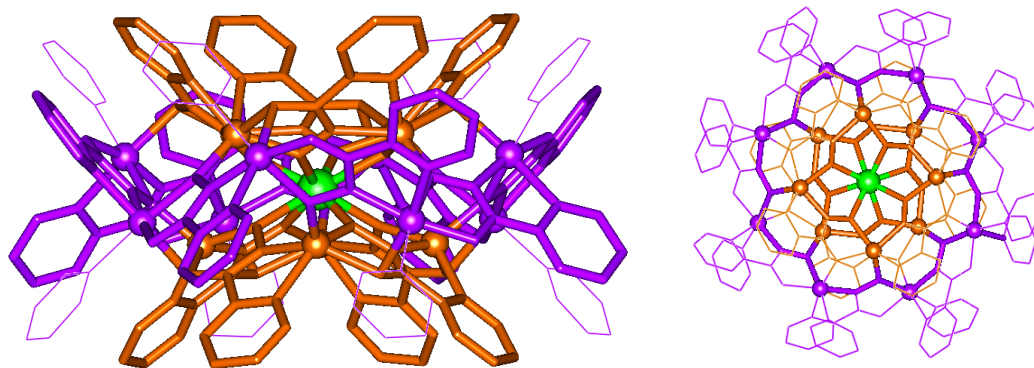


Figure 4.18: Crystal structure images of the $\text{TbZn}_{16}(\text{picHA})_{16}(\text{OTf})_3$ complex viewed from the side (left) and down the C4 axis (right) in colors meant to highlight the 12-MC-4 units (orange), 24-MC-8 (right), and central Tb(III) ion (green). Coordinated pyridine ligands are displayed as thin lines for clarity in the left figure. The figure on the right highlights the MC topology with bold lines.

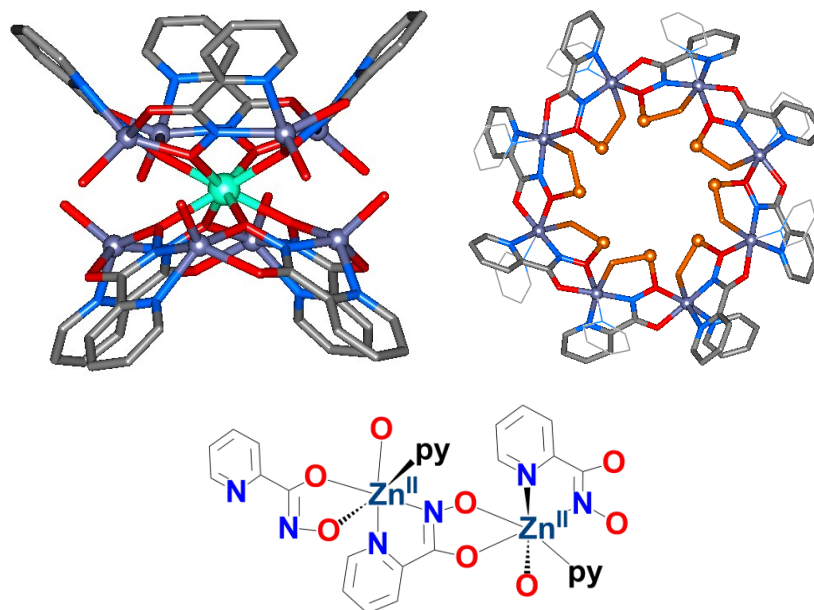


Figure 4.19: Highlight of the separate $\text{Tb(III)}[12\text{-MC-4}]_2$ sandwich complex (top-left), the $[24\text{-MC-8}]$ (top-right) from the crystal structure of the $\text{TbZn}_{16}(\text{picHA})_{16}$ and a diagram of the alternating Λ and Δ chirality in the 24-MC-8 (bottom).

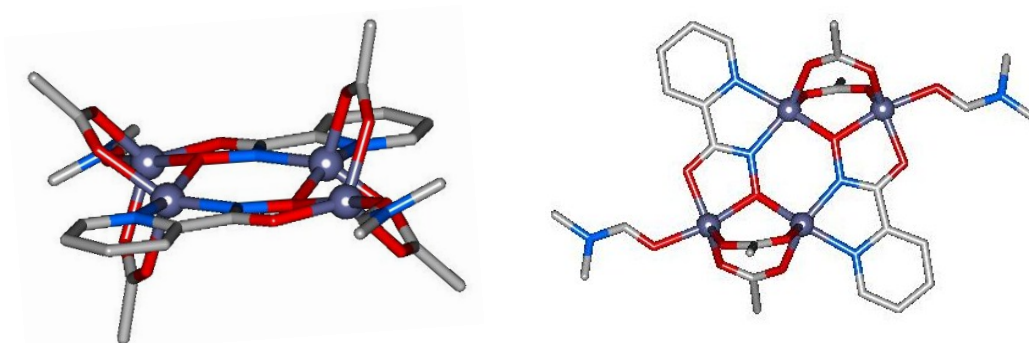


Figure 4.20: Crystal structure images of the $Zn_4(picHA)_2(acetate)_4(DMF)_2$ complex highlighting the along the picHA ligand plane and perpendicular to the plane. Color scheme: Grey = carbon, red = oxygen, blue = nitrogen, grey-purple = zinc.

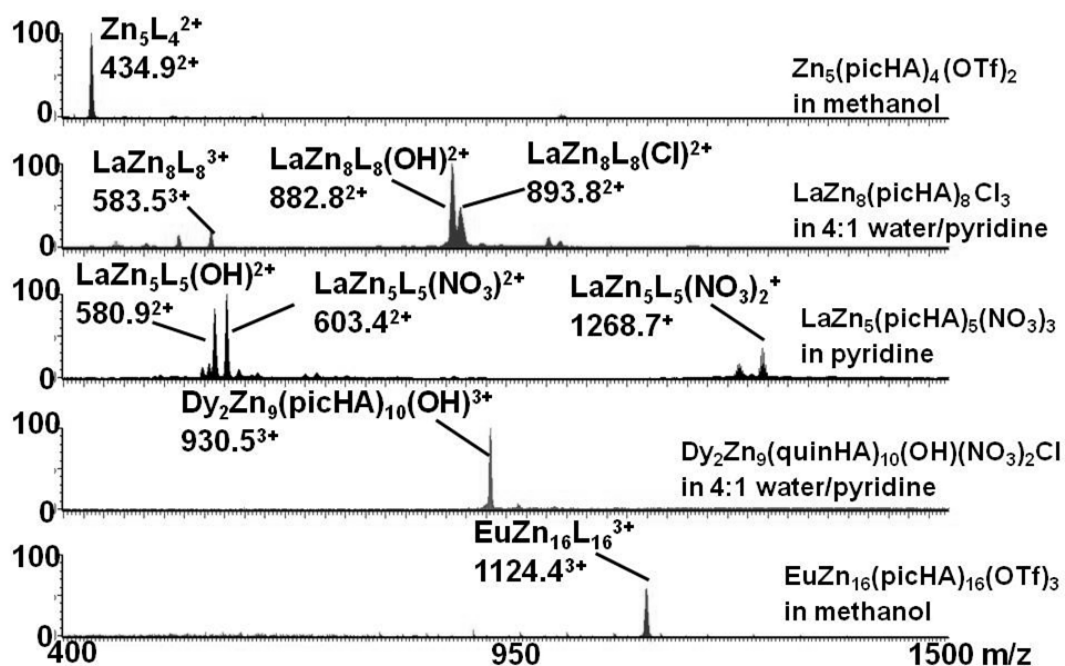


Figure 4.21: ESI-MS of isolated MCs in the indicated solvents.

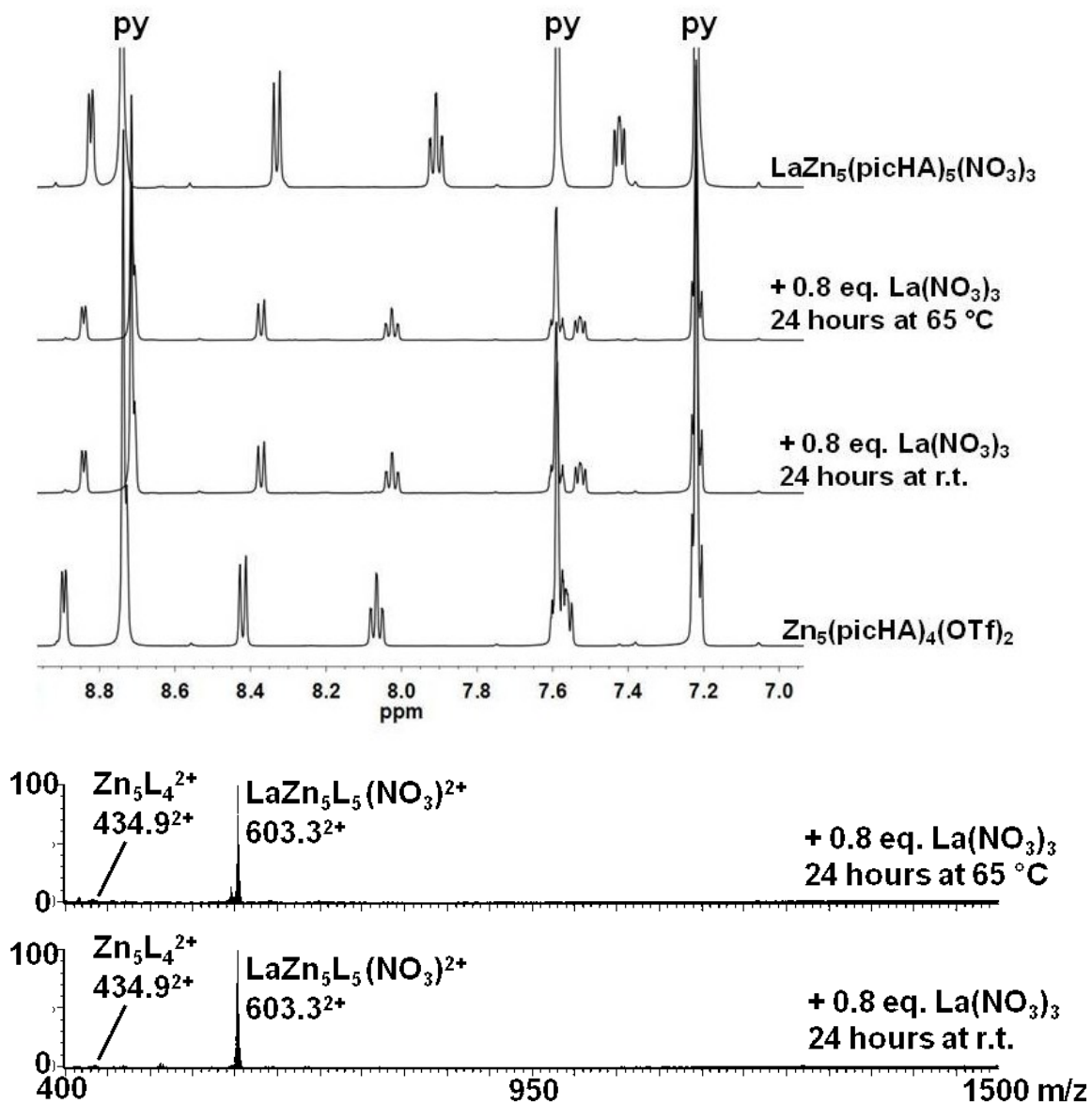


Figure 4.22: ^1H NMR and ESI-MS spectra of the titration of 0.8 equivalents of $\text{La}(\text{NO}_3)_3$ to $\text{Zn}_5(\text{picHA})_4(\text{OTf})_2$ in pyridine- D_5 .

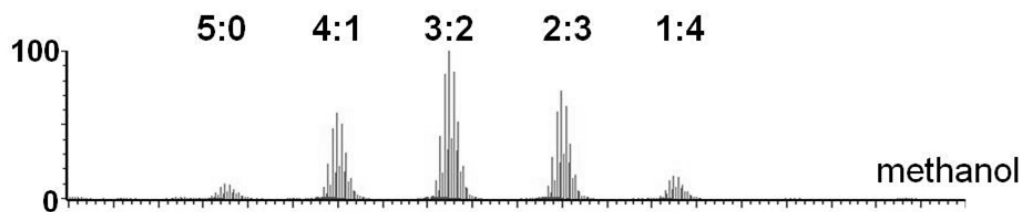


Figure 4.23: Mass spectra from ligand exchange experiments of the $Zn_5(\text{picHA})_4(\text{OTf})_2$ and four equivalents of $H_2\text{quinHA}$ in methanol.

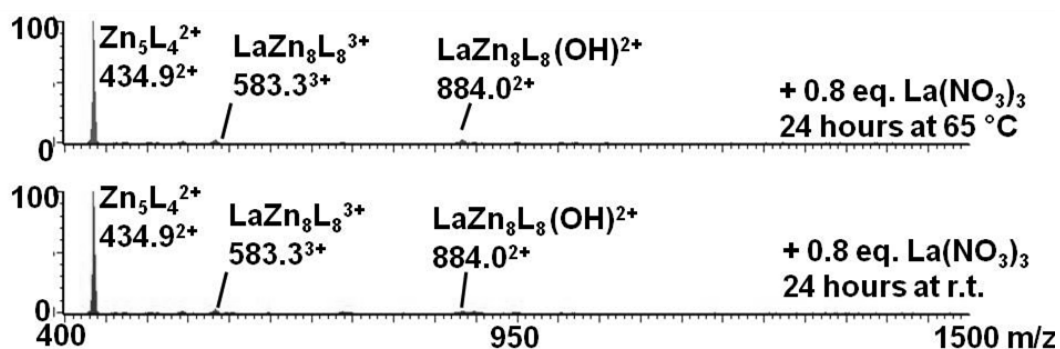
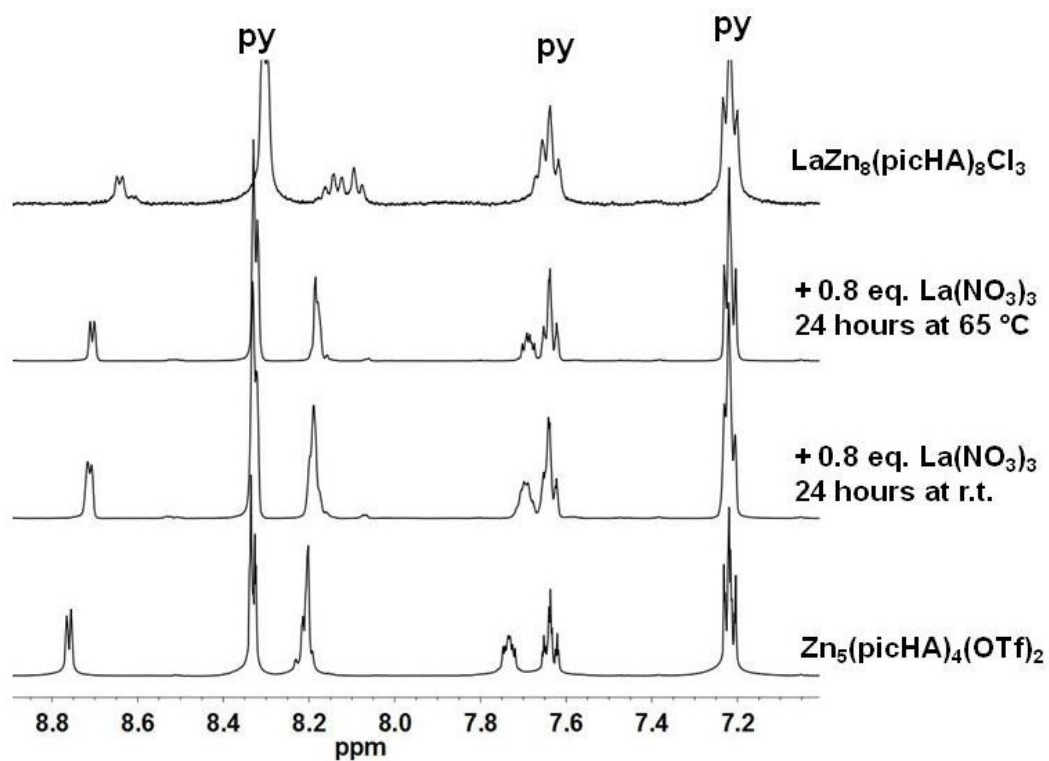


Figure 4.24: ^1H NMR and ESI-MS spectra of the titration of 0.8 equivalents of $\text{La}(\text{NO}_3)_3$ to $\text{Zn}_5(\text{picHA})_4(\text{OTf})_2$ in 4:1 D_2O /pyridine- D_5 .

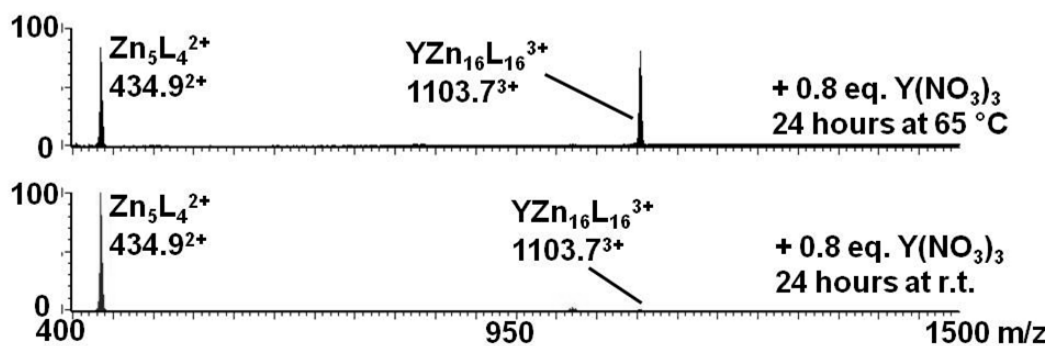
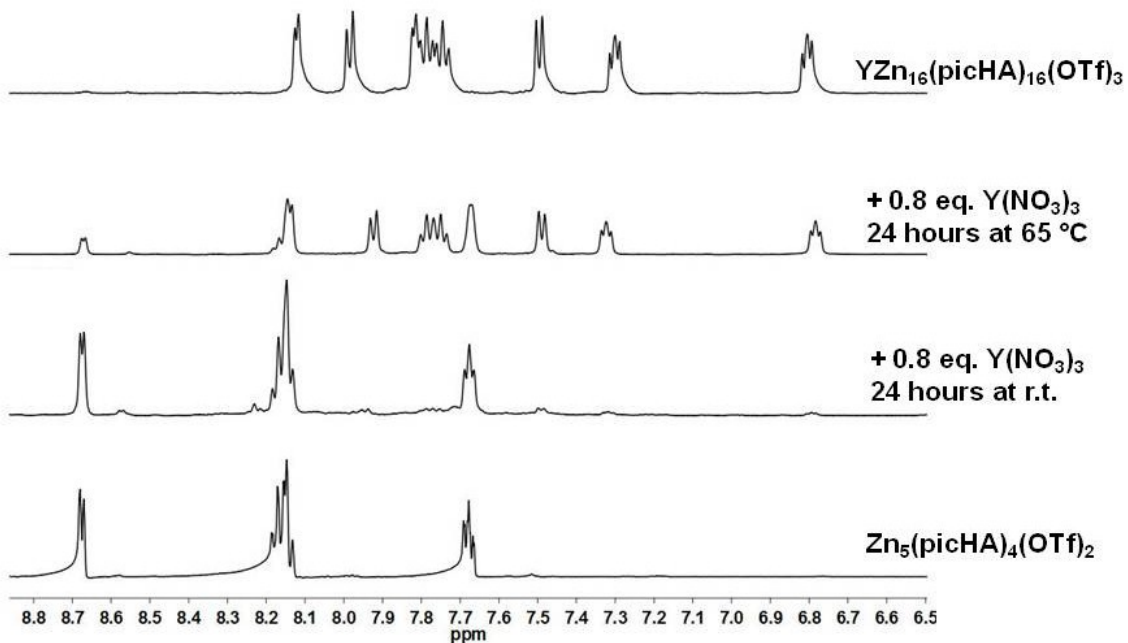


Figure 4.25: ¹H NMR and ESI-MS spectra of the titration of 0.8 equivalents of Y(NO₃)₃ to Zn₅(picHA)₄(OTf)₂ in methanol-D₄.

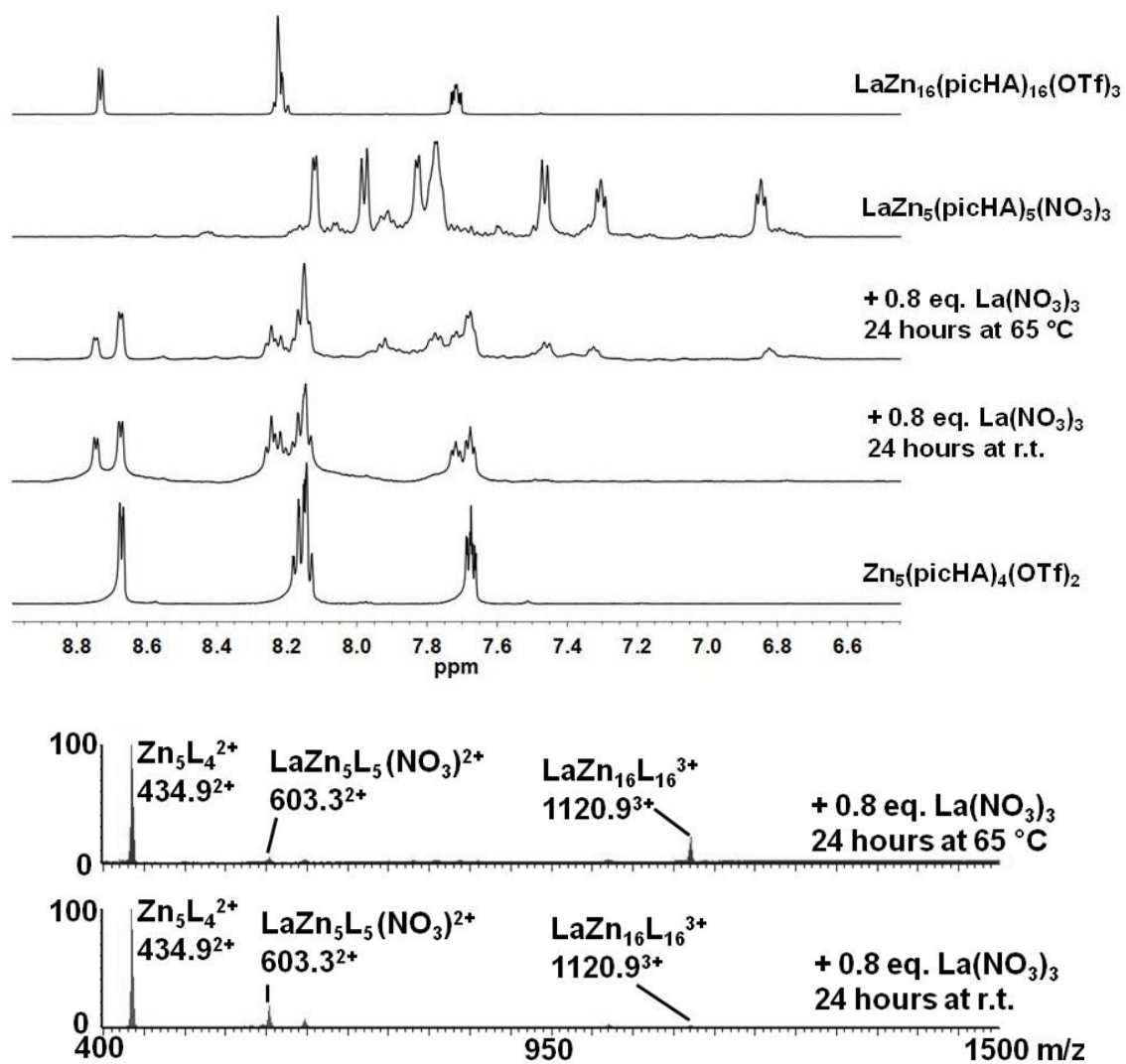


Figure 4.26: ^1H NMR and ESI-MS spectra of the titration of 0.8 equivalents of $\text{La}(\text{NO}_3)_3$ to $\text{Zn}_5(\text{picHA})_4(\text{OTf})_2$ in methanol- D_4 .

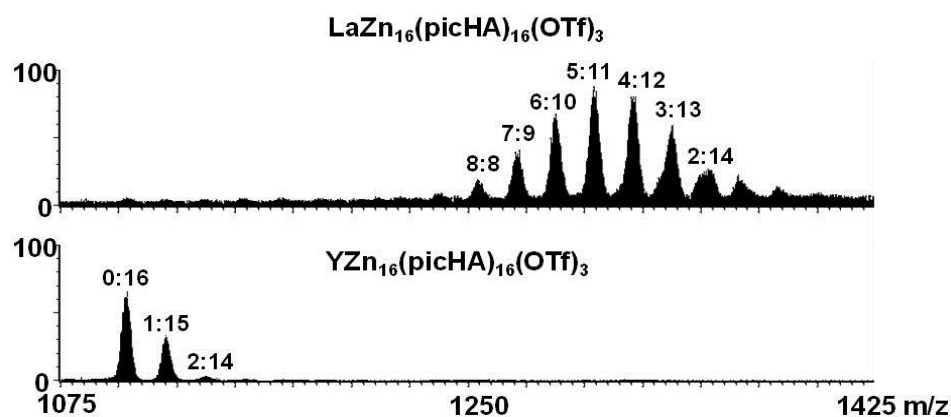


Figure 4.27: Mass spectra showing evidence for ligand exchange in the $\text{LaZn}_{16}(\text{picHA})_{16}(\text{OTf})_3$ (top) and $\text{YZn}_{16}(\text{picHA})_{16}(\text{OTf})_3$ (bottom) complexes. Spectra are of solutions of the $\text{LnZn}_{16}(\text{picHA})_{16}$ complexes with 32 equivalents of H_2quinHA after 6.5 hours in methanol at room temperature. The picHA:quinHA ratio in the LnZn_{16} is displayed above the peaks in the spectra.

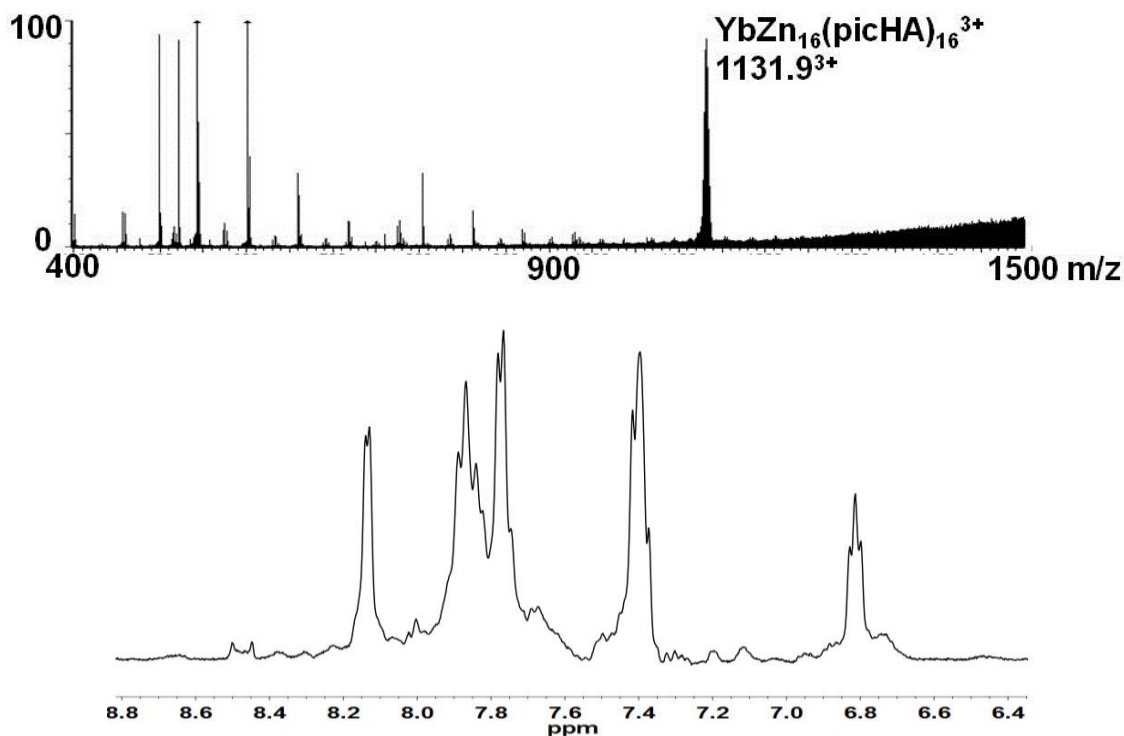


Figure 4.28: ESI-MS of the $\text{YbZn}_{16}(\text{picHA})_{16}(\text{OTf})_3$ in aqueous HEPES buffer (top) and ^1H NMR spectrum of the $\text{YZn}_{16}(\text{picHA})_{16}$ in D_2O (bottom). Unlabeled peaks in the mass spectrum are background signals.

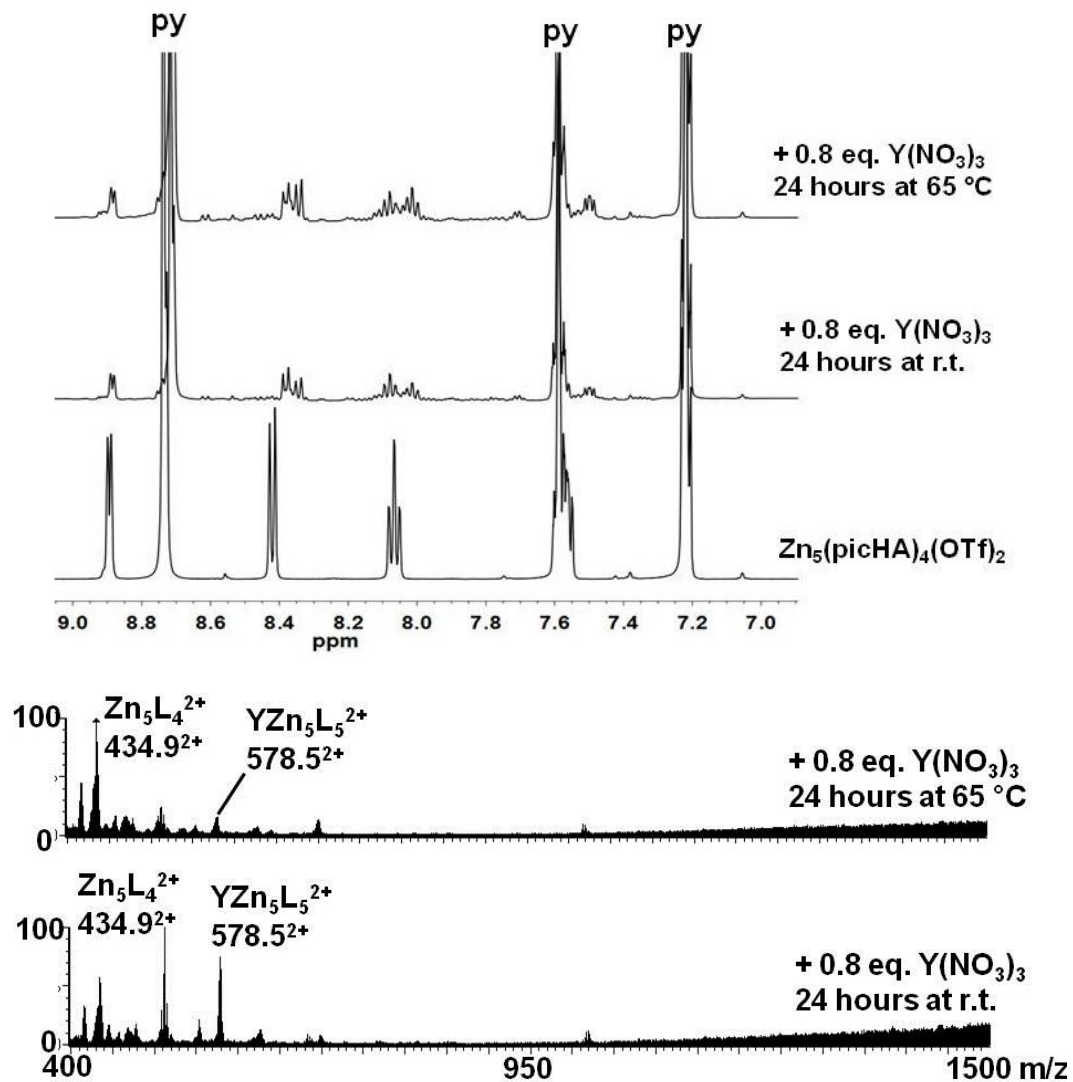


Figure 4.29: ^1H NMR and ESI-MS spectra of the titration of 0.8 equivalents of $\text{Y}(\text{NO}_3)_3$ to $\text{Zn}_5(\text{picHA})_4(\text{OTf})_2$ in pyridine- D_5 .

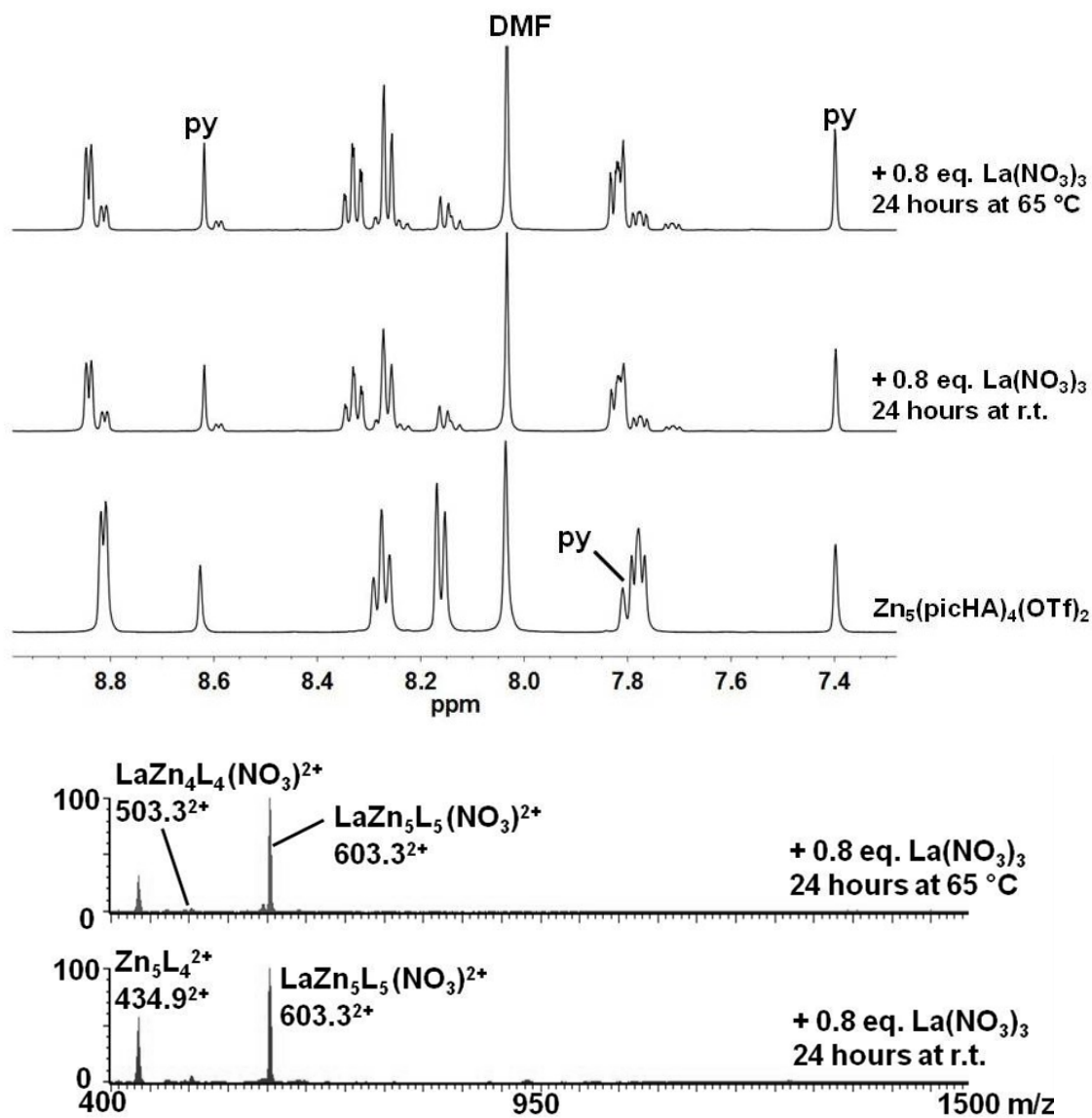


Figure 4.30: ^1H NMR and ESI-MS spectra of the titration of 0.8 equivalents of $\text{La}(\text{NO}_3)_3$ to $\text{Zn}_5(\text{picHA})_4(\text{OTf})_2$ in 9:1 DMF/pyridine.

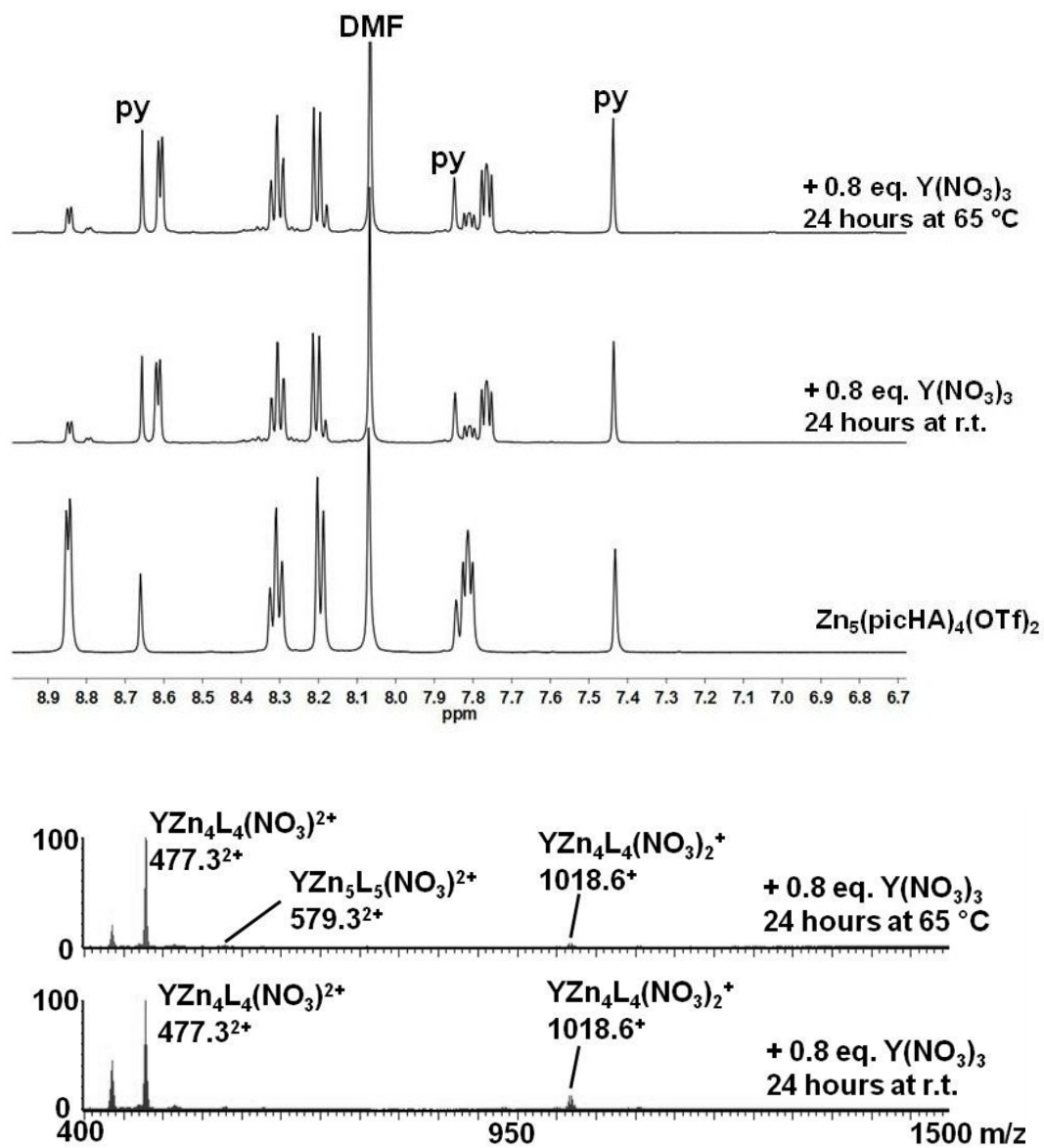


Figure 4.31: 1H NMR and ESI-MS spectra of the titration of 0.8 equivalents of $Y(NO_3)_3$ to $Zn_5(picHA)_4(OTf)_2$ in 9:1 DMF/pyridine.

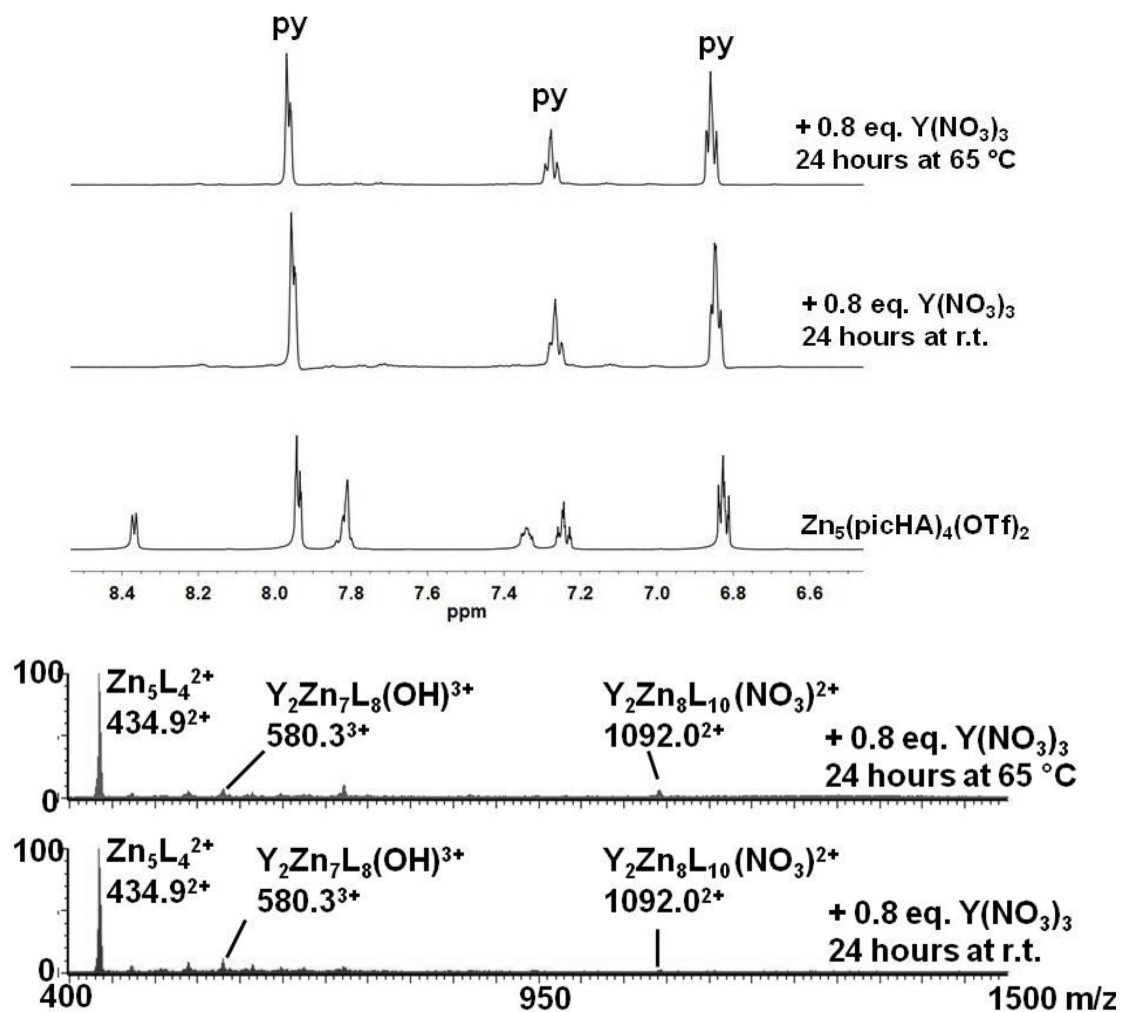


Figure 4.32: ^1H NMR and ESI-MS spectra of the titration of 0.8 equivalents of $\text{Y}(\text{NO}_3)_3$ to $\text{Zn}_5(\text{picHA})_4(\text{OTf})_2$ in 4:1 D_2O /pyridine- D_5 .

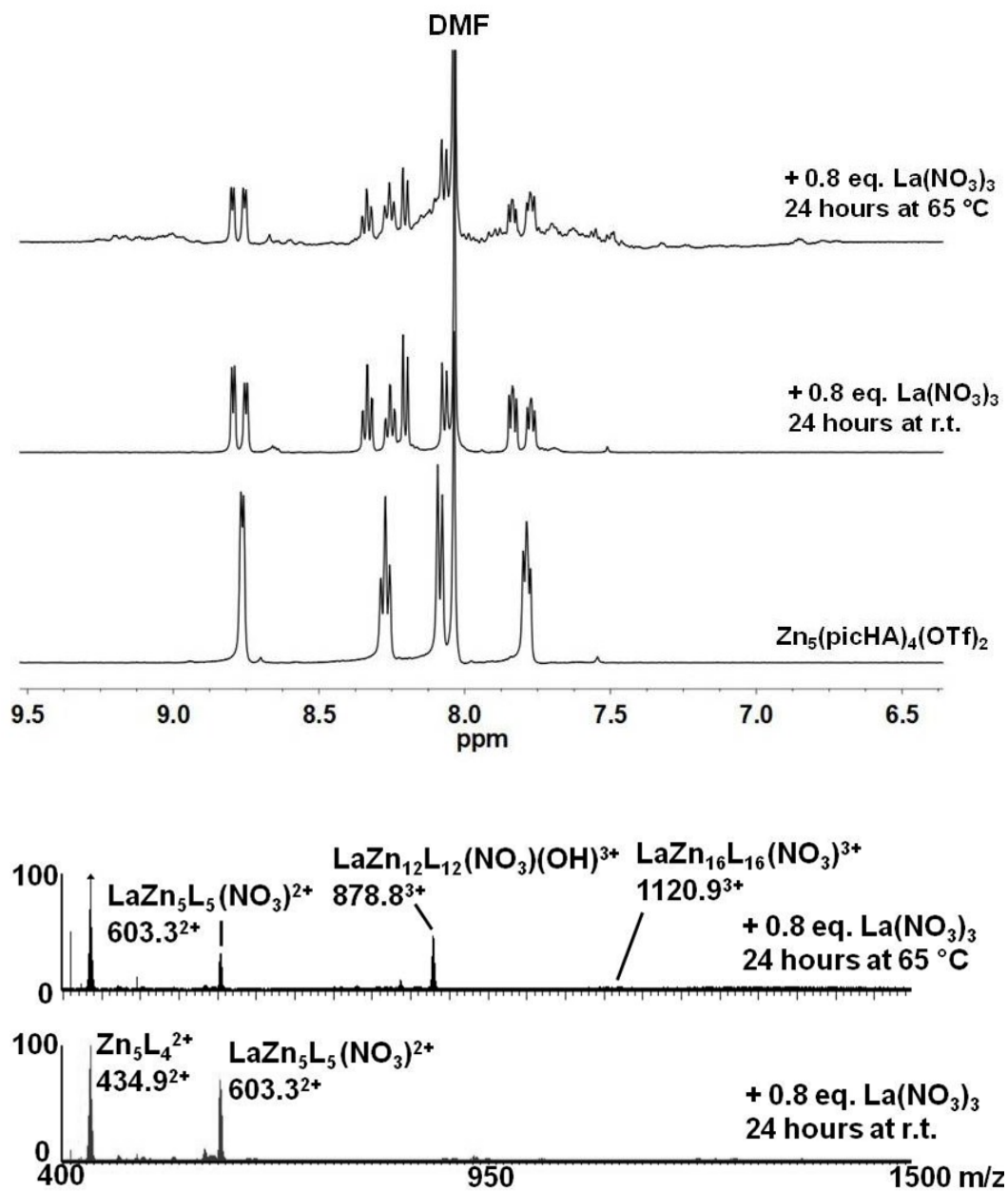


Figure 4.33: ^1H NMR and ESI-MS spectra of the titration of 0.8 equivalents of $\text{La}(\text{NO}_3)_3$ to $\text{Zn}_5(\text{picHA})_4(\text{OTf})_2$ in DMF.

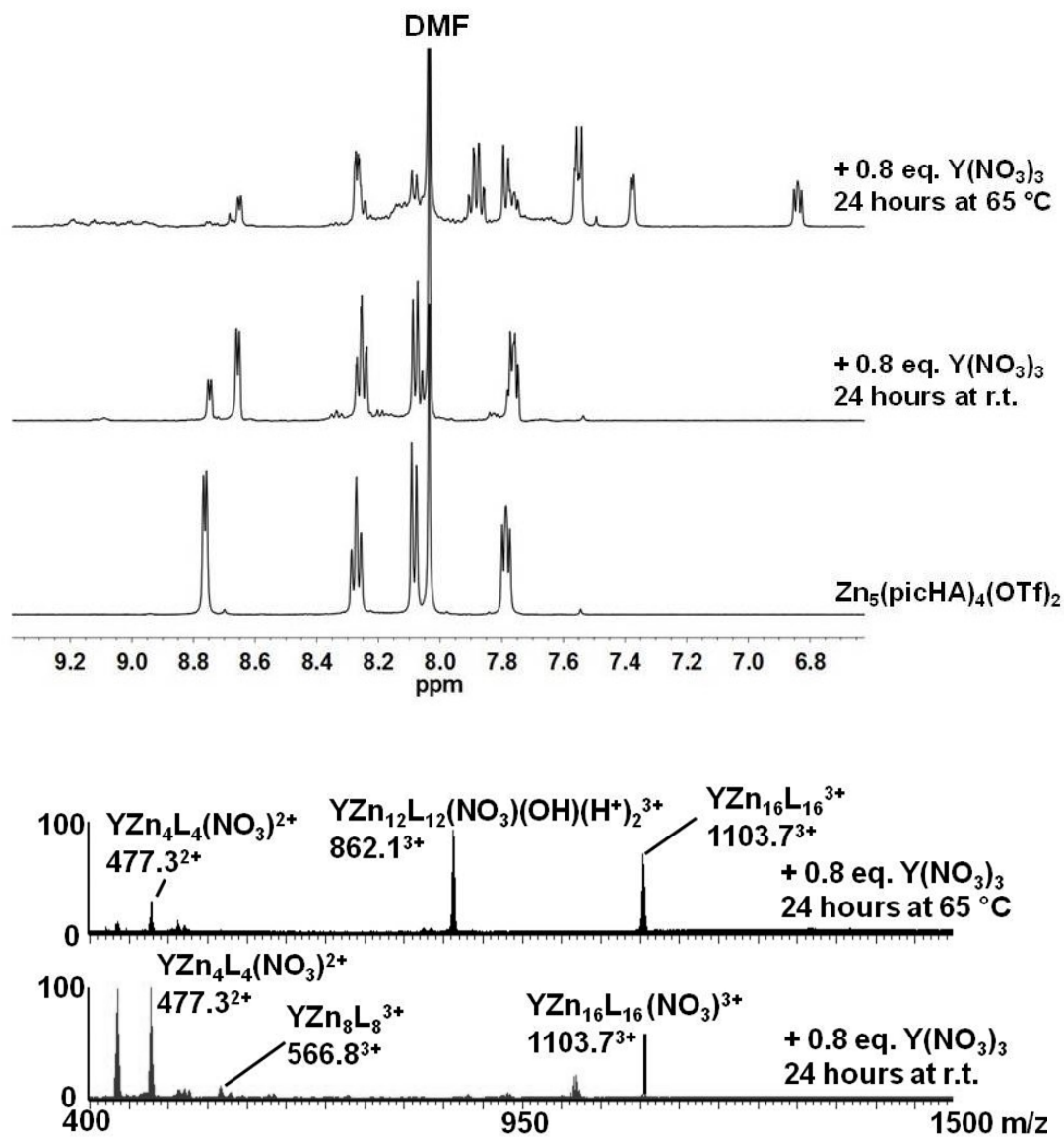


Figure 4.34: ^1H NMR and ESI-MS spectra of the titration of 0.8 equivalents of $\text{Y}(\text{NO}_3)_3$ to $\text{Zn}_5(\text{picHA})_4(\text{OTf})_2$ in DMF.

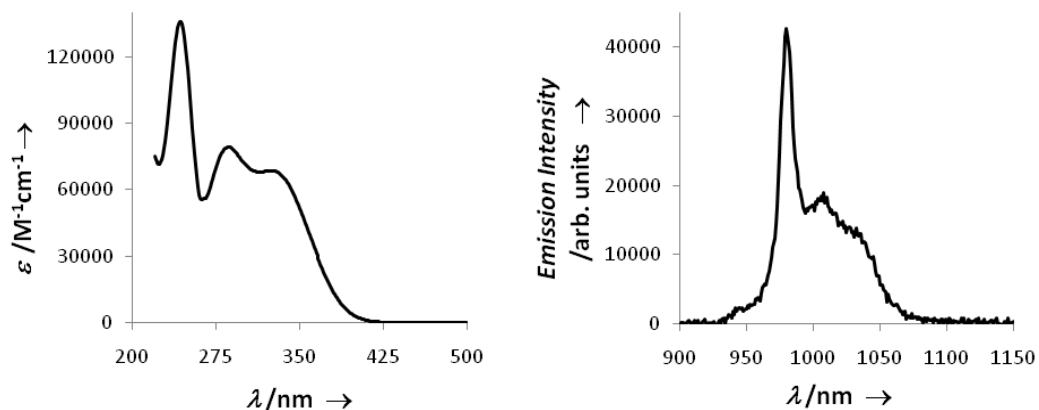


Figure 4.35: Absorption (top left) and emission spectra (top right) for $\text{YbZn}_{16}(\text{picHA})_{16}(\text{OTf})_3$ in methanol at 25.0 °C. The emission spectrum was collected by excitation at 280 nm (14.5 nm bandpass) in 1 nm increments with a 4.0 nm bandpass.

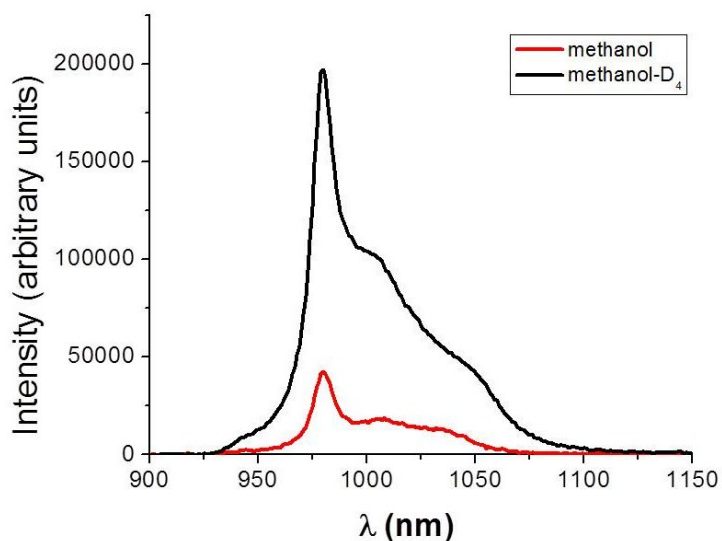


Figure 4.36: Emission spectra (4 nm bandpass) of $\text{YbZn}_{16}(\text{picHA})_{16}(\text{OTf})_3$ at 25.0 °C in MeOH (-) and CD_3OD (-). Emission spectra were collected with absorbance of ~ 0.1 at 280 nm by excitation at 280 nm (14.5 nm bandpass).

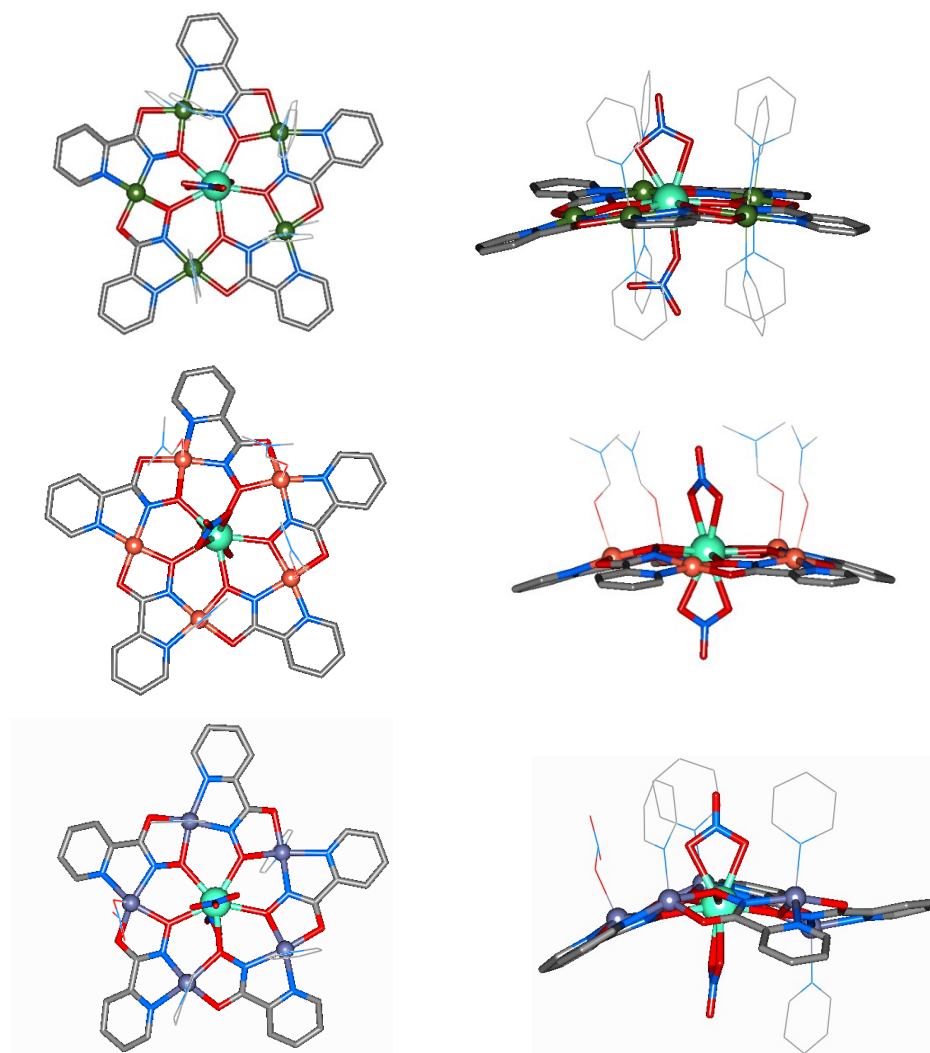


Figure 4.37: Crystal structure images of $\text{Eu(III)[15-MC}_{M(\text{II}),\text{picHA-5}}\text{](NO}_3\text{)}_3$ complexes ($M = \text{Ni}$ (top), Cu (middle), and Zn (bottom)) viewed perpendicular and parallel to the C_5 axis.

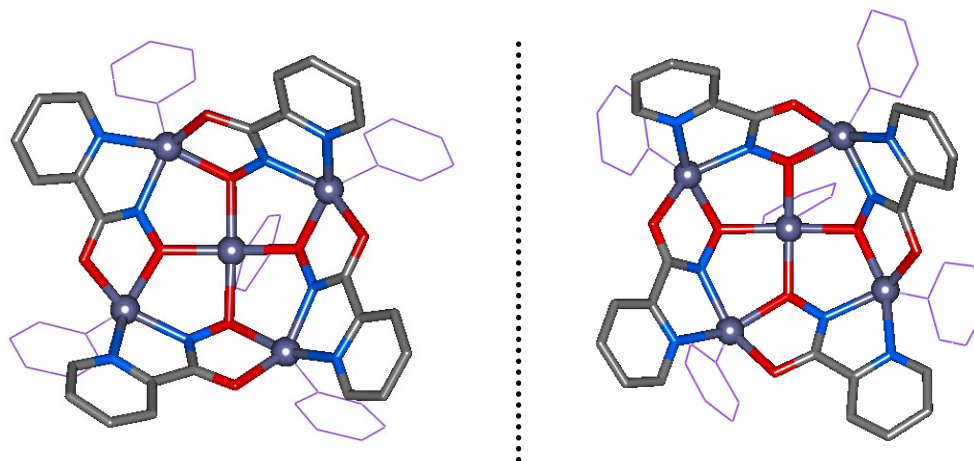


Figure 4.38: Crystal structure images of the *P* (left) and *M* (right) enantiomers of the inherently chiral $\text{Zn(II)[12-MC}_{\text{Zn(II),picHA-4}}\text{](OTf)}_2$ viewed down the concave face.

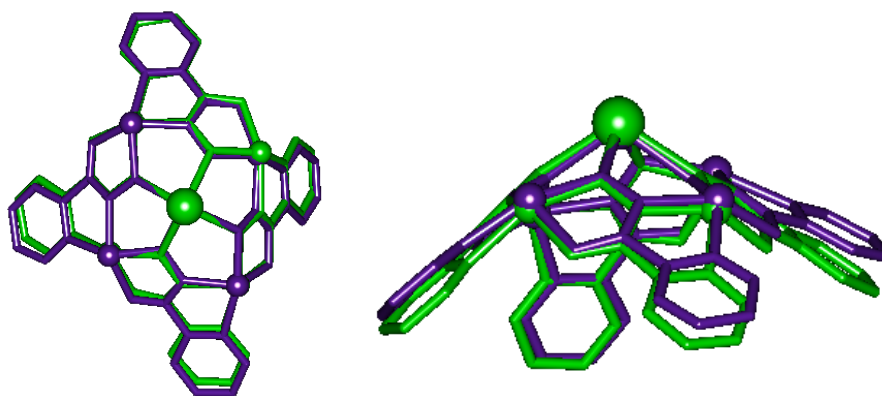


Figure 4.39: Overlay of Ln(III)[12-MC-4] units of the $\text{DyZn}_8(\text{picHA})_8(\text{OH})_3$ (purple) and $\text{LaZn}_8(\text{picHA})_8\text{Cl}_3$ (green) complexes. The $\text{LaZn}_8(\text{picHA})_8$ is more concave as the picHA ligands have a steeper pitch than the $\text{DyZn}_8(\text{picHA})_8(\text{OH})_3$.

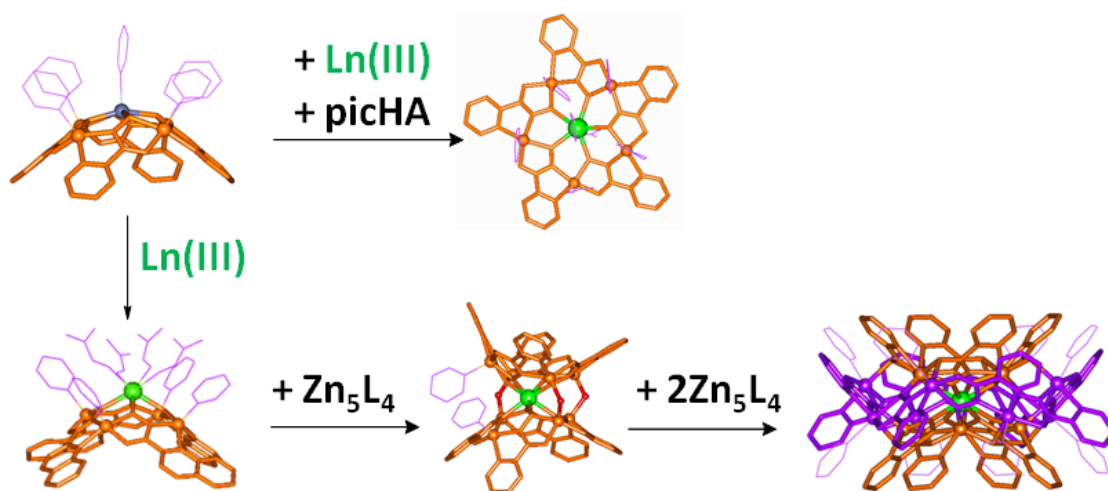


Figure 4.40: A minimal scheme of a possible assembly pathway for the conversion of the Zn_5L_4 to the monolanthanide MCs.

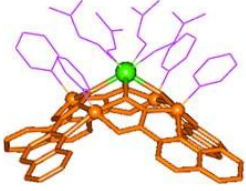
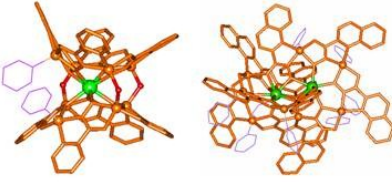
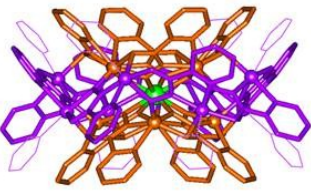
| | | Solvents that Coordinate to Ln(III) (DMF) | |
|--|-------------|--|--|
| | | Present | Not Present |
| Solvents that Coordinate to Zn(II) (pyridine w/o water) | Present | $LnZn_4L_4$  | $LnZn_8L_8$ Ln_2 Clusters  |
| | Not Present | $LnZn_{12}L_{12}$ Structure has not been obtained | $LnZn_{16}L_{16}$ Ln_4 Clusters  |

Figure 4.41: Chart that relates the LnMC that selectively assembles in solution to the presence of DMF and/or pyridine (or aqueous pyridine). The $LnZn_5L_5$ was omitted since the complex assembles and is thermodynamically stable in pyridine, 9:1 DMF/pyridine, and methanol.

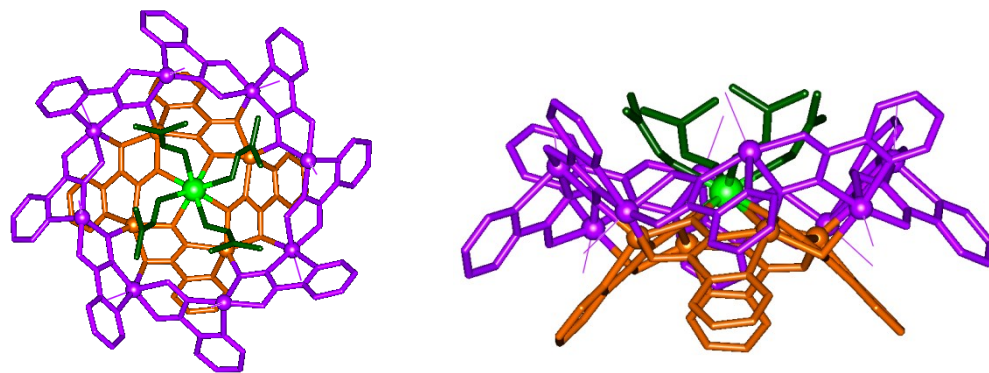


Figure 4.42: A model of the proposed $\text{Ln(III)[12-MC}_{\text{Zn(II),picHA}^{-4}}\text{][24-MC}_{\text{Zn(II),picHA}^{-8}}\text{]}(\text{DMF})_4$ structure for the $\text{LnZn}_{12}\text{L}_{12}$. Color scheme: light green = Ln(III), dark green = DMF, purple = $[\text{24-MC}_{\text{Zn(II),picHA}^{-8}}]$, orange = $[\text{12-MC}_{\text{Zn(II),picHA}^{-4}}]$.

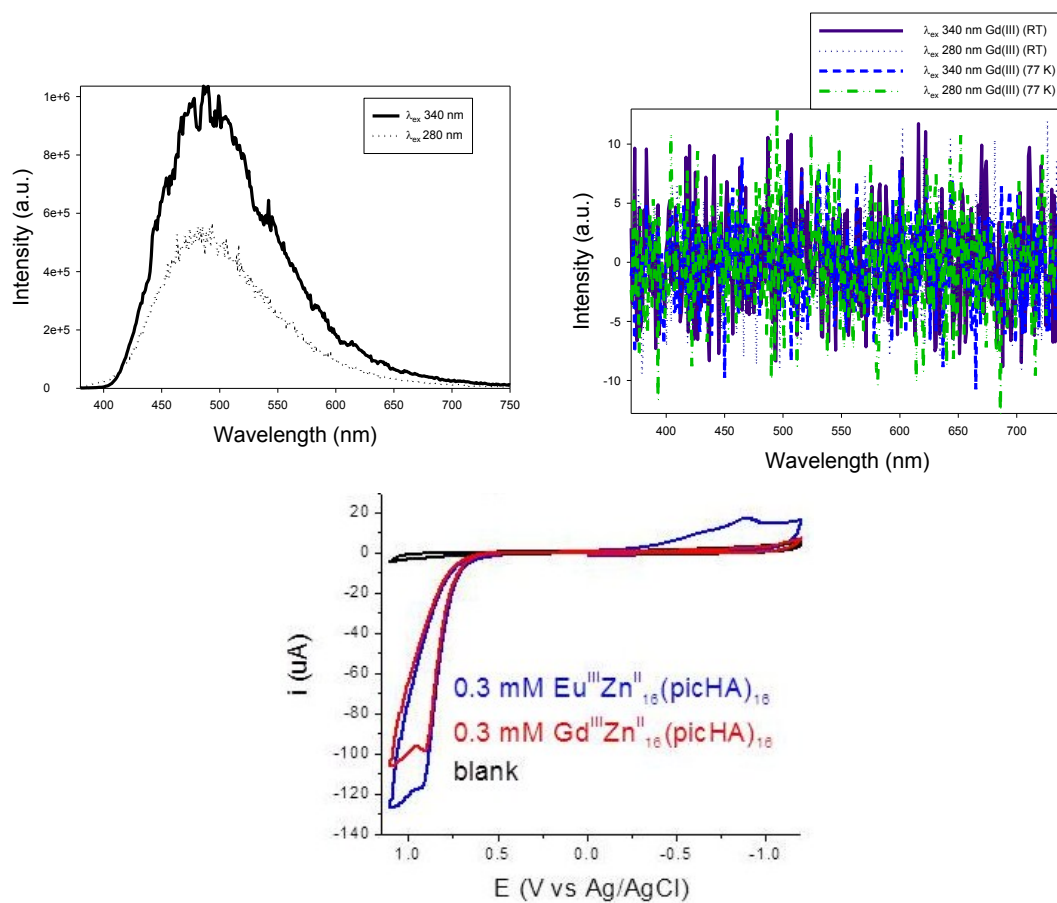


Figure 4.43: Fluorescence spectra of the $\text{GdZn}_{16}(\text{picHA})_{16}$ in 1:4 methanol/ethanol at 77 K with a no time delay (top left) and with 100 μs time delay (top right) and cyclic voltammograms of $\text{LnZn}_{16}(\text{picHA})_{16}(\text{OTf})_3$ complexes in 0.1 M aqueous KCl.

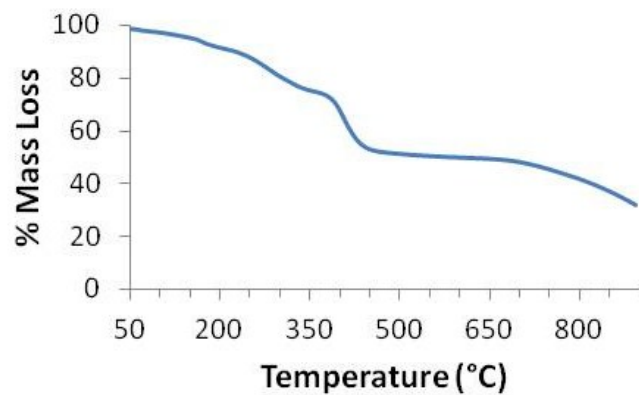


Figure 4.44: Thermogravimetric analysis plot showing mass loss of the $\text{YZn}_4(\text{quinHA})_4(\text{DMF})_4(\text{NO}_3)_3$ as a function of temperature.

References

- (1) Chakrabarty, R.; Mukherjee, P. S.; Stang, P. J. *Chem. Rev.* **2011**, *111*, 6810.
- (2) Holliday, B. J.; Mirkin, C. A. *Angew. Chem. Int. Ed.* **2001**, *40*, 2022.
- (3) Albrecht, M. *Chem. Rev.* **2001**, *101*, 3457.
- (4) Yoshizawa, M.; Klosterman, J. K.; Fujita, M. *Angew. Chem. Int. Ed.* **2009**, *48*, 3418.
- (5) Pluth, M. D.; Bergman, R. G.; Raymond, K. N. *Acc. Chem. Res.* **2009**, *41*, 1650.
- (6) Leung, D. H.; Fiedler, D.; Bergman, R. G.; Raymond, K. N. *Angew. Chem. Int. Ed.* **2004**, *43*, 963.
- (7) Brown, C. J.; Miller, G. M.; Johnson, M. W.; Bergman, R. G.; Raymond, K. N. *J. Am. Chem. Soc.* **2011**, *133*, 11964.
- (8) Merlau, M. L.; Mejia, M. d. P.; Nguyen, S. T.; Hupp, J. T. *Angew. Chem. Int. Ed.* **2001**, *40*, 4239.
- (9) Cavarzan, A.; Scarso, A.; Sgarbossa, P.; Strukul, G.; Reek, J. N. H. *J. Am. Chem. Soc.* **2011**, *133*, 2848.
- (10) Ono, K.; Yoshizawa, M.; Akita, M.; Kato, T.; Tsunobuchi, Y.; Ohkoshi, S.-i.; Fujita, M. *J. Am. Chem. Soc.* **2009**, *131*, 2782.
- (11) Sun, W.-Y.; Kusukawa, T.; Fujita, M. *J. Am. Chem. Soc.* **2002**, *124*, 11571.
- (12) Gianneschi, N. C.; III, M. S. M.; Mirkin, C. A. *Acc. Chem. Res.* **2005**, *38*, 825.
- (13) Frischmann, P. D.; Guieu, S.; Tabeshi, R.; MacLachlan, M. J. *J. Am. Chem. Soc.* **2010**, *132*, 7688.
- (14) Hui, J. K. H.; MacLachlan, M. J. *Coord. Chem. Rev.* **2010**, *254*, 2363.
- (15) Li, D.; Zhou, W.; Landskron, K.; Sato, S.; Kiely, C. J.; Fujita, M.; Liu, T. *Angew. Chem. Int. Ed.* **2011**, *50*, 5182.
- (16) Inokuma, Y.; Arai, T.; Fujita, M. *Nat. Chem.* **2010**, *2*, 780.
- (17) Dinolfo, P. H.; Hupp, J. T. *Chem. Mater.* **2001**, *13*, 3113.
- (18) Slone, R. V.; Benkstein, K. D.; Belanger, S.; Hupp, J. T.; Guzei, I. A.; Rheingold, A. L. *Coord. Chem. Rev.* **1998**, *171*, 221.
- (19) Imbert, D.; Cantuel, M.; Bunzli, J.-C. G.; Bernardinelli, G.; Piguet, C. *J. Am. Chem. Soc.* **2003**, *125*, 15698.
- (20) Zaleski, C. M.; Depperman, E. C.; Kampf, J. W.; Kirk, M. L.; Pecoraro, V. L. *Inorg. Chem.* **2006**, *45*, 10022.
- (21) Affronte, M.; Carretta, S.; Timco, G. A.; Winpenny, R. E. *Chem. Commun.* **2007**, 1789.
- (22) Piotrowski, H.; Severin, K. *Proc. Natl. Acad. Sci.* **2002**, *99*, 4997.
- (23) Fujita, M. *Chem. Soc. Rev.* **1998**, *27*, 417.
- (24) Fujita, M.; Yazaki, J.; Ogura, K. *J. Am. Chem. Soc.* **1991**, *112*, 5645.
- (25) Caulder, D. L.; Raymond, K. N. *Acc. Chem. Res.* **1999**, *32*, 975.
- (26) Caulder, D. L.; Powers, R. E.; Parac, T. N.; Raymond, K. N. *Angew. Chem. Int. Ed.* **1998**, *37*, 1840.
- (27) Caulder, D. L.; Raymond, K. N. *J. Chem. Soc., Dalton Trans.* **1999**, 1185.
- (28) Fujita, M.; Sasaki, O.; Mitsuhashi, T.; Fujita, T.; Yazaki, J.; Yamaguchi, K.; Ogura, K. *Chem. Commun.* **1996**, 1535.
- (29) Mugridge, J. S.; Fiedler, D.; Raymond, K. N. *J. Coord. Chem.* **2010**, *63*, 2779.
- (30) Campos-Fernandez, C. S.; Schottel, B. L.; Chifotides, H. T.; Bera, J. K.; Bacsa, J.; Koomen, J. M.; Russell, D. H.; Dunbar, K. R. *J. Am. Chem. Soc.* **2005**, *127*, 12909.
- (31) Scherer, M.; Caulder, D. L.; Johnson, D. W.; Raymond, K. N. *Angew. Chem. Int. Ed.* **1999**, *38*, 1588.
- (32) Johnson, D. W.; Raymond, K. N. *Supramol. Chem.* **2001**, *13*, 639.

- (33) Dallavalle, F.; Remelli, M.; Sansone, F.; Bacco, D.; Tegoni, M. *Inorg. Chem.* **2010**, *49*, 1761.
- (34) Pacco, A.; Parac-Vogt, T. N.; Besien, E. v.; Pierloot, K.; Gorler-Walrand, C.; Binnemans, K. *Eur. J Inorg. Chem.* **2005**, 3305.
- (35) Kilbas, B.; Mirtschin, S.; Scopelliti, R.; Severin, K. *Chem. Sci.* **2012**, *3*, 701.
- (36) Suzuki, K.; Kawano, M.; Fujita, M. *Angew. Chem. Int. Ed.* **2007**, *46*, 2819.
- (37) Mamula, O.; Lama, M.; Stoeckli-Evans, H.; Shova, S. *Angew. Chem. Int. Ed.* **2006**, *45*, 4940.
- (38) Baxter, P. N. W.; Khoury, R. G.; Lehn, J.-M.; Baum, G.; Fenske, D. *Chem. Eur. J.* **2000**, *6*, 4140.
- (39) Mezei, G.; Zaleski, C. M.; Pecoraro, V. L. *Chem. Rev.* **2007**, *107*, 4933.
- (40) Stemmler, A. J.; Kampf, J. W.; Pecoraro, V. L. *Angew. Chem. Int. Ed. Engl.* **1996**, *35*, 2841.
- (41) Pecoraro, V. L.; Stemmler, A. J.; Gibney, B. R.; Bodwin, J. J.; Wang, H.; Kampf, J. W.; Barwinski, A. In *Prog. Inorg. Chem.*; Karlin, K. D., Ed.; John Wiley and Sons, Inc.: New York, 1997; Vol. 45, p 83.
- (42) Stemmler, A. J.; Kampf, J. W.; Kirk, M. L.; Atasi, B. H.; Pecoraro, V. L. *Inorg. Chem.* **1999**, *38*, 2807.
- (43) Seda, S. H.; Janczak, J.; Lisowski, J. *Inorg. Chem. Commun.* **2006**, *9*, 792.
- (44) Bünzli, J.-C. G.; Eliseeva, S. V. In *Lanthanide Luminescence: Photophysical, Analytical, and Biological Aspects*; Hanninen, P., Harma, H., Eds.; Springer-Verlag: Berlin, 2010; Vol. 7, p 1.
- (45) Eliseeva, S. V.; Bunzli, J. C. *Chem. Soc. Rev.* **2010**, *39*, 189.
- (46) Bischof, C.; Wahsner, J.; Scholten, J.; Trosien, S.; Seitz, M. *J. Am. Chem. Soc.* **2010**, *132*, 14334.
- (47) Beeby, A.; Clarkson, I. M.; Dickins, R. S.; Faulkner, S.; Parker, D.; Royle, L.; de Sousa, A. S.; Williams, J. A. G.; Woods, M. *J. Chem. Soc., Perkin Trans. 2* **1999**, 493.
- (48) Bunzli, J. C.-G.; Piguet, C. *Chem. Rev.* **2002**, 102.
- (49) Jankolovits, J.; Andolina, C. M.; Kampf, J. W.; Raymond, K. N.; Pecoraro, V. L. *Angew. Chem. Int. Ed.* **2011**, *50*, 9660.
- (50) Reddy, A. S.; Kumar, M. S.; Reddy, G. R. *Tet. Lett.* **2000**, *41*, 6285.
- (51) Aebischer, A.; Gummy, F.; Bunzli, J. C. *Phys. Chem. Chem. Phys.* **2009**, *11*, 1346.
- (52) Brayshaw, P. A.; Bunzli, J.-C. G.; Froidevaux, P.; Harrowfield, J. M.; Kim, Y.; Sobolev, A. N. *Inorg. Chem.* **1995**, *34*, 2068.
- (53) *Saint Plus*, v. 7.60A; Bruker Analytical X-ray: Madison, WI, **2009**.
- (54) Sheldrick, G. M.; *SADABS, Program for Empirical Absorption Correction of Area Detector Data*, Gottingen, Germany, **2008**.
- (55) Sheldrick, G. M. *Acta Cryst.* **2008**, *A64*, 112.
- (56) Rigaku Corporation, *Crystal Clear 2.0*. Tokyo, Japan.
- (57) Sheldrick, G. M. *Acta Cryst.* **2008**, *A64*, 112.
- (58) Dallavalle, F.; Tegoni, M. *Polyhedron* **2001**, *20*, 2697.
- (59) Careri, M.; Dallavalle, F.; Tegoni, M.; Zagnoni, I. *J. Inorg. Biochem.* **2003**, *93*, 174.
- (60) Tegoni, M.; Remelli, M.; Bacco, D.; Marchio, L.; Dallavalle, F. *Dalton Trans.* **2008**, 2693.
- (61) Bacco, D.; Bertolasi, V.; Dallavalle, F.; Galliera, L.; Marchetti, N.; Marchio, L.; Remelli, M.; Tegoni, M. *Dalton Trans* **2011**, *40*, 2491.
- (62) Seda, S. H.; Janczak, J.; Lisowski, J. *Inorg. Chim. Acta* **2006**, *359*, 1055.
- (63) Seda, S. H.; Janczak, J.; Lisowski, J. *Eur. J. Inorg. Chem.* **2007**, *2007*, 3015.
- (64) Addison, A. W.; Rao, T. N.; Reedijk, J.; van Rijn, J.; Verschoor, G. C. *J. Chem. Soc., Dalton Trans.* **1984**, 1349.

- (65) Johnson, J. A.; Kampf, J. W.; Pecoraro, V. L. *Angew. Chem. Int. Ed.* **2003**, *42*, 546.
- (66) Tegoni, M.; Furlotti, M.; Tropiano, M.; Lim, C.-S.; Pecoraro, V. L. *Inorg. Chem.* **2010**, *49*, 5190.
- (67) Boron, T. T., 3rd; Kampf, J. W.; Pecoraro, V. L. *Inorg. Chem.* **2010**, *49*, 9104.
- (68) Unit cell parameters: 8.495 x 10.285 x 10.537 Å, 89.40 x 85.06 x 70.09°, volume = 862.22 cubic angstroms
- (69) Afrati, T.; Zaleski, C. M.; Dendrinou-Samara, C.; Mezei, G.; Kampf, J. W.; Pecoraro, V. L.; Kessissoglou, D. P. *Dalton Trans.* **2007**, 2658.
- (70) Cohen, Y.; Avram, L.; Frish, L. *Angew. Chem. Int. Ed.* **2005**, *44*, 520.
- (71) Aebischer, A.; Gummy, F.; Bünzli, J. G. *Phys. Chem. Chem. Phys.* **2009**, *11*, 1346.
- (72) Pope, S. J. A. *Polyhedron* **2007**, *26*, 4818.
- (73) Tegoni, M.; Remelli, M. *Coord. Chem. Rev.* **2012**, *256*, 289.
- (74) Bodwin, J. J.; Pecoraro, V. L. *Inorg. Chem.* **2000**, *39*, 3434.
- (75) Pavlishchuk, A. V.; Kolotilov, S. V.; Zeller, M.; Shvets, O. V.; Fritsky, I. O.; Lofland, S. E.; Addison, A. W.; Hunter, A. D. *Eur. J. Inorg. Chem.* **2011**, *2011*, 4826.
- (76) Lah, M. S.; Gibney, B. R.; Tierney, D. L.; Penner-Hahn, J. E.; Pecoraro, V. L. *J. Am. Chem. Soc.* **1993**, *115*, 5857.
- (77) Kessissoglou, D. P.; Bodwin, J. J.; Kampf, J.; Dendrinou-Samara, C.; Pecoraro, V. L. *Inorg. Chim. Acta* **2002**, *331*, 73.
- (78) Stemmler, A. J.; Barwinski, A.; Baldwin, M. J.; Young, V.; Pecoraro, V. L. *J. Am. Chem. Soc.* **1996**, *118*, 11962.
- (79) Halfen, J. A.; Bodwin, J. J.; Pecoraro, V. L. *Inorg. Chem.* **1998**, *37*, 5416.
- (80) Desreux, J. F.; Duyckaerts, G. *Inorg. Chim. Acta.* **1979**, *35*, L313.
- (81) Pedersen, C. J.; Frensdorff, H. K. *Angew. Chem. Int. Ed. Engl.* **1972**, *11*, 17.
- (82) Lah, M. S.; Kirk, M. L.; Hatfield, W.; Pecoraro, V. L. *J. Chem. Soc., Chem. Commun.* **1989**, 1606.
- (83) Ishikawa, N.; Sugita, M.; Ishikawa, T.; Koshihara, S.; Kaizu, Y. *J. Am. Chem. Soc.* **2003**, *125*, 8694.
- (84) Han, M. Y.; Min, K. S.; Suh, M. P. *Inorg. Chem.* **1999**, *38*, 4374.
- (85) Saalfrank, R. W.; Low, N.; Hampel, F.; Stachel, H.-D. *Angew. Chem. Int. Ed. Engl.* **1996**, *35*, 2209.
- (86) Saalfrank, R. W.; Low, N.; Kareth, S.; Seitz, V.; Hampel, F.; Stalke, D.; Teichert, M. *Angew. Chem. Int. Ed.* **1998**, *37*, 172.
- (87) Mezei, G.; Baran, P.; Raptis, R. G. *Angew. Chem. Int. Ed.* **2004**, *43*, 574.
- (88) Kwak, B.; Rhee, H.; Park, S.; Lah, M. S. *Inorg. Chem.* **1998**, *37*, 3599.
- (89) Liu, S.-X.; Lin, S.; Lin, B.-Z.; Lin, C.-C.; Huang, J.-Q. *Angew. Chem. Int. Ed.* **2001**, *40*, 1084.
- (90) Bunzli, J.-C. G. *Chem. Rev.* **2010**, *110*, 2729.
- (91) Psomas, G.; Stemmler, A. J.; Dendrinou-Samara, C.; Bodwin, J. J.; Schneider, M.; Xlexiou, M.; Kampf, J. W.; Kessissoglou, D. P.; Pecoraro, V. L. *Inorg. Chem.* **2001**, *40*, 1562.
- (92) Bunzli, J. C.; Piguet, C. *Chem Soc Rev* **2005**, *34*, 1048.
- (93) D'Aleo, A.; Picot, A.; Beeby, A.; Williams, J. A. G.; Guennic, B. L.; Andraud, C.; Maury, O. *Inorg. Chem.* **2008**, *47*, 10258.
- (94) Zhang, J.; Badger, P. D.; Geib, S. J.; Petoud, S. *Angew. Chem. Int. Ed.* **2005**, *44*, 2508.
- (95) Bassett, A. P.; Deun, R. V.; Nockemann, P.; Glover, P. B.; Kariuki, B. M.; Hecke, K. V.; Meervelt, L. V.; Pikramenou, Z. *Inorg. Chem.* **2005**, *44*, 6140.
- (96) W. D. Horrocks, J.; Bolander, J. P.; Smith, W. D.; Supkowski, R. M. *J. Am. Chem. Soc.* **1997**, *119*, 5972.

- (97) Ward, M. D. *Coord. Chem.Rev.* **2010**, 254, 2634.
- (98) Lazarides, T.; Alamiry, M. A.; Adams, H.; Pope, S. J.; Faulkner, S.; Weinstein, J. A.; Ward, M. D. *Dalton Trans.* **2007**, 1484.
- (99) Hickey, J. E.; Spritzer, M. S.; Elving, P. J. *Anal. Chim. Acta* **1966**, 35, 277.
- (100) Rehm, D.; Weller, A. *J. Isr. Chem.* **1970**, 8, 259.
- (101) Lazarides, T.; Tart, N. M.; Sykes, D.; Faulkner, S.; Barbieri, A.; Ward, M. D. *Dalton Trans.* **2009**, 3971.
- (102) Rinehart, J. D.; Long, J. R. *Chem. Sci.* **2011**, 2, 2078.
- (103) Shannon, R. D. *Acta Cryst.* **1976**, A32, 751.

Chapter V

Conclusions and Future Directions

Conclusions and Future Directions

Nature demonstrates how molecular recognition can be used to construct elaborate and functional molecular assemblies. Based on the precedent in nature, chemists have endeavored to exploit supramolecular interactions to control the organization of matter in artificial host-guest systems and self-assembled complexes. Increasingly, molecular recognition in artificial systems is being applied in areas of need, such as chemical separations and transformations or the preparation of molecules and materials with addressable properties.¹⁻³

Of the vast types of self-assembled systems in the literature, MCs are set apart in a historic sense by their analogy to crown ethers and in an application sense by their significant metal density and structural versatility. The metal density has given rise to single-molecule magnetism in a number of complexes. Furthermore, the dense array of open metal sites and the chirality of the ring can lead to diverse molecular recognition capabilities and solid-state architectures. Lastly, the electron-withdrawing effects of the ring metals in Ln(III)[15-MC_{Cu(II)}, α -aminoHA⁻⁵] complexes contribute to the strong Lewis-acidity of the central Ln(III) ion, evidenced by the pK_a of less than 5 for a water coordinated to the Ln(III) ions.⁴ The structural versatility of MCs is also remarkable, as MCs have been prepared as the typical 9-MC-3, 12-MC-4, 15-MC-5, and 18-MC-6 motifs, and large structure types sizes up to 60-MC-20 are known.⁵ Furthermore, many MCs are amenable to ring metal, central metal, ligand, and counterion or guest substitutions. This thesis has explored how MC structural versatility can be exploited to tune the guest recognition behavior, solid-state organization, structural motif, and physical properties of the complex. Systematic studies of how Ln(III)[15-MC_{Cu(II)}, α -aminoHA⁻⁵] ligand and central metal substitutions effect guest recognition in solution and the solid state were conducted to understand better how these hosts can be utilized in

separations, catalysis, and the design of crystalline molecular materials. This thesis also explores how MC structural versatility can be used to realize complexes with unique physical properties through the synthesis of Ln-MCs with Zn(II) ring metals for luminescence, single-ion magnetism, and second harmonic generation (SHG). The synthetic work uncovered an intricate solvent dependence in the assembly of Ln-MCs with Zn(II) which to date allowed for the isolation of 6 distinct MC structural motifs. Conclusions from this research and future directions are discussed below.

The Pecoraro group has recognized that Ln(III)[15-MC_{Cu(II), α -aminoHA-5}] complexes form discrete compartments in the solid-state that selectively encapsulate bridging anions based on size and composition criteria.⁶⁻⁸ Ln(III)[15-MC_{Cu(II), α -aminoHA-5}] compartments are novel from a supramolecular standpoint for their large interior volume of over 275 Å³, anion recognition behavior, and chirality. From a crystal engineering standpoint, the appeal of compartments is that their chirality enforces the non-centrosymmetric environment requisite for crystalline SHG materials, their consistent formation despite the flexibility of the MC, and their potential use as reaction templates given the capability of orienting multiple substrates in close proximity. Chapter two presented a systematic structural study that examined how substituting the ligand side-chain and central metal influences guest recognition by Ln(III)[15-MC_{Cu(II), α -aminoHA-5}] compartments.⁹⁻¹¹ Guidelines for considering the size and selectivity of Ln(III)[15-MC_{Cu(II), α -aminoHA-5}] compartments were established based on trends in the crystal structures. First, it was established that compartment height is constrained by the side chain length, as guests must template a MC dimer that can associate through hydrophobic interactions between phenyl side chain. Straightforward structural calculations based on guest and side chain length allows for the prediction of a suitable side chain that will allow for compartment formation. Furthermore, it was established that the nine-coordinate La(III) and compressed compartments promote the encapsulation of multiple guests, which is important for multimolecular reactions. Lastly, ESI-MS data suggests that the compartments persist in solution, making it reasonable to consider solution applications of the dimeric host.

This systematic crystallographic study was motivated in part by the prospect for application of the compartments in preparing crystalline SHG materials. Previous results

with $\text{Ln(III)[15-MC}_{\text{Cu(II),pheHA-5}}\text{]}(\text{isonicotinate})$ complexes show that the compartment enforces an antiparallel alignment of isonicotinate guests so that there is a net dipole through the lattice.¹² This was impressive considering that dipolar crystals are enthalpically and entropically unfavorable. The SHG intensity was modest for these complexes due to the absorption of frequency doubled light by the Cu(II) ring metals and the modest hyperpolarizability of isonicotinate. Regarding the visible light absorption, significant efforts have been concentrated on preparing visibly transparent MCs with Zn(II) ring metals (see chapter 4 and below). Results in these pursuits suggest that visibly transparent hosts should be obtainable. Regarding the modest hyperpolarizability of isonicotinate, it is well established that longer conjugated guests have greater hyperpolarizabilities. Wenbin Lin has shown that non-centrosymmetric metal-organic frameworks with long pyridyl-carboxylates exhibit SHG intensities greater than the commercially relevant LiNbO_3 .¹³ The theoretical framework for $\text{Ln(III)[15-MC}_{\text{Cu(II),}\alpha\text{-aminoHA-5}}\text{]}$ compartments will be useful in the rational design of crystalline inclusion complexes with long hyperpolarizable guests. The particular observation that the compartment height can be increased through simple substitutions to the phenyl side chain strongly supports the viability of this approach.

To build on the solid state work on $\text{Ln(III)[15-MC}_{\text{Cu(II),}\alpha\text{-aminoHA-5}}\text{]}$ compartments, future investigations should investigate the extent that these dimeric hosts assemble and recognize guests in solution. Quantitative data on solution dimerization would be especially useful for applying the host in supramolecular catalysis, separations, and responsive systems. Such thermodynamic data can be obtained with fluorescence assays that use bridging dicarboxylate fluorophores¹⁴ or isothermal titration calorimetry. Dimerization can also be probed electrochemically with redox active guests, such as ferrocene dicarboxylate or tetrathiafulvalene dicarboxylate. The author has obtained a number of crystal structures between ferrocene dicarboxylate²⁻¹⁵ or cobaltocenium dicarboxylate⁻ and $\text{Ln(III)[15-MC}_{\text{Cu(II),}\alpha\text{-aminoHA-5}}\text{]}$ hosts that are suggestive of compartment formation that can be controlled electrochemically with redox active guests (figure 5.1).^{16,17} Regardless of host paramagnetism, dimerization can also be studied with diffusion NMR or heteronuclear correlation NMR techniques. The latter

techniques can probe dimerization by examining associative interactions between carbon, hydrogen, deuterium, or fluorine atoms on the phenyl side chains.

To this point, guest recognition solution studies have focused on monomeric Ln(III)[15-MC_{Cu(II), α -aminoHA-5}] hosts. Chapter 3 describes the development of a voltammetric competitive binding assay that has been useful in measuring the thermodynamics of guest binding to the paramagnetic host.¹⁵ Drawbacks of the technique, such as its limitation to 1:1 host-guest systems and the high analyte and electrolyte concentrations required for voltammetry, will likely prevent its widespread use. Nevertheless, the technique is a solid contribution to the analytical toolbox of supramolecular chemists and should prove particularly useful for paramagnetic hosts and for researchers with limited access to expensive calorimeters and spectrometers.

The voltammetric competitive binding assay was used to probe how guest functional groups, guest chirality, and host side chains influence Ln(III)[15-MC_{Cu(II)-5}] guest recognition. The thermodynamic study on Gd(III)[15-MC_{Cu(II),pheHA-5}] recognition of α -amino acid derivatives¹⁸ provides some of the first data on functional group tolerance by a metallocavitand. Organic metallocavitands in aqueous solvents recognize guests primarily through hydrophobic interactions, so hydrophilic functionalities typically decrease the binding strength. In metallocavitands, the metal ions can potentially interact favorably with hydrophilic residues on the guest. The binding constants between Gd(III)[15-MC_{Cu(II),pheHA-5}] and the series of α -amino acid derivatives suggests that the hydrophobic character of the cavity largely dictates guest recognition behavior since binding strength generally decreases when hydrophilic functionalities are introduced to the guest. The exception is when the functionality introduces a more favorable binding mode, which is observed with the α -hydroxy acid guests. Importantly, the generally weaker binding seen with hydrophilic guests provides a potential route to overcoming product inhibition in supramolecular catalysis with metallocavitands. Transformation of a hydrophobic guest to a more hydrophilic guest could lead to relatively weak product binding and facilitate turnover.

The side chain dependent enantioselective guest binding of Gd(III)[15-MC_{Cu(II)-5}] is a particularly promising result.¹⁹ The enantioselectivity (K_S/K_R of up to 2.2 ± 0.6) is on par with the best selectivity observed with cyclodextrin hosts. Moreover, these MCs are

some of the first metallamacrocycles that display chiral selectivity.^{20,21} These values demonstrate the promise of utilizing these MCs in chiral separations.²² While many of the best organic hosts display K_S/K_R or K_R/K_S values of over 10, the selectivity seen with Gd(III)[15-MC_{Cu(II)}-5] hosts is appreciable given that a limited number of guests have been examined and these are first-generation ligands. Enantioselectivity can possibly be enhanced with different guests, so future studies should expand the substrate scope of MCs. Furthermore, substitutions of the MC central metal, such as with the 9-coordinate La(III) or soft Pb(II), ring metals, or side chains could enhance enantioselectivity. Bulkier side chains could increase steric clashes with particular enantiomers, thereby enhancing enantioselectivity (figure 5.2). In particular, side chains that orient steric bulk toward the center of the MC should be examined. In addition, the significant enantioselectivity with pgHA suggests the importance of using rigid groups to achieve greater selectivity.²³ To enhance side chain rigidity, it could be useful to eliminate the free rotation around the bond between the α - and β -carbons. This rotation can be prevented by linking the side chain to either the α -carbon or by using proline derivatives. Lastly, hydrogen bond donors or acceptors can be incorporated to enhance enantioselectivity through recognition of the carboxylate or other functional groups on the guests. In future studies of chiral recognition, combinatorial approaches should be used to accelerate the discovery of highly discriminating hosts or guests.²⁴ One advantage of MCs from a combinatorial standpoint is their facile synthesis by self-assembly, which will allow for the rapid synthesis of many hosts with different side chains, central metals, or ring metals. Furthermore, MCs utilize chiral ligands that can be prepared from α -amino acids in 1-2 step syntheses. Chiral α -amino acids are readily available and relatively inexpensive, making it straightforward to create libraries of chiral hydroxamic ligands. The chiral selectivity of these complexes could be rapidly assessed via chromatography. Ln(III)[15-MC_{Cu(II), α -aminoHA}-5] complexes are strongly absorbed and stable on silica. Partitioning of different enantiomers during chromatography on MC-coated silica, or other supports, could allow for rapid and facile screening of different enantioselective host-guest combinations. Once identified, the MC-guest interactions could be thoroughly analyzed through crystallography and thermodynamic measurements.

The observation of side chain dependent guest affinity and enantioselectivity is also exciting from the standpoint of using Ln(III)[15-MC-5] complexes as catalysts. As the side chain can influence the chemistry at the metal ions, secondary sphere interactions can likely influence the regioselectivity or enantioselectivity of a reaction. Considering the Ln(III)[15-MC-5] complexes are highly Lewis-acidic, it would be interesting to explore their hydrolytic or transesterification chemistry. The pK_a of a water molecule coordinated to Gd(III)[15-MC-5] is less than 5,⁴ meaning that the MC can generate a hydroxide ion in acidic solutions. *p*-nitrophenylacetate hydrolysis (figure 5.3) would be an appropriate reaction for exploring this type of catalytic activity, and advantageously the reaction can be monitored with absorption spectroscopy.²⁵ Considering enantioselective catalysis with Ln(III)[15-MC-5] complexes, chiral Ln(III) complexes are known to be adept Lewis-acid catalysts for a variety of reactions.^{26,27} Ln(III)[15-MC-5] complexes are most stable in highly coordination solvents, so it would be best to study a reaction that can be performed in aqueous conditions on catalysts with few open coordination sites. These criteria eliminate most reactions, though the Allen group has demonstrated enantioselective Mukaiyama Aldol reactions with chiral crown ether based complexes possessing three open coordination sites in aqueous conditions (figure 5.3).²⁸ This reaction should be suitable for assessing enantioselective catalysis with Ln(III)[15-MC-5] complexes. Lastly, from a supramolecular catalysis standpoint, Diels-Alder reactions are the ideal reaction for assessing how the cavity can influence reactivity. Following a similar approach to Kersting,²⁹ the Diels-Alder reaction of sorbate (figure 5.3) with acrylate could be performed in the Ln(III)[15-MC-5] metallocavitand. One might expect that with Gd(III)[15-MC-5], the steric constraints of the cavity could lead *anti*-selectivity. In contrast, the extra coordination site on La(III) could coordinate both sorbate and acrylate to the MC face, generating the *syn*-product. Though product inhibition is likely in this reaction, the reaction is promising for initial studies.

Chapter four of this thesis examines synthesis of Ln-MCs with Zn(II) ring metals in order to tune the assembly, spectroscopic, and magnetic behavior of the system. While Ln(III)[15-MC_{Cu(II)}-5] complexes have shown promise for separations, catalysis, and materials design, their assembly with Cu(II) introduces undesirable physical properties. *d-d* transitions absorb frequency-doubled light and provide a quenching pathway for

excited Ln(III) ions, leading to inefficient SHG and luminescence. Furthermore, the unpaired electrons on Cu(II) cause line broadening that obscures ^1H NMR characterization and precludes single-ion magnet behavior. Ln-MCs with Zn(II) ring metals could overcome all of these shortcomings while also expanding the scope of MC chemistry and providing a case study for coordination-driven self-assembly.

It was recognized that the structural promiscuity of Zn(II) would complicate the assembly process. Ln(III)[15-MC_{Cu(II)}-5] assembly with Cu(II) is straightforward because the Jahn-Teller distorted ring metal promotes an equatorial ligand arrangement, which complements the geometric preference of the picHA ligand to form a planar pentagon.³⁰ Zn(II) ions in the MCs in chapter four show primarily a distorted square pyramidal coordination geometry, which promotes the formation of the concave 12-MC-4 motif. The competing symmetry preferences of the two building blocks promote the formation of multiple structure types in solution. The particularly remarkable finding is that the competing structural preferences of the building blocks coupled with the open metal sites on the metal ions leads to a strong solvent dependence in the assembly. Remarkably, simply mixing H₂picHA, a base, Zn(II)(NO₃)₂, and a Ln(III)(NO₃)₃ salt leads to the assembly of five monolanthanide MCs, a range of multi-lanthanide complexes, and at least two high nuclearity Zn(II) complexes *in solution*. The different complexes assemble in solution based on how the solvent interacts with the metal ion. The importance of assembly in solution is that the ligand can be derivatized and the same complexes can be expected to form. Most of these complexes have been crystallographically characterized, and most are kinetically stable at room temperature in at least one solvent. Though the stability is lanthanide dependent, ESI-MS shows that all complexes assemble in solution with both La(III) and Y(III). From the self-assembly standpoint, the picHA, Zn(II), and Ln(III) system is unparalleled in the variety of complexes that form and the control over those different complexes provided by an external agent. Furthermore, the approach of using symmetry incompatible building blocks and metal ions with open metal sites should be a general strategy for synthesizing metal complexes by self-assembly. Serendipity certainly plays a role in determining the different motifs that might arise from such a complex solvent dependent assembly. However serendipity should be welcome considering that novel structural motifs can give rise to novel functionality. The series of

Ln-MCs with Zn(II) ring metals are being used to systematically study the effects of minor changes to the geometry of highly symmetrical Ln(III) complexes on single-ion magnet behavior. Preliminary magnetic measurements by Thaddeus Boron III demonstrate that the LnZn₁₆(picHA)₁₆ complexes with Dy(III), Er(III), and Yb(III) show slow magnetic relaxation below 3 K, consistent with single-ion magnetic behavior.

The luminescence properties of Ln-MCs are particularly exciting. Emission through Ln(III) *f-f* transitions show long lifetimes of up to milliseconds, large Stokes shifts, and narrow line widths. These unique features have led to intense interest in incorporating luminescent Ln(III) complexes in optical devices and biomedical imaging assays.³¹ One major drawback of luminescent Ln(III) complexes, particularly for near-infrared (NIR) emitting Ln(III) ions, is low efficiency due to vibrational quenching of the Ln(III) excited state.^{32,33} To minimize the effects of vibrational quenching, high energy C-H, N-H, and O-H oscillators must be eliminated from the proximity of the Ln(III) ion. While N-H and O-H oscillators can be avoided in coordination complexes through careful ligand design, C-H bonds cannot be removed without resorting to expensive ligand deuteration or fluorination. Vibrational quenching limits the very best NIR emitting Ln(III) complexes to luminescence lifetimes of less than 6 μ s in protic solvents, and quantum yields of less than 0.4 %.^{34,35} It was recognized that the inorganic ring on MC complexes extends C-H bonds on the ligand over 6.7 Å from the Ln(III) ion, while traditional organic ligands have C-H bonds within 5 Å of the Ln(III) ion. Impressively, the YbZn₁₆(picHA)₁₆ complex had a lifetime of 14 μ s in methanol and a quantum yield of 0.89 %.³⁶ This is the brightest NIR emission from a lanthanide coordination complex in a protic solvent among complexes without deuterated or fluorinated ligands and one of the brightest reported in any solvent.³⁷⁻³⁹ Importantly, the strategy of realizing bright luminescent lanthanide complexes with MCs is one of the only effective ways to reduce vibrational quenching in a coordination complex.

In the future, the remaining Ln(III)-MCs in the series should be characterized to see the effects of the open coordination sites on the luminescence efficiency. Vibrational quenching from high energy oscillators on solvent molecules will likely decrease efficiency, though the data would be useful for designing more efficient luminescent MCs. It would also be worthwhile to measure the luminescence of the YbZn₁₆ with a

deuterated picHA ligand to assess the effects of vibrational quenching from oscillators so far removed from the Yb(III) ion. To enhance the Ln-MC luminescence, it would be helpful to understand the mechanism of Yb(III) sensitization, which could be probed by transient spectroscopy. Based on precedents from previous systems,^{40,41} the observation of solvent dependent excitation wavelengths for LnZn₁₆ complexes, and the rapid quenching of the picHA triplet state within 100 μ s in GdZn₁₆(picHA)₁₆, the energy transfer mechanism likely involves a photoinduced intramolecular charge transfer state that sensitizes the Ln(III) ion upon back electron transfer. If this is the case, incorporating electron donor groups into picHA (figure 5.4) could tune the charge transfer state and enhance efficiency. Furthermore, Ln-MCs can be prepared with transition metal ions in the ring that have high energy, long lived metal to ligand-to-metal charge transfer states, such as Cr(III), Ru(II), or Os(II). Ln-MCs with these ring metals could be readily sensitized through *d-f* energy transfer, which is effective in other systems.^{42,43} Advantageously, tuning charge transfer through ligand functionalities or different ring metals can increase the excitation wavelength and possibly lead to emission from the visible emitting lanthanides, which is important for many applications.

A major goal of this thesis was to develop the molecular recognition chemistry of chiral Ln-MCs and to synthesize optically transparent Ln-MCs for the development of SHG materials. The aim was to utilize the crystal engineering and molecular recognition chemistry established in chapters 2 and 3 and the synthetic work Zn(II) MCs from chapter 4 to generate optically transparent, crystalline inclusion complexes of MCs with SHG chromophores, such as pyridyl carboxylates. SHG active solids have only been obtained through host-guest chemistry in two prior instances, though these systems were limited in the scope of guests that could be encapsulated.^{44,45} Furthermore, MC based hosts are known to generate dipolar crystalline complexes by orienting the guests in the compartment¹² and enforce noncentrosymmetric space groups through their chirality, which are two of the biggest challenges in preparing SHG materials.

The synthesis of chiral MCs with Zn(II) ring metals was pursued doggedly. It was established with ESI-MS that a LaZn₅(α -aminoHA)₅ assembles in pyridine, while a Zn₅(α -aminoHA)₄ complex forms in the absence of La(III) (figure 5.5). Furthermore, the addition of dimethylformamide leads to the formation of a LaZn₄(α -aminoHA)₄ complex.

With smaller lanthanides, the $\text{LnZn}_4(\alpha\text{-aminoHA})_4$ seems to be more favored based on ESI-MS peak intensity. A crystal structure was obtained of a $\text{LaZn}_4(\text{L-pheHA})_2(\text{L-HpheHA})_2(\text{NO}_3)_5$ from a pyridine solution (figure 5.6). The complex is a saddle-shaped 16-MC-6 with C_2 symmetry. The central La(III) is nine-coordinate and is bound by a bidentate nitrate and pyridine. The assignment of two protonated HpheHA ligands is based on charge balance and the unbound $\text{N}_{\text{hydroximate}}$ atoms that are within hydrogen-bonding distances of pyridine molecules in the lattice. This complex is unstable in solution, rapidly converts to the $\text{LaZn}_5(\alpha\text{-aminoHA})_5$ and $\text{Zn}_5(\alpha\text{-aminoHA})_4$. Importantly, ESI-MS shows that all of these MCs decompose in the presence of carboxylates. Unfortunately, crystallization of these Ln-MCs with pyridyl carboxylates did not yield the expected MC compartments, showing evidence for MC decomposition or yielding $\text{LaZn}_4(\text{L-pheHA})_2(\text{L-HpheHA})_2$ adducts with no net dipole. However, the Ln-MCs are stable with aromatic-sulfonates, though efforts to crystallize Ln-MCs with pyridyl-sulfonates have been unsuccessful to date. Given the promising solution data, it should be possible to isolate a variety of optically transparent chiral MCs as long as the proper crystallization conditions can be established. The inclusion of pyridyl-sulfonates in the dimeric compartments of these MCs should be a viable route to crystalline SHG materials.

As an alternative, a chiral, optically transparent MC host might be generated from $\text{Zn}(\text{II})[12\text{-MC}_{\text{Zn}(\text{II}),\text{picHA}}\text{-4}]$. This concave complex is inherently chiral⁴⁶ based on the rotational sense of the MC ring (figure 4.37). Based on the precedent with organic systems with similar topologies, chiral Zn_5L_4 complexes can likely recognize guests through interactions with the concave cavity exclusively. Thus the Zn_5L_4 might bind guests that do not coordinate to metals, potentially expanding the scope of chromophores that can be encapsulated in MC hosts. It should be noted that the Zn_5L_4 complexes are synthesized and crystallized as a racemic mixture, so they would have to be resolved for SHG applications. Resolution of the Zn_5L_4 could possibly be achieved by crystallization with a chiral substrate or by chiral chromatography.⁴⁷ If successful, the resolution of the Zn_5L_4 would be remarkable given the lability of Zn(II) and the scarcity of chiral metallamacrocycles.

In conclusion, MCs are versatile self-assembled complexes that are amenable to structural changes to the central metal, ring metal, ligand, and counterion. This thesis demonstrates how the structural versatility of MCs can be exploited to tune the guest recognition, solid-state organization, physical properties, and self-assembly behavior of the complex. Much of the work in this thesis described research on one specific research topic: crystal engineering, host-guest chemistry, self-assembly, or luminescence. The host-guest chemistry of chiral Ln(III)[15-MC-5] metallocavitands reveals guest affinity, selectivity, and solid-state organization that parallels or exceeds the behavior of benchmark organic systems. Novel strategies for assembling MCs and related metallamacrocycles have been established. Furthermore, MCs with exciting physical properties, such as luminescence and single-molecule magnetism have been realized. Taken together, MCs combine the molecular recognition chemistry of organic hosts and the physical properties of inorganic coordination complexes. Additionally, there is tremendous untapped potential for MCs in catalysis, with chiral Ln(III)[15-MC-5] metallocavitands showing particular promise. Admittedly, there are a number of complexes that bridge supramolecular and inorganic chemistry. However, this thesis has demonstrated three advantages of MCs. First, MCs are easily synthesized through self-assembly from simple ligands that are amenable to derivatization. Second, the chemistry of MCs can be tuned through structural changes to the ligand, ring metal, central metal, or guest. Third, the unique MC topology introduces properties that are difficult to achieve in other systems. Having developed fundamental aspects of MC chemistry at the interface of supramolecular and inorganic chemistry, this thesis and previous work on MCs will serve as the foundation for advancing interfacial areas of science, such as multifunctional molecules, SHG materials, or the use of molecular recognition in metal-based catalysis.

Charles Pedersen, the discoverer of crown ethers, ended his Nobel Lecture by stating that his hope was for something of great benefit be developed “that were it not for the crown compounds it would not be.”⁴⁸ Based on the broad potential of MCs, it seems reasonable to expect that something of great benefit will be developed that rely on this unique class of compounds.

Figures

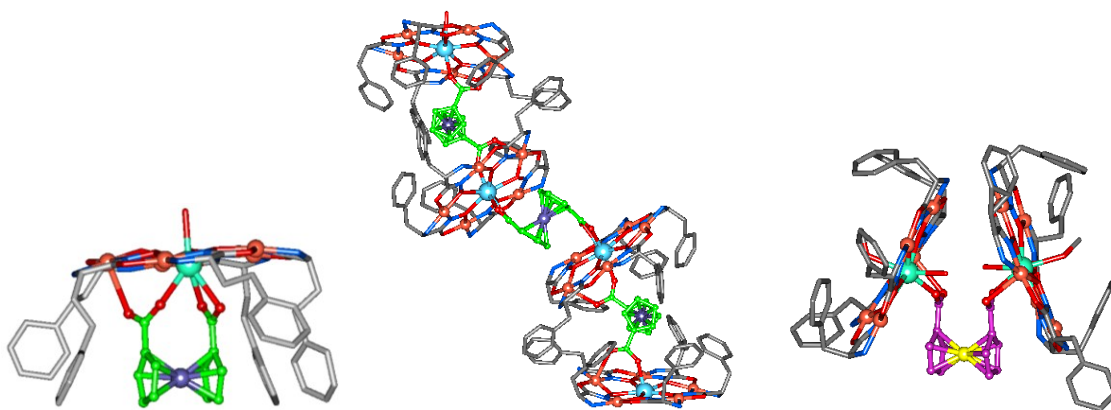


Figure 5.1: Crystal structures of Gd(III)[15-MC_{Cu(II),hpheHA-5}](ferrocenedicarboxylate) (left), La(III)[15-MC_{Cu(II),pheHA-5}](ferrocenedicarboxylate)¹⁵ (center) and Gd(III)[15-MC_{Cu(II),pheHA-5}](cobaltoceniumdicarboxylate) (right) that demonstrate how the side chain length and guest charge can influence how the MC host recognizes metallocene dicarboxylate guests. The structures allude to complex, redox responsive solution equilibria that can be analyzed through voltammetry and other techniques. It should be noted that the Gd(III)[15-MC_{Cu(II),pheHA-5}](ferrocenedicarboxylate) complex is isostructural with the La(III) complex shown in the figure.

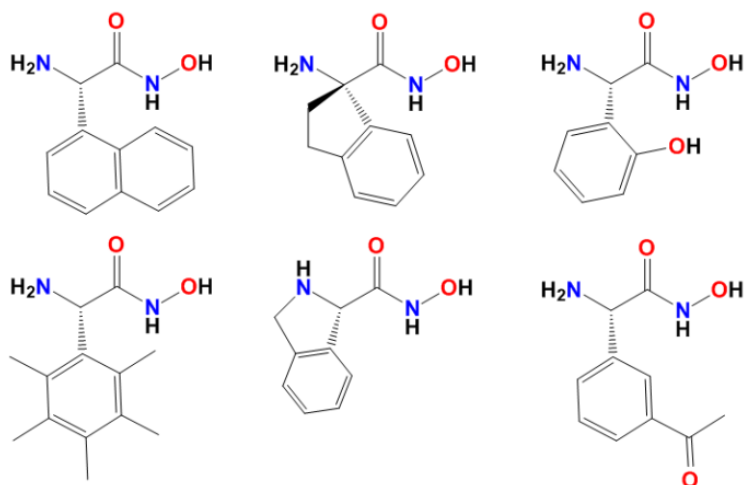


Figure 5.2: General Ln(III)[15-MC-5] ligand designs that could lead to enhanced chiral selectivity. The designs incorporate increased steric bulk (left), enhanced structural rigidity by preventing free rotation of the C_α - C_β bond (center), and hydrogen bond acceptors or donors (right).

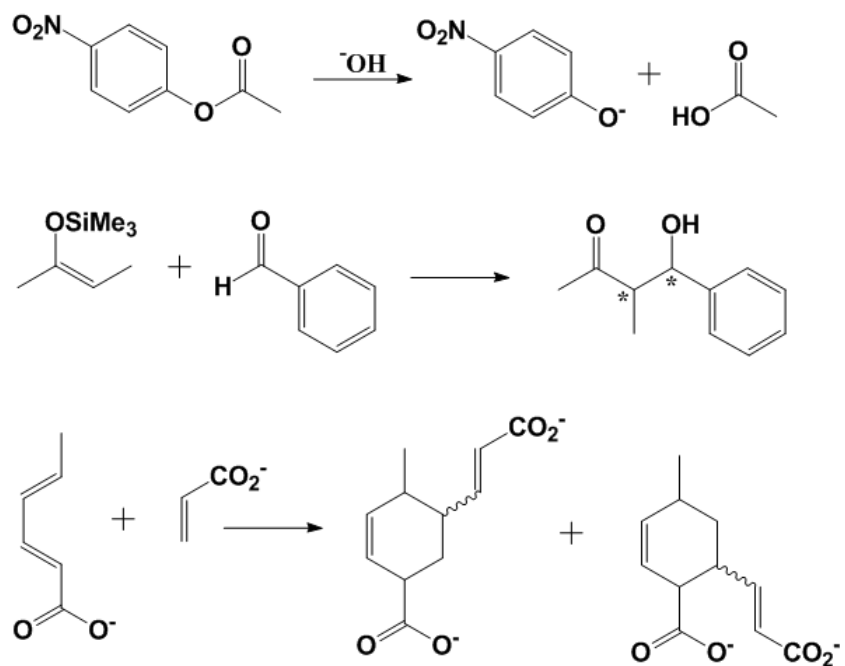


Figure 5.3: Diagrams of reactions that could probe catalysis with Ln(III)[15-MC-5] complexes. The depicted reactions are the hydrolysis of *p*-nitrophenylacetate (top), a Mukaiyama Aldol reaction (middle), and a Diels-Alder reaction (bottom).

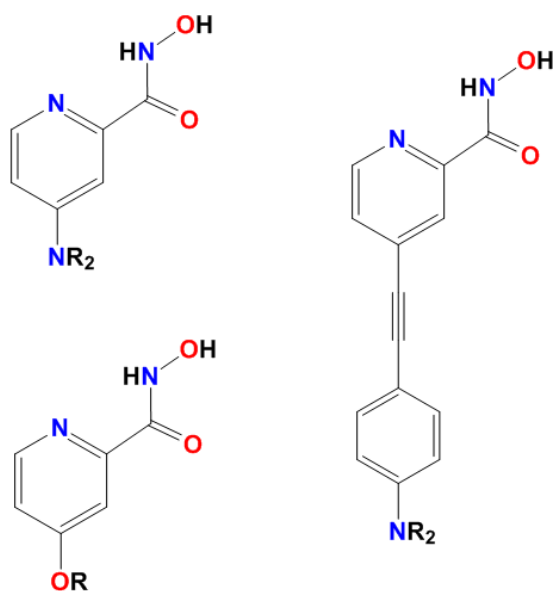


Figure 5.4: H_2picHA derivatives that incorporate electron donating groups for sensitization of Ln(III) ions via charge transfer states.

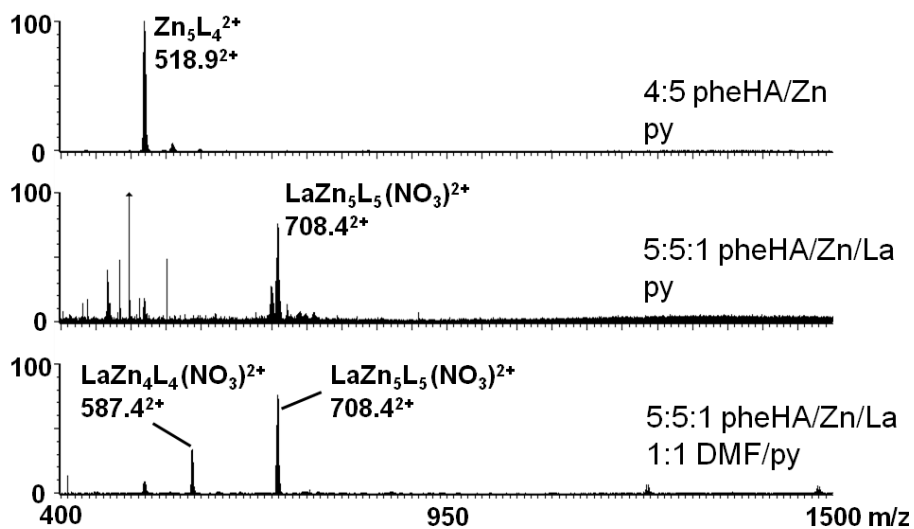


Figure 5.5: ESI-MS showing the MCs that assemble in reaction mixtures of pheHA, $\text{Zn}(\text{NO}_3)_2$, and $\text{La}(\text{NO}_3)_3$ in the indicated ratios and solvents. Two equivalents of triethylamine were added per pheHA ligand.

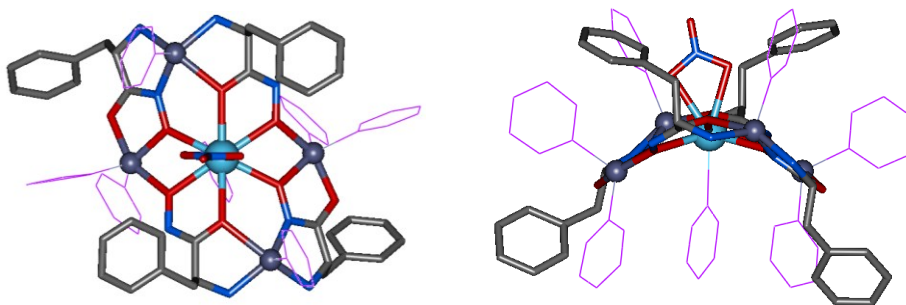


Figure 5.6: Crystal structure of a $\text{LaZn}_4(\text{L-pheHA})_2(\text{L-HpheHA})_2(\text{NO}_3)_5(\text{py})_7$ complex viewed perpendicular and parallel to the saddled 16-MC-6 ring.

References

- (1) Lehn, J. M. *Science* **2002**, *295*, 2400.
- (2) Whitesides, G. M.; Grzybowski, B. *Science* **2002**, *295*, 2418.
- (3) Reinhoudt, D. N.; Crego-Calama, M. *Science* **2002**, *295*, 2403.
- (4) Dallavalle, F.; Remelli, M.; Sansone, F.; Bacco, D.; Tegoni, M. *Inorg. Chem.* **2010**, *49*, 1761.
- (5) Mezei, G.; Zaleski, C. M.; Pecoraro, V. L. *Chem. Rev.* **2007**, *107*, 4933.
- (6) Cutland, A. D.; Malkani, R. G.; Kampf, J. W.; Pecoraro, V. L. *Angew. Chem. Int. Ed.* **2000**, *39*, 2690.
- (7) Lim, C.-S.; Cutland Van Noord, A.; Kampf, J. W.; Pecoraro, V. L. *Eur. J. Inorg. Chem.* **2007**, *2007*, 1347.
- (8) Cutland, A. D.; Halfen, J. A.; Kampf, J. W.; Pecoraro, V. L. *J. Am. Chem. Soc.* **2001**, *123*, 6211.
- (9) Jankolovits, J.; Lim, C.-S.; Kampf, J. W.; Pecoraro, V. L. *Z. Naturforsch.* **2010**, *65b*, 263.
- (10) Jankolovits, J.; Lim, C.-S.; Mezei, G.; Kampf, J. W.; Pecoraro, V. L. *Inorg. Chem.* **2012**, doi:10.1021/ic202347j.
- (11) Lim, C. S.; Jankolovits, J.; Kampf, J. W.; Pecoraro, V. L. *Chem. Asian. J.* **2010**, *5*, 46.
- (12) Mezei, G.; Kampf, J. W.; Pan, S.; Poepelmeier, K. R.; Watkins, B.; Pecoraro, V. L. *Chem. Commun.* **2007**, 1148.
- (13) Evans, O. R.; Lin, W. *Chem. Mater.* **2001**, *13*, 3009.
- (14) Amendola, V.; Bergamaschi, G.; Buttafava, A.; Fabrizzi, L.; Monzani, E. *J. Am. Chem. Soc.* **2010**, *132*, 147.
- (15) Jankolovits, J.; Kampf, J. W.; Maldonado, S.; Pecoraro, V. L. *Chem. Eur. J.* **2010**, *16*, 6786.
- (16) Philip, I. E.; Kaifer, A. E. *J. Am. Chem. Soc.* **2002**, *124*, 12678.
- (17) Philip, I.; Kaifer, A. E. *J. Org. Chem.* **2005**, *70*, 1558.
- (18) Lim, C. S.; Jankolovits, J.; Zhao, P.; Kampf, J. W.; Pecoraro, V. L. *Inorg. Chem.* **2011**, *50*, 4832.
- (19) Grant, J. T.; Jankolovits, J.; Pecoraro, V. L. *Submitted* **2012**.
- (20) Brumaghim, J. L.; Michels, M.; Raymond, K. N. *Eur. J. Org. Chem.* **2004**, *2004*, 4552.
- (21) Fiedler, D.; Leung, D. H.; Bergman, R. G.; Raymond, K. N. *J. Am. Chem. Soc.* **2004**, *126*, 3674.
- (22) Franco, P.; Mingullon, C. In *Chiral Separation Techniques: A Practical Approach*; 2nd ed.; Subramanian, G., Ed.; Wiley-VCH: Weinheim, 2007, p 1.
- (23) Xin, X.; Bradshaw, J. S.; Izatt, R. M. *Chem. Rev.* **1997**, *97*, 3313.
- (24) Svec, F.; Wulff, D.; Frechet, J. M. J. In *Chiral Separation Techniques: A Practical Approach*; 2nd ed.; Subramanian, G., Ed.; Wiley-VCH: Weinheim, 2007.
- (25) Goren, H. J.; Fridkin, M. *Eur. J. Biochem.* **1974**, *41*, 263.
- (26) Inanaga, J.; Furuno, H.; Hayano, T. *Chem. Rev.* **2002**, *102*, 2211.
- (27) Kobayashi, S.; Sugiura, M.; Kitigawa, H.; Lam, W. W.-L. *Chem. Rev.* **2002**, *102*, 2227.
- (28) Mei, Y.; Dissanayake, P.; Allen, M. J. *J. Am. Chem. Soc.* **2010**, *132*, 12871.
- (29) Kass, S.; Gregor, T.; Kersting, B. *Angew. Chem. Int. Ed.* **2006**, *45*, 101.
- (30) Stemmler, A. J.; Kampf, J. W.; Pecoraro, V. L. *Angew. Chem. Int. Ed. Engl.* **1996**, *35*, 2841.
- (31) Eliseeva, S. V.; Bunzli, J. C. *Chem. Soc. Rev.* **2010**, *39*, 189.

- (32) Bischof, C.; Wahsner, J.; Scholten, J.; Trosien, S.; Seitz, M. *J. Am. Chem. Soc.* **2010**, *132*, 14334.
- (33) Beeby, A.; Clarkson, I. M.; Dickins, R. S.; Faulkner, S.; Parker, D.; Royle, L.; de Sousa, A. S.; Williams, J. A. G.; Woods, M. *J. Chem. Soc., Perkin Trans. 2* **1999**, 493.
- (34) Comby, S.; Imbert, D.; Chauvin, A.-S.; Bunzli, J.-C. G. *Inorg. Chem.* **2006**, *45*, 732.
- (35) Moore, E. G.; Xu, J.; Dodani, S. C.; Jocher, C. J.; D'Aleo, A.; Seitz, M.; Raymond, K. N. *Inorg. Chem.* **2010**, *49*, 4156.
- (36) Jankolovits, J.; Andolina, C. M.; Kampf, J. W.; Raymond, K. N.; Pecoraro, V. L. *Angew. Chem. Int. Ed.* **2011**, *50*, 9660.
- (37) Bassett, A. P.; Deun, R. V.; Nockemann, P.; Glover, P. B.; Kariuki, B. M.; Hecke, K. V.; Meervelt, L. V.; Pikramenou, Z. *Inorg. Chem.* **2005**, *44*, 6140.
- (38) Pope, S. J. A.; Burton-Pye, B. P.; Berridge, R.; Khan, T.; Skabara, P. J.; Faulkner, S. *Dalton Trans.* **2006**, 2907.
- (39) D'Aleo, A.; Picot, A.; Beeby, A.; Williams, J. A. G.; Guennic, B. L.; Andraud, C.; Maury, O. *Inorg. Chem.* **2008**, *47*, 10258.
- (40) Lazarides, T.; Alamiry, M. A.; Adams, H.; Pope, S. J.; Faulkner, S.; Weinstein, J. A.; Ward, M. D. *Dalton Trans* **2007**, 1484.
- (41) W. D. Horrocks, J.; Bolander, J. P.; Smith, W. D.; Supkowski, R. M. *J. Am. Chem. Soc.* **1997**, *119*, 5972.
- (42) Imbert, D.; Cantuel, M.; Bunzli, J.-C. G.; Bernardinelli, G.; Piguet, C. *J. Am. Chem. Soc.* **2003**, *125*, 15698.
- (43) Ward, M. D. *Coord. Chem. Rev.* **2007**, *251*, 1663.
- (44) Verbiest, T.; Elshoct, S. V.; Kauranen, M.; Hellemans, L.; Snauwaert, J.; Nuckolls, C.; Katz, T. J.; Persoons, A. *Science* **1998**, *282*, 913.
- (45) Eaton, D. F.; Anderson, A. G.; Tam, W.; Wang, Y. *J. Am. Chem. Soc.* **1987**, *109*, 1886.
- (46) Szumna, A. *Chem. Soc. Rev.* **2010**, *39*, 4274.
- (47) Terpin, A. J.; Zeigler, M.; Johnson, D. W.; Raymond, K. N. *Angew. Chem. Int. Ed.* **2001**, *40*, 157.
- (48) Pedersen, C. J. *Angew. Chem. Int. Ed. Engl.* **1988**, *27*, 1021.